

# **Grating Coupled Surface Plasmons in Metallic Structures**

*Submitted by*

Zhuo Chen

To the University of Exeter as a thesis for the degree of Doctor of  
Philosophy in Physics, October 2007

This thesis is available for Library use on the understanding that it is  
copyright material and that no quotation from the thesis may be published  
without proper acknowledgement.

I certify that all material in this thesis which is not my own work has been  
identified and that no material has previously been submitted and approved  
for the award of a degree by this or any other University.

..... (signature)

# Abstract

Localised electromagnetic modes that propagate along the surface of a metal are known as surface plasmon polaritons (SPPs), or often simply surface plasmons (SPs). Control over the way in which these modes interact with incident radiation, by patterning the interface with a surface-relief periodic corrugation, opens up the possibility of developing new and exciting photonic devices. It is the purpose of the work presented in this thesis to investigate at a fundamental level several corrugated metallic structures which may provide control of the optical response by coupling radiation to surface plasmons.

The work presented is divided into three main sections. The initial experimental section is concerned with the coupling of incident radiation to localised SPP modes on short-pitch single-interface deep metal gratings. These SPP modes are observed experimentally even in the zero-order region of the spectrum, which was previously not thought possible. The frequency at which the localised SPP modes are excited is shown to be remarkably independent of the angle of incidence, i.e., they are extremely flat-banded.

In the second section the optical response of corrugated metallic microcavities is explored, with particular attention paid to the photonic band-gaps and anti-crossings of grating-coupled SPPs and waveguide modes. In particular, a flat photonic band caused by the anti-crossings between SPPs and waveguide modes is investigated and its presence is confirmed experimentally. The resonant frequency of this flat photonic band can be designed through appropriate choice of thickness of the guide medium and the amplitude of the grating.

In the third section the coupled SPPs on thin metal film gratings are investigated in both ‘classical’ and ‘conical’ mounts. In the classical mount investigations are concerned with the role the  $2k_g$  component in the grating profile plays in the appearance of band gaps. Two new phenomena are reported in the conical mount for TM polarization. Incident TM radiation is found to be strongly coupled to SPPs on relatively shallow thin metal gratings, while only very weak coupling is found for similar shallow single-interface metal gratings. A lack of coupling (zero coupling strength) to the Long Range SPP mode is also found for certain thicknesses of metal films.

## Table of Contents

---

# TABLE OF CONTENTS

<b><i>ABSTRACT</i></b> .....	2
<b><i>TABLE OF CONTENTS</i></b> .....	3
<b><i>LIST OF FIGURES</i></b> .....	6
<b><i>ACKNOWLEDGEMENTS</i></b> .....	25
<b><i>CHAPTER 1: INTRODUCTION</i></b> .....	27
<b><i>CHAPTER 2: SAMPLE FABRICATION, EXPERIMENTAL DATA MEASUREMENTS, AND MODELLING</i></b> .....	30
2.1 Sample Fabrication .....	30
2.1.1 One-dimensional dielectric gratings .....	30
2.1.2 Two-dimensional dielectric gratings .....	33
2.1.3 1-D and 2-D metal gratings.....	36
2.1.4 Corrugated microcavities .....	39
2.2 Measurement of the Optical Response of the Structures .....	40
2.3 Modelling .....	42
2.4 Summary .....	44
<b><i>CHAPTER 3: SURFACE PLASMON POLARITONS ON SHALLOW GRATINGS</i></b> .....	45
3.1 Introduction .....	45
3.2 The Surface Plasmon Polariton on a Planar Surface .....	47
3.2.1 The Dispersion Relation.....	47
3.2.2 Propagation Length .....	55
3.2.3 Penetration Depth.....	56
3.3 Grating Coupling to Surface Plasmon Polaritons .....	58
3.3.1 The Dispersion Relation.....	59

## Table of Contents

---

3.3.2 Coupling Strength and Reflectivity Features .....	63
3.3.3 Band Gaps in the Dispersion of Grating Coupled SPPs .....	66
3.3.4 Polarization Conversion.....	70
3.4 Summary .....	71
<b><i>CHAPTER 4: LOW DISPERSION OF SURFACE PLASMON Polaritons on Deep Silver Gratings .....</i></b>	<b>73</b>
4.1 Introduction .....	73
4.2 Self-coupled SPP Resonances and Flat SPP Bands on Deep Sinusoidal Silver Gratings .....	74
4.3 Self-coupled SPP Resonances on Deep Narrow Gaussian-grooved Silver Gratings .....	85
4.4 Summary .....	91
<b><i>CHAPTER 5: THE OPTICAL RESPONSE OF THIN SILVER SLABS Covered with Dielectric Films .....</i></b>	<b>92</b>
5.1 Introduction .....	92
5.2 Planar Waveguide – Planar Dielectric Films on the Metal Slabs ....	94
5.3 Corrugated Waveguide – Dielectric Gratings on the Metal Slabs ...	97
5.4 Summary .....	109
<b><i>CHAPTER 6: GRATING-COUPLED SPPS AND WAVEGUIDE MODES IN A SILVER-DIELECTRIC-SILVER STRUCTURE.....</i></b>	<b>111</b>
6.1 Introduction .....	111
6.2 Planar Silver Microcavity .....	112
6.3 Corrugated Silver Microcavity.....	117
6.3.1 Effective Mean Thickness of the Waveguide Medium .....	119
6.3.2 Band-gaps and anti-crossings in the dispersion curves.....	123
6.3.3 Flat photonic band with TM polarization.....	125
6.4 Summary .....	130

## **Table of Contents**

---

<b>CHAPTER 7: COUPLED SURFACE PLASMON POLARITONS ON THIN SILVER GRATINGS IN THE CLASSICAL MOUNT.....</b>	131
7.1 Introduction .....	131
7.2 SRSPP and LRSPP on Planar Silver Slabs .....	133
7.3 Coupled SPPs on Thin Silver Gratings in the Classical Mount....	136
7.4 Summary .....	153
<b>CHAPTER 8: COUPLED SURFACE PLASMON POLARITONS ON THIN SILVER GRATINGS IN THE CONICAL MOUNT .....</b>	155
8.1 Introduction .....	155
8.2 SPPs on Single Interface Metal Gratings in the Conical Mount ...	156
8.3 SPPs on Thin Metal Gratings in the Conical Mount .....	166
8.3.1 Coupling TE polarized radiation to coupled SPPs.....	167
8.3.2 Coupling TM polarized radiation to coupled SPPs.....	172
8.4 Summary .....	185
<b>CHAPTER 9: CONCLUSIONS AND FUTURE WORK.....</b>	186
9.1 Summary of Thesis .....	186
9.2 Possible Applications .....	188
9.3 Future Work.....	189
<b>PUBLICATIONS.....</b>	191
<b>REFERENCES .....</b>	192

## List of Figures

- Figure 2.1.1.1** A schematic of a typical two beam interferometer used for the fabrication of gratings. An expanded, collimated laser beam is split into two equal intensity beams which are then recombined on the face of a photoresist coated substrate. The pitch of the interference pattern and hence of the resulting grating is determined by the angle of incidence  $\theta$  and the radiation wavelength.
- Figure 2.1.1.2** One-dimensional numerically modelled map of the exposure across the surface of the photoresist produced by exposing the sample in the interferometer. The light regions represent high exposure, and the dark areas are low exposure.
- Figure 2.1.1.3** Scanning electron micrographs of top-view of a photoresist grating with a pitch of  $\sim 350$  nm. The side-view is shown in the inset.
- Figure 2.1.2.1** A numerically modelled map of the total exposure across the surface of the photoresist produced by exposing the sample twice in the interferometer. The substrate is rotated by  $90^\circ$  between exposures. The total exposure is therefore the sum of two sinusoidal patterns oriented at  $90^\circ$  to each other.
- Figure 2.1.2.2** SEM images of two-dimensional photoresist gratings prepared by using different exposure and developing time. (a), (b) exposed for 60 min at each exposure and developed for 4 seconds, (c), (d) exposed for 60 min at each exposure and developed for 7 seconds, and (d) exposed for 40 min the first exposure and 60 min the second exposure and developed for 5 seconds. The pitches of the gratings in two dimensions are set at  $\sim 250$  nm.
- Figure 2.1.3.1** A schematic of the vacuum deposition system used to evaporate silver on the sample.

## List of Figures

---

**Figure 2.1.3.2** SEM images of top-view of silver gratings fabricated by thermal evaporation of  $\sim 400$  nm thick silver on to the photoresist gratings with a pitch of  $\sim 262$  nm and a depth of (a)  $\sim 60$  nm, (b)  $\sim 500$  nm.

**Figure 2.1.3.3** Schematic of the fabrication of the silver gratings. First thick silver is evaporated on to the resist gratings. Then a substrate is attached to the silver film with epoxy resin. After removing the photoresist using acetone, the silver grating is prepared with the same pitch and depth as the resist grating, but reversed profile.

**Figure 2.1.3.3** SEM of one-dimensional (left image) and two-dimensional (right image) silver grating with a pitch of  $\sim 258$  nm and a depth of  $\sim 500$  nm.

**Figure 2.1.4.1** Schematic metallic waveguide structures comprising of the photoresist, with a periodically corrugated upper surface, deposited on an optically thin silver film supported by a silica substrate, (a) without top cladding silver layer, and (b) with top cladding silver layer.

**Figure 2.2.1** The coordinate system used with reference to the corrugation. The  $z$ -axis is parallel to the grating grooves, and the  $y$ -axis is perpendicular to the sample.  $\theta$  is the polar angle, and  $\varphi$  is the azimuth angle. The orientation of the incident beam is defined by  $\theta$  and  $\varphi$ .

**Figure 2.2.2** Schematic diagram illustrating the apparatus used to record the wavelength-dependent reflectivity data from the sample.

**Figure 2.2.3** (a) TM polarized angle-dependent reflectivity data, and (b) wavelength-dependent reflectivity data at  $\varphi = 0^\circ$  for single silver gratings.

**Figure 3.2.1.1** A schematic diagram of the incident, transmitted and reflected fields associated with a TM polarized electromagnetic wave incident on an interface bounded by two media described by complex dielectric constants  $\varepsilon_1(\omega)$  and  $\varepsilon_2(\omega)$ . The  $z$ -axis is out of the page.

**Figure 3.2.1.2** The SPP dispersion curve (solid line) for a planar silver/air interface. The dashed line is the light line. The dotted line represents the high  $k_x$  asymptotic limit of  $\omega_{sp}$ .

## List of Figures

---

- Figure 3.2.1.3** Total reflection of light at one side of a prism. The prism is a dielectric medium ( $\epsilon_p$ ) such as glass or quartz; around the prism is air or vacuum.
- Figure 3.2.1.4** (a) The Otto configuration. A dielectric gap lies between the prism and the metal surface. (b) The dispersion curve on a silver/air interface together with light-lines in air (dashed line) and silica (dotted line). At point A, a SPP mode with wave vector  $k_{\text{spp}} = 0.253 \times 10^8 \text{ m}^{-1}$  is excited by the light with a frequency  $\omega_L = 0.632 \times 10^{16} \text{ s}^{-1}$  and incident angle  $\theta = 55^\circ$ .
- Figure 3.2.1.5** (a) The Kretschmann-Raether configuration. The metal contacts the prism. (b) The dispersion curve for the silver/air and silver/silica interface together with light-lines in air (dashed line) and silica (dotted line). The incident light beam can excite a SPP mode at point A.
- Figure 3.2.2.1** Propagation length as a function of wavelength for a planar silver/air interface. The frequency dependent dielectric function for silver is modelled using a Drude model with  $\omega_p = 1.32 \times 10^{16} \text{ s}^{-1}$  and  $\tau = 1.45 \times 10^{-14} \text{ s}$ .
- Figure 3.2.3.1** The penetration depth of the SPP fields into (a) silver and (b) air for a planar silver/air system. The frequency dependent dielectric function for the silver is modelled using the Drude model with  $\omega_p = 1.32 \times 10^{16} \text{ s}^{-1}$  and  $\tau = 1.45 \times 10^{-14} \text{ s}$ .
- Figure 3.2.3.2** Schematic representation of the polarization surface charge density and associated electric field for the SPP mode. The field decays exponentially into both the metal ( $\epsilon_2$ ) and dielectric ( $\epsilon_1$ ).
- Figure 3.3.1.1** A schematic showing the grating system under consideration. The direction of the electric field vector ( $\mathbf{E}$ ) is shown for incident TM polarized radiation. Here  $\lambda_g$  is the grating pitch,  $\theta$  is the incident angle,  $\varphi$  is the azimuth angle,  $a$  is the grating amplitude.
- Figure 3.3.1.2** The dispersion curve for grating-coupled SPPs which has been folded at the Brillouin zone boundaries. Parts of the scattered dispersion

## List of Figures

---

curves (shaded) that fall between the light lines can be radiatively coupled.

**Figure 3.3.1.3** A 2-D reciprocal space representation of the SPP modes and light circles produced by a grating. The thick-dashed circle of  $k_0$  centred upon the origin describes the maximum wave vector available to a photon in the plane of the grating surface. The circle (thick-solid) at a slightly greater radius than this represents the momentum of the zero-order SPP mode ( $k_{\text{SPP}}$ ). Both of these circles may be scattered by  $\pm k_g$ , which results in the two circles centred at the reciprocal lattice points. The arrows indicate that via a grating vector of  $k_g$  a photon at angle of incidence  $\theta$  and azimuth angle  $\varphi$  is coupled to a SPP that propagates at an angle  $\Psi$  with respect to the  $k_x$ -axis.

**Figure 3.3.2.1** Theoretical zero-order TM reflectivity as a function of frequency for a 10 nm amplitude 650 nm pitch silver grating for normal incidence and  $\varphi = 0^\circ$ . The frequency dependent dielectric constant of silver is modelled as a Drude model with  $\omega_p = 1.32 \times 10^{16} \text{ s}^{-1}$  and  $\tau = 1.45 \times 10^{-14} \text{ s}$ . A reflectivity minimum arises at  $f = 0.449 \times 10^{15} \text{ Hz}$  due to the excitation of the first order SPP. A pseudo critical edge appears at  $f = 0.46 \times 10^{15} \text{ Hz}$  where the first diffracted order becomes evanescent.

**Figure 3.3.2.2** Theoretical zero-order TM reflectivity as a function of frequency at normal incidence and  $\varphi = 0^\circ$  for a silver grating with a pitch of 650 nm and different amplitudes. The dielectric constant of silver is described by a Drude model with  $\omega_p = 1.32 \times 10^{16} \text{ s}^{-1}$  and  $\tau = 1.45 \times 10^{-14} \text{ s}$ .

**Figure 3.3.3.1** Numerically modelled zero-order TM reflectivity of a purely sinusoidal metal grating with a fundamental amplitude of 5 nm and a pitch of 650 nm. The dielectric constant of the metal is fixed at  $\epsilon_r = -17.5$  and  $\epsilon_i = 0.6$ .

**Figure 3.3.3.2** Numerically modelled zero-order TM reflectivity of a metal grating structure with a pitch of 650 nm and  $a_1 = 5 \text{ nm}$ ,  $a_2 = 2 \text{ nm}$ , and  $\phi_2 = 0^\circ$ .

## List of Figures

---

The first harmonic component produces a band gap at the intersection of the  $\pm 1$  SPP branches. The dielectric constant of the metal is fixed at  $\varepsilon_r = -17.5$  and  $\varepsilon_i = 0.6$ .

- Figure 3.3.3.3** A schematic representation of the electric field and surface charge distributions for the two standing wave solutions at the gap boundaries of a band gap. The upper sketch is for the lower frequency solution ( $\omega^-$ ). The volume integrals of the energy density in the two field distributions show that  $\omega^+$  is of higher energy.
- Figure 3.3.3.4** Numerically modelled zero-order TM reflectivity of a metal grating structure with a pitch of 650 nm and  $a_1 = 5$  nm,  $a_2 = 2$  nm, and phase shift between the first and fundamental harmonic component (a)  $\phi_2 = +90^\circ$  and (b)  $\phi_2 = -90^\circ$ . The dielectric constant of the metal is  $\varepsilon_r = -17.5$  and  $\varepsilon_i = 0.6$ .
- Figure 3.3.3.5** Sketch of light at normal incidence coupling to the modes of a corrugated surface (solid line) containing  $k_g$  (dashed line) and  $2k_g$  (dotted line) components.
- Figure 4.2.1** Schematic diagram illustrating the sample and coordinate system. Here  $a$  is the grating amplitude,  $\lambda_g$  is the grating pitch,  $\theta$  is the polar angle, and  $\varphi$  is the azimuth angle.
- Figure 4.2.2** TM polarised reflectivity as a function of frequency and in-plane wave-vector for 258 nm pitch sinusoidal silver gratings with (a)  $d = 50$  nm and (b)  $d = 300$  nm at azimuth angle  $\varphi = 0^\circ$ . White dotted lines indicate the SPP modes.
- Figure 4.2.3** Time averaged  $|H_z|$  component of the field distributions for the SPP resonance at  $k_x = 0$  for (a)  $d = 50$  nm,  $f = 0.942 \times 10^{15}$  Hz, (b)  $d = 300$  nm,  $f = 0.3 \times 10^{15}$  Hz, (c)  $d = 300$  nm,  $f = 0.673 \times 10^{15}$  Hz, and (d)  $d = 300$  nm,  $f = 0.972 \times 10^{15}$  Hz. The white line represents the grating profile.

## List of Figures

---

- Figure 4.2.4** SEM images of silver gratings with the electron beam incident at  $62^\circ$  to the sample normal. The gratings both have the same pitch of 258 nm, but different depths of (a) 124 nm and (b) 166 nm.
- Figure 4.2.5** TM polarized experimental (square) and modelled (solid line) wavelength-dependent reflectivity data obtained at different incident angles ( $10^\circ \leq \theta \leq 70^\circ$ ) and a fixed azimuth angle  $\varphi = 0^\circ$  for a silver grating with a depth of 124 nm.
- Figure 4.2.6** TM polarized experimental (square) and modelled (solid line) wavelength-dependent reflectivity data obtained at different incident angles ( $10^\circ \leq \theta \leq 70^\circ$ ) and a fixed azimuth angle  $\varphi = 0^\circ$  for a silver grating with a depth of 166 nm.
- Figure 4.2.7** The dispersion curves of the SPP modes obtained from the reflectivity data for different incident angles. The solid lines are the light line and diffracted light line. The open squares, circles and triangles are computed from the model used to produce the fits shown in Figure 4.2.5 and Figure 4.2.6. Squares are for the first order SPP mode for the 124 nm deep sample, triangles are for the first order SPP mode and circles are for the second order SPP mode for the 166 nm deep sample. The crosses are the experimental data.
- Figure 4.2.8** Time averaged  $|H_z|$  component of the field distributions for the SPP resonance for (a)  $d = 124$  nm,  $f = 0.625 \times 10^{15}$  Hz,  $\theta = 35^\circ$ , (b)  $d = 166$  nm,  $f = 0.513 \times 10^{15}$  Hz,  $\theta = 35^\circ$ , and (c)  $d = 166$  nm,  $f = 0.721 \times 10^{15}$  Hz,  $\theta = 35^\circ$ . The white line represents the grating profile.
- Figure 4.3.1** SEM image (a) and modelled profile (b) of 520 nm deep, 38 nm wide Gaussian-grooved, 258 nm pitch silver grating.
- Figure 4.3.2** Reflectivity as a function of frequency and in-plane wave vector for TM polarized light incident on a 520 nm deep, 38 nm wide Gaussian-grooved, 258 nm pitch silver grating oriented at azimuth angle  $\varphi = 0^\circ$ . White dotted lines indicate the SPP modes.

## List of Figures

---

- Figure 4.3.3** The results of the wavelength-dependent reflectivity for TM polarization at polar angles (a) – (f)  $\theta = 15^\circ, 25^\circ, 35^\circ, 45^\circ, 55^\circ$ , and  $65^\circ$  respectively.
- Figure 4.3.4** The modelled TM polarized wavelength dependent reflectivity spectra of the structure shown in Figure 4.3.1 (b) at polar angle  $\theta = 35^\circ$  and azimuth angle  $\varphi = 0^\circ$ . The positions indicated by numbers 1, 2, and 3 are SPPs resonant reflection dips. The peak indicated by number 4 corresponds to the diffracted order pseudo critical edge. The position indicated by number 5 represents an arbitrary off-resonance position.
- Figure 4.3.5** The dispersion of the experimental reflectivity minima (indicated by squares) obtained from the reflection spectra. The modes marked as (I) – (IV) can be identified as 2<sup>nd</sup>, 3<sup>rd</sup>, 4<sup>th</sup>, and 5<sup>th</sup> order SPP modes respectively. The dashed and dotted lines are the light line and the diffracted order light line. The open triangles are the experimental reflection peaks.
- Figure 4.3.6**  $|H_z|$  for the second, third, and fourth order self-coupled SPPs on a 520 nm deep, 38 nm wide, Gaussian-grooved grating at  $\theta = 35^\circ$  and  $\varphi = 0^\circ$ . (a)  $f = 0.329 \times 10^{15}$  Hz, (b)  $f = 0.49 \times 10^{15}$  Hz, and (c)  $f = 0.624 \times 10^{15}$  Hz.
- Figure 4.3.7**  $|H_z|$  for (a) the diffracted order pseudo critical edge  $f = 0.734 \times 10^{15}$  Hz, which is indicated by number 4 in Figure 4.3.4, and (b) an off-resonant frequency  $f = 0.44 \times 10^{15}$  Hz, which is indicated by number 5 in Figure 4.3.4, at  $\theta = 35^\circ$  and  $\varphi = 0^\circ$ .
- Figure 5.2.1** Schematic diagram illustrating a planar waveguide structure consisting of a photoresist layer (with a thickness of  $d$ ) deposited on a thin silver film (with a thickness of  $t$ ). The silver film is attached to the silica prism with matching fluid to create an ATR system.
- Figure 5.2.2** Band structures for a planar waveguide with a fixed thickness of silver film  $t = 60$  nm and with photoresist film thicknesses (a)  $d = 0$  nm, (b)  $d = 50$  nm, (c)  $d = 100$  nm, and (d)  $d = 150$  nm. The open triangles represent the SPP modes that propagate along the silica/silver interface,

## List of Figures

---

open circles indicate the SPP modes supported at the top surface of the silver film, and open squares are the waveguide modes.

**Figure 5.2.3** The theoretical reflectivity of the planar waveguide structure with the thickness of photoresist layer  $d = 150$  nm, the same as that used in Figure 5.2.2 (d), for (a) TM polarization and (b) TE polarization. The white polygon in the bottom right corner indicates the inaccessible region beyond the silica light line.

**Figure 5.3.1** Schematic diagram illustrating the sample, coordinate system, and experimental geometry used in this work. Here  $a$  is the grating amplitude,  $d$  is the average thickness of the photoresist layer,  $t$  is the thickness of the silver tunnel barrier,  $\theta$  is the polar angle, and  $\varphi$  is the azimuth angle. The silica substrate is optically attached to the silica prism with matching fluid.

**Figure 5.3.2** The results of the absolute wavelength-dependent reflectivity for p-polarised incident light at polar angles (a)  $\theta = 45^\circ$  and (b)  $\theta = 58.5^\circ$ . The solid lines are theoretically modelled results. The squares are experimental data. The density of experimental data points has been reduced for clarity.

**Figure 5.3.3** The theoretical band structure for the waveguide structure at  $\varphi = 0^\circ$ . The unscattered modes can be identified as (i) the SPP mode that propagates at the silver/silica interface, (ii) the SPP mode that is supported by silver/resist interface, (iii) TE<sub>1</sub>, (iv) TM<sub>1</sub>, (v) TE<sub>2</sub>, and (vi) TM<sub>2</sub> mode respectively. All of these modes will suffer Bragg-scattering thereby ‘reflecting’ at the Brillouin zone boundary.

**Figure 5.3.4** The theoretical TM reflectivity (a) and TE reflectivity (b) as a function of frequency and in-plane wave vector for the waveguide structure with light incident at  $\varphi = 0^\circ$ . The white polygon in the bottom right corner indicates the inaccessible region beyond the silica light line. Two modes, TM<sub>1</sub> and TM<sub>2</sub>, can be accessed in the visible for TM polarisation. The squares in (a) are the mapped reflection dips that are taken from the experimental reflectivity spectra. One band-gap is

## List of Figures

---

formed at the first Brillouin zone boundary ( $2k_x/k_g = 1$ ) with the centre frequency  $f_c = 0.491 \times 10^{15}$  Hz.

**Figure 5.3.5** The theoretical TM reflectivity at azimuthal angle  $\varphi = 90^\circ$  as a function of frequency and in-plane wave vector for the structure with the corrugation on the top surface of the photoresist (a), and planar structure without top corrugation (b). The white squares in (a) are the experimental data taken from the reflection spectra. The in-plane wavevector components  $k_z$  and  $k_x$  are scaled to  $k_g/2$ .

**Figure 5.3.6** TM reflectivity for the waveguide structure at  $\varphi = 10^\circ$  to  $80^\circ$ . The white squares in each plot indicate the corresponding experimental data. The dashed line box in (a) – (e) indicates the band gap at the first BZ boundary. The two dashed lines in (d) indicate the polar angle  $\theta = 45^\circ$  and  $58.5^\circ$ .

**Figure 5.3.7** The magnetic field amplitude distribution for the guided modes resonance at polar angle  $\theta = 58.5^\circ$  and azimuth angle  $\varphi = 40^\circ$  for (a)  $f = 0.522 \times 10^{15}$  Hz, (b)  $f = 0.532 \times 10^{15}$  Hz, (c)  $f = 0.571 \times 10^{15}$  Hz, (d)  $f = 0.635 \times 10^{15}$  Hz and (e)  $f = 0.709 \times 10^{15}$  Hz. The white line represents the wave guide structure.

**Figure 5.3.8** The magnetic field amplitude distribution for the guided modes resonance at polar angle  $\theta = 45^\circ$  and azimuth angle  $\varphi = 40^\circ$  for (a)  $f = 0.394 \times 10^{15}$  Hz, (b)  $f = 0.585 \times 10^{15}$  Hz, (c)  $f = 0.643 \times 10^{15}$  Hz, (d)  $f = 0.682 \times 10^{15}$  Hz and (e)  $f = 0.729 \times 10^{15}$  Hz. The white line represents the wave guide structure.

**Figure 6.2.1** Schematic diagram illustrating the sample and the coordinate system used in this work. Here  $t$  is the thickness of the silver tunnel barrier,  $\theta$  is the polar angle, and  $d$  is the thickness of the photoresist layer. The silver cladding layer is semi-infinite. The silica substrate is optically attached to the silica prism with matching fluid.

**Figure 6.2.2** Band structure for the planar silver microcavity with thickness of the silver film  $t = 56.8$  nm and the photoresist layer  $d = 300.8$  nm. The

## List of Figures

---

open squares represent the SPP modes that are supported by the silica/silver and silver/photoresist interface. The open triangles, circles, and stars indicate the first, second, and third order TM/TE polarized waveguide modes respectively. The horizontal line represents the usual cavity cutoff frequency  $0.2695 \times 10^{15}$  Hz.

**Figure 6.2.3** The theoretical reflectivity as a function of frequency and in-plane wave vector for (a) TM polarization and (b) TE polarization. The white triangular region in the bottom right corner indicates the inaccessible region beyond the silica light line.

**Figure 6.2.4** Time averaged  $|E_x|$  component of field distributions at  $\theta = 0^\circ$  for (a) first order wave guide mode,  $f = 0.2695 \times 10^{15}$  Hz, (b) second order wave guide mode,  $f = 0.514 \times 10^{15}$  Hz, and (c) third order wave guide mode,  $f = 0.7615 \times 10^{15}$  Hz. The dashed lines schematically show the  $E_x$  field profiles for 1<sup>st</sup>, 2<sup>nd</sup>, and 3<sup>rd</sup> order standing wave.

**Figure 6.3.1** Schematic diagram illustrating the sample, the coordinate system, and the experimental geometry used in this work. Here  $a$  is the grating amplitude,  $t$  is the thickness of the silver tunnel barrier,  $\theta$  is the polar angle,  $\varphi$  is the azimuth angle, and  $d$  is the average thickness of the photoresist layer. The silica substrate is optically attached to the silica prism with matching fluid. Note in our experiments to set the different azimuth angles ( $\varphi$ ) only the sample is rotated, not the prism.

**Figure 6.3.2** The results of the wavelength-dependent reflectivity for TM polarization at angles (a)  $\theta = 55.2^\circ$ ,  $\varphi = 0^\circ$ , and (b)  $\theta = 58.6^\circ$ ,  $\varphi = 90^\circ$ , and for TE polarization at angles (c)  $\theta = 25.0^\circ$ ,  $\varphi = 0^\circ$ , and (d)  $\theta = 34.8^\circ$ ,  $\varphi = 90^\circ$ . The solid lines on each of the graphs correspond to the experimental data. The black open squares are theoretically modelled results.

**Figure 6.3.1.1** The theoretical TE reflectivity for (a)  $\varphi = 0^\circ$  and (c)  $\varphi = 90^\circ$ , and TM reflectivity for (b)  $\varphi = 0^\circ$  and (d)  $\varphi = 90^\circ$  as a function of frequency and in-plane wave vector. The open black squares are the mapped

## List of Figures

---

reflection dips that are taken from the experimental reflectivity spectra. The dashed straight line indicates the silica light line. The dotted line in the upper two diagrams represents the first order diffracted silica light line. The white triangular region in the bottom right corner indicates the inaccessible region beyond the silica light line.

- Figure 6.3.1.2** The theoretical band structure for the waveguide structure at  $\phi = 0^\circ$ . The unscattered modes can be identified as (i) SPP mode that is supported by silver/photoresist interface, (ii) the SPP mode that propagates at the silver/silica interface, (iii) TM<sub>1</sub> waveguide mode, (iv) TE<sub>1</sub> guide mode, and (vi) TE<sub>2</sub> mode respectively. Note the flat character of mode (v).
- Figure 6.3.1.3** Time averaged  $|E_x|$  and  $|E_z|$  profiles for TE<sub>2</sub> guided modes at  $\theta = 0^\circ$ . (a)  $|E_x|$  profile in the planar structure at  $f = 0.514 \times 10^{15}$  Hz,  $\phi = 90^\circ$ , (b)  $|E_z|$  profile in the planar structure at  $f = 0.514 \times 10^{15}$  Hz,  $\phi = 0^\circ$ , (c)  $|E_x|$  profile in the microcavity structure with corrugations at  $f = 0.4295 \times 10^{15}$  Hz,  $\phi = 90^\circ$ , and (d)  $|E_z|$  profile in the microcavity structure with corrugations at  $f = 0.5245 \times 10^{15}$  Hz,  $\phi = 0^\circ$ . The thickness of the upper silver layer and resist waveguide medium are 56.8 nm and 300.8 nm for the planar structure.
- Figure 6.3.2.1** Time averaged  $|E_z|$  profiles for TE polarization  $\phi = 0^\circ$  at (a)  $f = 0.6545 \times 10^{15}$  Hz and  $\theta = 38.2^\circ$ , (b)  $f = 0.6125 \times 10^{15}$  Hz and  $\theta = 41.6^\circ$ . The top white solid line represents the silica/silver interface; the middle one represents the silver/resist plane interface and the bottom, corrugated, one represents the silver/resist interface.
- Figure 6.3.2.2** Time averaged  $|E_z|$  profiles for TE polarization with  $\theta = 25.0^\circ$  and  $\phi = 0^\circ$  at (a)  $f = 0.65765 \times 10^{15}$  Hz and (b)  $f = 0.554 \times 10^{15}$  Hz. The white solid lines represent the profile of the structure.
- Figure 6.3.3.1** The theoretical band predictions for the waveguide structure at  $\phi = 0^\circ$ , with a sinusoidal grating of amplitude (a) 5 nm, (b) 15 nm, (c) 30 nm, and (d) 40 nm. The modes in (a) can be identified as (i) unscattered

## List of Figures

---

SPP at the silver/resist interface, (ii) unscattered SPP at the silver/silica interface, (iii) unscattered TM<sub>1</sub> guided mode, (iv) unscattered TM<sub>2</sub> guided mode, (v) scattered SPP at the silver/resist interface ( $+k_g$ ), (vi) scattered TM<sub>1</sub> guided mode( $+k_g$ ), (vii) scattered SPP at the silver/silica interface ( $+k_g$ ), and (viii) scattered TM<sub>2</sub> guided mode ( $+k_g$ ). The dashed line box in each plot indicates the anti-crossing caused by mode iv (unscattered TM<sub>2</sub> guided mode) interfering with both mode vi (scattered TM<sub>1</sub> mode) and mode v (scattered SPP mode).

- Figure 6.3.3.2** Time averaged  $|H_z|$  profile for the mode at  $\varphi = 0^\circ$  with a resonant frequency  $f = 0.4295 \times 10^{15}$  Hz and polar angle  $\theta = 4.9^\circ$ .
- Figure 6.3.3.3** The theoretical band predictions for the waveguide structure at  $\varphi = 0^\circ$ , with sinusoidal grating of amplitudes (a) 60 nm, (b) 75 nm, (c) 100 nm, and (d) 140 nm.
- Figure 7.2.1** Schematic diagram illustrating the geometry and coordinate system. Here  $t$  is the thickness of the silica layer,  $d$  is the thickness of the silver film, and  $\theta$  is the polar angle. A dielectric prism with refractive index of 2.5 is optically attached to the top surface of the silica layer. The position  $y = 0$  corresponds to the bottom silver/silica interface.
- Figure 7.2.2** (a) TM polarized reflectivity as a function of thickness of silver film and incident angles for incident light with a fixed frequency  $f = 0.501 \times 10^{15}$  Hz and the thickness of silica gap  $t = 440$  nm. (b) TM polarized angle-scan reflectivity for thicknesses of silver film  $d = 40$  nm and 140 nm at a fixed frequency  $f = 0.501 \times 10^{15}$  Hz.
- Figure 7.2.3** Schematics showing the charge distributions for (a) the LRSPP, and (b) the SRSPP.
- Figure 7.2.4** Instantaneous electric field profiles for the (a) LRSPP and (b) SRSPP.  $E_x$  and  $E_y$  ( $x$  and  $y$  defined in Figure 7.2.1) are parallel and perpendicular components respectively. The silver film locates between  $y = 0$  and  $y = 40$  nm.

## List of Figures

---

- Figure 7.3.1** Schematic diagram illustrating the sample, coordinate system, and experimental geometry used in this work. Here  $\lambda_g$  is the grating pitch,  $d$  is the thickness of the silver layer, and  $\theta$  is the polar angle. The silver layer is bounded with identical silica media.
- Figure 7.3.2** The optical response, (a) reflection, (b) transmission (log scale), and (c) absorption as a function of frequency and silver film thickness at normal incidence for a silver film with conformal sinusoidal corrugations (fundamental amplitude  $a_0 = 20$  nm and pitch  $\lambda_g = 335$  nm) on both sides in the classical mount.
- Figure 7.3.3** Typical wavelength-dependent absolute reflectivity data (open squares) together with the model fits (solid lines) when the light is incident from the 1<sup>st</sup> prism with a  $+\pi/2$  phase shift between the first harmonic and the fundamental at polar angle (a)  $\theta = 6.2^\circ$  and (b)  $\theta = 25.0^\circ$ , and from the 2<sup>nd</sup> prism with  $-\pi/2$  phase shift at polar angle (c)  $\theta = 6.2^\circ$  and (d)  $\theta = 25.0^\circ$ . The density of experimental data points has been reduced for clarity.
- Figure 7.3.4** The model band structures for silver gratings having different profiles in the classical mount. The profile describing the structures is given by (a)  $[20 \sin(k_g x)]$  nm, and (b)  $[20 \sin(k_g x) + 5 \sin(2k_g x + \pi/2)]$  nm, and (c)  $[20 \sin(k_g x)]$  nm for the bottom surface and  $[20 \sin(k_g x) + 27]$  nm for the top surface, and (d)  $[20 \sin(k_g x) + 5 \sin(2k_g x + \pi/2)]$  nm for the bottom surface and  $[20 \sin(k_g x) + 5 \sin(2k_g x + \pi/2) + 27]$  nm for top surface. The inset graphs correspond to the gratings that have been used in the calculations. The dashed line box in the last two graphs indicates the crossing point that arises from scattering of the LRSPP by  $+k_g$  and scattering of the SRSPP by  $-k_g$ .
- Figure 7.3.5** The model TM reflectivity as a function of frequency and in-plane wave vector with light incident from (a) the 1<sup>st</sup> prism and (b) the 2<sup>nd</sup> prism. The open white squares are the mapped reflection dips that are taken from the experimental reflectivity spectra. The dashed straight

## List of Figures

---

line indicates the first order diffracted light line. The dashed line box indicates the crossing point between the LRSPP and the SRSPP.

**Figure 7.3.6** Time averaged  $|H_z|$  component of the fields of (a) the SRSPP and (b) the LRSPP modes that can be excited at normal incidence, together with the instantaneous  $E_{xy}$  vector fields for (c) the SRSPP and (d) the LRSPP modes on the same structure as described in Figure 7.3.4(a) (incident from the 1<sup>st</sup> prism with the phase shift  $\phi = +\pi/2$ ). The continuous black lines represent the thin metal grating.

**Figure 7.3.7** Schematics showing the positions of maximum surface charge density of the possible standing wave coupled modes for normal incidence that may be excited on the structure. The black lines represent the thin metal grating. The dashed lines indicate the  $2k_g$  component of the grating.

**Figure 7.3.8** Time averaged  $|H_z|$  component of the fields of (a) the SRSPP and (b) the LRSPP modes that can be excited at normal incidence, together with the instantaneous  $E_{xy}$  vector fields for (c) the SRSPP and (d) the LRSPP modes on the same structure as described in Figure 7.3.5 (b) (incident from the 2<sup>nd</sup> prism with phase shift  $\phi = -\pi/2$ ). The continuous black lines represent the thin metal grating.

**Figure 7.3.9** The values taken from the scattering matrix calculated for a thin silver grating in the classical mount over a range of frequencies at normal incidence. The inset graph corresponds to the grating that has been used in the calculations. The profile describing the structure is given by  $[20 \sin(k_g x) + 5 \sin(2k_g x)]$  nm for the bottom surface and  $[20 \sin(k_g x) + 5 \sin(2k_g x) + 27]$  nm for the top surface. Note that the phase shift  $\phi$  between  $2k_g$  and  $k_g$  is 0.

**Figure 7.3.10** Schematics showing the positions of maximum surface charge density of the possible short range SPP modes for normal incidence that may be excited on the structure. The black lines represent the thin metal grating. The dashed lines indicate the  $2k_g$  component of the grating.

## List of Figures

---

- Figure 7.3.11** Time averaged  $|H_z|$  component of the fields (a) together with the instantaneous  $E_{xy}$  vector fields (b) of the SRSPP mode ( $f = 0.468 \times 10^{15}$  Hz) that can be excited at normal incidence on the same structure as described in Figure 7.3.9 (with phase shift  $\phi = 0^\circ$ ). The continuous lines represent the thin metal grating.
- Figure 7.3.12** The model band structure for silver gratings in the classical mount. The profile describing the structure is given by  $[20 \sin(k_g x) + 5 \sin(2k_g x - \pi/2)]$  nm for the bottom surface and  $[20 \sin(k_g x) + 5 \sin(2k_g x + \pi/2) + 27]$  nm for top surface. The inset graph corresponds to the model dispersion of the optical modes over a range of frequencies for  $k_x = 0$ .
- Figure 7.3.13** Schematics showing the positions of maximum surface charge density of the possible short range SPP modes for normal incidence that may be excited on the structure. The black lines represent the thin metal grating. The dashed lines indicate the  $2k_g$  component of the grating.
- Figure 7.3.14** The model band structure for silver gratings in the classical mount. The profile describing the structure is given by  $[10 \sin(k_g x)]$  nm for the bottom surface and  $[-10 \sin(k_g x) + 27]$  nm for the top surface. The inset graph (bottom-left) corresponds to the grating that has been used in the calculations. The inset graph (upper-right) corresponds to the model dispersion of the optical modes over a range of frequencies for  $k_x = 0$ .
- Figure 8.2.1** Schematic diagram illustrating the sample and coordinate system used in this work. Here  $\lambda_g$  is the grating pitch,  $d$  is the thickness of the silver layer,  $\theta$  is the polar angle, and  $\varphi$  is the azimuth angle which is set to  $90^\circ$  in this chapter. The silver layer is bounded with silica media.
- Figure 8.2.2** Model reflectivity, for (a) TE and (b) TM polarized radiation incident upon a 252 nm pitch sinusoidal silver grating at  $\theta = 25.0^\circ$  and  $\varphi = 90^\circ$ , plotted as a function of the frequency and the amplitude. The dashed line represents the pseudo-critical edge. The inset graph plots the

## List of Figures

---

reflectivity minimum as a function of amplitude for the lowest frequency mode.

**Figure 8.2.3** Instantaneous electric field vector  $E_{xy}$  distributions at  $\theta = 25.0^\circ$  and  $\varphi = 90^\circ$  for (a) TE mode (resonant frequency  $f = 0.725 \times 10^{15}$  Hz) and (b) TM mode (resonant frequency  $f = 0.729 \times 10^{15}$  Hz) on the silver grating with a pitch of 252 nm and an amplitude of 10 nm. The black line represents the silica/silver corrugated interface.

**Figure 8.2.4** Instantaneous electric field vector  $E_{xz}$  distributions on the grating surface of (a) TE mode ( $f = 0.725 \times 10^{15}$  Hz) and (b) TM mode ( $f = 0.729 \times 10^{15}$  Hz) at  $\theta = 25.0^\circ$  and  $\varphi = 90^\circ$  for the silver grating with a pitch of 252 nm and an amplitude of 10 nm. The fields are plotted in the  $x$ - $z$  plane and one repeat period of the structure is shown ( $\lambda_g$ ). Solid black line ( $x = -189.2$  nm) represents the grating peak. Dashed black line ( $x = -63.2$  nm) represents the grating trough.

**Figure 8.2.5** Theoretical Absorption ( $A = 1 - R$ ), for (a) TE and (b) TM polarized 381 nm ( $f = 0.785 \times 10^{15}$  Hz) radiation incident upon a 252 nm pitch sinusoidal silver grating at  $\varphi = 90^\circ$ , plotted as a function of incident angle and amplitude.

**Figure 8.2.6** Typical angle-scan TM polarized absorption peak for 381 nm ( $f = 0.785 \times 10^{15}$  Hz) radiation incident upon a 252 nm pitch sinusoidal silver grating at  $\varphi = 90^\circ$ . Open circles represent the theoretical calculation results. The solid line represents the fitted Lorentz function with parameters:  $f_0 = 0.01935$ ,  $x_c = 42.31553$ ,  $w = 1.53536$ , and  $A = 0.95851$ .

**Figure 8.2.7** The mode width ( $\Delta\theta$ ) of TE and TM polarized absorption peak for 381 nm ( $f = 0.785 \times 10^{15}$  Hz) radiation incident upon a 252 nm pitch sinusoidal silver grating at  $\varphi = 90^\circ$ , plotted against the amplitude square ( $a^2$ ). Open triangles represent the TM polarized single-interface SPP (SISPP) case. Open squares represent the TE polarized SISPP

## List of Figures

---

case. Dashed and dotted lines represent the linear fitting for TM and TE polarizations respectively.

- Figure 8.3.1.1** Theoretical TE polarized (a) reflection and (b) transmission as a function of frequency and thickness at  $\theta = 42.3^\circ$  in the conical mount ( $\varphi = 90^\circ$ ) for a thin silver grating with conformal sinusoidal corrugations (fundamental amplitude  $a_0 = 8$  nm and pitch  $\lambda_g = 252$  nm) on both sides.
- Figure 8.3.1.2** Theoretical TE polarized absorption as a function of frequency and silver film thickness at  $\theta = 42.3^\circ$  for thin silver film gratings with same pitch  $\lambda_g = 252$  nm but different fundamental amplitude (a)  $a_0 = 4$  nm, (b)  $a_0 = 8$  nm, (c)  $a_0 = 12$  nm, and (d)  $a_0 = 16$  nm in the conical mount ( $\varphi = 90^\circ$ ). The dashed line represents the thickness  $d = 23$  nm.
- Figure 8.3.1.3** Instantaneous  $E_{xy}$  vector fields of (a) the SRSPP ( $f = 0.625 \times 10^{15}$  Hz), (b) the second order SRSPP ( $f = 0.859 \times 10^{15}$  Hz), and (c) the LRSPP ( $f = 0.933 \times 10^{15}$  Hz) that can be excited on a thin silver film grating with thickness of 23 nm, pitch of 252 nm and amplitude of 8 nm at  $\theta = 42.3^\circ$  and  $\varphi = 90^\circ$ . The continuous lines represent the thin metal grating.
- Figure 8.3.1.4** Theoretical TE polarized Absorption ( $A = 1 - R - T$ ) as a function of incident angle and amplitude for (a) the LRSPP excited by a fixed frequency  $f = 0.785 \times 10^{15}$  Hz and (b) the SRSPP excited by a fixed frequency  $f = 0.625 \times 10^{15}$  Hz on a 252 nm pitch thin silver grating with thickness of 23 nm in the conical mount, together with the mode width ( $\Delta\theta$ ) of (c) the LRSPP and (d) the SRSPP absorption peak plotted against the amplitude square ( $a^2$ ).
- Figure 8.3.2.1** Experimental wavelength-dependent reflectivity data (open circles) together with the model fits (solid lines) when TM polarized light is incident on a thin silver sinusoidal grating with thickness of 23 nm, pitch of 252 nm, and amplitude of 8 nm at different polar angles

## List of Figures

---

$\theta = 71.1^\circ, 65.0^\circ, 58.6^\circ, 51.8^\circ, 45.0^\circ$ , and  $38.2^\circ$  in the conical mount ( $\varphi = 90^\circ$ ).

**Figure 8.3.2.2** Experimental reflection (open squares), transmission (open triangles), and absorption (open stars) together with the model fits (solid lines) when the TM polarized light is incident on a thin silver sinusoidal grating with thickness of 23 nm, pitch of 252 nm, and amplitude of 8 nm at polar angle  $\theta = 65.0^\circ$  in the conical mount ( $\varphi = 90^\circ$ ). Also theoretical reflection (dashed line), transmission (dotted line), and absorption (dash-dotted line) for a plane thin silver film with thickness of 23 nm are plotted.

**Figure 8.3.2.3** Theoretical TM polarized Absorption ( $A = 1 - R - T$ ) at polar angle  $\theta = 65.0^\circ$  in the conical mount for (a) a thin silver film with corrugation (dashed line) and without corrugation (solid line) together with the absorption difference (open circles) and (b) a single-interface with corrugation (dashed line) and without corrugation (solid line) together with the absorption difference (open circles). The thickness of the thin silver film is 23 nm. The corrugation in both cases has a pitch of 252 nm and amplitude of 8 nm.

**Figure 8.3.2.4** Instantaneous  $E_{xy}$  vector fields at resonant frequency  $f = 0.595 \times 10^{15}$  Hz for a thin silver film grating ( $d = 23$  nm,  $\lambda_g = 252$  nm, and  $a = 8$  nm) at  $\theta = 65.0^\circ$  and  $\varphi = 90^\circ$ . The continuous lines represent the thin metal grating.

**Figure 8.3.2.5** Theoretical TM polarized Absorption ( $A = 1 - R - T$ ) as a function of frequency and silver film thickness at  $\theta = 42.3^\circ$  for thin silver film gratings with the same pitch  $\lambda_g = 252$  nm but different fundamental amplitude (a)  $a = 4$  nm, (b)  $a = 8$  nm, (c)  $a = 12$  nm, and (d)  $a = 16$  nm in the conical mount ( $\varphi = 90^\circ$ ). The dashed line represented the thickness  $d = 23$  nm.

**Figure 8.3.2.6** Instantaneous  $E_{xy}$  vector fields of (a) the LRSPP ( $f = 0.95 \times 10^{15}$  Hz) and (b) the second order SRSPP ( $f = 0.83 \times 10^{15}$  Hz) that can be excited on a thin silver film grating with thickness of 23 nm, pitch of 252 nm

## List of Figures

---

and amplitude of 16 nm at  $\theta = 42.3^\circ$  and  $\varphi = 90^\circ$ . The continuous lines represent the thin metal grating.

- Figure 8.3.2.7** Instantaneous electric field vector  $E_{xz}$  distributions at  $\theta = 42.3^\circ$  and  $\varphi = 90^\circ$  for the LRSPP on the top surface of a thin silver grating with a same pitch of 252 nm and a same amplitude of 16 nm but different thicknesses (a)  $d = 65$  nm,  $f = 0.801 \times 10^{15}$  Hz, (b)  $d = 60$  nm,  $f = 0.8055 \times 10^{15}$  Hz, (c)  $d = 55$  nm,  $f = 0.811 \times 10^{15}$  Hz, (d)  $d = 52$  nm,  $f = 0.8151 \times 10^{15}$  Hz, (e)  $d = 48$  nm,  $f = 0.8216 \times 10^{15}$  Hz, and (f)  $d = 43$  nm,  $f = 0.831 \times 10^{15}$  Hz. The fields are plotted in the  $x$ - $z$  plane and one repeat period of the structure is shown ( $\lambda_g$ ). The grating peak and trough locate at  $x = -189.2$  nm and  $-63.2$  nm respectively.
- Figure 8.3.2.8** Theoretical TM polarized Absorption ( $A = 1 - R - T$ ) as a function of the incident angle and the amplitude for (a) the LRSPP excited by a fixed frequency  $f = 0.785 \times 10^{15}$  Hz and (b) the SRSPP excited by a fixed frequency  $f = 0.625 \times 10^{15}$  Hz on a 252 nm pitch thin silver grating with thickness of 23 nm in the conical mount, together with the mode width  $\Delta\theta$  of (c) the LRSPP and (d) the SRSPP absorption peak plotted against the amplitude square ( $a^2$ ).
- Figure 8.3.2.9** Theoretical TM excited SRSPP (indicated as open triangles) and LRSPP (indicated as open stars) absorption peak height as a function of amplitude at  $\theta = 42.3^\circ$  and  $\varphi = 90^\circ$  for different film thicknesses (a)  $d = 73$  nm, (b)  $d = 50$  nm, and (c)  $d = 23$  nm. The absorption peak height for the TM excited SISPP (indicated as open squares) is also plotted in each of graphs.
- Figure 8.3.2.10** Time averaged  $|E_{\text{total}}|^2$  distributions for the TM excited SRSPP ( $f = 0.6296 \times 10^{15}$  Hz) on a thin silver grating ( $d = 23$  nm,  $\lambda_g = 252$  nm, and  $a = 8$  nm) and the TM excited SISPP ( $f = 1.0207 \times 10^{15}$  Hz) at  $\theta = 42.3^\circ$  in the conical mount. The dotted line represents the silica/silver interface.

# Acknowledgements

Here I would like to take this opportunity to thank all the people who have offered me help, advice and support during my time as a postgraduate researcher in the Thin Film Photonics Group at Exeter.

Firstly I would like to express my gratitude and appreciation to my supervisor Professor Roy Sambles, without whom I would never have been doing a PhD. His invaluable support and guidance made my thesis work possible. He has always been actively interested in my work and has always been available to advise me. I am very grateful for his patience, motivation, enthusiasm, and immense knowledge that, taken together, make him a great supervisor. Also many thanks to my mentor Professor Bill Barnes, who kept an eye on the progress of my work and was always available when I needed his advice. And I would also like to take this opportunity to acknowledge the financial support of an Overseas Research Studentship and from the University of Exeter.

I would like to thank Dr. Ian Hooper for helping me through my postgraduate research. Ian has patiently taught me how to fabricate samples, use the monochromator, and implement the modeling codes. He has always been ready to listen to problems and try to help out, and proof read every scientific piece of work that I have ever written.

Next I want to thank all of the members of the group, both present and past, who helped out throughout the last three years. I am happy that I have come to know them. Thanks to Andy and George for characterizing the samples by SEM and AFM. Thanks to Matt for helping to model the reflectivity of deep mono-gratings by using HFSS. Thanks to Steve for his invaluable assistance with the interferometer and reactive ion etching. To Tim A, Tim T, and Jimmy for patiently helping me to improve my oral English. To Baptiste for introducing the 3-D field plot software. And thanks to Martyn for providing his model codes and many good comments. Thanks to Joe and Stephen for good advice. And many thanks to Pete Cann, who was always willing to help with technical problems, and always managed to produce work of the highest quality. Also I appreciate his ‘Dartmoor Walk’ organization. Other people who I have not mentioned so far, such as Mike, Pete V, Lucy, Sharon, Alastair, Fuzi, and Lizhen have all helped at times, and therefore also deserve many thanks. All of you gave me the feeling of being

## **Acknowledgements**

---

at home at work. I would like to thank you again for contributing to such an inspiring and pleasant atmosphere.

Finally I would like to thank my parents ZhenXin Chen and JiangFang Su for their support over all of the years of my education. And special thanks go to my wife Junfeng for her love and patience during the PhD period. One of the best experiences that we lived through in this period was the birth of our son Youyou, who provided an additional and joyful dimension to our life mission.

# **Chapter 1**

## **Introduction**

The work presented in this thesis is related to the area of surface plasmon polariton (SPP) modes which are currently generating great interest within the optical sciences community. It contains a substantial body of original experimental data on optical excitation of surface plasmons on gratings which is fully modelled and interpreted. Generally, this thesis can be categorised into four main sections. The first section (chapter 2 and 3) deals with the background theory and experimental techniques needed to investigate the optical response of a variety of surface plasmon supporting structures. The second section (chapter 4) is an experimental investigation of the effect of increasing the corrugation depth on the nature of the SPPs excited at a single air/metal interface. The third section (chapter 5 and 6) focuses on the band structures of grating-coupled SPPs and wave-guide modes in corrugated metallic microcavities, and the final section (chapter 7 and 8) investigates the optical response of two-interface metal grating structures with shallow corrugations on both interfaces in the classical and conical mount. A brief outline of the contents of each chapter is given below.

Chapter 2 presents the sample fabrication, the experimental measurement approach and theoretical modelling method used extensively throughout this thesis. The photolithography technique combined with reactive ion etching (RIE) used in fabricating the 1-D and 2-D photoresist and silica gratings is described. Then these dielectric gratings are used as replica templates to produce smooth-surface silver gratings. By measuring the absolute reflectivity spectra and mapping all of the reflectivity minima into a plot as a function of wave vector and frequency, the optical dispersion curve of the structure is determined experimentally. In addition, the scattering matrix technique based on a conical version of the differential formalism of Chandeson *et al* [1980, 1982] by which the photonic band structures, the dispersion curves of the optical modes, and the electromagnetic field distributions at the various resonance frequency is described.

In chapter 3, a brief overview of the physics understanding of the SPP – an oscillation of the surface charge density at the boundary between a metal and a

dielectric with mixed longitudinal and transverse character is introduced. The dispersion relation of the SPP mode for a planar interface is derived, and the spatial extent of the fields associated with the mode is examined. The methods for coupling incident light into the SPP modes are described, with particular emphasis on grating-coupling. The formation of band gaps at the points where two branches of the SPP dispersion curve cross is explored. In addition, the phenomenon of SPP mediated polarization conversion from gratings is discussed. This chapter provides the theoretical basis for all of the systems studied involving metal layers.

In chapter 4, an original study of the form of the TM polarized dispersion of a family of flat-banded self-coupled SPPs on very deep sinusoidal and narrow Gaussian-grooved silver gratings in the classical mount is presented. The prediction that the SPP modes shift to lower frequency, and become flat banded, effectively localized, modes with increasing grating depth is verified experimentally from comparison of the modes for sinusoidal gratings with different depths. These flat bands may have potential applications in selective absorbers or in resonant enhanced Raman scattering. In particular, the sharp reflection peaks that we have observed in the experiments for narrow Gaussian-grooved deep silver gratings may be of interest for filtering applications.

Chapters 5 and 6 present original studies of grating-coupled SPPs and waveguide modes in corrugated metallic microcavities. In chapter 5, the optical properties of a short-pitch periodically corrugated photoresist waveguide structure on a thin silver tunnel barrier are explored for TM polarization over the azimuth angle range  $\varphi = 0^\circ$  to  $90^\circ$ . The introduction of the corrugation into the waveguide introduces band gaps in the dispersion of the guided modes. To understand the nature of these band gaps, the optical magnetic field distributions at resonant frequencies are explored. In chapter 6, the same waveguide structures as in chapter 5 are explored for both TM and TE polarization at azimuth angles of  $\varphi = 0^\circ$  and  $90^\circ$ , but with a thick cladding metal layer. The photonic band-gaps at the Brillouin zone boundary and anti-crossings within the Brillouin zone are observed directly in the experimental dispersion curves. The presence of a flat photonic band caused by the anti-crossings between SPP and waveguide modes is confirmed experimentally. It is worth noting that the resonant frequency of this flat photonic band can be designed through appropriate choice of thickness of the guide medium and the amplitude of the grating.

In chapters 7 and 8 there is a change of focus from single interface metal gratings, concentrating on two-interface shallow metal gratings bounded with the same dielectric media. When the thickness of the metal slab is very small, SPPs may be excited on both surfaces and coupled to each other to form the short range SPP (SRSPP) and the long range SPP (LRSPP). Chapter 7 presents the TM polarized optical response of thin silver films with identical corrugations on both interfaces in the classical mount ( $\varphi = 0^\circ$ ). A band gap within the Brillouin zone, formed by the anti-crossing of the LRSPP scattered by  $+k_g$  and the SRSPP scattered by  $-k_g$  is confirmed in the experimental dispersion curves. It is shown that the  $2k_g$  component in the grating profile is the key factor leading to the appearance of band gaps in these relatively shallow gratings. Non-conformal structures with  $2k_g$  components are also theoretically studied showing band gaps at normal incidence for the LRSPP and the SRSPP modes. In chapter 8, the SRSPP and the LRSPP modes on conformal thin silver shallow gratings are investigated in the conical mount ( $\varphi = 90^\circ$ , the grating vector perpendicular to the incidence plane) for both TM and TE polarization. In particular remarkably strong resonant coupling to an SPP is observed in the TM polarized reflectivity which, on single interface shallow gratings, would be expected to be very weak.

Finally, chapter 9 contains a summary of the work presented in this thesis, possible applications for the structures investigated, and ideas for future work.

## Chapter 2

# Sample Fabrication, Experimental Data Measurements, and Modelling

### 2.1 Sample Fabrication

Wavelength-scale periodic structures provide unique optical and electronic properties that make them of interest to workers in a number of fields. Accordingly, fabrication techniques have been extensively developed over the past one hundred years, and can be divided into two main categories: “top-down” and “bottom-up”. The bottom-up approaches seek to have smaller components arrange themselves into more complex assemblies, of which the self-assembly technique in the fabrication of photonic crystals is a representative example. While the top-down approaches, such as photolithography and electron beam lithography (EBL), often use the microfabrication methods to create the desired structures. We utilize the photolithography approach to fabricate the grating samples studied in this thesis. The simplest sample is a one-dimensional photoresist grating and is also the essential basis to more complex samples.

#### 2.1.1 One-dimensional dielectric gratings

The fabrication starts with the procedure of cleaning 6 mm thick and 25 mm square optical flat silica substrates. First, they were cleaned thoroughly by immersing them into concentrated nitric acid for 1hr, followed by immersing them into acetone for another 1hr. At this stage one side of the substrate was painted black to prevent any reflection from this side, which can cause standing waves normal to the surface that destroy the formation of desired pattern in the exposure. Then the silica surface was “drag cleaned” using lens tissue soaked in acetone to remove any dust on the surface. Immediately the cleaned substrate was taken into a clean room for spin-coating a layer

of Shipley SPR700 photoresist. The thickness of the film is controlled by the choice of concentration of photoresist and spin speed. If the substrate is spin-coated at 4000 rpm with non-diluted photoresist a film thickness of  $\sim 1.2 \mu\text{m}$  is produced. After spinning is complete, the substrates are placed in a light-proof box and baked at a carefully controlled temperature ( $90^\circ\text{C}$ ) for a prescribed time (30 min) to drive off the remaining solvent, leaving a hard layer of resist polymer.

The sample is then exposed to an interference pattern generated using two beams of UV laser light ( $\lambda_0 = 325 \text{ nm}$ ). A schematic of the typical two-beam interferometer (Hutley [1982]) is shown in Figure 2.1.1.1. The angle of incidence  $\theta$  and wavelength of light  $\lambda_0$  determines the pitch of the grating to be produced, which is given by,

$$2\lambda_g \sin \theta = \lambda_0$$

where  $\lambda_g$  is the desired grating pitch. The minimum pitch obtainable is half of the wavelength of the laser light, which is 162.5 nm in this case.

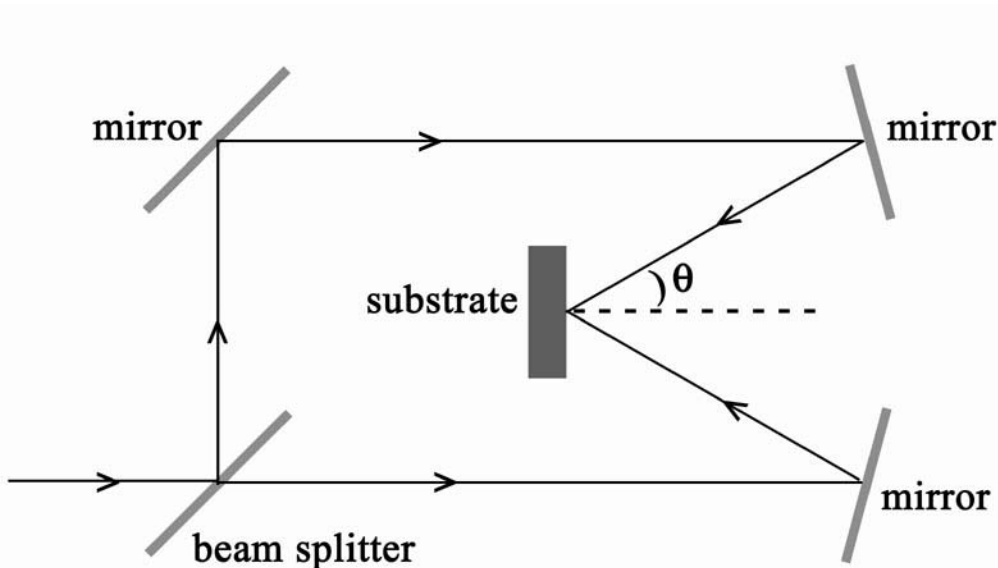


**Figure 2.1.1.1** A schematic of a typical two beam interferometer used for the fabrication of gratings. An expanded, collimated laser beam is split into two equal intensity beams which are then recombined on the face of a photoresist coated substrate. The pitch of the interference pattern and hence of the resulting grating is determined by the angle of incidence  $\theta$  and the radiation wavelength.

Exposure to light induces a chemical reaction in the photoresist modifying its solubility in a developer solution. For positive photoresist, exposure breaks down the

polymer chains into shorter units that are soluble in some kind of developer. In negative photoresist UV light causes the cross-linking of the polymer chains, and the unexposed resist is more soluble. Thus, the sinusoidal intensity profile in the interference pattern is converted into a periodically modulated solubility. Figure 2.1.1.2 shows such one-dimensional (1-D) numerically modelled map of the periodic exposure across the photoresist film. The light regions represent high exposure, while the dark areas represent low exposure.

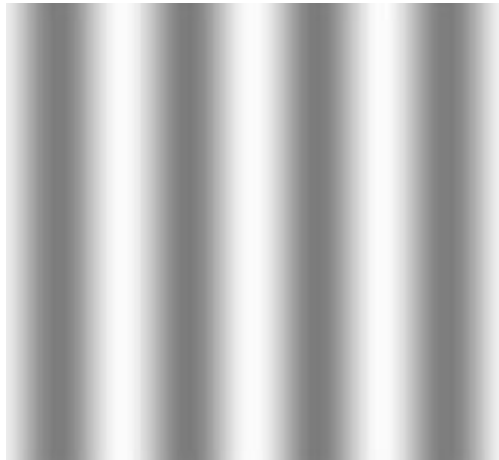


**Figure 2.1.1.2** One-dimensional numerically modelled map of the exposure across the surface of the photoresist produced by exposing the sample in the interferometer. The light regions represent high exposure, and the dark areas are low exposure.

The next step in the fabrication process is to develop the exposed samples. Since the Shipley SPR700 resist used in our experiments is a positive photoresist, the exposed area (light regions, as shown in Figure 2.1.1.2) will be washed away. The developer is 0.8% - 1% sodium hydroxide solution. We found that control of the developer concentration was critical. If the developer was too concentrated then it removed all the photoresist in less than one second. If it was too dilute then it failed to fully dissolve the polymer film even in the most exposed regions. Here 0.8% - 1% concentration of developer solution allows for control of the development time within several seconds.

Figure 2.1.1.3 shows scanning electron micrograph (SEM) images of top-view and side-view of such a sinusoidal photoresist grating fabricated by using the steps mentioned above. In this case, the photoresist layer ( $\sim 1.5 \mu\text{m}$ ) was exposed to UV light for 40 minutes, and developed in 1% sodium hydroxide solution for 4 seconds. The pitch of the grating is set at  $\sim 350 \text{ nm}$ . Post treatment of the resist by thermal baking at

90 °C for 30 min and overnight exposure to incoherent UV is also applied to ensure that the resist is fully stabilised.

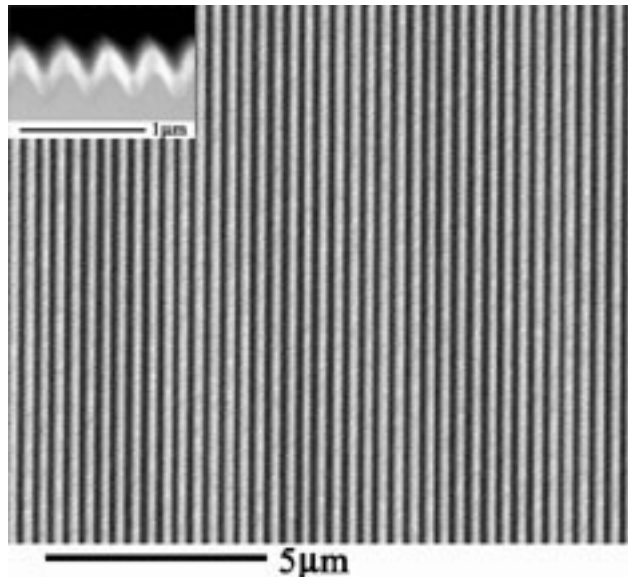


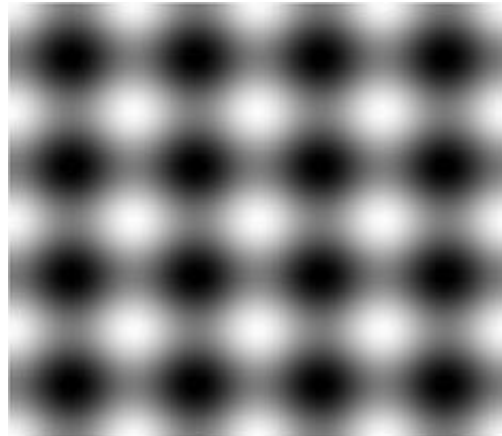
**Figure 2.1.1.3** Scanning electron micrographs of top-view of a photoresist grating with a pitch of ~350 nm. The side-view is shown in the inset.

Under some circumstances the shape of the photoresist grating is required to be transferred into the silica substrate. This can be accomplished by using reactive ion etching (RIE), where the oxygen plasma is used to remove the photoresist and CHF<sub>3</sub> plasma to chemically remove the silica. If the flow ratio of O<sub>2</sub> to CHF<sub>3</sub> is such that the photoresist is etched by the oxygen plasma at the same rate as the silica is etched by the CHF<sub>3</sub>, then the resultant etched profile would be expected to be almost the same as that of the photoresist grating.

## **2.1.2 Two-dimensional dielectric gratings**

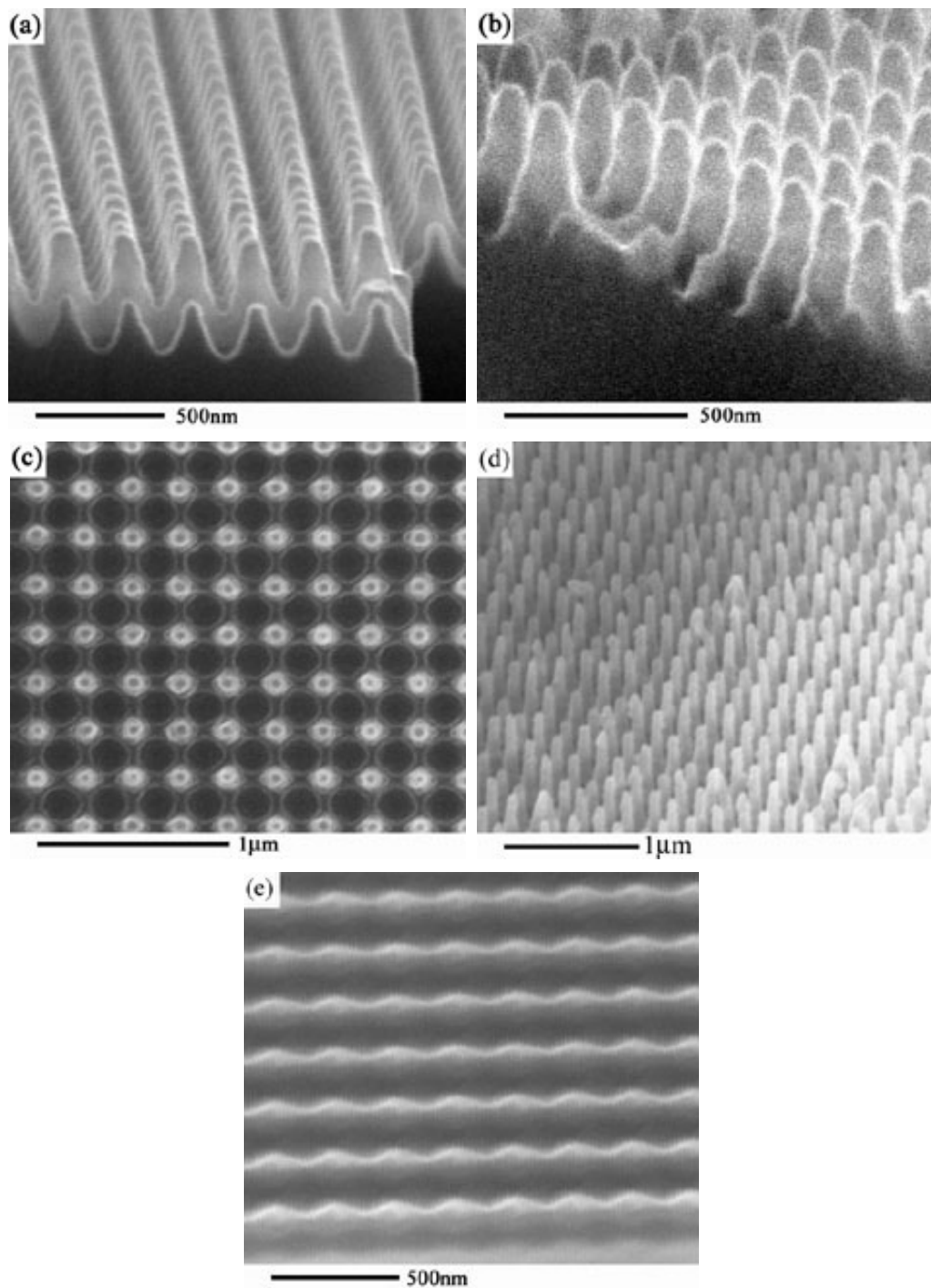
The fabrication process of two-dimensional (2-D) dielectric gratings is similar to that used in the one-dimensional photoresist gratings except the exposure step. Instead of using a single exposure, the sample is exposed twice to the same interference pattern in a two-beam interferometer, with the substrate rotated by 90° about its surface normal between exposures. Figure 2.1.2.1 shows the sum of two such interference patterns and

represents the total exposure at each point across the photoresist film. This pattern clearly has square symmetry.



**Figure 2.1.2.1** A numerically modelled map of the total exposure across the surface of the photoresist produced by exposing the sample twice in the interferometer. The substrate is rotated by 90° between exposures. The total exposure is therefore the sum of two sinusoidal patterns oriented at 90° to each other.

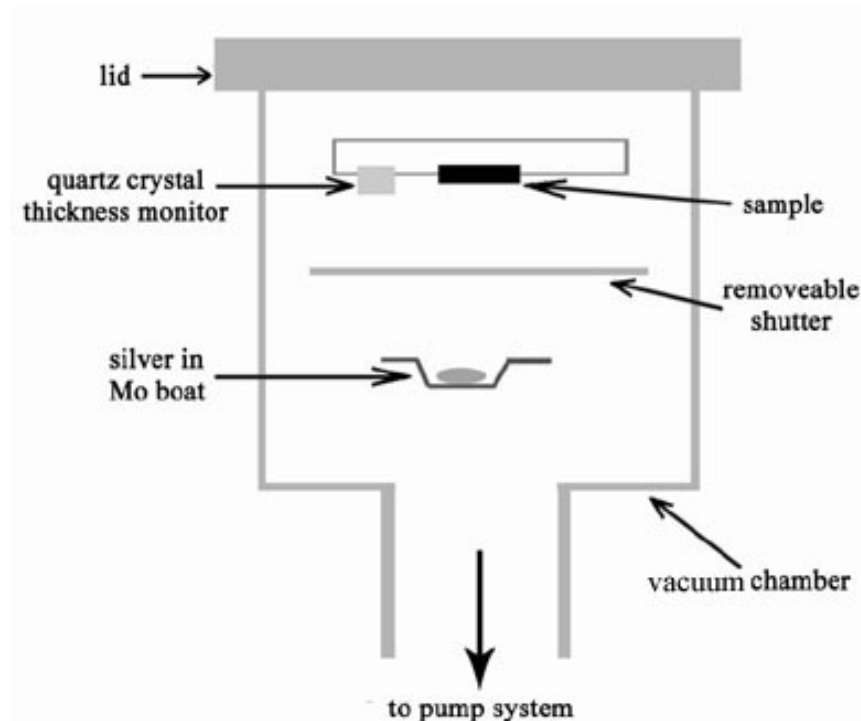
After exposure the sample is developed in the 0.8% sodium hydroxide solution for several seconds. Figure 2.1.2.2 shows SEM images of two-dimensional resist gratings prepared using this multiple exposure technique. The pitches of the bi-gratings are both set to  $\sim 250$  nm. Note that the depths of the bi-gratings in two dimensions are dependent on the exposure time for each exposure. As shown in Figure 2.1.2.2 (a) and (c), the depths of bi-gratings in two dimensions are identical since the samples were exposed for the same time (60 min) for each exposure. However, in Figure 2.1.2.2 (e), the depths in two dimensions are very different since the sample was exposed for 40 min on the first exposure and for 60 min on the second exposure. Also note that the development time can control the profiles of the gratings due to the nonlinearities in the development process. By comparing Figure 2.1.2.2 (a) with (d), we can clearly see that the grating in Figure 2.1.2.2 (a) is more sinusoidal in both dimensions, while in Figure 2.1.2.2 (d) the grating becomes more narrow-peaked. It is the nonlinearities that make the fabrication of a grating containing higher harmonics possible.



**Figure 2.1.2.2** SEM images of two-dimensional photoresist gratings prepared by using different exposure and developing time. (a), (b) exposed for 60 min at each exposure and developed for 4 seconds, (c), (d) exposed for 60 min at each exposure and developed for 7 seconds, and (d) exposed for 40 min the first exposure and 60 min the second exposure and developed for 5 seconds. The pitches of the gratings in two dimensions are set at ~250 nm.

### 2.1.3 1-D and 2-D metal gratings

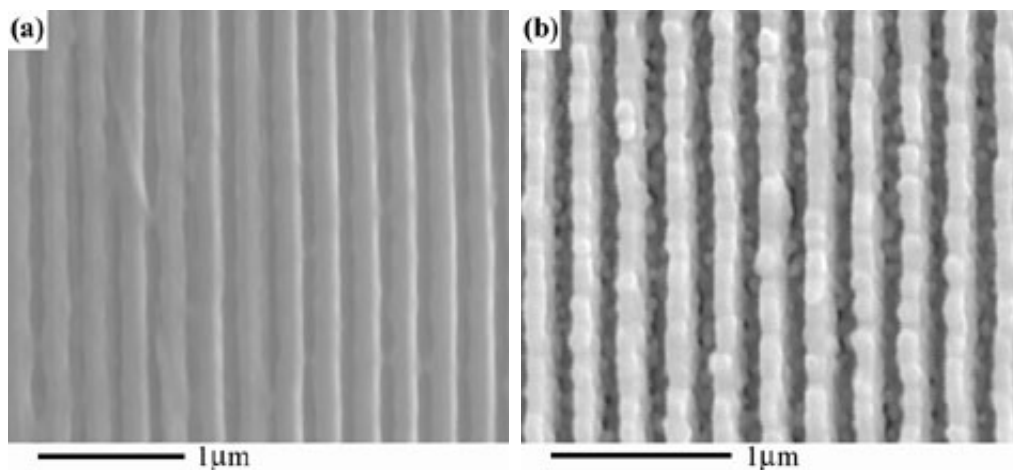
We have now seen the fabrication of 1-D and 2-D dielectric gratings. Let's turn to the fabrication of metal gratings. Obviously, thermal evaporating silver on the dielectric gratings can directly result in silver gratings. A schematic of the system used to do this is shown in Figure 2.1.3.1.



**Figure 2.1.3.1** A schematic of the vacuum deposition system used to evaporate silver on the sample.

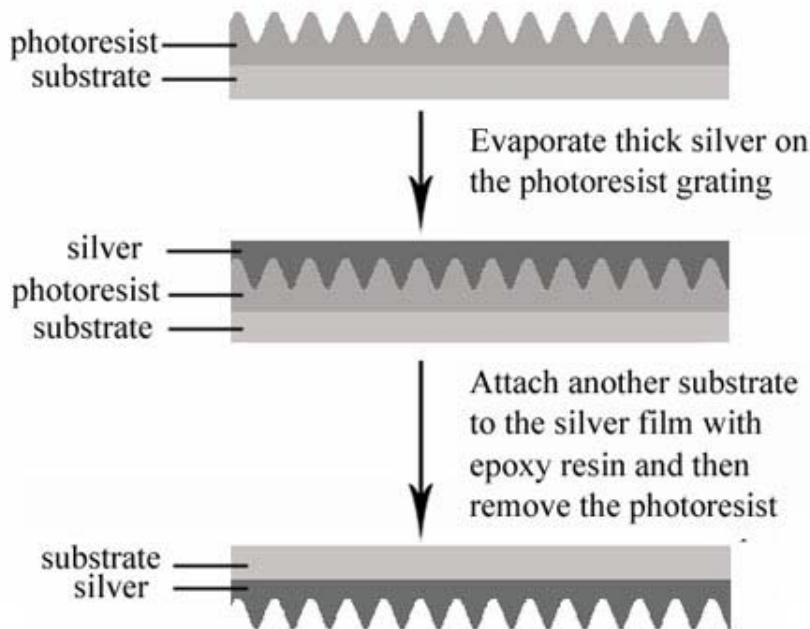
The sample is placed in a vacuum chamber with the face of the structure to be coated facing a molybdenum boat in which 99.999% pure silver is contained. The vacuum chamber is pumped down to a pressure of  $\sim 10^{-6}$  mTorr by use of both a rotary pump and a diffusion pump. When the base pressure has been obtained a current is passed through the boat so that it heats sufficiently for the silver to evaporate, with the silver vapour then condensing on to the structure. The rate at which the silver evaporates is controlled by the current being passed through the boat, and is monitored using a quartz crystal thickness monitor. After cooling for 1hr the sample was removed from the chamber.

Figure 2.1.3.2 (a) shows top-view SEM of such a periodically corrugated silver-air smooth interface fabricated by depositing silver on a resist grating with a pitch of ~262 nm and a depth of ~60 nm. Though this technique is very simple and direct, it is limited to the production of shallow silver gratings only, since depositing silver on a deep photoresist grating results in a very rough silver-air interface grating which gives strong optical scatter. A silver grating with rough surface can be clearly seen in Figure 2.1.3.2 (b), where we evaporated ~800 nm thick silver on to the deep resist grating with a depth of ~500 nm.



**Figure 2.1.3.2** SEM images of top-view of silver gratings fabricated by thermal evaporation of ~400 nm thick silver on to the photoresist gratings with a pitch of ~262 nm and a depth of (a) ~60 nm, (b) ~500 nm.

Note that the surface of either shallow or deep photoresist grating is relatively smooth. It is possible to utilize the photoresist gratings as replica templates to obtain smooth surface silver gratings. The scheme for fabrication is shown in Figure 2.1.3.3. The first step of this approach is to evaporate thick enough silver on to the photoresist gratings. Then a substrate is attached to the silver film with epoxy resin glue. After the glue is hardened, the sample is immersed into the acetone for 12hr to dissolve the photoresist completely. This produces a smooth surface silver grating with the same pitch and depth as the sacrificed photoresist grating except with reversed profile.



**Figure 2.1.3.3** Schematic of the fabrication of the silver gratings. First thick silver is evaporated on to the resist gratings. Then a substrate is attached to the silver film with epoxy resin. After removing the photoresist using acetone, the silver grating is prepared with the same pitch and depth as the resist grating, but reversed profile.

Figure 2.1.3.4 shows SEM images of 1-D and 2-D silver gratings prepared using this technique with a pitch of  $\sim 258$  nm and a depth of  $\sim 500$  nm. Compared to the grating shown in Figure 2.1.3.2 (b), one clearly sees that the ‘buried’ surface of these deep silver gratings is much improved over the top surfaces.

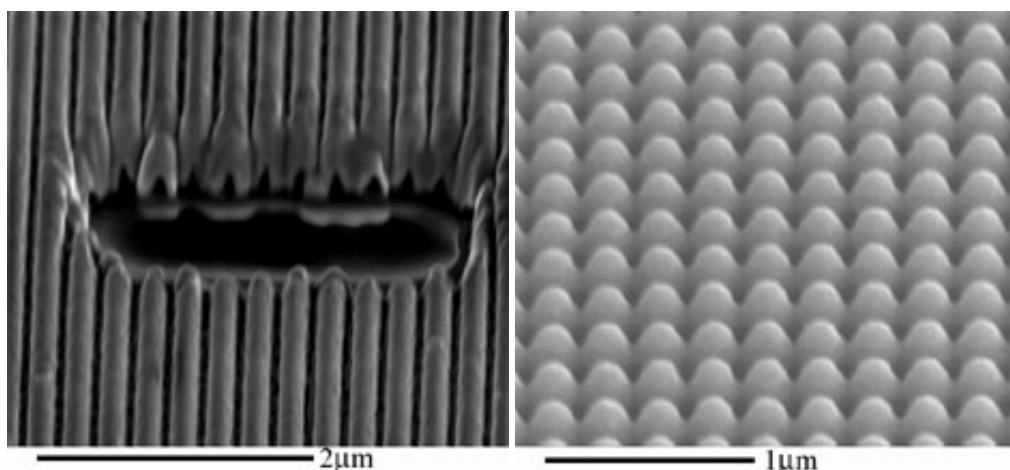


**Figure 2.1.3.3** SEM of one-dimensional (left image) and two-dimensional (right image) silver grating with a pitch of  $\sim 258$  nm and a depth of  $\sim 500$  nm.

### **2.1.4 Corrugated microcavities**

In the work presented in this thesis, we also studied metallic waveguide structures consisting of a waveguide medium, with a periodically modulated upper surface, deposited on an optically thin silver film supported by a silica substrate. The schematic sample geometry is shown in Figure 2.1.4.1 (a). Sample fabrication begins with the evaporation of a thin silver film (approximately 60 nm) onto the surface of the silica substrate. The substrate is then spin-coated with photoresist to give a layer approximately 350 nm thick, exposed to an interference pattern (as shown in Figure 2.1.1.2), and then chemically developed. Finally, as shown in Figure 2.1.4.1 (b), the sample can be capped by another optically thick layer of silver to form the silver-photoresist-silver layered microcavity structure in which the upper interface between the photoresist and silver is periodically corrugated.

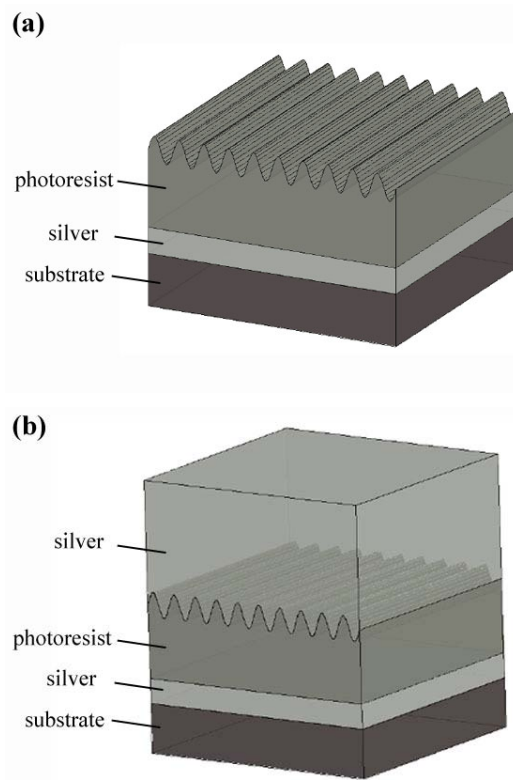


**Figure 2.1.4.1** Schematic metallic waveguide structures comprising of the photoresist, with a periodically corrugated upper surface, deposited on an optically thin silver film supported by a silica substrate, (a) without top cladding silver layer, and (b) with top cladding silver layer.

## 2.2 Measurement of the Optical Response of the Structures

In order to experimentally determine the optical response of the structure, in this thesis, we measured the reflectivity data in the visible range. Figure 2.2.1 illustrates the coordinate system used in the study with reference to the grating, where the  $y$ -axis is perpendicular to the sample and the  $z$ -axis is parallel to the grating grooves. The polar angle ( $\theta$ ) and azimuth angle ( $\varphi$ ) define the orientation of the incident beam.

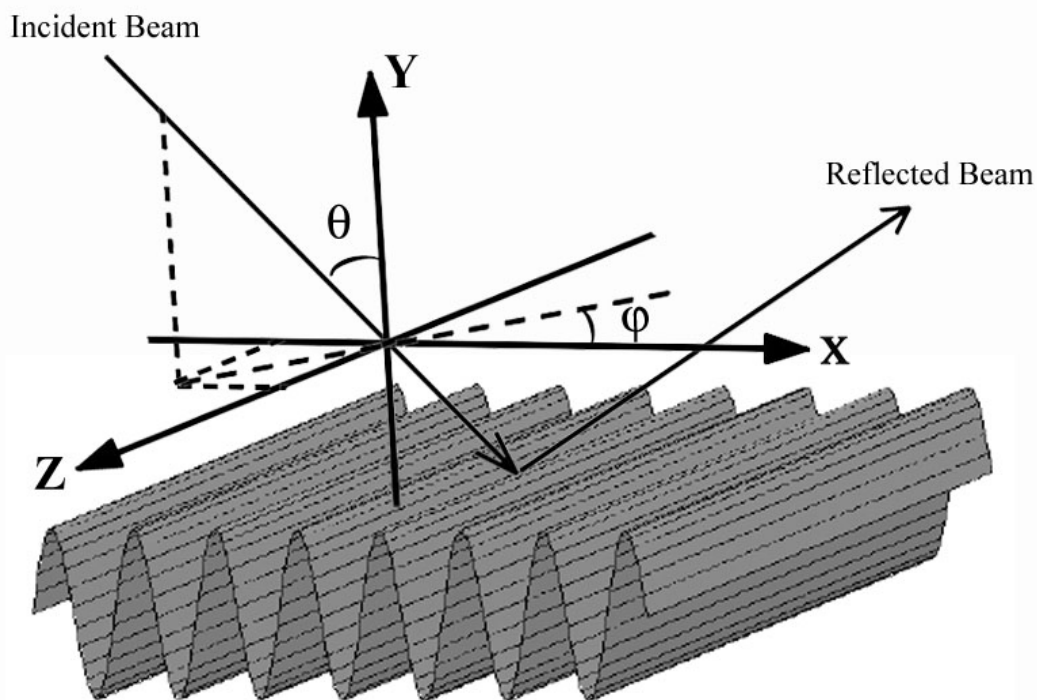


**Figure 2.2.1** The coordinate system used with reference to the corrugation. The  $z$ -axis is parallel to the grating grooves, and the  $y$ -axis is perpendicular to the sample.  $\theta$  is the polar angle, and  $\varphi$  is the azimuth angle. The orientation of the incident beam is defined by  $\theta$  and  $\varphi$ .

Figure 2.2.2 shows the apparatus used to study reflection from the sample. The sample is mounted on a rotating table, so that it can be automatically turned to suit any required angle of incidence ( $\theta$ ). The sample can also be manually rotated about the  $y$ -axis to vary the azimuth angle ( $\varphi$ ), as defined in Figure 2.2.1. White light from a 250 W Osram Xenophot HLX bulb is passed through a spectrometer, with which the required wavelength is then selected via computer control. The approximate spectral half-width

of the output light is 1.5 nm. The typical divergence of this beam from the final aperture to the sample was found to be  $0.04^\circ$ . The polarisation of the light is set to either transverse magnetic (TM, p) or transverse electric (TE, s) using the first polariser. After the first polariser the light passes through an optical chopper operating at approximately 2.0 kHz. This allows the resultant modulated signal to be recovered from two detectors using a pair of photomultiplier tubes (PMTS). One is used to measure the reflection from the sample, and the other is used as reference via a glass beam-splitter. A second polariser is also placed directly in front of the signal detector. This second polariser is used to match that of the first polariser to measure the  $R_{pp}$  and  $R_{ss}$  reflectivities, or it may be set at right angle to the first polariser to study the polarisation conversion of the sample. In this case either  $R_{ps}$  or  $R_{sp}$  reflectivities are recorded.

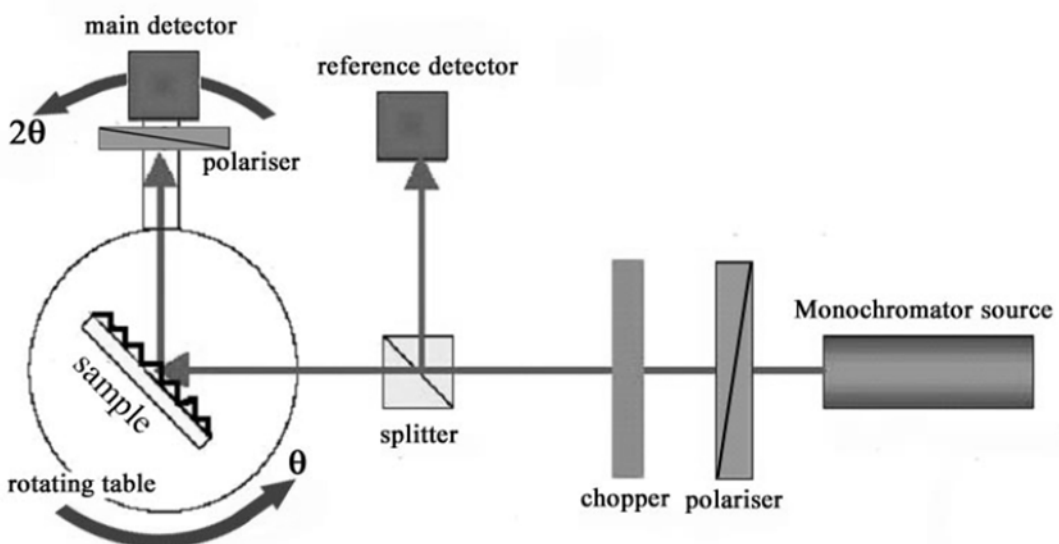


**Figure 2.2.2** Schematic diagram illustrating the apparatus used to record the wavelength-dependent reflectivity data from the sample.

The scan procedure is automated, with wavelength selection and angle of incidence both controlled by computer. If we fix the incident wavelength, the final reflectivity data are produced as a function of incident angle. Similarly, if we fix the incident angle, the reflectivity data as a function of wavelength can be obtained. The typical TM polarized angle-dependent (fixed incident wavelength  $\lambda_0 = 632.8$  nm) and wavelength-dependent (fixed incident angle  $\theta = 40^\circ$ ) reflectivity data ( $R_{pp}$ ) at  $\varphi = 0^\circ$  are shown in Figure 2.2.3 (a) and (b) respectively. The single silver grating has a pitch and

depth of  $\sim 345$  nm and  $\sim 21$  nm respectively in Figure 2.2.3 (a), and  $\sim 258$  nm and  $\sim 35$  nm respectively in Figure 2.2.3 (b).

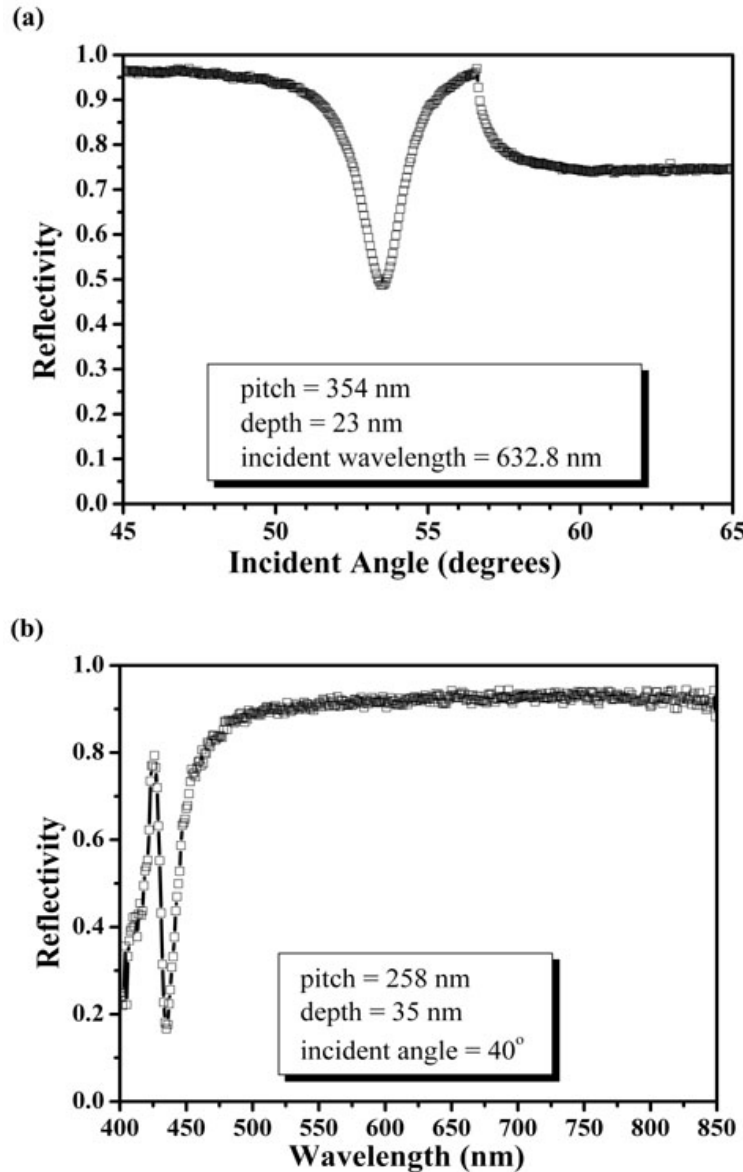


**Figure 2.2.3** (a) TM polarized angle-dependent reflectivity data, and (b) wavelength-dependent reflectivity data at  $\varphi = 0^\circ$  for single silver gratings.

## 2.3 Modelling

The theoretical method employed in this thesis is based upon a conical version of the differential formalism originally proposed by Chandezon *et al* [1980, 1982], whose basic feature is that it uses a co-ordinate transformation that maps the interfaces

of a multi-layer system onto parallel planes, thereby enabling the expression of the boundary conditions to be made much simpler. This requires that the field amplitudes are represented as a Fourier expansion. The corrugated surface itself is also described by a Fourier series:

$$f(x) = a_1 \sin(k_g x + \phi_1) + a_2 \sin(2k_g x + \phi_2) + \dots + a_N \sin(Nk_g x + \phi_N),$$

where  $a_N$  provides the amplitude of the  $N^{\text{th}}$  order harmonic component.

When this method was first demonstrated in 1980 (Chandezon *et al.* [1980]), the system was a single corrugated interface separating vacuum and a perfectly conducting metal. In 1982 the system was extended to a multi-layer system with absorbing media (Chandezon *et al.* [1982]). This multi-layer method used a transfer matrix approach in order to relate the fields in the upper and lower media by a recursive product of individual transfer matrices across each layer. The problem with a transfer matrix method is that there are a large number of evanescent decaying and growing fields across a layer, which leads to instabilities when the layer thickness becomes large.

Therefore the scattering matrix, which is used in many fields of study which involve multi-layered systems, was introduced by Preist *et al.* [1995] in order to overcome this limitation. Simultaneously an R-matrix technique was developed by Li [1995], which is almost identical to the scattering matrix method. The scattering matrix approach relates the incident fields to the output fields by a scattering matrix product, and avoids the instabilities inherent within the transfer matrix method, however the scattering matrix method does involve a few extra calculations and so the increase in stability is gained at a slight cost to the calculation time. By using this approach, the reflectivities and transmissivities of systems can be calculated within the region of  $\omega$ - $k$  space available to the incident radiation. In addition, the photonic band structures and the dispersion curves of the optical modes associated with the systems can be obtained for all values of  $\omega$  and  $k$ , and not just those available to the incident radiation, by directly investigating the scattering matrices of the system as a function of  $\omega$  and  $k$ .

The scattering matrix approach applied to the method of Chandezon *et al* has been extensively developed and widely used within the research group for a number of years. In the past works (Wood *et al.* [1995], Watts, Sambles, and Harris [1997], Watts, Preist, and Sambles [1997]), this computational approach has been proven to agree well

with experimental data. For this reason, and the fact that a complete description of the method is beyond the scope of this work, the details are not explored.

## **2.4 Summary**

In this chapter, the sample fabrication, the experimental measurement approach and theoretical modelling method have been briefly introduced. Firstly, the photolithography technique combined with RIE used in fabricating the 1D and 2D photoresist and silica gratings has been described. To facilitate coupling to surface plasmon resonances on a silver-air interface the dielectric gratings were used as replica templates to produce smooth surface silver gratings. In our study, the optical response of the structure is determined experimentally by measuring the absolute reflectivity spectra. The experimental apparatus and coordinate system used to record such reflectivity spectra from the sample have also been presented. Finally, the scattering matrix technique based on a conical version of the differential formalism of Chandezon *et al* allows the comparison between the experimentally derived reflectivity scans and the theoretical model. In addition, this theoretical method is used to model the photonic band structures, the dispersion curves of the optical modes, and the electromagnetic field distributions at the various resonance frequencies.

# Chapter 3

## Surface Plasmon Polaritons on Shallow Gratings

### 3.1 Introduction

Surface plasmon polaritons (SPPs) have been extensively studied over the past century. It was Wood [1902] who studied the spectra of ruled metallic gratings illuminated with a continuous light source, and first reported the observation of anomalies (a series of light and dark bands) in the transverse magnetic (TM) polarized wavelength dependent reflectivity spectra. At the time no theory was able to explain these features which were only found for TM polarization, and they became known as “Wood anomalies”. It was not until Rayleigh [1907] published his Dynamical Theory of Gratings that some aspects of these observed bright bands were explained. He showed that some features were pseudo-critical edges caused by a diffracted order becoming evanescent and its energy being redistributed among the other propagating orders. However, Strong [1935] demonstrated that the angular position of the reflection minima (dark bands) was dependent upon the metal of which the grating was made, and not solely due to the gratings geometry as was the case for the pseudo-critical edge. It was not until Fano [1941] published a seminal paper on the subject that the nature of the dark bands was fully explained. He described these dark bands in terms of the diffracted order becoming evanescent and producing a pair of surface waves travelling along the grating surface and exponentially damped in the direction perpendicular to it. These waves are not able to leave the interface since both the dielectric and the metal repeatedly reflect them, and no part of their energy is dispersed outside the surface region.

Due to further understanding of metals, and the development of the plasma concept for describing the free electrons, Ferrell [1958] predicted that a beam of electrons incident upon a metal film would emit radiation at the plasma frequency. Steinmann [1960] observed this to be the case, whilst Ritchie and Eldridge [1961] showed that the emitted radiation had characteristic energies of  $h\omega_p/2\pi$  and  $h\omega_p/2\pi\sqrt{2}$ , where  $\omega_p$  is the plasma frequency and  $\omega_p/\sqrt{2}$  is the surface plasma

frequency for air. This work lead to the superficial waves described by Fano becoming known as surface plasmon polaritons (SPPs), or often simply surface plasmons.

According to Fano: Surface EM wave, at metal-air interfaces, are evanescent waves whose wave vectors are greater than those of the incident and diffracted bulk EM waves, and that the grating augments the wave vector of the incident EM waves enabling them to couple with the surface EM waves. Teng and Stern [1967] used an optical grating that could impart some additional momentum to the SPP, so that it could couple to a radiating electromagnetic field. Their experiment consisted of illuminating the grating with a high-energy electron beam and observing peaks in the out-coupled TM polarized radiation. To verify that these peaks are caused by the excitation of the SPP, electromagnetic radiation incident at the emission angle and of the same frequency as the peaks should be absorbed as it excites the SPP. This was the case, and as the angle of incidence with respect to the grating normal was varied, minima appeared at the same position as the peaks in the electron-beam experiment. Using the angular positions of these peaks, Teng *et al.* determined the wave vector parallel to the surface of the grating of the SPP and hence the dispersion curve could be mapped out. This confirmed the excitation of SPPs unequivocally and presaged their direct optical coupling with the use of a grating, confirming Wood's observations. Up to now, the surface plasmon has been well established (Raether [1988]) and applied as an analytical tool for surface analysis in a wide variety of disciplines.

In this chapter, we shall briefly describe some of the physics and properties of SPPs propagating on a planar surface. The dispersion relation of SPPs on a planar metal-dielectric interface is derived. Coupling incident radiation to the SPP modes is discussed with emphasis on grating coupling. We shall explain the phenomenon of SPP mediated polarisation conversion and the formation of photonic band gaps in the SPP dispersion curve on shallow gratings.

## 3.2 The Surface Plasmon Polariton on a Planar Surface

As discussed above it is now well known that the interface between a metal and a dielectric can support surface charge density oscillations known as surface plasmons (SPs), which occur at a different frequency to the bulk plasmons oscillations and are confined to the interface. Typically they are excited with EM radiation and when this is coupled to the surface charge oscillation the resultant surface wave is known as a surface plasmon polariton (SPP), and has mixed transverse and longitudinal character. This trapped surface wave decays exponentially away from the interface into both bounding media. If TM polarized light is incident upon a metal/dielectric interface with a non-zero incident angle there is an electric field component normal to the surface. This field is not continuous across the interface, and therefore a surface charge is induced upon it. However there is no component of electric field normal to the surface for any incident angles and no charge is induced at the surface for transverse electric (TE) polarized light. Hence, on a flat surface only TM polarized light could possibly excite the SPP.

### 3.2.1 The Dispersion Relation

Let us first consider an interface between two semi-infinite isotropic media that are characterised by frequency dependent and complex dielectric constants  $\varepsilon(\omega) = \varepsilon_r + i\varepsilon_i$ , where the subscripts  $r$  and  $i$  refer to the real and imaginary parts of the dielectric constant respectively. From Maxwell's equations, it can be shown that the normal component of the electric displacement  $\mathbf{D}$  must be continuous across the interface. Further, the relation that links the electric displacement to the electric field  $\mathbf{E}$  states

$$\mathbf{D} = \varepsilon_r \varepsilon_0 \mathbf{E} \quad 3.2.1.1$$

where  $\varepsilon_r$  is the relative dielectric constant of the medium and  $\varepsilon_0$  is the permittivity of free space. It is clear that if the upper medium is a dielectric with positive  $\varepsilon_r$  and the lower medium is a metal possessing a negative  $\varepsilon_r$ , then the normal component of  $\mathbf{E}$  will change direction as the interface is traversed. It is this discontinuity in the normal  $\mathbf{E}$  field that is responsible for setting up the sheet of polarization charge trapped at the interface. We shall now derive the dispersion relation for the SPP surface mode in this

section.

TE polarized light propagating in the  $xy$ -plane possesses only an electric field component parallel to the surface,  $\mathbf{E} = (0, 0, E_z)$ , and hence can not induce a surface charge. Only TM polarized light propagating in the  $xy$ -plane can couple to SPP modes. Figure 3.2.1.1 shows a TM polarized electromagnetic wave incident at the interface between two semi-infinite media, the upper medium being a dielectric with dielectric constant  $\varepsilon_1(\omega)$  and the lower a metal with a dielectric constant  $\varepsilon_2(\omega)$ , and a reflected and transmitted beam are produced.

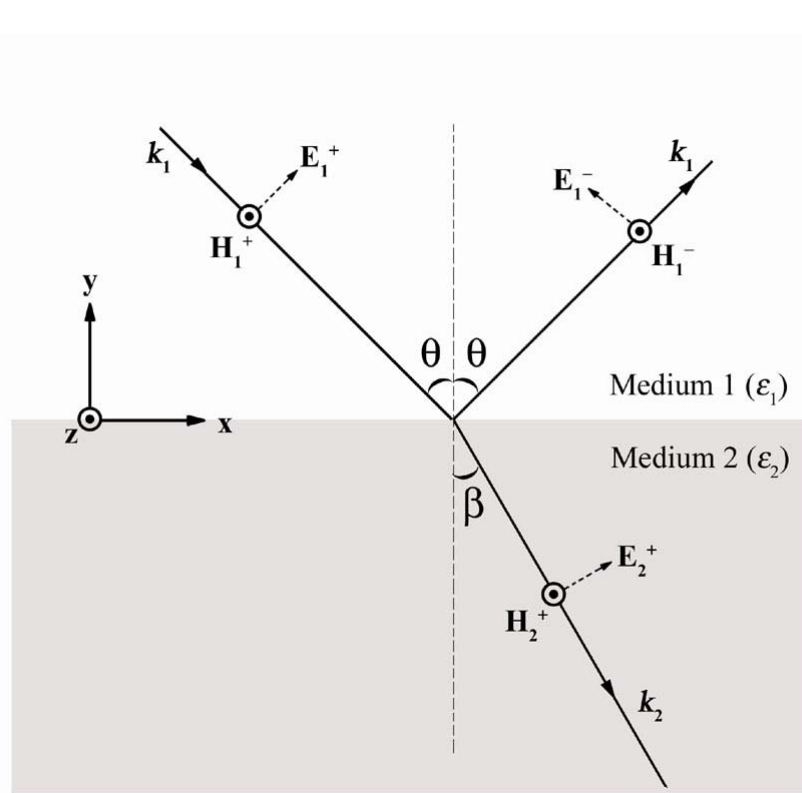


**Figure 3.2.1.1** A schematic diagram of the incident, transmitted and reflected fields associated with a TM polarized electromagnetic wave incident on an interface bounded by two media described by complex dielectric constants  $\varepsilon_1(\omega)$  and  $\varepsilon_2(\omega)$ . The  $z$ -axis is out of the page.

For TM polarized incident light with wave vector  $\mathbf{k} = (k_x, k_y, 0)$  the incident electric and magnetic fields may be written as:

$$\mathbf{E} = [E_x, E_y, 0] \exp(i(k_x x + k_y y - \omega t)) \quad 3.2.1.2$$

$$\mathbf{H} = [0, 0, H_z] \exp(i(k_x x + k_y y - \omega t)) \quad 3.2.1.3$$

By applying Maxwell's equation without free charge:

$$\nabla \times \mathbf{H} = \epsilon \frac{\partial \mathbf{E}}{\partial t} \quad 3.2.1.4$$

we obtain

$$H_z = \frac{\epsilon \omega E_x}{k_y} = -\frac{\epsilon \omega E_y}{k_x} \quad 3.2.1.5$$

and by combining equations 3.2.1.2 and 3.2.1.3 with equation 3.2.1.5 we obtain the following expressions for the incident, reflected and transmitted fields:

$$\mathbf{E}_1^+ = E_{x1}^+[1, -\frac{k_x}{k_{y1}}, 0] \exp(i(k_x x + k_{y1} y - \omega t))$$

$$\mathbf{E}_1^- = E_{x1}^-[1, +\frac{k_x}{k_{y1}}, 0] \exp(i(k_x x - k_{y1} y - \omega t))$$

$$\mathbf{E}_2^+ = E_{x2}^+[1, -\frac{k_x}{k_{y2}}, 0] \exp(i(k_x x + k_{y2} y - \omega t))$$

$$\mathbf{H}_1^+ = E_{x1}^+[0, 0, +\frac{\omega \epsilon_1}{k_{y1}}] \exp(i(k_x x + k_{y1} y - \omega t))$$

$$\mathbf{H}_1^- = E_{x1}^-[0, 0, -\frac{\omega \epsilon_1}{k_{y1}}] \exp(i(k_x x - k_{y1} y - \omega t))$$

$$\mathbf{H}_2^+ = E_{x2}^+[0, 0, +\frac{\omega \epsilon_2}{k_{y2}}] \exp(i(k_x x + k_{y2} y - \omega t)) \quad 3.2.1.6$$

Since the SPP is non-radiative either the incident or reflected field may be set to zero, and we also have the boundary condition at a metal/dielectric interface such that the tangential components ( $x$  and  $z$  directions) of the electric and magnetic fields must be continuous across the interface. Hence,

$$E_{x1} = E_{x2} \quad 3.2.1.7$$

$$H_{z1} = H_{z2} \quad 3.2.1.8$$

and

$$H_z = -E_{x1}^- \frac{\epsilon_1 \omega}{k_{y1}} = +E_{x2}^+ \frac{\epsilon_2 \omega}{k_{y2}} \quad 3.2.1.9$$

By combining equation 3.2.1.7 and 3.2.1.9 we then obtain:

$$\frac{\epsilon_1}{k_{y1}} = -\frac{\epsilon_2}{k_{y2}} \quad 3.2.1.10$$

The  $y$  component of the wave vector of the reflected and transmitted fields in

terms of the total wave vector and the in-plane wave vector of the fields may also be obtained:

$$\begin{aligned} k_{y1}^2 &= \varepsilon_1 k_0^2 - k_x^2 \\ k_{y2}^2 &= \varepsilon_2 k_0^2 - k_x^2 \end{aligned} \quad 3.2.1.11$$

By substituting equation 3.2.1.11 into equation 3.2.1.10 we obtain the SPP dispersion relation:

$$k_{spp} = k_x = k_0 \left( \frac{\varepsilon_1 \varepsilon_2}{\varepsilon_1 + \varepsilon_2} \right)^{1/2} \quad 3.2.1.12$$

In this case, medium 1 is a dielectric and has a real dielectric function  $\varepsilon_1$ , and medium 2 is a metal with the dielectric function  $\varepsilon_2 = \varepsilon_{2r} + \varepsilon_{2i}$ . Assuming  $|\varepsilon_{2r}| > \varepsilon_{2i}$ , we obtain a complex wave vector  $k_x = k_{xr} + ik_{xi}$  with

$$\begin{aligned} k_{xr} &= k_0 \left( \frac{\varepsilon_1 \varepsilon_{2r}}{\varepsilon_1 + \varepsilon_{2r}} \right)^{1/2} \\ k_{xi} &= k_0 \left( \frac{\varepsilon_1 \varepsilon_{2r}}{\varepsilon_1 + \varepsilon_{2r}} \right)^{3/2} \frac{\varepsilon_{2i}}{2\varepsilon_{2r}} \end{aligned} \quad 3.2.1.13$$

If the condition that  $\varepsilon_{2r} < 0$  and  $|\varepsilon_{2r}| > \varepsilon_1$  is fulfilled, then a real  $k_{xr}$  is obtained. The imaginary part of wave vector  $k_{xi}$  specifies the internal absorption.

We shall now show that the expression derived in equation 3.2.1.12 and the Brewster mode dispersion relation are equivalent. The dispersion relation for the Brewster mode is derived separately below.

As shown in Figure 3.2.1.1, light is incident upon a planar interface between two media with dielectric constants  $\varepsilon_1$  and  $\varepsilon_2$  respectively. The tangential component of the incident wave vector must be conserved upon transmission through the interface:

$$k_{x1} = \sqrt{\varepsilon_1} k_0 \sin \theta = k_{x2} = \sqrt{\varepsilon_2} k_0 \sin \beta \quad 3.2.1.14$$

This is a form of Snell's law, which is more frequently written as:

$$\sqrt{\varepsilon_1} \sin \theta = \sqrt{\varepsilon_2} \sin \beta \quad 3.2.1.15$$

The Brewster angle is the angle at which TM polarized light is totally transmitted through the interface. The physical mechanism for this can be qualitatively understood from the manner in which electric dipoles in the media respond to TM polarized light. One can imagine that light incident on the surface is absorbed, and then

reradiated by oscillating electric dipoles at the interface between the two media. The polarization of freely propagating light is always perpendicular to the direction in which the light is travelling. The dipoles that produce the transmitted light oscillate in the polarization direction of that light. These same oscillating dipoles also generate the reflected light. However, dipoles do not radiate any energy in the direction along which they oscillate. Consequently, if the direction of the refracted light is perpendicular to the direction in which the light is predicted to be specularly reflected, the dipoles will not create any reflected light. This occurs at an angle  $\theta_B = 90^\circ - \beta$  and equation 3.2.1.15 then becomes:

$$\sqrt{\epsilon_1} \sin \theta_B = \sqrt{\epsilon_2} \sin(90^\circ - \theta_B) = \sqrt{\epsilon_2} \cos \theta_B \quad 3.2.1.16$$

This equation can be used to determine the dispersion relation for the Brewster mode:

$$\sin \theta_B = \left( \frac{\epsilon_2}{\epsilon_1 + \epsilon_2} \right)^{1/2} \quad 3.2.1.17$$

and combining this with equation 3.2.1.14 we can obtain:

$$k_x = \sqrt{\epsilon_1} k_0 \sin \theta_B = k_0 \left( \frac{\epsilon_1 \epsilon_2}{\epsilon_1 + \epsilon_2} \right)^{1/2} \quad 3.2.1.18$$

The equivalence of equation 3.2.1.18 and equation 3.2.1.12 demonstrates that the SPP is a manifestation of the Brewster mode on a metal/dielectric interface.

The dispersion relation for a planar silver/air interface is shown in Figure 3.2.1.2 with  $\epsilon_1 = 1.0$  for air and the dielectric function of the metal ( $\epsilon_2$ ) modelled as that of silver, being described by a Drude model of the form:

$$\begin{aligned} \epsilon_{2r} &= 1 - \frac{\omega_p^2 \tau^2}{1 + \omega^2 \tau^2} \\ \epsilon_{2i} &= \frac{\omega_p^2 \tau}{\omega(1 + \omega^2 \tau^2)} \end{aligned} \quad 3.2.1.19$$

with a plasma frequency of  $\omega_p = 1.32 \times 10^{16} \text{ s}^{-1}$  and a relaxation time of  $\tau = 1.45 \times 10^{-14} \text{ s}$ .

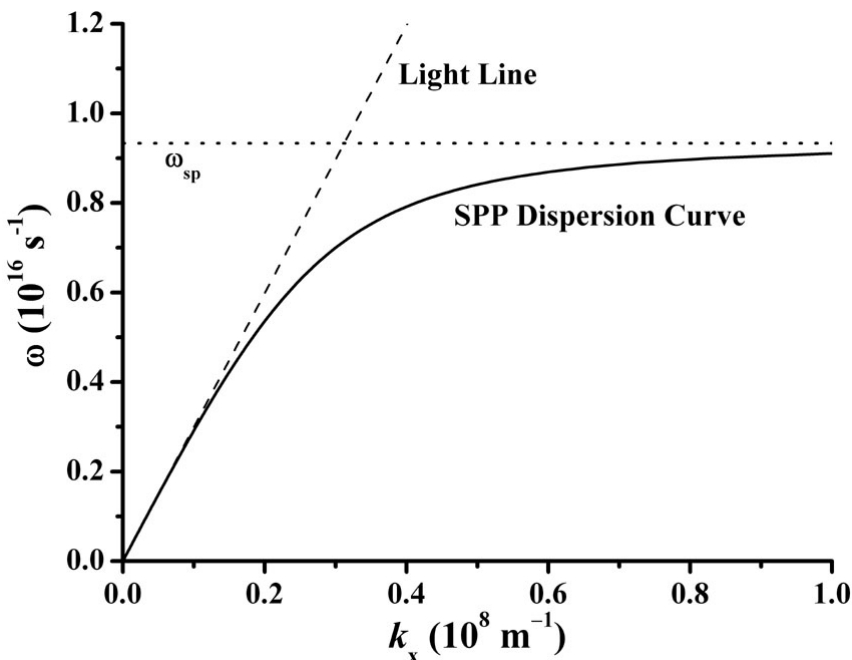


**Figure 3.2.1.2** The SPP dispersion curve (solid line) for a planar silver/air interface. The dashed line is the light line. The dotted line represents the high  $k_x$  asymptotic limit of  $\omega_{sp}$ .

It is clear that at large  $k_x$  the SPP dispersion curve becomes asymptotic to the surface plasmon frequency  $\omega_{sp} = \omega_p/(1 + \epsilon_1)^{1/2}$ , at which the real part of the dielectric constant of the silver ( $\epsilon_{2r}$ ) is equal, but opposite in sign, to the dielectric function of the dielectric  $\epsilon_1$ . This limit arises since at frequencies  $\omega_{sp} < \omega < \omega_p$  wave vector  $k_x$  (given by equation 3.2.1.12) is purely imaginary, and at  $\omega > \omega_p$  wave vector  $k_y$  (given by equation 3.2.1.11) is real indicating that it is no longer a trapped surface wave. Also note that at small  $k_x$  the SPP dispersion curve approaches the light line  $\omega/c$ , but remains larger than  $\omega/c$ , so that the SPP cannot transform into light, i.e. it is ‘nonradiative’. For this reason the SPP may not be excited on a planar metal/dielectric interface without some coupling mechanism to enable the incident photon to gain additional in-plane wave vector for the wave vector matching condition to be satisfied.

Coupling to a SPP may be achieved optically by two main methods: prism coupling and grating coupling. Prism coupling has two configurations, Otto and Kretschmann-Raether. Both rely on the increase in the photon wave vector through passing from a medium with a low refractive index to a higher refractive index. See Figure 3.2.1.3, an evanescent field is set-up at the prism-air interface for  $\theta > \theta_c$ , where  $\theta_c$  is the critical angle. The in-plane momentum of this field is given by

$$k_{\parallel} = \sqrt{\epsilon_p} \frac{\omega}{c} \sin \theta \quad 3.2.1.20$$

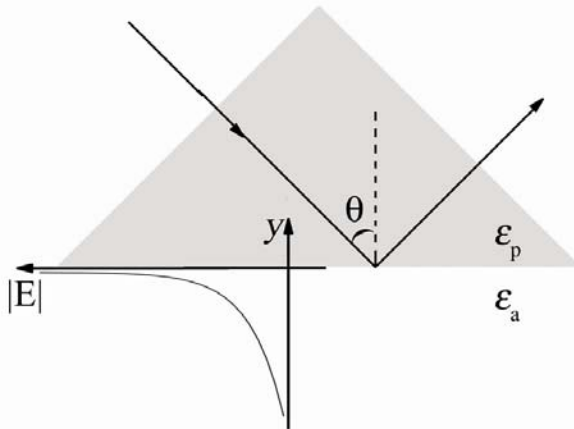


**Figure 3.2.1.3** Total reflection of light at one side of a prism. The prism is a dielectric medium ( $\epsilon_p$ ) such as glass or quartz; around the prism is air or vacuum.

On the basis of Figure 3.2.1.3, Otto [1968] first devised the attenuate total reflection (ATR) method for the coupling of incident optical light to a SPP on a smooth planar surface. As shown in Figure 3.2.1.4 (a), a flat metal surface is now brought into this decaying evanescent wave but such that an air gap remains between the prism and the metal. Then the evanescent field can excite the surface plasmon polarizations at the metal-air interface. Figure 3.2.1.4 (b) shows the dispersion relation for a planar silver/air interface with the dielectric constants of air  $\epsilon_a = 1.0$ , silica prism  $\epsilon_p = 2.129$ , and silver being described by a Drude model ( $\omega_p = 1.32 \times 10^{16} \text{ s}^{-1}$  and  $\tau = 1.45 \times 10^{-14} \text{ s}$ ). When the relation  $k_{spp} = k_{\parallel} = (\sqrt{\epsilon_p} \omega / c) \sin \theta$  is satisfied we have resonant energy transfer from the incident light beam to the SPP mode. Clearly from Figure 3.2.1.4 (b), one sees that the incident light with a frequency of  $\omega_L$  and an incident angle  $\theta = 55^\circ$  would excite a SPP (propagating on the silver/air interface) at point A. This approach has proved useful for studying single crystal metal surfaces and absorption on them. However, due to the fact that the coupling gap is very small (within 200 nm) to give a deep minimum for visible radiation it is difficult to use this method in practice.

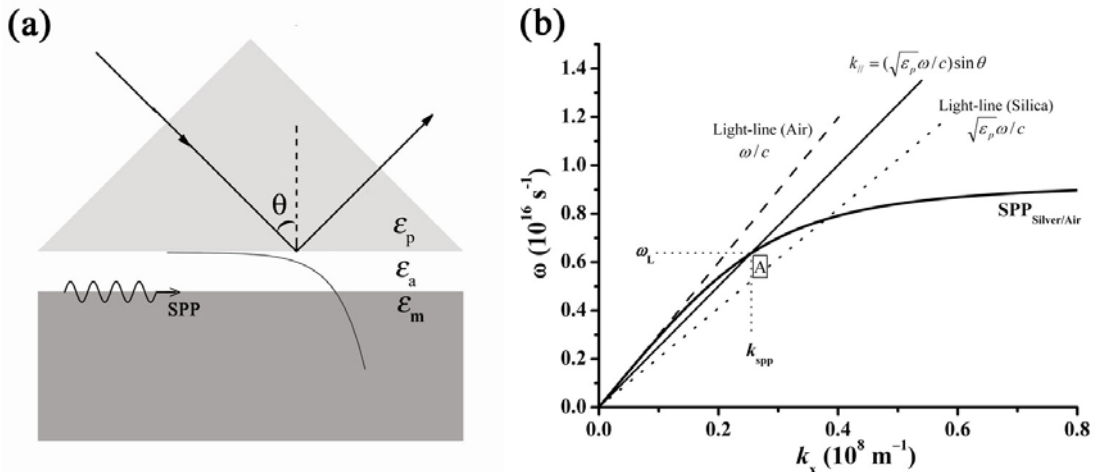


**Figure 3.2.1.4** (a) The Otto configuration. A dielectric gap lies between the prism and the metal surface. (b) The dispersion curve on a silver/air interface together with light-lines in air (dashed line) and silica (dotted line). At point A, a SPP mode with wave vector  $k_{\text{spp}} = 0.253 \times 10^8 \text{ m}^{-1}$  is excited by the light with a frequency  $\omega_L = 0.632 \times 10^{16} \text{ s}^{-1}$  and incident angle  $\theta = 55^\circ$ .

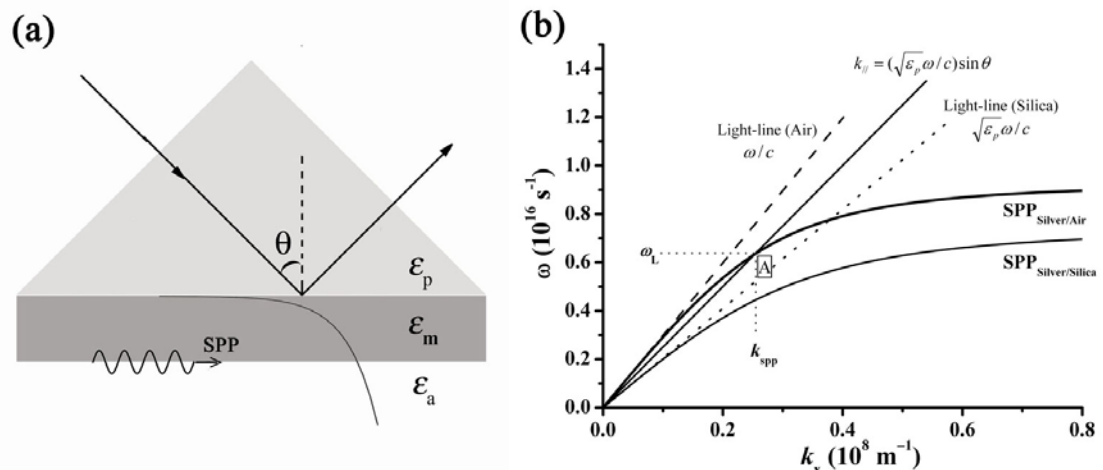


**Figure 3.2.1.5** (a) The Kretschmann-Raether configuration. The metal contacts the prism. (b) The dispersion curve for the silver/air and silver/silica interface together with light-lines in air (dashed line) and silica (dotted line). The incident light beam can excite a SPP mode at point A.

Kretschmann and Raether [1968] realized that one could use the metal as the spacing layer. As shown in Figure 3.2.1.5 (a), an evanescent wave generated at the prism/metal interface may excite SPPs at the metal/air interface so long as the thickness of the metal is not too great. The dispersion curves for silver/air and silver/silica interfaces are shown in Figure 3.2.1.5 (b), in which the dielectric constants are the same as that used in Figure 3.2.1.4 (b). Again, since at point A the relation

$k_{spp} = k_{\parallel} = (\sqrt{\epsilon_p} \omega / c) \sin \theta$  is satisfied, the incident light beam can now excite the SPP mode. For ideal coupling to the SPP the metal film thickness should be of the order of 45 nm at visible wavelengths.

The method of interest throughout the remainder of this thesis is that of grating coupling, and this will be described later in section 3.3.

### 3.2.2 Propagation Length

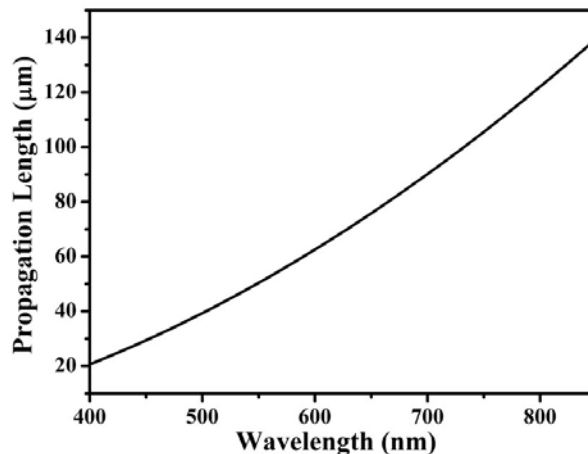


**Figure 3.2.2.1** Propagation length as a function of wavelength for a planar silver/air interface. The frequency dependent dielectric function for silver is modelled using a Drude model with  $\omega_p = 1.32 \times 10^{16}$  s<sup>-1</sup> and  $\tau = 1.45 \times 10^{-14}$  s.

Since the SPP wave vector expressed in equation 3.2.1.13 is a complex function, the real component  $k_{xr}$  is that of a travelling wave, and the imaginary component  $k_{xi}$  (a damping term) leads to an exponential decay of the mode as it propagates along the interface between the metal and the dielectric. From equation 3.2.1.2 the electric fields associated with the SPP will fall off as  $\exp(-k_{xi}x)$  and so the intensity falls off as  $\exp(-2k_{xi}x)$ . Thus the propagation length  $L_x$  is defined as the distance at which the intensity decreases to 1/e of its initial value, which is given by

$$L_x = \frac{1}{2k_{xi}} = \frac{1}{k_0} \left( \frac{\epsilon_1 + \epsilon_{2r}}{\epsilon_1 \epsilon_{2r}} \right)^{3/2} \frac{\epsilon_{2r}^2}{\epsilon_{2i}} \quad 3.2.2.1$$

It is thus possible, using equation 3.2.2.1 and values obtained for the dielectric constant of silver being described by a Drude model ( $\omega_p = 1.32 \times 10^{16}$  s<sup>-1</sup> and  $\tau = 1.45 \times 10^{-14}$  s), to

obtain the SPP propagation length at a planar silver/air interface for a range of wavelengths, as shown in Figure 3.2.2.1. For silver at 632.8 nm ( $\epsilon_{\text{Ag}} = -18.7 + i0.46$ ) the propagation length is 71.1  $\mu\text{m}$ .

### 3.2.3 Penetration Depth

When a SPP is excited at the surface between a dielectric and a metal, the amplitudes of its fields decrease exponentially into the surrounding media due to the imaginary nature of the normal wave vector component  $k_y$ . A useful measure of this decay is the penetration depth  $L_y$ . In order to obtain this it is necessary to obtain an expression for the imaginary part of  $k_y$ , combining equation 3.2.1.11 with 3.2.1.12,

$$k_{yj} = \pm \left( \epsilon_j k_0^2 - \frac{\epsilon_1 \epsilon_2}{\epsilon_1 + \epsilon_2} k_0^2 \right)^{1/2} = \pm k_0 \left( \frac{\epsilon_j^2}{\epsilon_1 + \epsilon_2} \right)^{1/2} \quad 3.2.3.1$$

where the subscript  $j$  denotes the medium in which  $k_y$  is being determined ( $j = 1$  (air), 2 (metal)). Therefore, the penetration depth  $L_y$ , defined as the distance normal to the interface over which the field strength falls to  $1/e$  of its value at the interface, is given by:

$$L_{y1} = \frac{1}{|k_{y1i}|} \text{ and } L_{y2} = \frac{1}{|k_{y2i}|} \quad 3.2.3.2$$

Figure 3.2.3.1 shows the penetration depth as a function of frequency ( $\omega/\omega_{\text{sp}}$ ) for a planar silver/air interface with the frequency dependent dielectric function described by a Drude model with  $\omega_p = 1.32 \times 10^{16} \text{ s}^{-1}$  and  $\tau = 1.45 \times 10^{-14} \text{ s}$ . In this case the dielectric medium is air and its dielectric constant  $\epsilon_1 = 1.0$ , hence the surface plasmon frequency is  $\omega_{\text{sp}} = \omega_p / \sqrt{2} = 0.933 \times 10^{16} \text{ s}^{-1}$ . For  $\lambda_0 = 632.8 \text{ nm}$  one obtains penetration depths of  $L_{y2} = 22.6 \text{ nm}$  for silver and  $L_{y1} = 420.3 \text{ nm}$  for air.

It is clear from Figure 3.2.3.1 that in the limit  $\epsilon_{2r} \rightarrow -\infty$  (a perfect metal), the penetration depth in the dielectric becomes infinite. The conditions closely pertaining to this situation correspond to those of the dispersion curve at very low frequencies where most metals may be considered as perfect metals. As shown in Figure 3.2.1.2, at these low frequencies the SPP dispersion curve asymptotically approaches the light-line. Also note that at the other limit of  $\omega = \omega_{\text{sp}}$  ( $|\epsilon_{2r}| = \epsilon_1$ ) the decay length of the fields in both

media will reduce to zero, which indicates that there are no longer exponentially decaying fields present. The dispersion curve at this point has infinite wave vector  $k_x$  ( $k_{\text{spp}}$ ), and since  $k_y^2 = k_0^2 - k_{\text{spp}}^2$ ,  $k_y$  must equal  $i$  times minus infinity which corresponds to a decay length of zero.

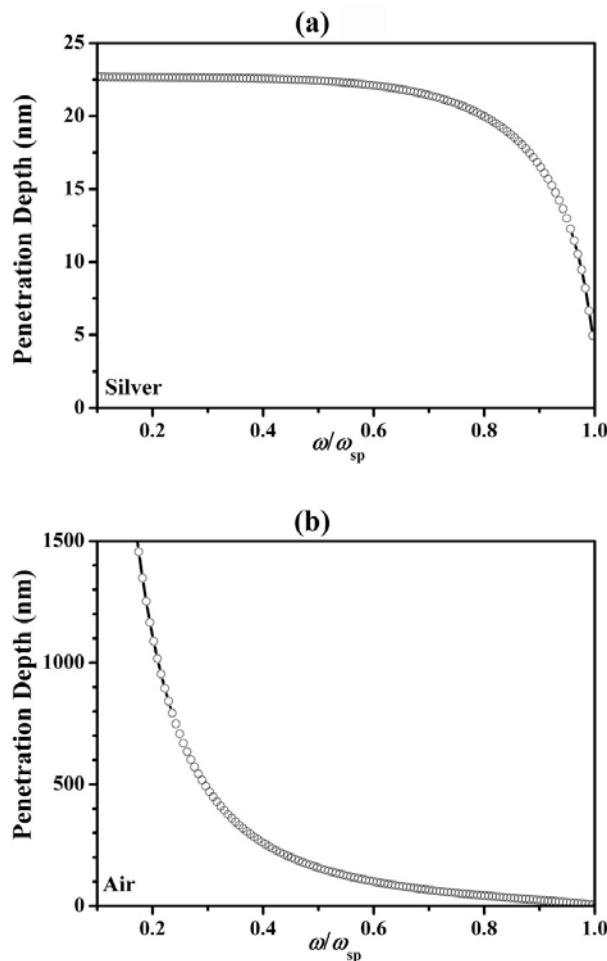


**Figure 3.2.3.1** The penetration depth of the SPP fields into (a) silver and (b) air for a planar silver/air system. The frequency dependent dielectric function for the silver is modelled using the Drude model with  $\omega_p = 1.32 \times 10^{16} \text{ s}^{-1}$  and  $\tau = 1.45 \times 10^{-14} \text{ s}$ .

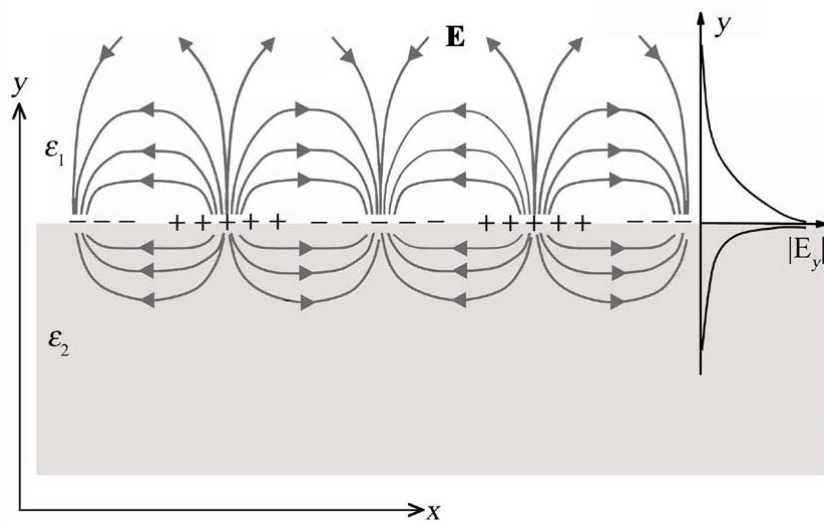


**Figure 3.2.3.2** Schematic representation of the polarization surface charge density and associated electric field for the SPP mode. The field decays exponentially into both the metal ( $\varepsilon_2$ ) and dielectric ( $\varepsilon_1$ ).

From these results we now have a physical view of the SPP on a planar metal/dielectric interface. It is a longitudinal surface charge oscillation coupled to incident EM radiation which, at optical frequencies, is propagating along the surface. This surface charge oscillation then causes field loops in the two media. Since the total fields of the SPP decay exponentially away from the surface into both media, the SPP field is trapped at the surface. The localised nature of the SPP field is shown schematically in Figure 3.2.3.2.

### 3.3 Grating Coupling to Surface Plasmon Polaritons

It has been shown that a SPP mode on a flat metal surface can not be directly excited by incident radiation in the dielectric because the wave vector of the SPP is always beyond that of a grazing incidence photon-polariton of the same frequency. In section 3.2 of this chapter, the prism coupling technique has been introduced to couple the incident light to the SPPs. In this section we shall describe the method of coupling to, and the properties of, SPPs on shallow metal gratings.

### 3.3.1 The Dispersion Relation

A schematic of the grating discussed and the coordinate system used to describe the orientation is shown in Figure 3.3.1.1, where  $a$  is the grating amplitude and  $\lambda_g$  is the grating pitch (periodicity). The polar angle  $\theta$  is defined as the angle of incidence as measured from normal to the average surface plane of the profile. The azimuth angle  $\varphi$  describes the rotation of the plane of incidence from the positive  $x$ -axis (parallel to the grating vector), and the polarization of the incident radiation is defined with respect to the plane of incidence, i.e. TM ( $p$ -polarized) radiation has its electric vector in the plane of incidence, and TE ( $s$ -polarized) has its electric vector normal to the plane of incidence.

By introducing a surface corrugation to the interface between two media, the translational symmetry of the surface is destroyed, and a photon incident upon the surface can be scattered by subtracting or adding an integer multiple of the grating vector  $\mathbf{k}_g$  ( $k_g = 2\pi/\lambda_g$ ) in the direction normal to the grating grooves. This is the origin of the diffracted orders produced by such a surface. If the grating is oriented such that it is in the classical mount (azimuth angle  $\varphi = 0^\circ$ , the plane of incidence normal to the grating grooves) and the frequency of the incident light and the incident polar angle are such that the diffracted order is evanescent, then the enhanced momentum of these evanescent fields allows the incident radiation to couple to surface modes according to the equation:

$$k_{spp} = k_0 \sin \theta \pm N k_g \quad 3.3.1.1$$

where  $k_0 \sin \theta$  is the in-plane wave vector of the incident radiation, and  $N$  is an integer.

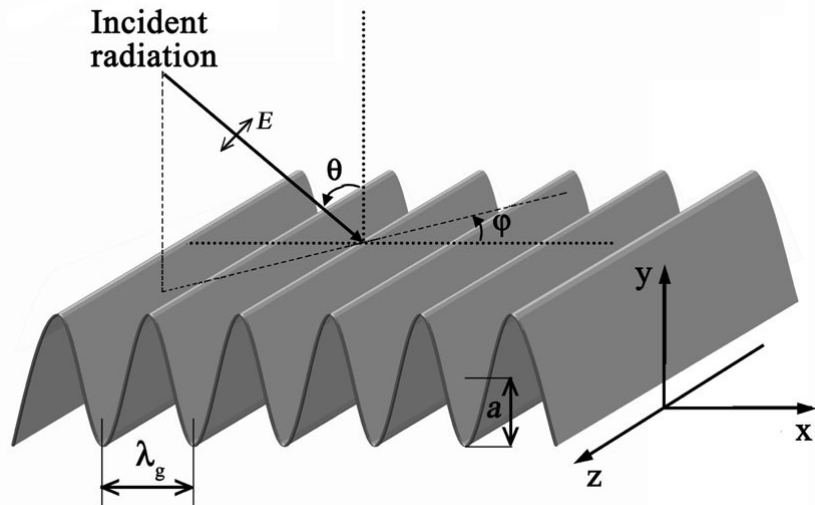


**Figure 3.3.1.1** A schematic showing the grating system under consideration. The direction of the electric field vector ( $\mathbf{E}$ ) is shown for incident TM polarized radiation. Here  $\lambda_g$  is the grating pitch,  $\theta$  is the incident angle,  $\phi$  is the azimuth angle,  $a$  is the grating amplitude.

The mechanism for grating coupling to the SPP is best described by considering the influence of the periodic corrugation on the SPP dispersion curve (equation 3.2.1.12 and Figure 3.2.1.2) as illustrated schematically by Figure 3.3.1.2. The periodicity of the surface corrugation may be represented as a line of points in reciprocal space separated by the grating vector  $k_g$ . The SPP dispersion curve as well as the incident light may be ‘scattered’ from these lattice points. Since the dispersion curve of the diffracted SPP now exists between the light lines, radiative coupling of incident TM polarized light to the SPP may now be achieved. Note here that by corrugating the surface, the dispersion relation for the planar interface may be distorted due to the introduction of effective surface impedance, but in the limit of a small amplitude corrugation, the planar dispersion relation is a good approximation.

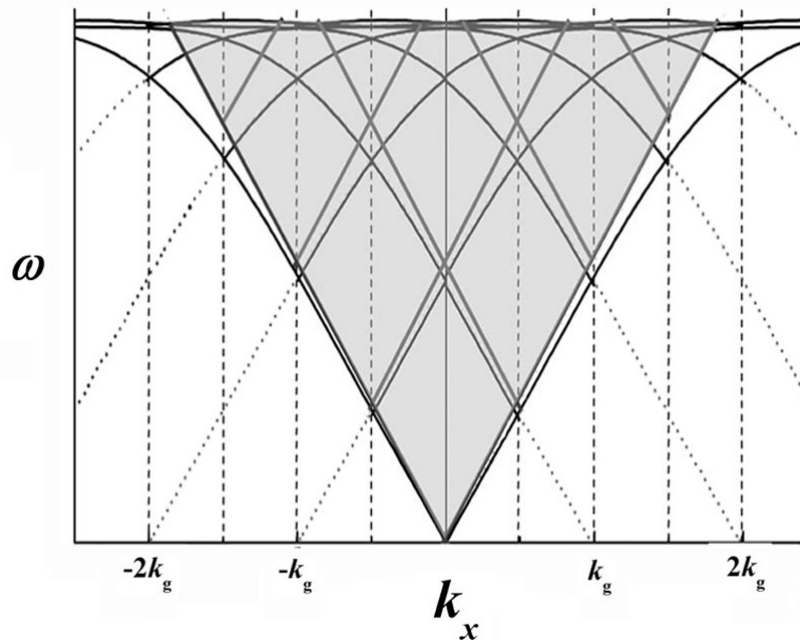


**Figure 3.3.1.2** The dispersion curve for grating-coupled SPPs which has been folded at the Brillouin zone boundaries. Parts of the scattered dispersion curves (shaded) that fall between the light lines can be radiatively coupled.

Unlike the planar system case the dispersion curve is not identical in all directions in reciprocal space since the periodicity is in the  $x$ -axis only, and therefore the scattering lattice points only occur in the  $x$  direction. When the light is incident at non-zero azimuth angles (in the conical mount), the vectors  $\mathbf{k}_{\text{spp}}$ ,  $\mathbf{k}_0$  and  $\mathbf{k}_g$  are no longer collinear and the coupling condition of equation 3.3.1.1 is, by simple trigonometry, now given by:

$$k_{\text{SPP}}^2 = k_0^2 \sin^2 \theta + N^2 k_g^2 \pm 2Nk_g k_0 \sin \theta \cos \varphi \quad 3.3.1.2$$

In order to show this it is useful to plot out the dispersion curve in the  $k_x$ - $k_z$  plane for a constant  $\omega$ . Figure 3.3.1.3 shows a schematic 2-D reciprocal space illustrating the possible solutions of equation 3.3.1.2 ( $N = 1$  only).

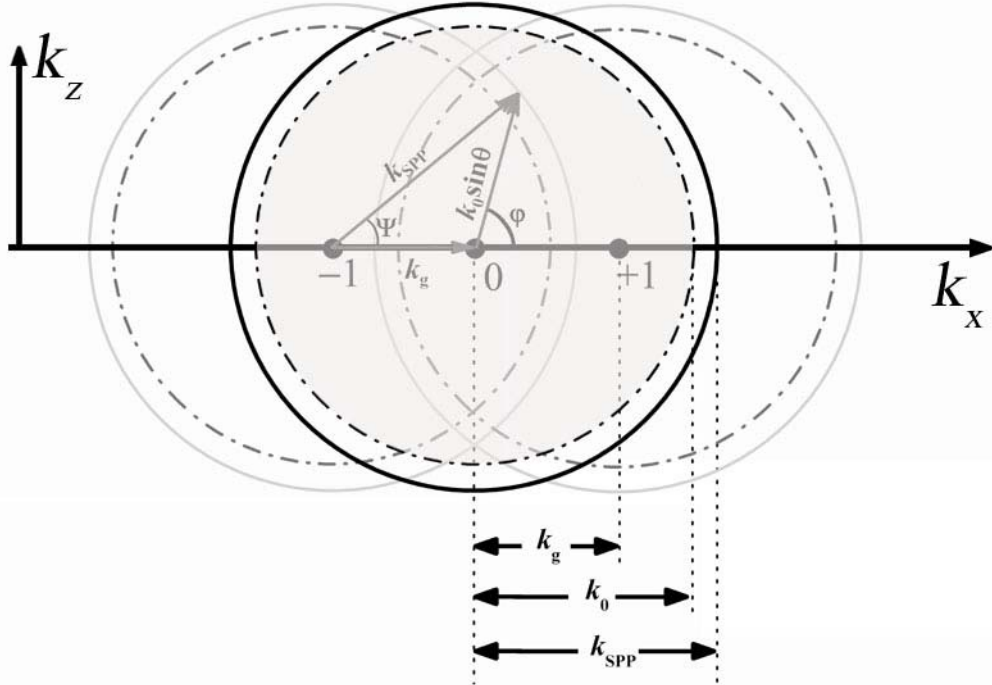


**Figure 3.3.1.3** A 2-D reciprocal space representation of the SPP modes and light circles produced by a grating. The thick-dashed circle of  $k_0$  centred upon the origin describes the maximum wave vector available to a photon in the plane of the grating surface. The circle (thick-solid) at a slightly greater radius than this represents the momentum of the zero-order SPP mode ( $k_{SPP}$ ). Both of these circles may be scattered by  $\pm k_g$ , which results in the two circles centred at the reciprocal lattice points. The arrows indicate that via a grating vector of  $k_g$  a photon at angle of incidence  $\theta$  and azimuth angle  $\varphi$  is coupled to a SPP that propagates at an angle  $\Psi$  with respect to the  $k_x$ -axis.

The light circle and SPP dispersion curve originating at the origin and those scattered by the lattice point at  $\pm k_g$  are shown in Figure 3.3.1.3. Note that the light circle (dashed) centred at the origin represents the maximum wave vector available to the incident photon. Hence coupling is only possible to the modes that fall within this circle (shaded area). A mechanism for coupling a photon at angle of incidence  $\theta$  and azimuth angle  $\varphi$  to the SPP scattered from  $-k_g$  is also shown in Figure 3.3.1.3. In this case, the SPP propagates at an angle with respect to the  $k_x$ -axis,  $\Psi$ , given by

$$\psi = 90 - \cos^{-1} \left( \frac{k_0 \sin \theta \sin \varphi}{k_{SPP}} \right) \quad 3.3.1.3$$

It is clear from Figure 3.3.1.3 that if light is incident in the  $y$ - $z$  plane (azimuth

angle  $\phi = 90^\circ$ ) both of the two SPPs scattered from  $\pm k_g$  can be excited. The two contributing SPPs are respectively propagating at  $\Psi^+$  and  $\Psi^-$ :

$$\psi^\pm = \pm \tan^{-1} \left( \frac{k_0 \sin \theta}{k_g} \right) \quad 3.3.1.4$$

which is clearly not in the plane of the incident light. Due to the equal magnitudes and opposite directions of the  $x$ -component of two SPP wave vectors, the resulting SPP is, therefore, a standing wave in the  $x$ -direction but propagating in the  $z$ -direction.

Previously, for the planar interface, the polarization of the incident radiation was defined with respect to the plane of incidence. It was shown that only TM polarized incident radiation could excite the SPP, since a component of electric field perpendicular to the interface is required to set up the necessary surface charge. Now that the surface of the metal has been corrugated the symmetry of the surface is broken. Incident radiation may now have a component of electric vector normal to the interface for both TM and TE polarizations, depending upon the orientation of the grating grooves with respect to the plane of incidence. If the light is incident in the classical mount only TM polarized light may excite the SPP, since TE polarized light has its electric field parallel to the grating grooves. For an azimuth angle  $0^\circ < \phi < 90^\circ$  both TM and TE polarized light may result in SPP excitation. While at azimuth angle  $\phi = 90^\circ$ , the electric field of TE polarized light is normal to the non-zero gradient surface and may be used to excite the SPP. TM polarized light has a component of its electric field normal to the surface only for non-zero polar angles, but in general does not couple well to SPPs at  $\phi = 90^\circ$ . However Watts *et al.* [1997] reported a special case that TM polarized light may excite the SPP on a very deep grating. In chapter 8, we will demonstrate another special case that at  $\phi = 90^\circ$  a significant SPP mode is excited by TM polarized light for a thin silver slab with even very shallow corrugations on both sides.

### 3.3.2 Coupling Strength and Reflectivity Features

Consider Figure 3.3.2.1, the theoretical TM reflectivity as a function of frequency, obtained using the computer code based upon the method of Chandezon described in chapter 2, for a sinusoidal silver grating with amplitude  $a = 10$  nm and

pitch  $\lambda_g = 650$  nm at normal incidence  $\theta = 0^\circ$  and azimuth angle  $\varphi = 0^\circ$ . In the calculation the dielectric constant of silver is modelled as a Drude model with  $\omega_p = 1.32 \times 10^{16} \text{ s}^{-1}$  and  $\tau = 1.45 \times 10^{-14} \text{ s}$ .

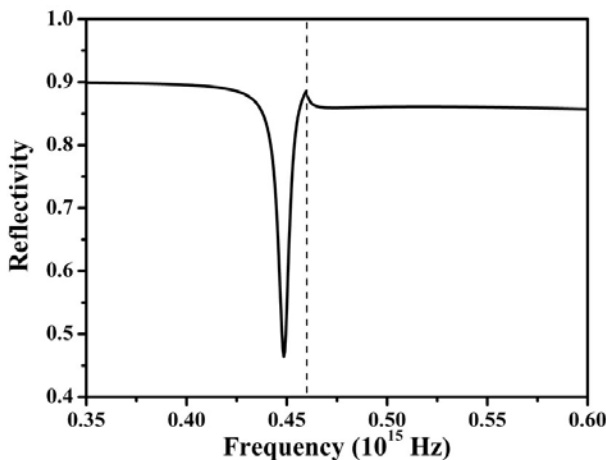


**Figure 3.3.2.1** Theoretical zero-order TM reflectivity as a function of frequency for a 10 nm amplitude 650 nm pitch silver grating for normal incidence and  $\varphi = 0^\circ$ . The frequency dependent dielectric constant of silver is modelled as a Drude model with  $\omega_p = 1.32 \times 10^{16} \text{ s}^{-1}$  and  $\tau = 1.45 \times 10^{-14} \text{ s}$ . A reflectivity minimum arises at  $f = 0.449 \times 10^{15} \text{ Hz}$  due to the excitation of the first order SPP. A pseudo critical edge appears at  $f = 0.46 \times 10^{15} \text{ Hz}$  since the first diffracted order becomes evanescent.

There are two main features to be seen readily in Figure 3.3.2.1. Firstly, a pseudo critical edge (the Rayleigh anomaly), marked by the dotted line, appears at  $f = 0.46 \times 10^{15} \text{ Hz}$  which correspond to the frequency at which the first diffracted order has become evanescent and redistributed its energy into the remaining propagating orders. The second, and most noticeable feature in the reflectivity spectrum arises at  $f = 0.449 \times 10^{15} \text{ Hz}$  which is the frequency at which the SPPs corresponding to the first order diffraction process occur. It is clear that the reflectivity feature for this SPP is manifested as a reflectivity minimum in the zero-order reflection from the structure. This reflection minimum arises due to the combination of the specularly reflected light, and the re-radiated light from the coupled SPP. The light incident onto the grating may undergo two processes: direct reflection into the specular beam, and when the coupling condition is satisfied (equation 3.3.1.1) scattering into a diffracted order which excites the SPP propagating along the surface. The SPP may then suffer a second scattering process, re-radiating it back into the specularly reflected beam direction. Since the

electric field is reversed upon reflection from a metal surface the specularly reflected light is  $180^\circ$  out of phase with respect to the incident light. The phase of the evanescent first diffracted order is  $90^\circ$  out of phase with the incident light, and then undergoes a further  $90^\circ$  phase shift when exciting the SPP, since the SPP is resonant as a forced damped oscillator. This process is repeated to couple the SPP back out into the specularly reflected beam so that the re-radiated light is in phase with the incident light. Therefore, since the specularly reflected light and the re-radiated light are  $180^\circ$  out of phase, they cancel to produce a reflectivity minimum.

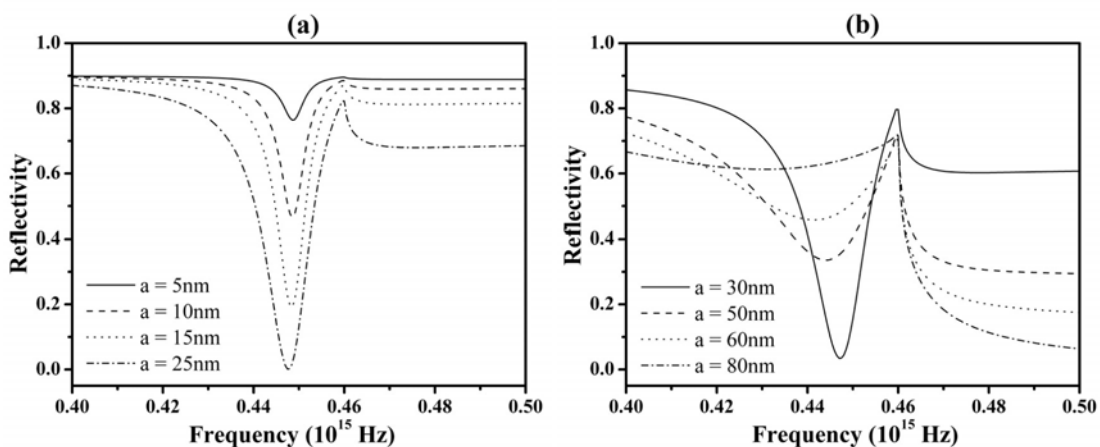


**Figure 3.3.2.2** Theoretical zero-order TM reflectivity as a function of frequency at normal incidence and  $\varphi = 0^\circ$  for a silver grating with a pitch of 650 nm and different amplitudes. The dielectric constant of silver is described by a Drude model with  $\omega_p = 1.32 \times 10^{16} \text{ s}^{-1}$  and  $\tau = 1.45 \times 10^{-14} \text{ s}$ .

The shape of the SPP resonance is governed by the strength of the coupling into and out of the SPP, and the absorption of energy into the metal. The re-radiated and absorption of energy are the damping terms, and as with all resonant systems, the width of the resonance is due to the total damping of the oscillator. The re-radiation term increases as approximately  $a^2$  to first order.

Also the depth of the resonance is given by the ratio of the radiative damping to the absorptive part of the damping, with maximum depth occurring when these two terms are equal ( $\Delta\omega_{rad} = \Delta\omega_{abs}$ ). Figure 3.3.2.2 shows the theoretical zero-order TM reflectivity around the first order SPP resonance frequency at normal incidence ( $\theta = 0^\circ$ ) and azimuth angle  $\varphi = 0^\circ$  for silver grating with a pitch of 650 nm and different amplitudes. Clearly, for a very shallow grating ( $a = 5 \text{ nm}$ ) the SPP resonance is

manifested as a narrow, but shallow resonance and, with increasing amplitude, the resonance widens and deepens until, when the radiative part of the damping is equal to the absorptive part of the damping ( $a = 25 \text{ nm}$ ), the minimum of the resonance is at a reflectivity of zero. On further increasing the amplitude the width of the resonance continues to increase, but the depth of the minimum decreases. As shown in Figure 3.3.2.2 (b), for a very deep grating  $a = 80 \text{ nm}$ , a very broad and shallow minimum results.

### 3.3.3 Band Gaps in the Dispersion of Grating Coupled SPPs

In a similar way to the electrons in a crystal, energy gaps may open up in the dispersion relation of SPPs propagating along a metal grating.

Consider a SPP propagating perpendicular to the grooves on a metallic grating with a grating vector  $k_g$  ( $k_g = 2\pi/\lambda_g$ ) and profile given by a Fourier series

$$f(x) = a_1 \sin(k_g x + \phi_1) + a_2 \sin(2k_g x + \phi_2) + \dots + a_N \sin(Nk_g x + \phi_N) \quad 3.3.3.1$$

where  $a_N$  is the amplitude of the  $N^{\text{th}}$  order harmonic component of the corrugation, and  $\phi_N$  is the relative phase (usually  $\phi_1$  is set to  $0^\circ$ ). Due to the introduction of the periodicity, the SPP modes in momentum space are “reflected” at the Brillouin zone (BZ) boundary (Bragg scattering) resulting in crossing points between the different branches. In this section we shall concentrate on the crossing between the branches scattered by  $\pm k_g$ , which occurs at normal incidence.

We start by mapping the TM reflectivity of a purely sinusoidal silver grating with a pitch of 650 nm and fundamental amplitude of 5 nm as a function of incident frequency and angle, as shown in Figure 3.3.3.1. It is clear that for this sinusoidal profile there is no significant interaction between the two branches of the dispersion curve as shown by the absence of a gap in this case. In fact it is possible for the  $k_g$  component to produce a band gap via a two scattering process. However, this two scattering process is quite weak for the small amplitude of the primary component used here.

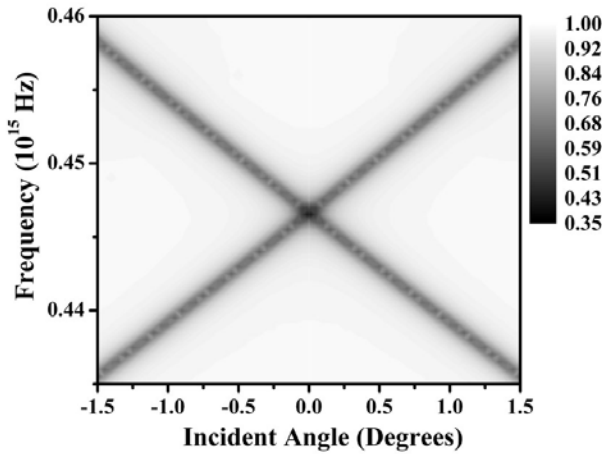


**Figure 3.3.3.1** Numerically modelled zero-order TM reflectivity of a purely sinusoidal metal grating with a fundamental amplitude of 5 nm and a pitch of 650 nm. The dielectric constant of the metal is fixed at  $\epsilon_r = -17.5$  and  $\epsilon_i = 0.6$ .

If a  $2k_g$  component is added to a grating profile then a band gap at the crossing point of the SPP at normal incidence is opened. Another way of looking at this is that the  $k_g$  component of the grating scatters two SPPs (from  $+ k_g$  and from  $- k_g$ ) so that they cross at normal incidence and are counter propagating. The  $2k_g$  component then provides an interaction between these two branches, the forward and backward travelling surface modes are coupled together by this component and an energy gap opens up as shown in Figure 3.3.3.2.

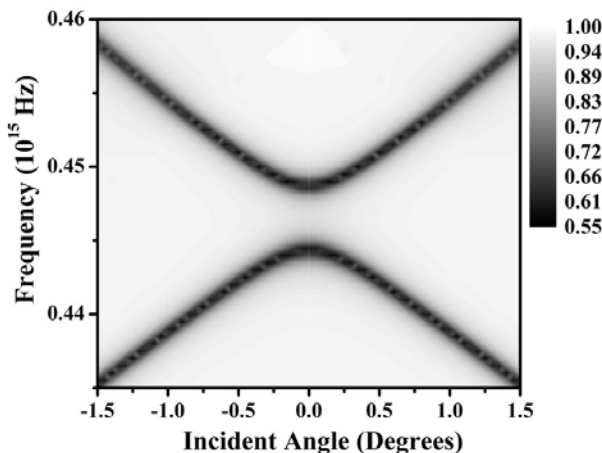


**Figure 3.3.3.2** Numerically modelled zero-order TM reflectivity of a metal grating structure with a pitch of 650 nm and  $a_1 = 5$  nm,  $a_2 = 2$  nm, and  $\phi_2 = 0^\circ$ . The first harmonic component produces a band gap at the intersection of the  $\pm 1$  SPP branches. The dielectric constant of the metal is fixed at  $\epsilon_r = -17.5$  and  $\epsilon_i = 0.6$ .

When radiation is incident upon a grating with a finite first harmonic component, the  $2k_g$  will result in the forward and backward travelling waves interfering constructively to set up a standing wave. We shall now investigate the origin of the energy gap in terms of the field distributions between the two standing wave solutions. Using simple symmetry arguments, the two possible solutions on either side of the band gap are

$$\Psi_1 = \exp(ik_g x) + \exp(-ik_g x) = 2\cos(k_g x) \quad 3.3.3.2$$

$$\Psi_2 = \exp(ik_g x) - \exp(-ik_g x) = 2i\sin(k_g x) \quad 3.3.3.3$$

Obviously one of these solutions has its nodes at the peaks of the  $2k_g$  component of the grating, and the other at the troughs of the  $2k_g$  component of the grating. The field distributions and hence the energies of the two solutions are different and thus a band gap opens up at the crossing point. By deriving the field distribution around the interface, one sees that the high energy solution has its extrema of the normal field component and surface charge distribution in the troughs of the  $2k_g$  component, whereas for the low energy solution they occur on the peaks of the  $2k_g$  component (Barnes *et al.* [1996]), which is due to the more distorted field lines leading to a greater stored energy. These distributions are schematically shown in Figure 3.3.3.3.

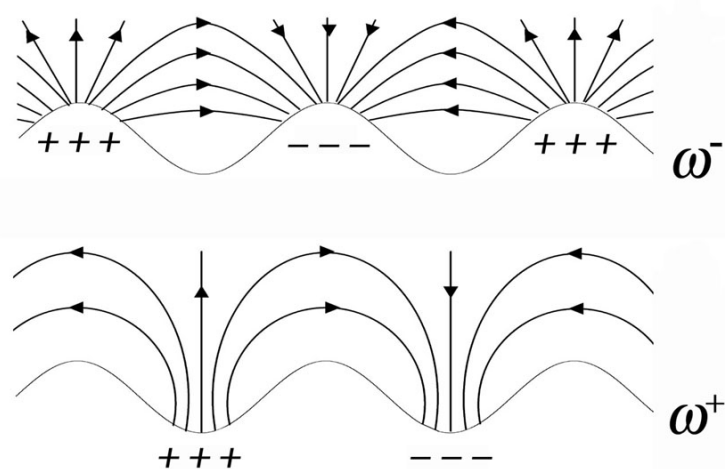


**Figure 3.3.3.3** A schematic representation of the electric field and surface charge distributions for the two standing wave solutions at the gap boundaries of a band gap. The upper sketch is for the lower frequency solution ( $\omega^-$ ). The volume integrals of the energy density in the two field distributions show that  $\omega^+$  is of higher energy.

Finally we shall discuss the influence of the phase shift between the fundamental and first harmonic components of the grating. The relative phase  $\phi_2$  between the  $k_g$  and  $2k_g$  components determines the coupling strength around the band edges. If the  $2k_g$  component is in phase with the  $k_g$  component ( $\phi_2 = 0^\circ$ ) then both band edges are coupled to equally, as shown in Figure 3.3.3.2. However, as shown in Figure 3.3.3.4, if the relative phase  $\phi_2 = \pm 90^\circ$  then only one of the band edges is readily coupled to (Weber and Mills [1985], Nash *et al.* [1995]).

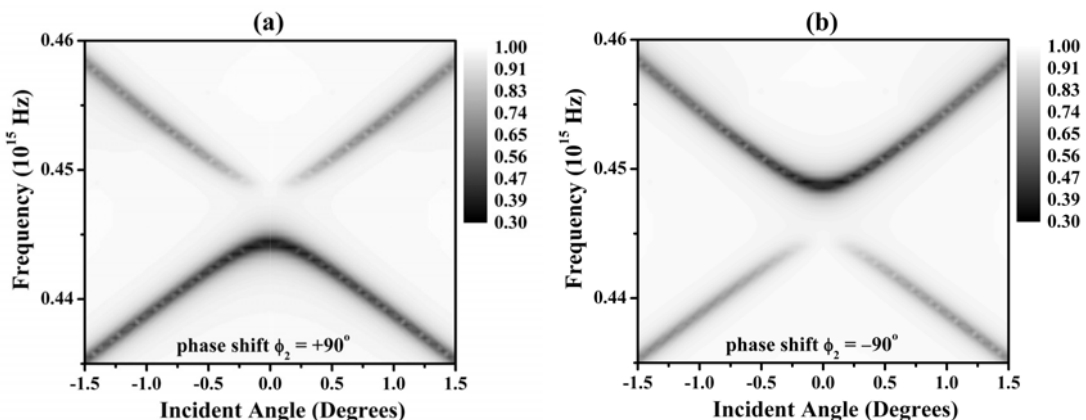


**Figure 3.3.3.4** Numerically modelled zero-order TM reflectivity of a metal grating structure with a pitch of 650 nm and  $a_1 = 5$  nm,  $a_2 = 2$  nm, and phase shift between the first and fundamental harmonic component (a)  $\phi_2 = +90^\circ$  and (b)  $\phi_2 = -90^\circ$ . The dielectric constant of the metal is  $\varepsilon_r = -17.5$  and  $\varepsilon_i = 0.6$ .

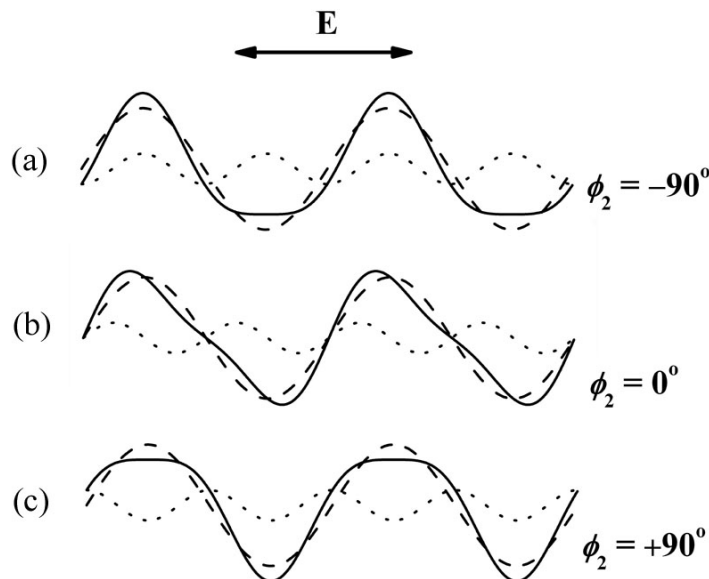


**Figure 3.3.3.5** Sketch of light at normal incidence coupling to the modes of a corrugated surface (solid line) containing  $k_g$  (dashed line) and  $2k_g$  (dotted line) components.

As mentioned previously for coupling between the photons and the SPP modes to occur there must be a component of the incident electric field normal to the surface. For the standing waves which form the band edges of the band gap the electric field must be normal to the surface at the point on the grating profile where the surface charges are oscillating. The  $k_g$  and  $2k_g$  components of the profile for the three cases considered in this section are shown schematically in Figure 3.3.3.5. For normal incidence there will be no component of the electric field normal to the surface where the surface has a zero gradient. When  $\phi_2 = +90^\circ$ , the troughs of the  $2k_g$  component correspond to flat regions of the surface. For the high energy mode the charges are located on the troughs of the  $2k_g$  component, and from Figure 3.3.3.5 (c) these occur at the peaks and troughs of the  $k_g$  component. Since there is no normal component of the electric field at these points there can be **no** coupling to the SPP. However, the low energy solution has its charges located at the peaks of the  $2k_g$  component, and these corresponding to the sloping sides of the  $k_g$  component. Therefore there is a normal component of the incident field in this case, and coupling occurs, as shown in Figure 3.3.3.4 (a). The reverse is true for the case where  $\phi_2 = -90^\circ$  as shown in Figure 3.3.3.4 (b), since the troughs of the  $2k_g$  component now appear on the sides of the  $k_g$  component. For  $\phi_2 = 0^\circ$  since the peaks and troughs of the  $2k_g$  component occur at equivalent points with respect to the  $k_g$  component, the coupling is therefore the same for both, as shown in Figure 3.3.3.2.

### 3.3.4 Polarization Conversion

There are two mechanisms by which linearly polarized incident radiation upon a grating may be converted to an orthogonal polarization state. The first is mediated via SPP excitation (Inagaki *et al.* [1986], Bryan-Brown *et al.* [1990], Elston *et al.* [1991], and Depine and Lester [2001]). As discussed in section 3.3.1, when a grating is orientated such that  $0^\circ < \phi < 90^\circ$  both TM and TE polarized incident radiation may excite the SPP. This implies that when radiation is re-radiated back out into the specular or diffracted order, both TM and TE polarized radiation may be emitted. If TM polarized radiation is used to excite the SPP then in this situation both TM and TE polarized light will be re-radiated so that when the specularly reflected light is

investigated it consists of both polarizations. For shallow gratings it may be shown that the polarization converted signal varies approximately as  $\sin^2(2\varphi)$ , by considering the electric field components relative to the grating profile (Bryan-Brown *et al.* [1990]). The maximum in polarization conversion occurs when the grating grooves are orientated at an azimuth angle  $\varphi = 45^\circ$  since at this orientation coupling strength for TM and TE polarized incident radiation is nearly equal. It should also be noted that a second set of polarization conversion maxima occur when the propagation direction of the SPP is at  $45^\circ$  to the direction of the grating vector in the plane containing the grating (see Depine and Lester [2001]).

The second way in which polarization conversion occurs is also  $\varphi$  dependent, but cyclically dependent upon the grating amplitude (Watts and Sambles [1997]). The mechanism by which this polarization conversion occurs is as follows. The electric field of the incident radiation may be split into two components, one parallel to the grating vector ( $E_x$ ) and one parallel to the grating grooves ( $E_z$ ). Since the  $E_z$  component does not cut the grating grooves, it will be reflected as if it were reflected from a planar surface at the position of the average surface plane of the grating. However, the  $E_x$  component does cut across the grating grooves and may produce circulating fields within the grating grooves, which alters the effective average plane of the grating for this component. The difference in the mean positions of these ‘effective mirrors’ for the two electric field components results in a phase difference between them and this rotates the plane of polarization. The phase difference between the two components depends upon the grating amplitude with a maximum occurring when the phase difference between  $E_x$  and  $E_z$  is  $180^\circ$ .

### 3.4 Summary

In this chapter we have introduced the surface plasmon polariton (SPP) as an oscillation of the surface charge density at the interface between a metal and a dielectric with its associated fields. We have derived the dispersion of the SPP mode for a planar interface, and shown the spatial extent of the SPP fields. On a planar surface the SPP is non-radiative and can **not** be excited since its momentum is greater than that available of incident radiation. Therefore mechanisms, such as prism coupling and grating

coupling, to enhance the momentum of incident photons are required. We have then determined the dispersion of the SPP on gratings, including a brief discussion on the formation of band gaps in the SPP dispersion curves. Finally the polarization conversion from gratings has been explained.

## Chapter 4

# Low Dispersion of Surface Plasmon Polaritons on Deep Silver Gratings

### 4.1 Introduction

In chapter 3, we have considered the optical response of relatively shallow silver grating structures. In the regime of such shallow gratings which have a small ratio of depth (the distance from peak to trough, twice the amplitude) to pitch ( $\lambda_g$ ), the excitation of SPPs on metal gratings can be very well described by perturbation theory (Maradudin [1982]) and much experimental evidence for these electromagnetic resonances has been reported. In this chapter we shall study the dispersion curves of SPPs on single interface deep silver gratings, where the definition of the term deep is that the depth of the grating is of the order of, or greater than, the grating pitch.

It is well known that for shallow metallic grating structures the SPP can only be excited in a small corner of the dispersion curve in the zero-order (non-diffracting for all angles of incidence) region. The reason for this is that even with the added momentum available to the incident radiation due to scattering from the grating, the momentum of the SPP on such a structure is still close to the grazing photon momentum and it is thus excited just beyond the diffraction edge. However, for high-aspect ratio metallic monogratings the SPP dispersion curve may be so severely modified that resonant absorption of light due to SPP excitation may occur well within the zero-order region of the spectrum. It has been shown that such structures can display very strong optical features. Sobnack *et al* [1998] modelled the scattering of EM waves from zero-order silver gratings at a fixed wavelength and noted that as the grating depth is increased a set of reflection minima occur due to the excitation of SPP modes localized in the deep grooves. Experimentally it has been found that deep lamellar gratings can support highly localized resonances within the grooves with grating pitches of 1.75  $\mu\text{m}$ .

and depths of up to 1  $\mu\text{m}$  (Lopez-Rios *et al* [1998], and Garcia-Vidal *et al* [1999]). These flat-banded resonances are very different to the SPPs excited on shallow gratings, and have been explained as being due to hybrid waveguide-SPP resonances. Also, Porto *et al* [1999] evaluated the optical band structures for lamellar transmission gratings with a pitch of 3.5  $\mu\text{m}$  and a depth of 4  $\mu\text{m}$  and showed flat-banded resonances in the infrared region of the spectrum and predicted almost total resonant transmittance of the incident light in the zero-order of the spectrum. In other previous theoretical studies, Tan *et al* [1999], and Hooper and Sambles [2002], calculated the dispersion of SPPs for short-pitch deep metal gratings and found that very flat SPP bands are formed in the zero-order region of the spectrum.

Despite the conceptual and practical interest of these resonances and well documented theoretical predictions, until now almost no experimental evidence of these hybrid electromagnetic resonances has been reported for visible optical frequencies. In this chapter, we shall investigate these self-coupled SPP resonances on deep sinusoidal silver gratings and narrow Gaussian-grooved silver gratings. In particular, the flat SPP bands formed in the zero-order region of the spectrum, as predicted for these deep gratings, are confirmed experimentally.

## 4.2 Self-coupled SPP Resonances and Flat SPP Bands on Deep Sinusoidal Silver Gratings

The formation of significant band-gaps in the SPP dispersion curve (for shallow gratings) when the grating profile contains a  $2k_g$  component has been demonstrated in chapter 3. Scattering from this  $2k_g$  component allows the forward and backward propagating SPPs to couple together to form two standing wave states with different energies. These are thus excited at different frequencies with a forbidden region (band-gap) between, with the size of the band-gap being largely determined by the amplitude of the  $2k_g$  component in the grating profile. Of course, as well as scattering from the  $2k_g$  component, two scattering events from the fundamental  $k_g$  component of the grating will also produce a band-gap, though this process is much weaker. If the grating has a sufficiently large  $2k_g$  component, or, in the case of a sinusoidal grating, has sufficient amplitude, the band-gaps formed may be substantial. This means that the lower energy

branches at the band-gaps reduce in frequency sufficiently such that even on a zero-order grating some of these may be coupled to at all angles of incidence. Note in addition that in very deep channels in good conductors standing-wave waveguide resonances may be excited. These may be regarded as open ended organ pipe modes (Went and Sambles [2001]). Thus for very deep gratings the lower branch modes at or near the band-gaps become essentially waveguide resonances. It is therefore clear that in the visible region of the spectrum the modes have a hybrid nature which is both SPP-like and waveguide-mode-like simultaneously.

In this section we will consider the case for transverse magnetic (TM) polarized radiation incident on the sinusoidal gratings with sufficient fundamental amplitudes. A schematic view of the structure and associated coordinate system under study is shown in Figure 4.2.1. The polar angle  $\theta$  and the azimuth angle  $\varphi$  define the orientation of the incident beam. The profile of the grating is given by

$$f(x) = a \sin(k_g x),$$

where  $a$  is the fundamental amplitude and  $k_g$  is the grating wave-vector ( $k_g = 2\pi/\lambda_g$ ).

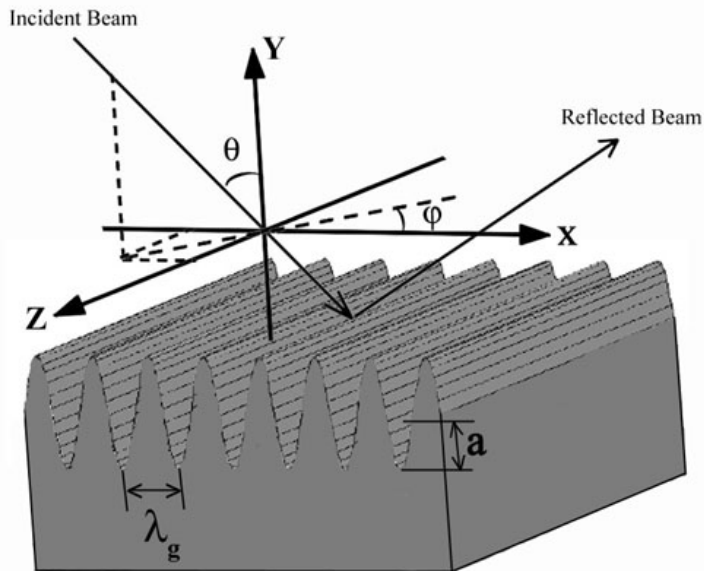


**Figure 4.2.1** Schematic diagram illustrating the sample and coordinate system. Here  $a$  is the grating amplitude,  $\lambda_g$  is the grating pitch,  $\theta$  is the polar angle, and  $\varphi$  is the azimuth angle.

Figure 4.2.2 shows the grey-scale plot of modelled TM polarised reflectivity as a function of wave-vector and frequency for the first Brillouin zone of a 258 nm pitch silver grating with 50 nm and 300 nm depths. In this calculation we have described the frequency dependent dielectric function of the silver using the Drude model with a plasma frequency of  $\omega_p = 1.32 \times 10^{16} \text{ s}^{-1}$ , and a relaxation time of  $\tau = 1.45 \times 10^{-14} \text{ s}$ .

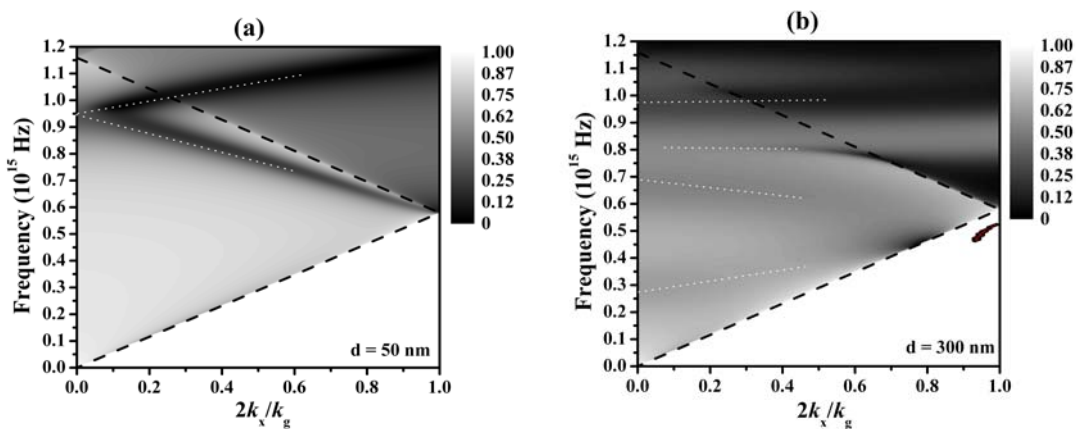


**Figure 4.2.2** TM polarised reflectivity as a function of frequency and in-plane wave-vector for 258 nm pitch sinusoidal silver gratings with (a)  $d = 50 \text{ nm}$  and (b)  $d = 300 \text{ nm}$  at azimuth angle  $\varphi = 0^\circ$ . White dotted lines indicate the SPP modes.

As for the dispersion curves that we have explored previously for shallow gratings, we see from Figure 4.2.2 (a) that only two modes, indicated by white dotted lines, can be accessed in the frequency range  $0 \leq f \leq 1.2 \times 10^{15} \text{ Hz}$ , in which the two modes can be identified as the SPP mode scattering by  $+k_g$  and  $-k_g$  respectively. At normal incidence ( $k_x = 0$ ), a crossing point arises at  $f \approx 0.95 \times 10^{15} \text{ Hz}$ . Due to the relatively small grating depth (50 nm) there is no significant interaction at this crossing point as shown by the absence of a band-gap. When the depth is increased, the second order scattering from the  $k_g$  component becomes stronger and possibly gives rise to a gap at  $k_x = 0$ . If the depth is increased further, this band gap will widen with the low energy solutions reducing in energy and higher order low energy branches will pass through the first order high energy branch. As shown in Figure 4.2.2 (b), for a grating depth of  $d = 300 \text{ nm}$ , the first order low energy branch has shifted to the zero-order region (for 258 nm pitch grating)  $0 \leq f \leq 0.5795 \times 10^{15} \text{ Hz}$  and has a positive gradient close to the light line. The low energy branches of the second and third order SPPs have

been pushed into the frequency range  $0 \leq f \leq 1.2 \times 10^{15}$  Hz and formed flat bands with a small negative gradient.

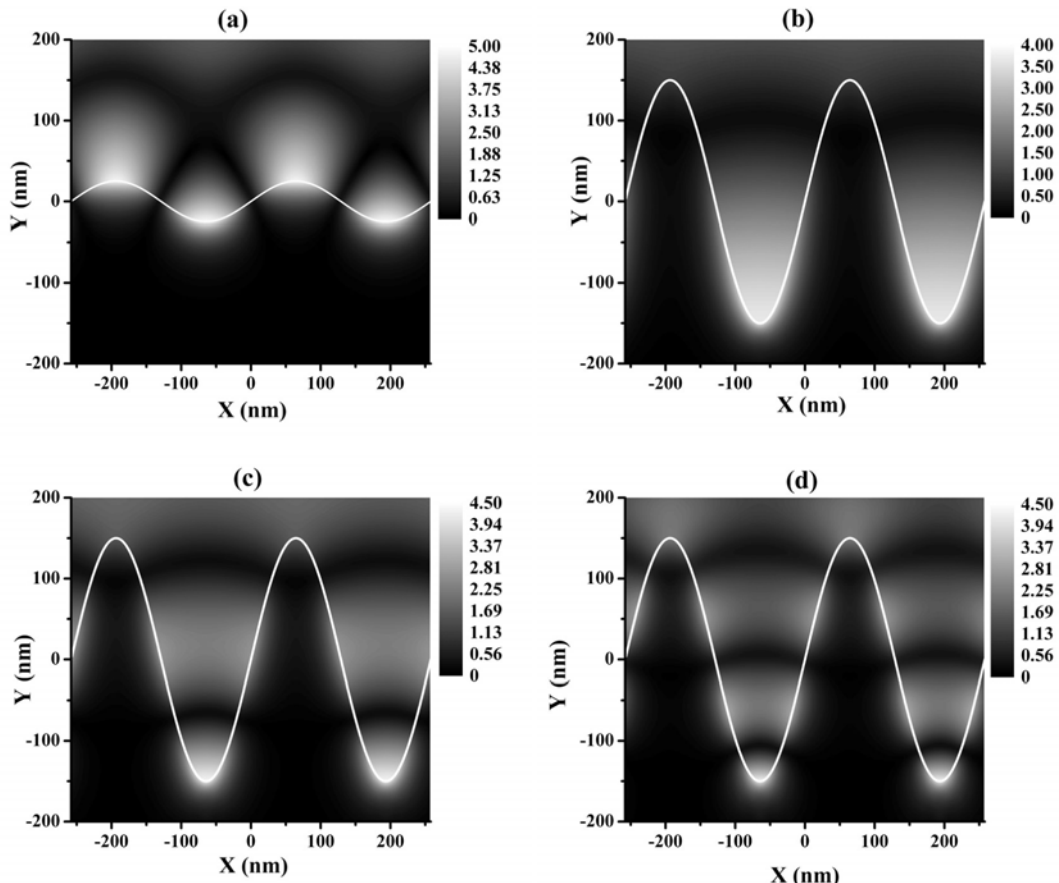


**Figure 4.2.3** Time averaged  $|H_z|$  component of the field distributions for the SPP resonance at  $k_x = 0$  for (a)  $d = 50$  nm,  $f = 0.942 \times 10^{15}$  Hz, (b)  $d = 300$  nm,  $f = 0.3 \times 10^{15}$  Hz, (c)  $d = 300$  nm,  $f = 0.673 \times 10^{15}$  Hz, and (d)  $d = 300$  nm,  $f = 0.972 \times 10^{15}$  Hz. The white line represents the grating profile.

To understand the nature of these resonances it is instructive to investigate their field profiles. Figure 4.2.3 shows the time averaged  $|H_z|$  ( $z$  is along the groove direction) component of the fields for the SPP resonance at  $k_x = 0$  for 50 nm ( $f = 0.942 \times 10^{15}$  Hz) and 300 nm ( $f = 0.3 \times 10^{15}$  Hz,  $0.673 \times 10^{15}$  Hz, and  $0.972 \times 10^{15}$  Hz) deep sinusoidal gratings. As shown in Figure 4.2.3 (a), for the resonance on a relatively shallow 50 nm deep grating field maxima are observed on the peaks of the grating and also at the bottoms of the grating grooves. When the depth is increased to 300 nm, as shown in Figure 4.2.3 (b) for the first order SPP mode, the field maxima on the grating peaks are hardly seen and the fields are almost entirely localised within the grating grooves. In

particular, in Figure 4.2.3 (c) and (d), for the second and third order SPP modes respectively, the fields on the opposing sides of a groove have coupled together. These coupled resonances in the deep gratings can be described as self coupled SPPs. It is also noticeable that the number of field maxima contained within the grating grooves is equal to the order of the mode.

In order to experimentally confirm that the SPP bands are compressed, shifting to lower frequencies and becoming flatter as the grating depth increases, two silver gratings with the same pitch ( $\lambda_g = 258$  nm) but different depth are investigated here. Figure 4.2.4 shows SEM images of these two silver gratings prepared by using the replica template technique mentioned in chapter 2. The gratings shown in Figure 4.2.4 (a) and (b) have depths of  $d = 124$  nm and  $166$  nm respectively. In our experiments, we only consider the case for a fixed azimuth angle of  $\varphi = 0^\circ$  (grating grooves oriented perpendicular to the plane of incidence).

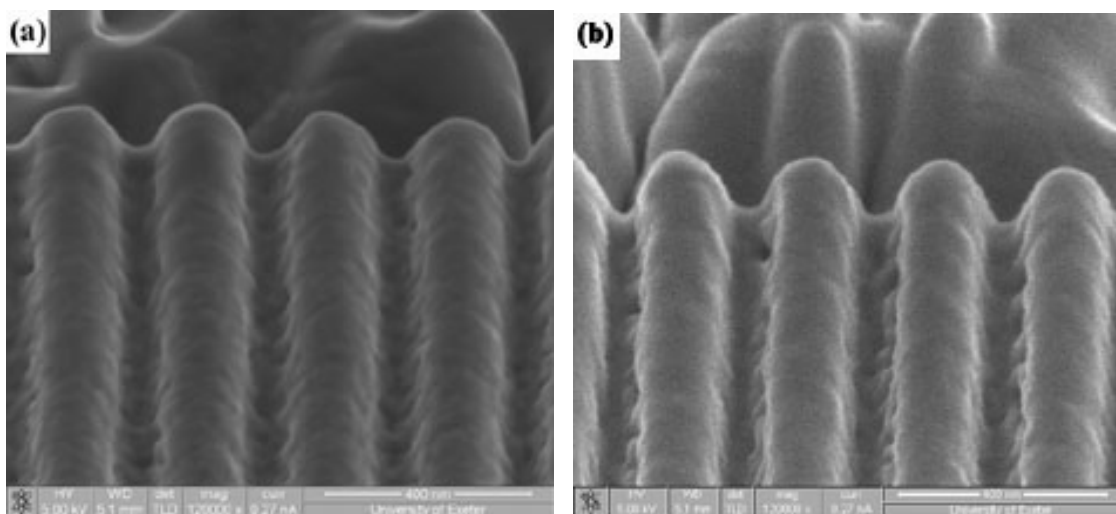


**Figure 4.2.4** SEM images of silver gratings with the electron beam incident at  $62^\circ$  to the sample normal.

The gratings both have the same pitch of 258 nm, but different depths of (a) 124 nm and (b) 166 nm.

To determine the dispersion of the modes associated with the structure, TM polarized wavelength dependent reflectivity data in the range 400 nm to 850 nm are obtained using the apparatus described in chapter 2 for 12 different polar angles ( $10^\circ \leq \theta \leq 70^\circ$ ) at a fixed azimuth angle  $\varphi = 0^\circ$ . Figure 4.2.5 shows reflectivity data for a grating with a ratio of depth to pitch of  $\delta = 0.48$ . Figure 4.2.6 shows the data for a deeper grating with a ratio of  $\delta = 0.58$ . Resonant modes are observed as minima in the

wavelength-dependent reflectivity, which are circled in the figures. From Figure 4.2.5 and Figure 4.2.6, we can see that the SPP minima on these gratings are extremely broad and shallow. Previous modelling studies (Hooper and Sambles [2002]) have shown far more pronounced minima, but these have been for narrow Gaussian grooved gratings, for which the coupling is much reduced. The gratings studied here are sinusoidal in character and thus the modes are over-coupled leading to the shallow modes. Later in this chapter we will experimentally and theoretically discuss the SPP modes of narrow-grooved ultra-deep silver gratings ( $\delta = 2.01$ ).

The modelled response of the structure is also shown in Figure 4.2.5 and Figure 4.2.6, which is calculated by using the conical version of the differential formalism grating theory described in chapter 2. The best comparison between the model full curves and the experimental data is achieved when the following fitting parameters are used:  $f(x) = 62\sin(k_g x)$  (Figure 4.2.5) and  $f(x) = 83\sin(k_g x)$  (Figure 4.2.6), while the optical dielectric function of the silver is described by polynomials for both the real and imaginary parts of the permittivity,

$$\varepsilon_r = -409.585 + 431.8\omega - 199.9\omega^2 + 49.33\omega^3 - 6.385\omega^4 + 0.342\omega^5,$$

$$\varepsilon_i = 178.764 - 218.7\omega + 105.2\omega^2 - 24.6\omega^3 + 2.772\omega^4 - 0.119\omega^5,$$

where  $\omega = 2\pi c/\lambda \times 10^{-15} \text{ s}^{-1}$ . The small differences in  $\varepsilon_r$  and  $\varepsilon_i$  to that used by Nash *et al* [1996] are caused by the roughness of the silver surface and the variable polycrystalline character of the silver film.

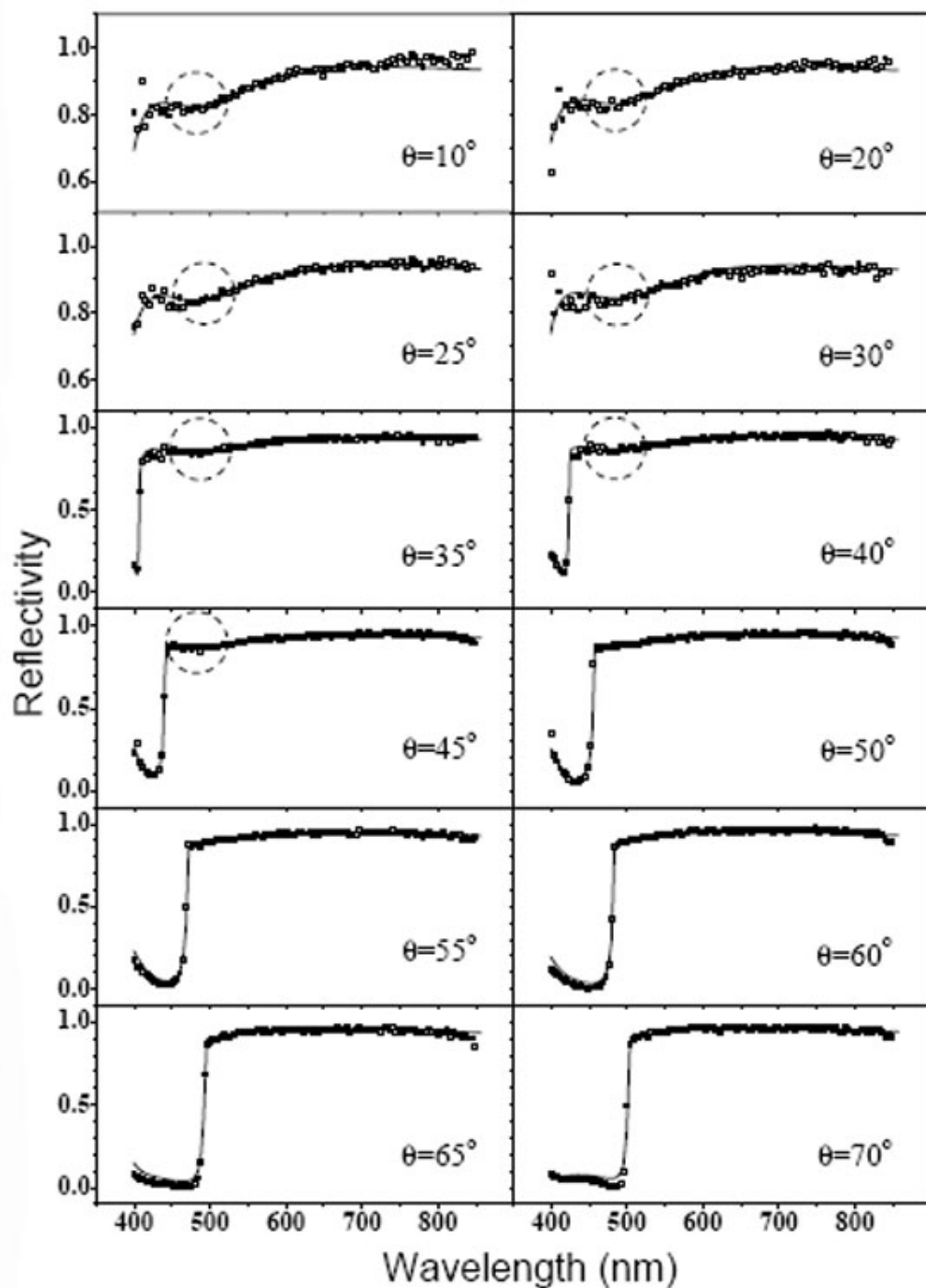


**Figure 4.2.5** TM polarized experimental (square) and modelled (solid line) wavelength-dependent reflectivity data obtained at different incident angles ( $10^\circ \leq \theta \leq 70^\circ$ ) and a fixed azimuth angle  $\varphi = 0^\circ$  for silver grating with a depth of 124 nm.

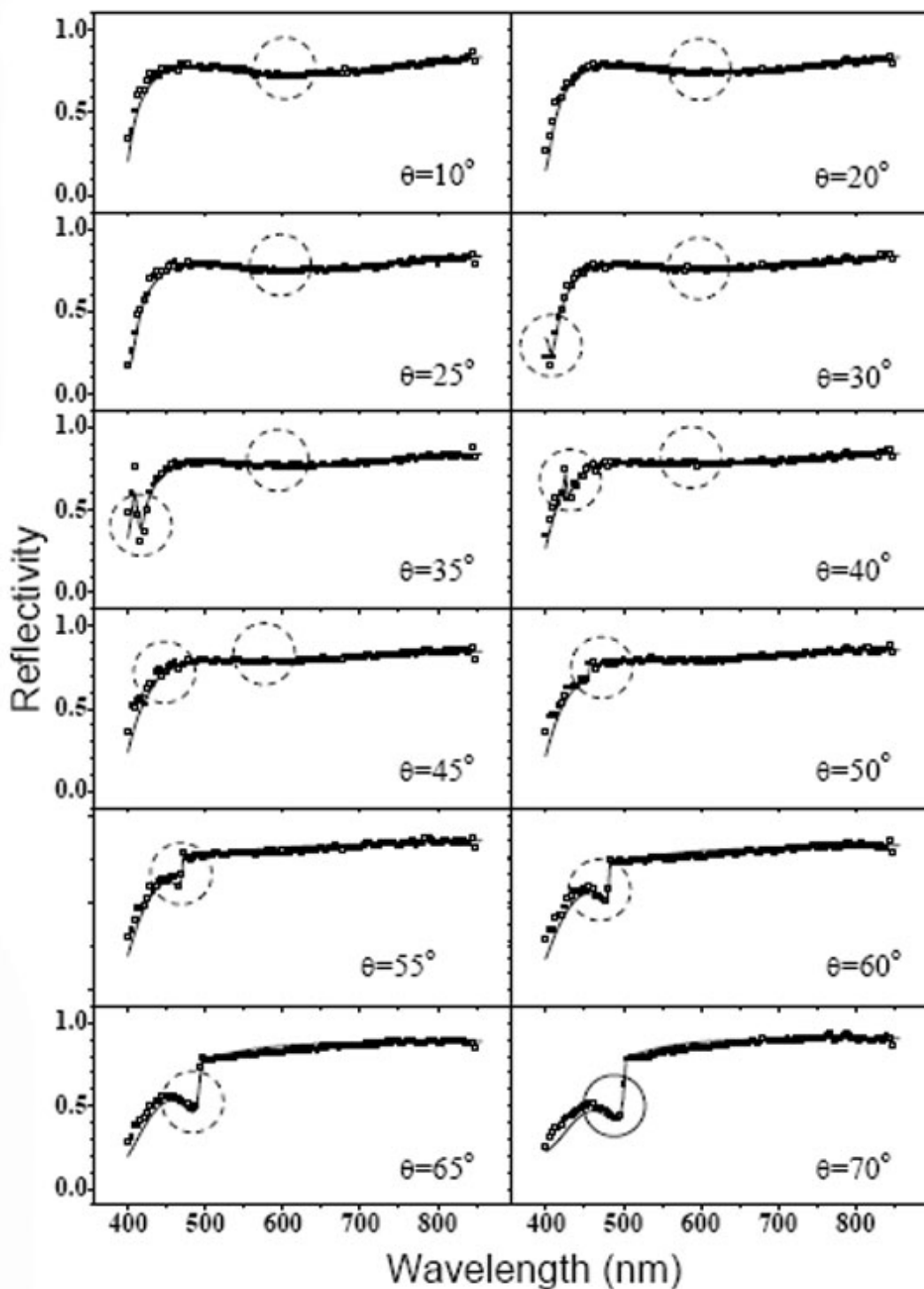


**Figure 4.2.6** TM polarized experimental (square) and modelled (solid line) wavelength-dependent reflectivity data obtained at different incident angles ( $10^\circ \leq \theta \leq 70^\circ$ ) and a fixed azimuth angle  $\varphi = 0^\circ$  for silver grating with a depth of 166 nm.

For silver gratings with a pitch of  $\lambda_g = 258$  nm, the true zero-order spectrum region exists for wavelengths beyond  $2\lambda_g = 516$  nm. In Figure 4.2.5 with the 124 nm depth grating there is only one SPP minimum which occurs below 516 nm for all the different incident angles. Figure 4.2.6, with the 166 nm deep grating, shows that one SPP minimum has shifted above 516 nm, and is strongly radiative and very broad with a second SPP minimum appearing below 516 nm for some incident angles. Also from Figure 4.2.6, we can see that these two minima shift in opposite directions as the incident angle increases. The minimum at the lower frequency has a blue-shift and the minimum at the higher frequency has a red-shift. Both modes tend towards the lightline/diffracted lightline at higher wavevectors. Hence the lower frequency mode tends towards the lightline, with a positive group velocity and a blue shift, whereas the higher frequency mode tends towards the diffracted lightline, with a negative group velocity and a red shift. However, from previous modeling studies (Hooper and Sambles [2002]) in which the dispersion curves of these standing wave SPP modes have been calculated it has been shown that the mode which experiences a red shift eventually passes through the diffracted light-line. There is some evidence of this in the data presented here, though it is by no means conclusive. In Figure 4.2.6 at an angle of  $\theta = 70^\circ$ , for example, at a wavelength slightly below the critical edge (around 500 nm) there is a clear minimum which is not found in the data obtained from the shallower grating in Figure 4.2.5.

If the positions in wavelength of the reflectivity minima are measured and converted to frequency ( $f = c/\lambda$ ) then they can be plotted against in-plane wave vector  $2k_x/k_g$  to form the dispersion curves. This has been performed and the results are shown in Figure 4.2.7. Data indicated by squares are for the first order SPP mode of the grating with a depth of 124 nm. Data given by triangles represent the first order SPP mode of the grating with a depth of 166 nm. Data represented by circles are for the second order SPP mode of the deeper grating. This has been shifted down enormously in frequency from originally being well into the diffracted region for a shallow grating to now being well inside the radiative region. (Also shown in the figure is a line describing the predicted dispersion of the second order mode outside the first diffracted order light-line.) From comparison of these modes for different grating depth, we can see that for low-aspect ratio gratings high order modes only occur in the diffracted region, while for

high-aspect ratio gratings these modes may appear in the zero-order region as, with increasing depth, the SPP modes shift to lower frequency. We also notice from Figure 4.2.7 that the flattest band occurs when its frequency approximates to that of a free photon having half the frequency of that which forms a zero momentum standing wave on the grating.

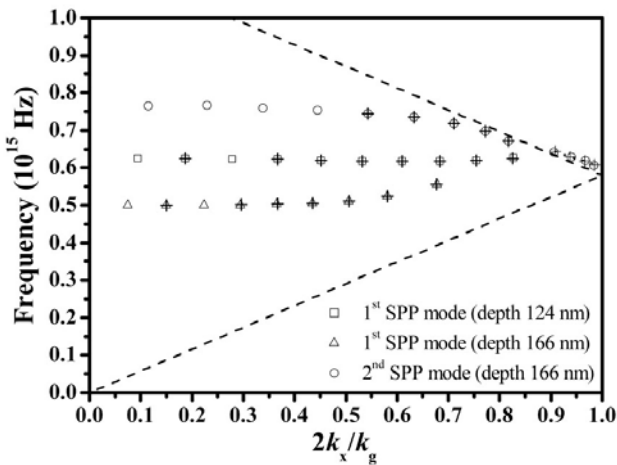


**Figure 4.2.7** The dispersion curves of the SPP modes obtained from the reflectivity data for different incident angles. The solid lines are the light line and diffracted light line. The open squares, circles and triangles are computed from the model used to produce the fits shown in Figure 4.2.5 and Figure 4.2.6. Squares are for the first order SPP mode for the 124 nm deep sample, triangles are for the first order SPP mode and circles are for the second order SPP mode for the 166 nm deep sample. The crosses are the experimental data.

To understand the nature of these resonances it is instructive to investigate their optical field profiles. Figure 4.2.8 shows the time averaged  $|H_z|$  ( $z$  is along the grating groove direction) component of the fields for 124 nm ( $f = 0.625 \times 10^{15}$  Hz) and 166 nm ( $f = 0.513 \times 10^{15}$  Hz,  $f = 0.721 \times 10^{15}$  Hz) deep gratings at an incident angle of  $\theta = 35^\circ$ . For the first order resonance on the shallower 124 nm deep grating optical field maxima are observed on the tops of the gratings and also at the bottoms of the grating grooves. When the depth is increased to 166 nm the field maxima for the first order resonance are still very similar to those of the shallower grating. However, for the second order resonance, there are field maxima at the bottom of the grating grooves, a small maximum at the top of the grating grooves, and two extra field maxima found on the sides of the grating grooves. These additional maxima arise since the second order

mode has been scattered by twice the grating vector (as opposed to by a single grating vector, as for the first order mode), and thus its in-plane wave vector must be twice that of the first order mode.

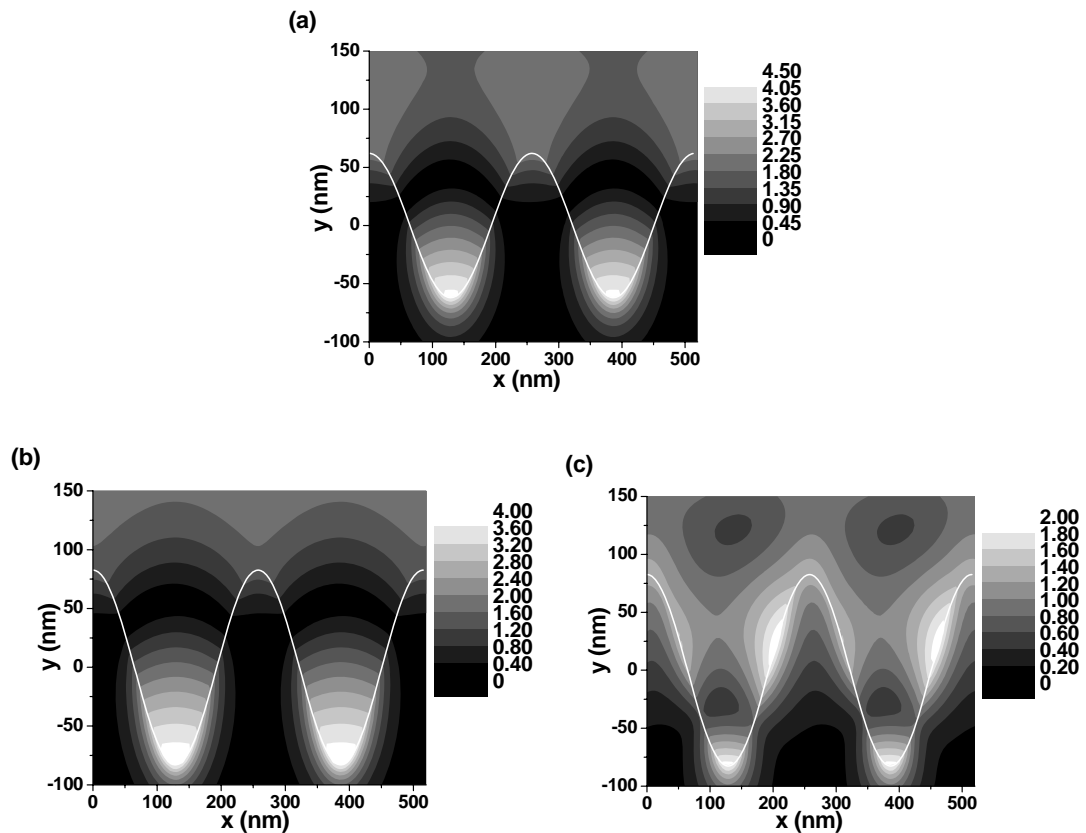


**Figure 4.2.8** Time averaged  $|H_z|$  component of the field distributions for the SPP resonance for (a)  $d = 124 \text{ nm}$ ,  $f = 0.625 \times 10^{15} \text{ Hz}$ ,  $\theta = 35^\circ$ , (b)  $d = 166 \text{ nm}$ ,  $f = 0.513 \times 10^{15} \text{ Hz}$ ,  $\theta = 35^\circ$ , and (c)  $d = 166 \text{ nm}$ ,  $f = 0.721 \times 10^{15} \text{ Hz}$ ,  $\theta = 35^\circ$ . The white line represents the grating profile.

### 4.3 Self-coupled SPP Resonances on Deep Narrow Gaussian-grooved Silver Gratings

In the previous section the SPP modes which may be excited on deep sinusoidal silver gratings have been described. In this section we shall examine the self-coupled SPPs on deep narrow Gaussian-grooved silver gratings. Figure 4.3.1 (a) shows the SEM image of such a deep narrow Gaussian-grooved silver grating fabricated by using the replica template technique. Directly from the SEM image of the cross section, the depth ( $d$ ), width ( $w$ ), and pitch ( $\lambda_g$ ) of the grating can be determined to be  $\sim 520$  nm,  $\sim 38$  nm, and  $\sim 258$  nm respectively. The modelled profile using these parameters is shown in Figure 4.3.1 (b) and is defined by

$$f(x) = -d \sum_{m=-\infty}^{\infty} \exp\left[-\left(\frac{x-m\lambda_g}{w}\right)^2\right].$$

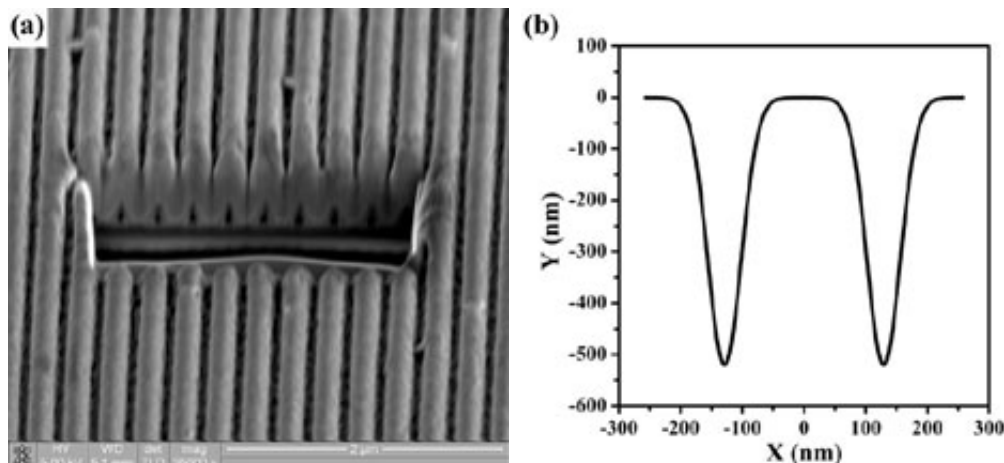


**Figure 4.3.1** SEM image (a) and modelled profile (b) of 520 nm deep, 38 nm wide Gaussian-grooved, 258 nm pitch silver grating.

Figure 4.3.2 shows the model TM polarized reflectivity as a function of frequency and in-plane wave vector for azimuth angle  $\varphi = 0^\circ$ . In the calculations here we have described the frequency dependent dielectric function of the silver using the Drude model with  $\omega_p = 1.32 \times 10^{16}$  s $^{-1}$  and  $\tau = 1.45 \times 10^{-14}$  s. One can see that a series of flat bands possessing near zero group velocity over a large range of incident wave vectors are formed in the dispersion curves. The details of the formation of these flat bands due to the excitation of self-coupled SPP resonances for sinusoidal gratings have

been investigated in the previous section, and for narrow Gaussian-grooved gratings have been reported by Hooper and Sambles [2002]. It is also noticeable that in Figure 4.3.2 the low energy branches of the first, second, and third order SPPs have been pushed into the zero-order region of the spectrum ( $0 \leq f \leq 0.5795 \times 10^{15}$  Hz).

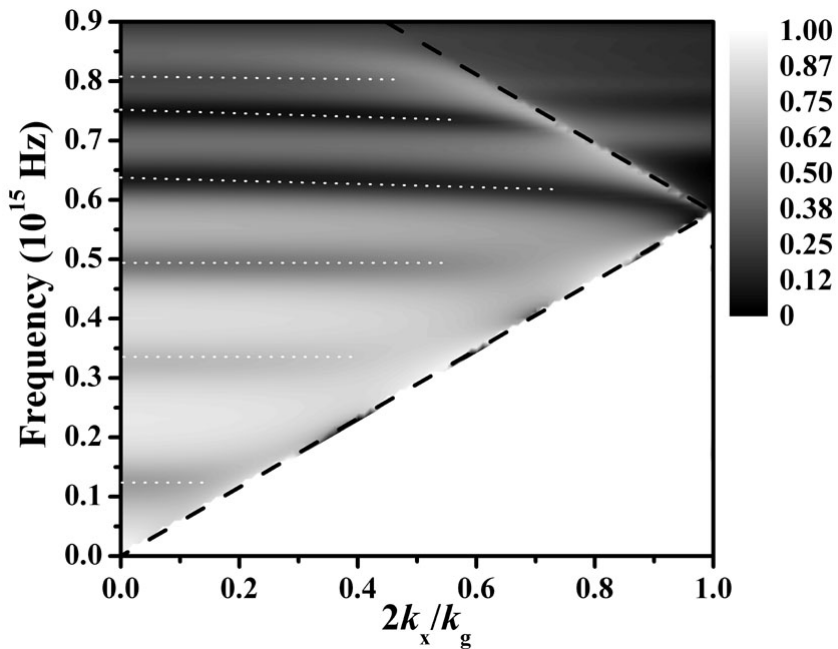


**Figure 4.3.2** Reflectivity as a function of frequency and in-plane wave vector for TM polarized light incident on a 520 nm deep, 38 nm wide Gaussian-grooved, 258 nm pitch silver grating oriented at azimuth angle  $\varphi = 0^\circ$ . White dotted lines indicated the SPP modes.

To acquire the dispersion of the modes associated with the structure experimentally, absolute TM polarized reflectivity spectra are recorded as scans in wavelength ( $400 \leq \lambda_0 \leq 850$  nm) at azimuth angle  $\varphi = 0^\circ$  (the grating grooves being perpendicular to the incident plane) for 14 different polar angles ( $15^\circ \leq \theta \leq 80^\circ$  with steps of  $5^\circ$ ). Figure 4.3.3 illustrates typical TM polarized wavelength dependent absolute reflectivity data at different polar angles. Also the modelling TM polarized reflectivity spectra for the structure shown in Figure 4.3.1 (b) at azimuth angle  $\varphi = 0^\circ$  and polar angle  $\theta = 35^\circ$  is plotted in Figure 4.3.4.

The first point to note is that in Figure 4.3.3 (a) and (b), for low polar angles  $15^\circ$  and  $25^\circ$ , the level of the reflectivity is extremely low when compared to the off-resonant reflectivity in the modelling spectra, which can be seen in Figure 4.3.4. When the polar

angle is increased to higher values, as shown in Figure 4.3.3 (c) – (f), in addition to the low level of the reflectivity a sharp and high reflection peak is readily observed. Compared to Figure 4.3.4, we can see that such a reflection peak is situated at the diffracted order pseudo critical edge with the same level as that in the modelling results. Later in this section, we will explain the reason for the reduction in the reflectivity and the formation of sharp reflection peak at the diffracted order pseudo critical edge.

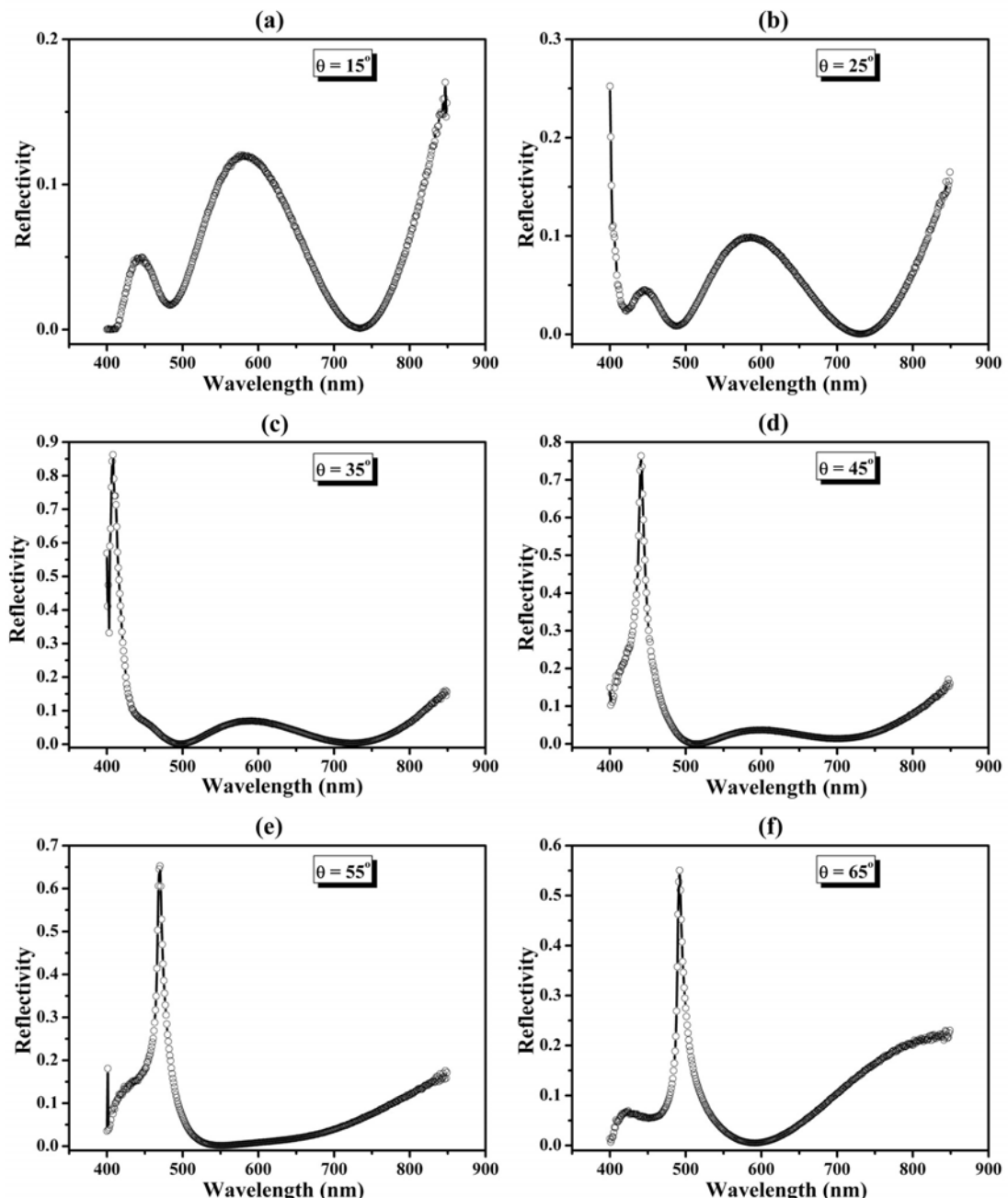


**Figure 4.3.3** The results of the wavelength-dependent reflectivity for TM polarization at polar angles (a) – (f)  $\theta = 15^\circ, 25^\circ, 35^\circ, 45^\circ, 55^\circ$ , and  $65^\circ$  respectively.

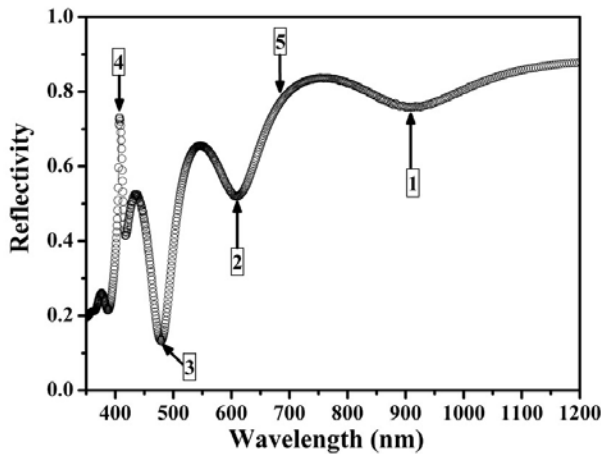


**Figure 4.3.4** The modelled TM polarized wavelength dependent reflectivity spectra of the structure shown in Figure 4.3.1 (b) at polar angle  $\theta = 35^\circ$  and azimuth angle  $\varphi = 0^\circ$ . The positions indicated by numbers 1, 2, and 3 are SPPs resonant reflection dips. The peak indicated by number 4 corresponds to the diffracted order pseudo critical edge. The position indicated by number 5 represents an arbitrary off-resonance position.

Figure 4.3.5 shows the experimental dispersion curve, acquired by noting all of the reflection dips (indicated by open squares) which are then mapped into the plot as a function of frequency and in-plane wave vector. Comparing Figure 4.3.5 with the numerical modelled dispersion curve in Figure 4.3.2, it is noticeable that the dispersion of the four modes ( $2^{\text{nd}}$ ,  $3^{\text{rd}}$ ,  $4^{\text{th}}$ , and  $5^{\text{th}}$  order self-coupled SPP modes) is very similar, which strongly suggests that the reflectivity minima are due to the excitation of self-coupled SPPs. Mode (I) is almost flat with a small positive gradient close to the light line. Mode (II) is similar to mode (I). Both mode (I) and (II) are completely located within the zero-order region. Mode (III) decreases in frequency as it approaches the conjunction of the light line and diffracted order light line. Mode (IV) has a negative gradient close to the diffracted order light line while remaining quite flat. Also plotted in Figure 4.3.5 are the reflection peaks, which are indicated by the open triangles. Clearly the open triangles overlap with the modelling diffracted order light line (indicated by dotted line) which confirms that these sharp reflection peaks are the diffracted pseudo critical edge.

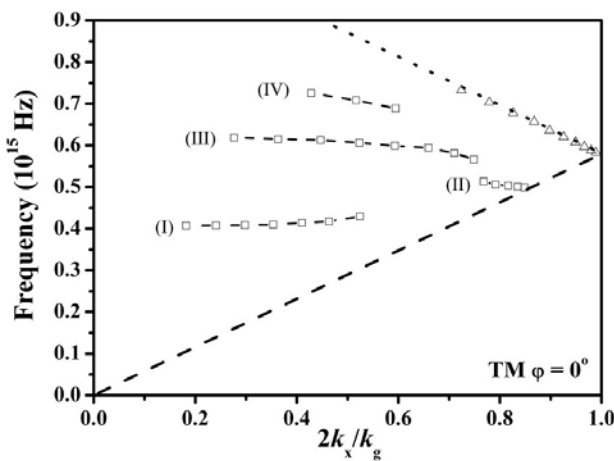


**Figure 4.3.5** The dispersion of the experimental reflectivity minima (indicated by squares) obtained from the reflection spectra. The modes marked as (I) – (IV) can be identified as 2<sup>nd</sup>, 3<sup>rd</sup>, 4<sup>th</sup>, and 5<sup>th</sup> order SPP modes respectively. The dashed and dotted lines are the light line and the diffracted order light line. The open triangles are the experimental reflection peaks.

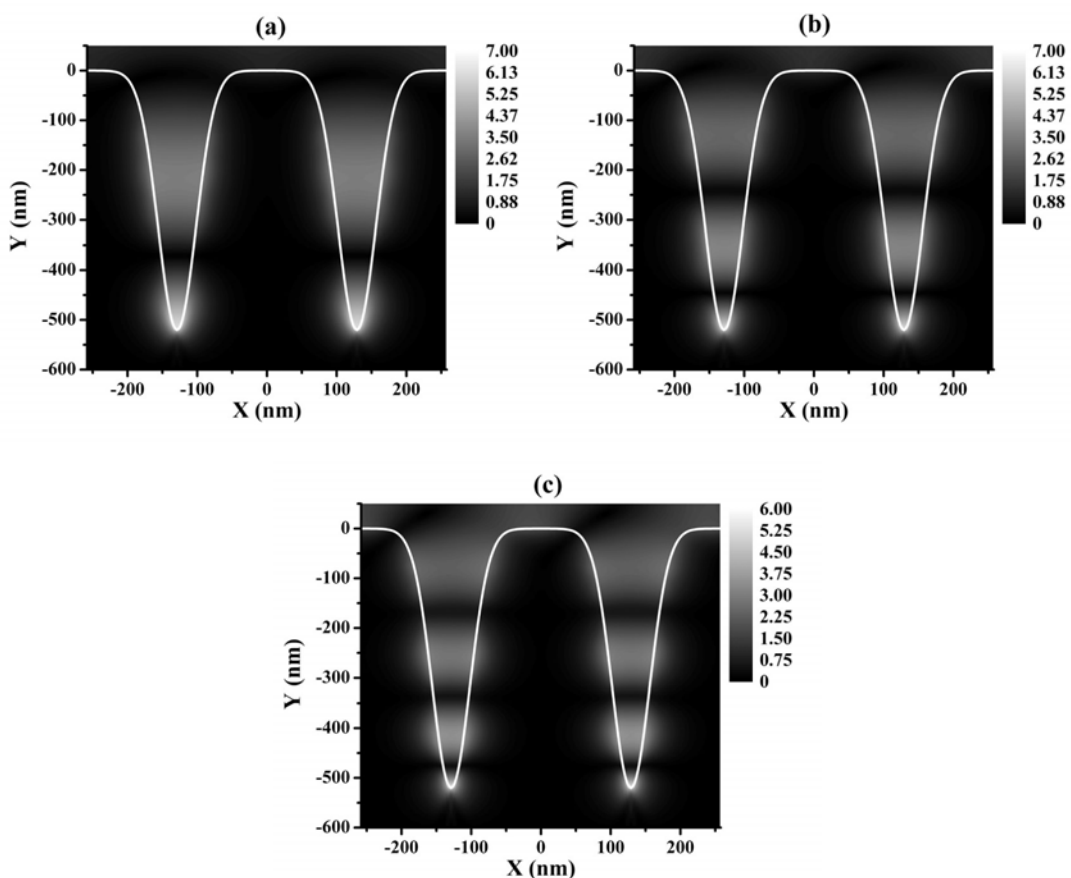


**Figure 4.3.6**  $|H_z|$  for the second, third, and fourth order self-coupled SPPs on a 520 nm deep, 38 nm wide, Gaussian-grooved grating at  $\theta = 35^\circ$  and  $\varphi = 0^\circ$ . (a)  $f = 0.329 \times 10^{15}$  Hz, (b)  $f = 0.49 \times 10^{15}$  Hz, and (c)  $f = 0.624 \times 10^{15}$  Hz.

The  $|H_z|$  component of the fields at azimuth angle  $\varphi = 0^\circ$  and incident angle  $\theta = 35^\circ$  for the second ( $f = 0.329 \times 10^{15}$  Hz), third ( $f = 0.49 \times 10^{15}$  Hz), and fourth order ( $f = 0.624 \times 10^{15}$  Hz) SPP modes, which are indicated by numbers 1, 2, and 3 respectively in Figure 4.3.4, are shown in Figure 4.3.6. Once again, these show that there are a family of almost entirely localised self-coupled SPP resonance whose number of field maxima contained within the grating grooves is equal to the order of the mode.

Now we shall turn back to the explanation for the intensity reduction of the off-resonant reflectivity and the formation of sharp reflection peaks at higher polar angles. If we carefully examine the SEM image of the sample grating shown in Figure 4.3.1 (a), it is apparent that the surface roughness of the silver grating is not uniform. In this case, the sample is fabricated by using the template replica technique (described in chapter 2), in which the photoresist grating has a corresponding deep narrow Gaussian-peaked profile. The huge difference between the gradient of the bottom surface (nearly zero) and the side surface of photoresist grating grooves (nearly infinite) results in different silver nucleation. This leads to the surface on each side of the silver grating grooves being very rough, while the top surface is relatively smooth. The large reduction in the off-resonant reflectivity is due to the rough grating groove side surfaces which cause scatter of the incident light and thereby a loss of energy in the specularly reflected order. By investigating the field distributions for an arbitrary off-resonance frequency, as shown in Figure 4.3.7 (b) (here  $f = 0.44 \times 10^{15}$  Hz is selected), we can clearly see that most of the fields are localised in the grating grooves, which means that the off-resonant reflectivity will suffer greater unexpected scattering.

However it is a little surprising that the reflectivity at the diffracted pseudo critical edge did not suffer this intensity reduction and instead forms a sharp reflection peak. This can be well explained by investigating the field distributions for the critical edge. Figure 4.3.7 (a) shows  $|H_z|$  component of the fields for the diffracted order pseudo critical edge ( $f = 0.734 \times 10^{15}$  Hz), which is indicated by number 4 in Figure 4.3.4, at  $\theta = 35^\circ$  and  $\varphi = 0^\circ$ . Obviously, in this case the fields are mostly concentrated on the top surface of the grating. Thereby due to the smooth top surface the reflectivity at the critical edge should keep its original level compared with the modelling results, which, in combination with the large reduction of reflectivity at other than the critical edge, results in a sharp reflection peak.

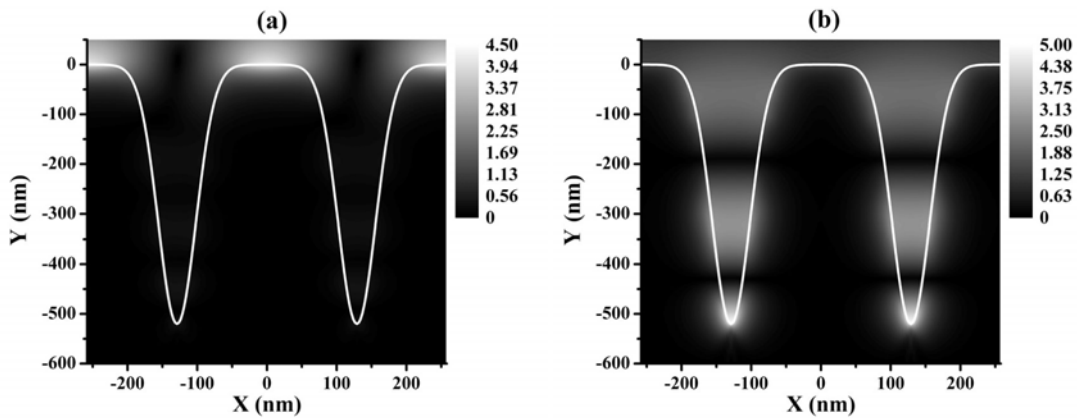


**Figure 4.3.7**  $|H_z|$  for (a) the diffracted order pseudo critical edge  $f = 0.734 \times 10^{15}$  Hz, which is indicated by number 4 in Figure 4.3.4, and (b) an off-resonant frequency  $f = 0.44 \times 10^{15}$  Hz, which is indicated by number 5 in Figure 4.3.4, at  $\theta = 35^\circ$  and  $\varphi = 0^\circ$ .

## 4.4 Summary

The form of the TM polarized dispersion of a family of flat-banded self-coupled surface plasmon polaritons on very deep sinusoidal and narrow Gaussian-grooved silver gratings at azimuth angle  $\varphi = 0^\circ$  has been explored. The reflectivity studies over the region, 400 to 850 nm, of deep silver sinusoidal gratings with different depths are presented in the first section. Experimental data shows excellent agreement with the model predictions. From comparison of the modes for gratings with different depths, we verify the prediction that with increasing grating depth the SPP modes shift to lower frequency, and become flat banded effectively localized modes.

In the case of deep narrow Gaussian-grooved silver gratings, the flat bands in the zero-order region are also observed experimentally. Due to the rough grating groove side surface, it was not possible to fit the data obtained to theory, and therefore it was not possible to categorically attribute these reflectivity minima to the excitation of self-coupled SPP resonances. However the experimental dispersion of these modes was found to be very similar to the modelled dispersion, and therefore we believe that it is these self-coupled SPP modes which have been excited. These flat bands may have potential applications in selective absorbers or in resonant enhanced Raman scattering. In particular, the sharp reflection peaks that we have observed in the experiments for high incident angles may be of interest for filtering applications.

# Chapter 5

## The Optical Response of Thin Silver Slabs Covered with Dielectric Films

### 5.1 Introduction

In the previous chapters the SPP modes excited on a periodically modulated metal surface have been described. In this chapter, we shall investigate the optical response of the structure comprising a flat thin metal slab covered with a dielectric layer. Such a structure may support guided waves in addition to SPPs.

The simplest geometry of this structure is that of a planar dielectric layer deposited on to a metal film. Hornauer and Raether [1973] were two of the first people to record Attenuated Total Reflection (ATR) studies of planar waveguide structures, comprising a 20  $\mu\text{m}$  thick LiF film deposited on a silver tunnel barrier of 50 nm thickness. Through observing the light arising from the scattering of the SPPs by the roughness of the surface, they recorded a series of ATR maxima associated with the excitation of transverse magnetic (TM) and transverse electric (TE) polarised planar guided waves in the LiF layer.

More recently, Müller *et al.* [1997] reported a new kind of grating-coupled SPP method, coupling of incoming photons via a dielectric grating to a SPP that propagates on a planar metal surface. In their study, a surface-relief grating is introduced into the dielectric film, which was used to successfully couple visible (632.8 nm) radiation to the SPP mode. Their sample consisted of an evaporated silver substrate, coated with a 5 nm layer of gold and corrugated photoresist grating. This new grating coupling method has also been successfully applied by Hibbins and Sambles [2000] to couple microwave photons to SPPs. A similar geometry is also used by Salakhutdinov, Sychugov, and Parriaux [1998] who provided a theoretical and experimental study of increased diffraction efficiency over a conventional metallic grating due to the excitation of leaky

modes in the dielectric layer. Other recent studies involving dielectric gratings on flat metal surfaces include that of Park *et al.* [2003]. They reported the efficient outcoupling of the SPPs to transmission modes propagating in free space by use of dielectric diffraction gratings on flat metallic surfaces. Salt and Barnes [1999], and Salt *et al.* [2001] extended such structures by depositing thin cladding metal layers onto the top surface of dielectric gratings/flat metal structures to form asymmetric metallic microcavities. They experimentally and theoretically studied the photonic band gaps in guided modes of microcavities with transmission measurements at two different azimuth angles,  $0^\circ$  and  $45^\circ$ . The influence of the one dimensional band gap on the two dimensional dispersion has been demonstrated by comparing the center frequency and width of the band gap for two azimuth angles. However, most of studies are concentrated on the photonic band-gaps at the Brillouin zone boundary.

In the first section of the chapter metal slabs coated with planar dielectric films are investigated theoretically. We shall study how the thickness of the dielectric film can modify the dispersion of SPP modes and guided modes associated with the planar waveguide structure.

In the second section the short-pitch surface-relief grating is introduced into the dielectric film. The dispersion curves for the whole range of azimuth angles ( $0^\circ \leq \varphi \leq 90^\circ$ ) in the visible are presented both experimentally and theoretically. Particularly, the formation of different band-gaps caused by the modes self-crossing at the Brillouin zone (BZ) boundary and by different modes anti-crossing at other than the BZ boundary are investigated. In addition the optical magnetic field distribution at the resonant frequency for each of the modes is explored to unravel their character.

## 5.2 Planar Waveguide –Planar Dielectric Films on the Metal Slabs

In chapter 3, we investigated SPPs that propagate on a planar metal/dielectric interface, in which the thickness of the dielectric medium is infinite ( $d = \infty$ ) or the condition  $d \gg \lambda$  is fulfilled. Therefore, it is a one-boundary system. In this section we shall theoretically explore the optical properties of the structure consisting of a planar photoresist layer with finite thickness ( $d$ ) deposited on an optically thin silver film for use in the Kretschmann-Raether configuration. A schematic of the sample geometry used in this section is shown in Figure 5.2.1, where  $\theta$  is the incident angle,  $t$  is the thickness of the silver film, and  $d$  is the thickness of the photoresist layer. In this case, we have a two-boundary system.

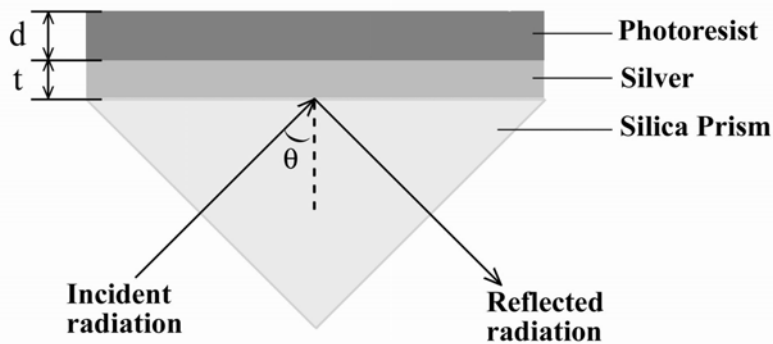


**Figure 5.2.1** Schematic diagram illustrating a planar waveguide structure consisting of a photoresist layer (with a thickness of  $d$ ) deposited on a thin silver film (with a thickness of  $t$ ). The silver film is attached to the silica prism with matching fluid to create an ATR system.

Figure 5.2.2 shows the band structure associated with the planar waveguide for a thickness of the silver film of  $t = 60$  nm and with different thicknesses of photoresist  $d = 0$  nm, 50 nm, 100 nm, and 150 nm. In the calculations, a Drude model ( $\omega_p = 1.32 \times 10^{16}$  rad/s,  $\tau = 1.45 \times 10^{-14}$  s) is used to describe the silver, and the dielectric constants of the photoresist and silica are  $\epsilon_{\text{photoresist}} = 2.85 + 0.012i$  and  $\epsilon_{\text{silica}} = 2.53 + 0.0i$  respectively.

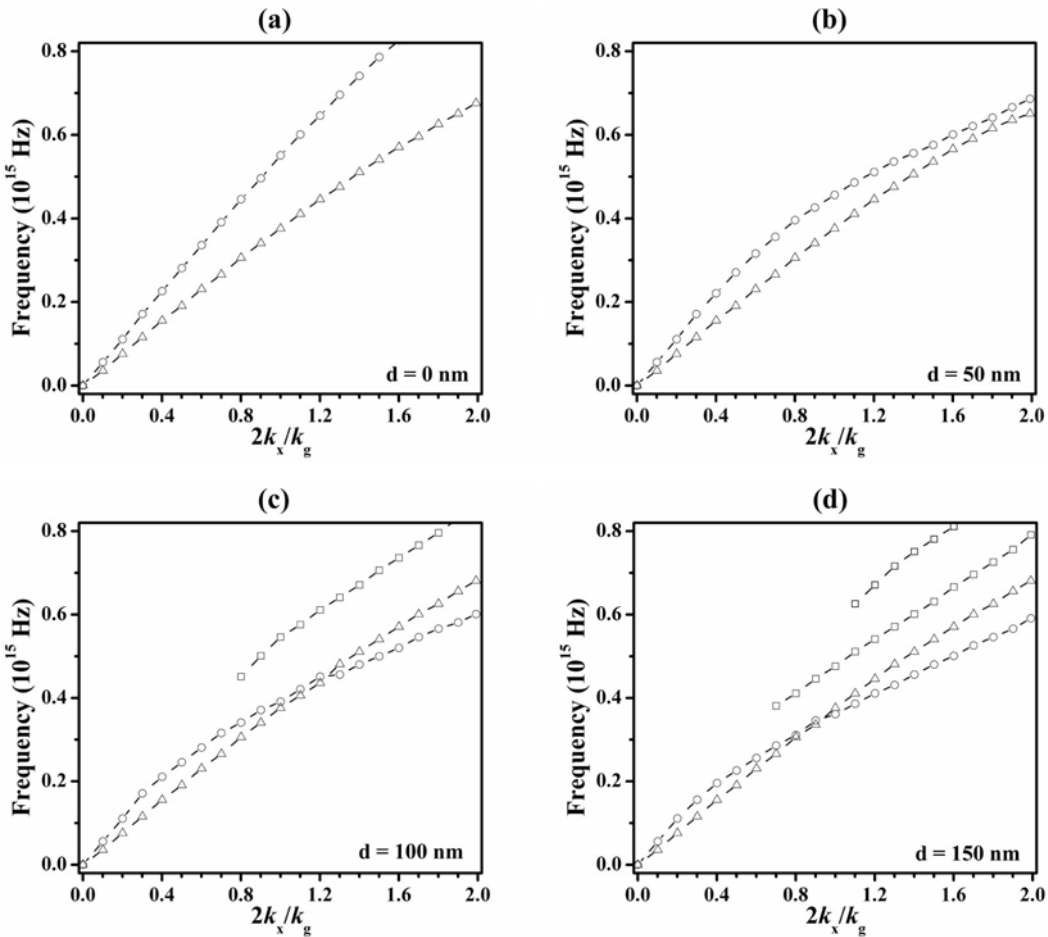


**Figure 5.2.2** Band structures for a planar waveguide with a fixed thickness of silver film  $t = 60$  nm and with photoresist film thicknesses (a)  $d = 0$  nm, (b)  $d = 50$  nm, (c)  $d = 100$  nm, and (d)  $d = 150$  nm. The open triangles represent the SPP modes that propagate along the silica/silver interface, open circles indicate the SPP modes supported at the top surface of the silver film, and open squares are the waveguide modes.

The modes indicated by open triangles in Figure 5.2.2 are the SPP modes that propagate along the silica/silver interface, and do not concern us here. Since no photoresist exists (the thickness  $d = 0$  nm) in Figure 5.2.2 (a), the modes indicated by open circles are obviously the SPP modes propagating on the silver/air interface. When the thickness of photoresist is increased, the SPPs on the top surface of the silver film will reduce its resonant frequency. As shown in 5.2.2 (b) for the thickness of photoresist  $d = 50$  nm, a shift of the resonant frequency of this mode to lower frequencies at large wave-vectors is clearly demonstrated. On further increase of thickness to 100 nm and 150 nm, as shown in Figure 5.2.2 (c) and (d), in addition to the frequency reduction of the SPP mode supported by the silver/photoresist interface, some additional modes

(indicated as open squares) appear in the band structure. These modes are guided modes in the photoresist waveguide medium. Also note that in Figure 5.2.2 (d), even for  $d = 150$  nm, at lower wave-vectors the SPP supported by the silver/photoresist interface is still higher in frequency than the SPP on the silica/silver interface. Only when the photoresist is thick enough, can one expect that the silver/photoresist SPP drops in frequency below the silica/silver SPP.

In the band structures we have shown the waveguide modes for both TM and TE polarizations. To identify these waveguide modes, the theoretical TM and TE polarized reflectivity of the planar waveguide structure with the thickness of photoresist  $d = 150$  nm are plotted in Figure 5.2.3. By comparing the band structure with the reflectivity, the higher frequency branch of waveguide mode, as indicated by open squares in Figure 5.2.2 (d), is identified as the TM polarized waveguide mode, and the branch with lower frequency is the TE polarized waveguide mode. Also note the SPP modes supported by the silver/photoresist interface can be excited in the low frequency range (below  $\sim 0.3 \times 10^{15}$  Hz).

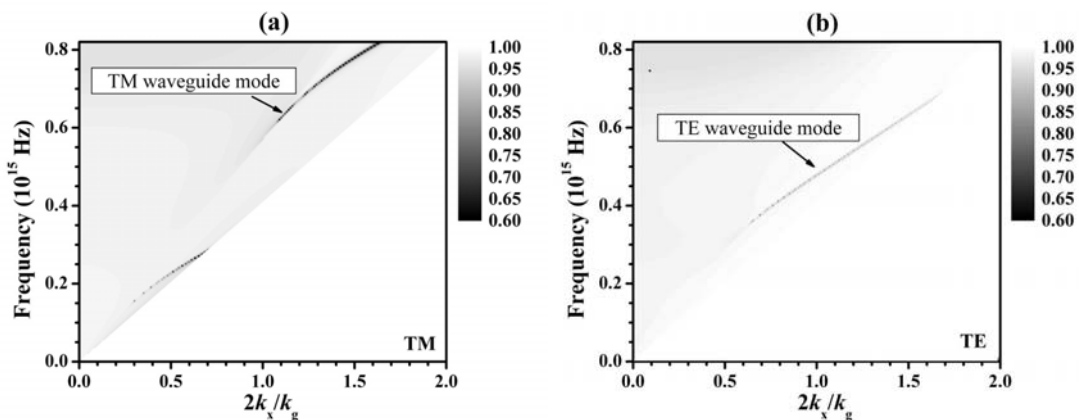


**Figure 5.2.3** The theoretical reflectivity of the planar waveguide structure with the thickness of photoresist layer  $d = 150$  nm, the same as that used in Figure 5.2.2 (d), for (a) TM polarization and (b) TE polarization. The white polygon in the bottom right corner indicates the inaccessible region beyond the silica light line.

### 5.3 Corrugated Waveguide – Dielectric Gratings on the Metal Slabs

To more clearly demonstrate how a short-pitch single surface corrugation can modify the dispersion of guided modes, a waveguide structure, simpler in form to that used in the work of Salt *et al* [1999], is used: it has no cladding metal layer. The primary simplification is that there is then no SPP mode associated with the upper boundary. Furthermore the only grating in the structure is an amplitude grating on the dielectric.

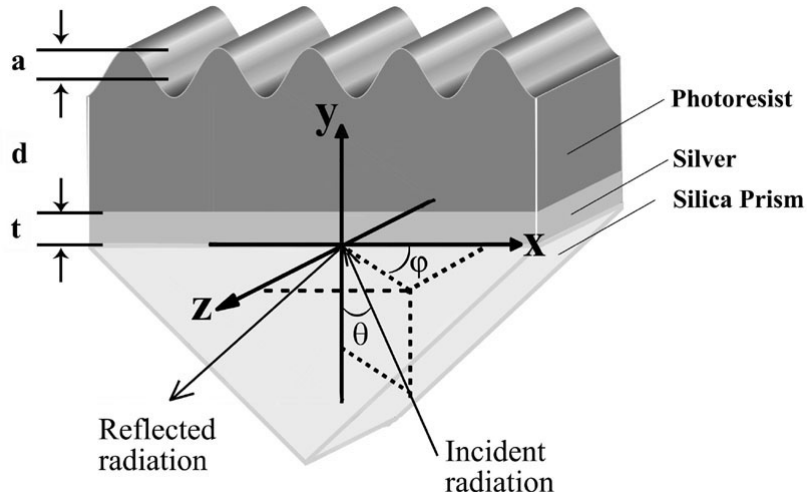


**Figure 5.3.1** Schematic diagram illustrating the sample, coordinate system, and experimental geometry used in this work. Here  $a$  is the grating amplitude,  $d$  is the average thickness of the photoresist layer,  $t$  is the thickness of the silver tunnel barrier,  $\theta$  is the polar angle, and  $\varphi$  is the azimuth angle. The silica substrate is optically attached to the silica prism with matching fluid.

The structure consists of the waveguide medium, with a periodically modulated upper surface, deposited on an optically thin silver film supported by a silica substrate. The details of the sample fabrication are described in chapter 2. In brief, the waveguide material is Shipley SPR700 photoresist which is readily corrugated on its upper surface by developing the pattern produced when the surface is exposed to interfering laser beams. The silver layer, as the tunnel barrier and mirror, should be thick enough to provide a significant reflectivity. However, it should also be thin enough to ensure that there is suitable strength of tunnelling of the evanescent optical field. The silica

substrate is optically attached to the silica prism with matching fluid to create an ATR system, used for coupling the light into and out of the resist grating structure and also for avoiding any effect of stray reflection in the substrate. When the frequency and in-plane wave vector of the incident light matches a mode in the resist the reflectivity will show a resonant dip. This thereby allows the guided modes within the photoresist to be studied by observing the reflectivity in the ATR geometry. A schematic of the sample arrangement, together with the coordinate system used in this section, is shown in Figure 5.3.1, where  $a$  is the amplitude of the grating,  $t$  is the thickness of the silver tunnel barrier, and  $d$  is the average thickness of the photoresist layer. The values of these parameters are given in the fitting process later.

To determine the dispersion of the modes associated with the structure, absolute reflectivity spectra are recorded as scans in wavelength ( $400 \leq \lambda_0 \leq 850$  nm) at various fixed polar and azimuth angles. In this work, at each azimuth angle ( $0 \leq \varphi \leq 90^\circ$  in steps of  $10^\circ$ ) the TM polarized reflectivity data was determined for 6 different polar angles ( $\theta = 41.6^\circ, 45^\circ, 48.4^\circ, 51.8^\circ, 55.2^\circ$ , and  $58.5^\circ$ ). Figure 5.3.2 illustrates just two sets of this reflectivity data together with the modelling results for  $\theta = 45^\circ$  and  $58.5^\circ$  at different azimuth angles. The theoretical method employed here is a conical version of the differential formalism grating theory described in chapter 2. The refractive index of the silica is  $n_{\text{silica}} = 1.459$ . The permittivity of the photoresist and silver are described by polynomials for both the real and imaginary parts of the permittivity,

$$\begin{aligned} \varepsilon_{\text{photoresist}}(\omega) = & -36.69501 + 62.313\omega - 38.187\omega^2 + 11.338\omega^3 - 1.633\omega^4 + 0.091629\omega^5 \\ & + i(0.01319 - 8.7131 \times 10^{-16}\omega - 1.1024 \times 10^{-3}\omega^2 - 1.6659 \times 10^{-24}\omega^3 + 9.663 \times 10^{-5}\omega^4 - \\ & 1.4567 \times 10^{-18}\omega^5), \quad \text{and} \end{aligned}$$

$$\begin{aligned} \varepsilon_{\text{silver}}(\omega) = & -1056.98604 + 1393.3\omega - 754.49\omega^2 + 205.61\omega^3 - 27.963\omega^4 + 1.51149\omega^5 \\ & + i(178.76439 - 218.68\omega + 105.182\omega^2 - 24.5992\omega^3 + 2.77223\omega^4 - 0.118922\omega^5), \end{aligned}$$

where  $\omega = 2\pi c/\lambda \times 10^{-15}$  s<sup>-1</sup>. The dielectric constants stated above are only valid in the visible range. In all of the calculations, for those frequencies that exceed the visible the dielectric constant of silver is modelled as a Drude model with  $\omega_p = 1.32 \times 10^{16}$  rad/s and  $\tau = 1.45 \times 10^{-14}$  s, while the dielectric constant of the photoresist is fixed to  $2.85 + 0.012i$ .

The corrugated photoresist surface is given by:

$$f(x) = a_0 \cos(k_g x + \phi_0) + a_1 \cos(2k_g x + \phi_1) + \dots + a_N \cos(Nk_g x + \phi_N),$$

where  $a_N$  is the amplitude of the  $N^{\text{th}}$  component and  $\phi_N$  is its associated phase shift.

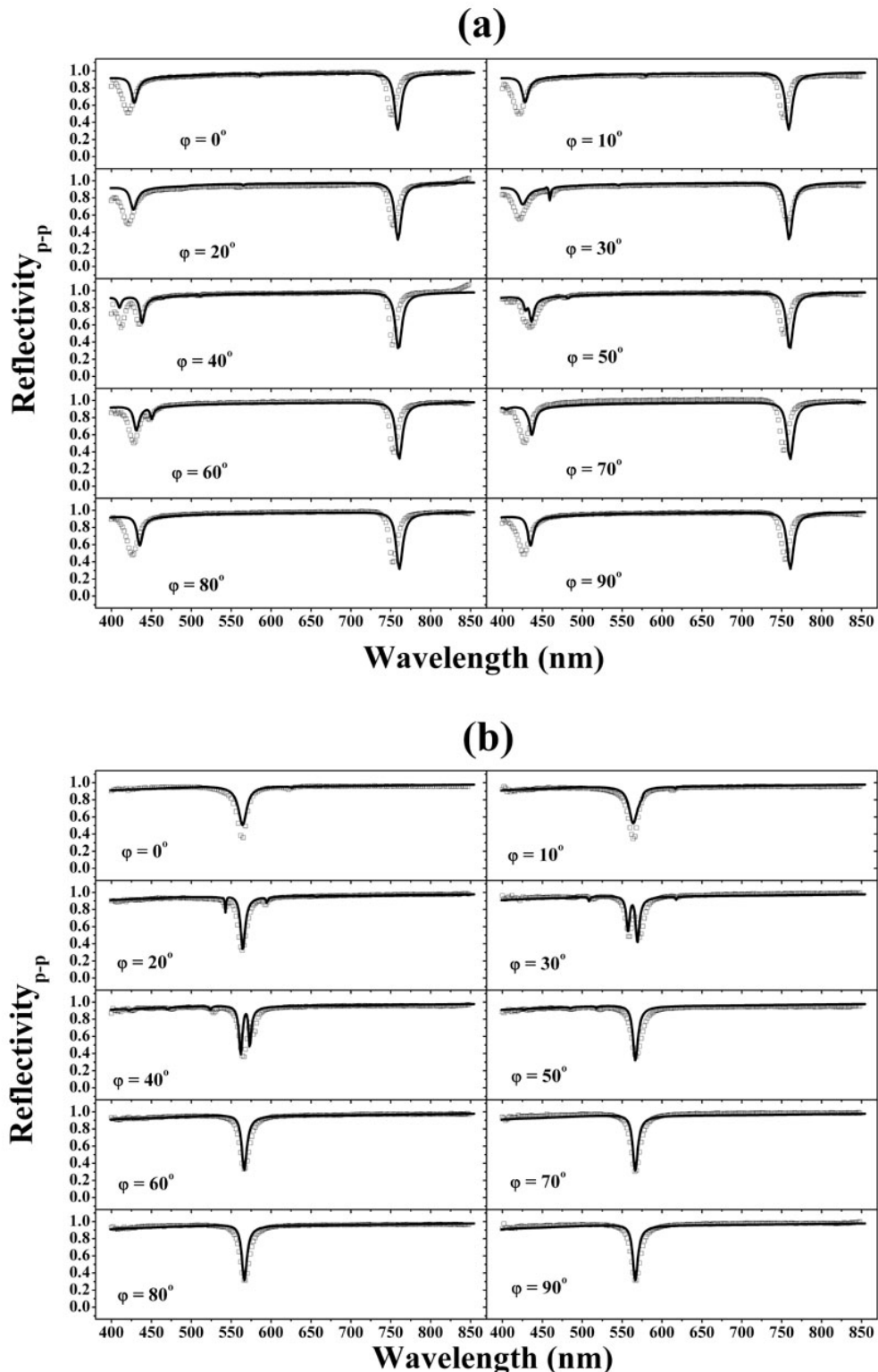


**Figure 5.3.2** The results of the absolute wavelength-dependent reflectivity for p-polarised incident light at polar angles (a)  $\theta = 45^\circ$  and (b)  $\theta = 58.5^\circ$ . The solid lines are theoretically modelled results. The squares are experimental data. The density of experimental data points has been reduced for clarity.

As shown in Figure 5.3.2, the best comparison between the model and the experimental data is achieved when the following fitting parameters are used:  $a_0 = 35$  nm,  $\phi_0 = 90^\circ$ ,  $a_2 = -5$  nm,  $\phi_2 = 90^\circ$ ,  $t = 60.8$  nm (the thickness of the silver tunnel barrier, as defined in Figure 5.3.1), and  $d = 290.8$  nm (the average thickness of the photoresist). From the discussion in the above section we know that when the thickness of the photoresist is larger than  $\sim 150$  nm the SPPs supported by the silver/photoresist interface can not be excited in the visible range ( $0.35 \times 10^{15}$  Hz –  $0.75 \times 10^{15}$  Hz), so that in this system the SPP modes are not considered.

Also from these reflectivity spectra it is apparent that some reflectivity dips do not change their positions while varying the azimuth angle (for fixed polar angle) except over a small range of azimuth angles, in which the reflection dip is interfered with by a Bragg-scattered mode. In Figure 5.3.2 (a), there are two such reflection dips at  $\sim 425$  nm and  $\sim 750$  nm respectively. For example at  $\varphi = 40^\circ$ , the reflection dip that should be at  $\sim 425$  nm is significantly red-shifted. In Figure 5.3.2 (b), a similar effect is seen at  $\sim 565$  nm.

Figure 5.3.3 shows the model band structure for all the modes (both TM and TE polarisation) supported by the waveguide structure over a certain range of frequency and in-plane wave vector ( $k_x$ ) at  $\varphi = 0^\circ$ , including the evanescent modes. The two horizontal dashed lines indicate the visible range that can be accessed in the experiments. Clearly the mode (i) beyond the silica light line is the SPP mode that is supported by the silver/silica interface. Mode (ii) is identified as the SPP mode that propagates at the silver/resist interface. We have used the labels  $TM_m$  and  $TE_m$  to identify the guided modes, where  $m$  is an integer indicating the order of the mode. Identification of the other modes (iii) – (vi) has been made possible by studying the model reflectivity plots.

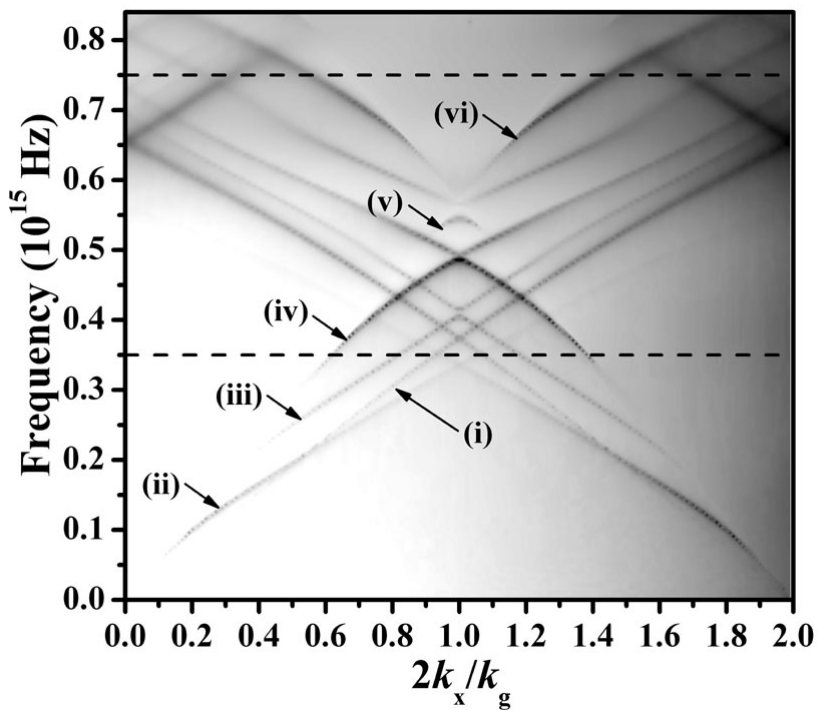


**Figure 5.3.3** The theoretical band structure for the waveguide structure at  $\varphi = 0^\circ$ . The unscattered modes can be identified as (i) SPP mode that propagates at the silver/silica interface, (ii) the SPP mode that is supported by silver/resist interface, (iii) TE<sub>1</sub>, (iv) TM<sub>1</sub>, (v) TE<sub>2</sub>, and (vi) TM<sub>2</sub> mode respectively. All of these modes will suffer Bragg-scattering thereby ‘reflecting’ at the Brillouin zone boundary.

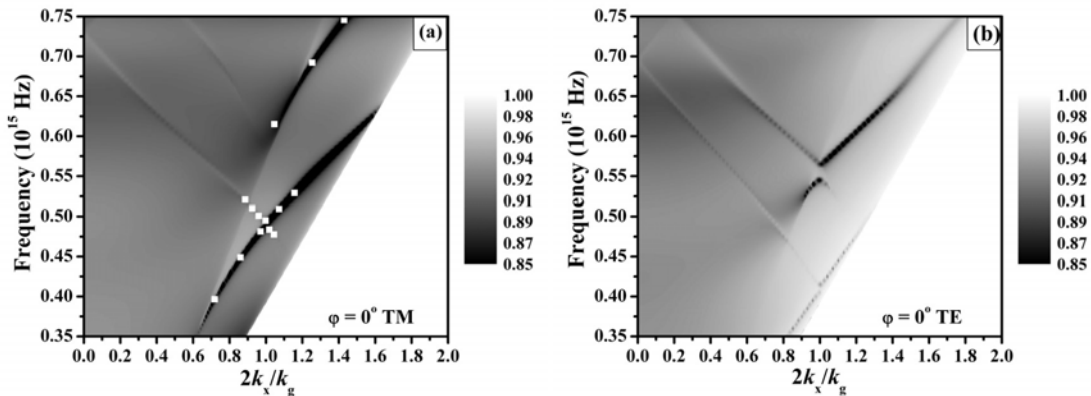


**Figure 5.3.4** The theoretical TM reflectivity (a) and TE reflectivity (b) as a function of frequency and in-plane wave vector for the waveguide structure with light incident at  $\varphi = 0^\circ$ . The white polygon in the bottom right corner indicates the inaccessible region beyond the silica light line. Two modes, TM<sub>1</sub> and TM<sub>2</sub>, can be accessed in the visible for TM polarisation. The squares in (a) are the mapped reflection dips that are taken from the experimental reflectivity spectra. One band-gap is formed at the first Brillouin zone boundary ( $2k_x/k_g = 1$ ) with the centre frequency  $f_c = 0.491 \times 10^{15}$  Hz.

In Figure 5.3.4 (a), the model TM reflectivity is plotted as a function of frequency and in-plane wave vector for  $\phi = 0^\circ$ , with the experimental data also being mapped onto this plot: they agree very well. Also plotted is the model TE reflectivity in Figure 5.3.4 (b). The white polygon in the bottom right corner of these plots indicates the inaccessible region beyond the silica light line. By comparing the band structure with the reflectivity plots, it is clear that modes (iv) and (vi) are  $TM_1$  and  $TM_2$  guided modes, and modes (iii), and (v) are  $TE_1$ , and  $TE_2$  guided modes respectively. Figure 5.3.3 also demonstrates that all these modes will be ‘reflected’ at the Brillouin zone boundary. Figure 5.3.4 (a) clearly shows that both  $TM_1$  and  $TM_2$  modes suffer this Bragg-scattering, and that a band-gap is formed at the first Brillouin zone boundary ( $2k_x/k_g = 1$ ) where the Bragg-scattered mode interferes with the unscattered mode. The experimental data also confirms this Bragg-scattering and the formation of band-gaps. The centre frequency of this particular band-gap is  $0.491 \times 10^{15}$  Hz.

At  $\phi = 90^\circ$ , the positions of the minima, obtained from the experimental reflection spectra, together with the model TM reflectivity as a function of frequency and in-plane wave vector ( $k_z$ ) are shown in Figure 5.3.5 (a). Also plotted in Figure 5.3.5 (b) is the model TM reflectivity for the planar structure (the top surface of the photoresist is uncorrugated) using the same parameters as described above (the thickness of the resist is taken to be the mean thickness). With TM polarisation at azimuthal angle  $\phi = 90^\circ$ , the optical electric field is parallel to the grating grooves. In which case we see, by comparing Figure 5.3.5 (a) with (b), that if the modulation of the grating is weak (the amplitude of the grating is small compared to the mean thickness of the photoresist layer), the TM optical response of this system is similar to that of the planar structure. Then comparing the two modes in Figure 5.3.5 (a) with the modes in Figure 5.3.3, we find that these two modes can be identified as the  $TM_1$  and  $TM_2$  guided modes respectively. Also comparing with the modes in Figure 5.3.4 (a), Figure 5.3.6 and Figure 5.3.7, we can see that these two modes keep the same positions and profiles when the azimuthal angle is varied from  $0^\circ$  to  $90^\circ$  except over a small range in which they are interfered with by a Bragg-scattered mode. These  $TM_1$  and  $TM_2$  modes are the unscattered TM polarised modes mentioned above.

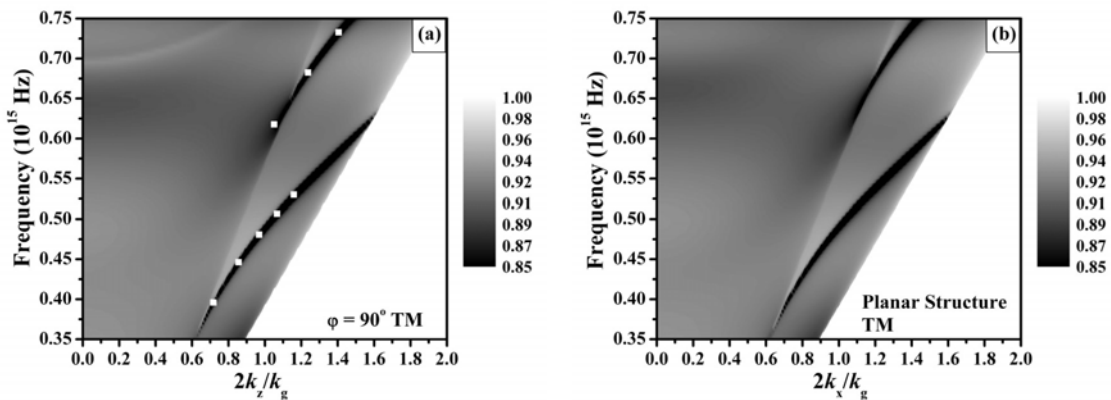


**Figure 5.3.5** The theoretical TM reflectivity at azimuthal angle  $\varphi = 90^\circ$  as a function of frequency and in-plane wave vector for the structure with the corrugation on the top surface of the photoresist (a), and planar structure without top corrugation (b). The white squares in (a) are the experimental data taken from the reflection spectra. The in-plane wavevector components  $k_z$  and  $k_x$  are scaled to  $k_g/2$ .

When the azimuth angle  $\varphi \neq 0^\circ$  or  $90^\circ$ , the dispersion curve becomes more complicated. The major reason for this is that TM polarised light may now excite TE guided modes through the broken symmetry. This will then result in extra corresponding dips in the reflection spectra. These TE guided modes may well be Bragg-scattered and cross with the TM modes. Figure 5.3.6 shows the calculated TM reflectivity as a function of frequency and in-plane wave vector ( $k_{xz}$ ) in the direction of propagation together with experimental data (white squares) for azimuthal angles  $\varphi = 10^\circ$  to  $80^\circ$ . We know, at the first Brillouin zone (BZ) boundary  $2k_x/k_g$  should be 1, where the  $k_x$  component is given by  $k_{xz} \cdot \cos\varphi$ . Hence, in these plots, the value of  $k_{xz}$  at the first Brillouin zone boundary is given by  $1/\cos\varphi$ . Note that at normal incidence (polar angle  $\theta = 0^\circ$ ) none of the modes vary their resonant frequencies as the azimuth angle is varied. It is possible to identify each of the modes found in Figure 5.3.6, which are marked (i) – (vi), by comparing with the normal incident resonant frequencies of the band structure in Figure 5.5.3. Modes (i), (ii), (iii), and (iv) are unscattered TM<sub>1</sub> and TM<sub>2</sub>, and scattered TM<sub>1</sub> and TM<sub>2</sub> guided modes respectively. Modes (v) and (vi) are scattered TE<sub>1</sub> and TE<sub>2</sub> modes.

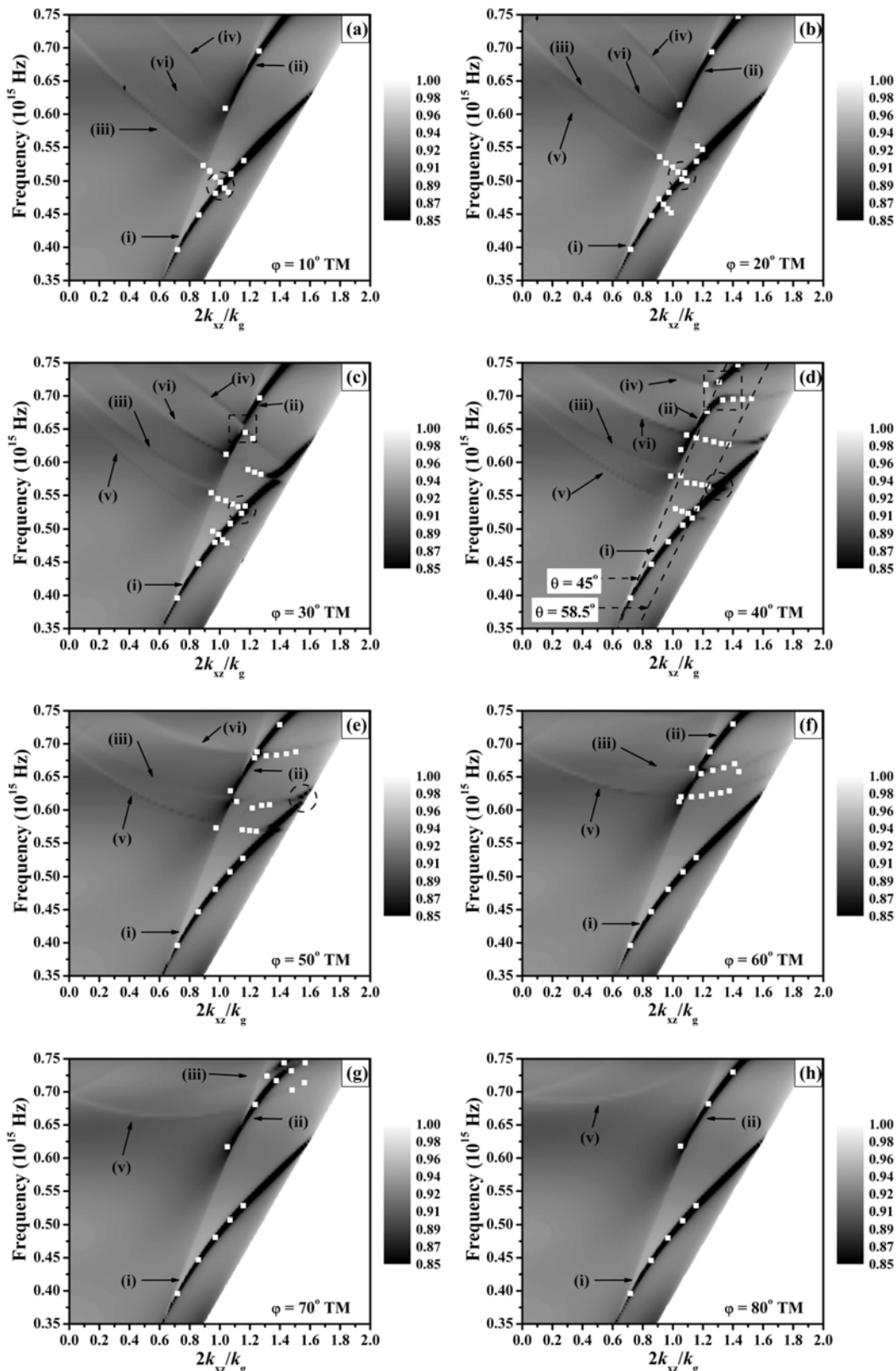


**Figure 5.3.6** TM reflectivity for the waveguide structure at  $\varphi = 10^\circ$  to  $80^\circ$ . The white squares in each plot indicate the corresponding experimental data. The dashed line box in (a) – (e) indicates the band gap at the first BZ boundary. The two dashed lines in (d) indicate the polar angle  $\theta = 45^\circ$  and  $58.5^\circ$ .

In Figure 5.3.6 (a) – (e), the region surrounded by a dashed circle clearly indicates one of the band-gaps. As described previously, this band gap is formed by the interference between scattered and unscattered  $\text{TM}_1$  modes and occurs at the first Brillouin zone boundary. The central frequencies of this band gap for  $\varphi = 10^\circ, 20^\circ, 30^\circ, 40^\circ$ , and  $50^\circ$  are  $0.496, 0.509, 0.532, 0.565$ , and  $0.620 (\times 10^{15} \text{ Hz})$  respectively. The band gap central frequency increases with increasing  $\varphi$ . Furthermore, examination of Figure 5.3.6 (e) reveals that there is clear coupling to the lower branch of this band gap up to about  $0.614 \times 10^{15} \text{ Hz}$ . Comparing this with Figure 5.3.4 (a), it is apparent that this value exceeds the position of the upper band edge for  $\varphi = 0^\circ$ , which is positioned at approximately  $0.495 \times 10^{15} \text{ Hz}$ . In other words, the rise in frequency of the centre of the band gap from  $\varphi = 0^\circ$  to  $\varphi = 50^\circ$  is greater than the overall gap width at  $\varphi = 0^\circ$ . This clearly demonstrates that this band gap is not two-dimensional. At  $\varphi = 30^\circ$  and  $40^\circ$ , a second band gap is clearly visible in the region surrounded by a square dashed box at the first BZ boundary, as shown in Figure 5.3.6 (c) and (d). This band gap is caused by the interference of the unscattered  $\text{TM}_2$  mode (ii) and the scattered  $\text{TM}_2$  mode (iv). For the same reason as that discussed for the first band-gap caused by scattered/unscattered  $\text{TM}_1$  mode, this band gap is also not a complete two-dimensional band gap.

In addition to the band-gaps at the BZ boundary, the anti-crossing within the BZ can be observed. As shown in Figure 5.3.6 (e), an anti-crossing caused by the scattered  $\text{TM}_1$  mode (iii) and unscattered  $\text{TM}_2$  (ii) mode is opened up at in-plane wave vector values of  $2k_{xz}/k_g = 1.084$ . Figure 5.3.6 also shows the anti-crossings between TE Bragg-scattered modes and unscattered TM modes when polarization conversion is present. Figure 5.3.6 (c) and (d) clearly show that the scattered  $\text{TE}_1$  mode (v) and scattered  $\text{TE}_2$  mode (vi) cross with the unscattered  $\text{TM}_1$  mode (i) at  $2k_{xz}/k_g = 1.0$  and  $1.385$  with  $\varphi = 30^\circ$  and  $2k_{xz}/k_g = 1.125$  and  $1.6$  with  $\varphi = 40^\circ$  respectively. At these crossings there is an energy gap which is similar to the band-gap at the BZ boundary. As the azimuth angle is increased the scattered  $\text{TE}_1$  mode (v) and  $\text{TE}_2$  mode (vi) increase in frequency and become flatter. Hence, the position of the mode crossing will rise in both frequency and in-plane wave vector. As shown in Figure 5.3.6 (e), the anti-crossing between  $\text{TE}_1$  mode (v) and  $\text{TM}_1$  mode (i) occurs now at  $2k_{xz}/k_g = 1.355$ , and beyond  $\varphi \sim 50^\circ$  this crossing will move outside the range accessible through silica prism coupling. For the

anti-crossing caused by TE<sub>2</sub> (vi) mode and TM<sub>1</sub> mode (i), it has moved outside the accessible range beyond  $\phi \sim 40^\circ$ .

In addition to the crossings caused by the unscattered TM<sub>1</sub> mode (i) a further similar crossing is visible. This crossing is from interference between the scattered TE<sub>2</sub> mode (vi) and the unscattered TM<sub>2</sub> mode (ii), which appears at  $2k_{xz}/k_g = 1.125$  and 1.252 in Figures 5.3.6 (d) and (e) respectively. As for the anti-crossing discussed above, it shifts its frequency and in-plane wave vector with increasing azimuth angle. Again, these crossings have the same behaviour as discussed above.

To understand these modes better, the optical magnetic field distribution is computed, as shown in Figure 5.3.7 and Figure 5.3.8, for an azimuth angle of  $\phi = 40^\circ$  and at each resonant frequency for polar angles of  $\theta = 58.5^\circ$  and  $45^\circ$ .

Note from Figure 5.3.6 (d) that the first two modes at  $\theta = 58.5^\circ$  are around the mode crossing of the Bragg-scattered TE<sub>1</sub> mode (v) and the unscattered TM<sub>1</sub> mode (i). Figure 5.3.7 (a) shows the magnetic field distribution for the lower branch of the crossing, and Figure 5.3.7 (b) shows the field distribution for the upper branch. Relative to the photoresist grating, the field amplitude maxima near to the grating are observed in the troughs in both Figure 5.3.7 (a) and (b). However, the field maxima close to the silver/resist interface align with the troughs in Figure 5.3.7 (a) but align with the peaks in 5.3.7 (b). This of course leads to the energy gap at the crossing. Figure 5.3.7 (c), (d), and (e) show the field distribution for scattered TM<sub>1</sub> mode (the third mode at  $\theta = 58.5^\circ$ ), the scattered TE<sub>2</sub> mode (the fourth mode at  $\theta = 58.5^\circ$ ), and the scattered TM<sub>2</sub> mode (the fifth mode at  $\theta = 58.5^\circ$ ) respectively. It is straightforward to determine the order of these modes by counting the number of optical field minima per period. There is one optical field minimum per period in Figure 5.3.7 (c) and two minima per period in Figure 5.3.7 (d) and (e). Hence, they are the first order and second order modes respectively.

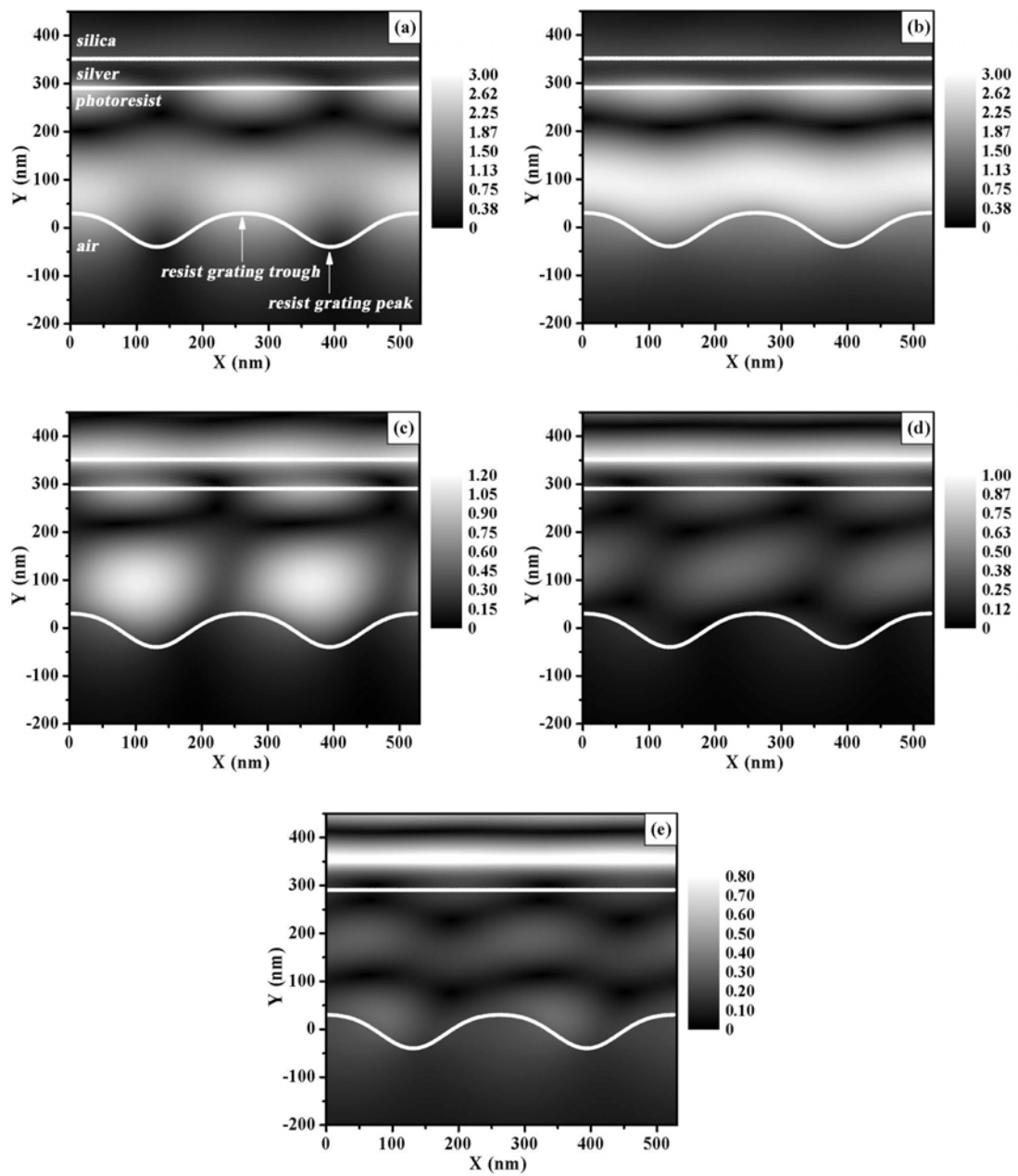


**Figure 5.3.7** The magnetic field amplitude distribution for the guided modes resonance at polar angle  $\theta = 58.5^\circ$  and azimuth angle  $\varphi = 40^\circ$  for (a)  $f = 0.522 \times 10^{15} \text{ Hz}$ , (b)  $f = 0.532 \times 10^{15} \text{ Hz}$ , (c)  $f = 0.571 \times 10^{15} \text{ Hz}$ , (d)  $f = 0.635 \times 10^{15} \text{ Hz}$  and (e)  $f = 0.709 \times 10^{15} \text{ Hz}$ . The white line represents the wave guide structure.

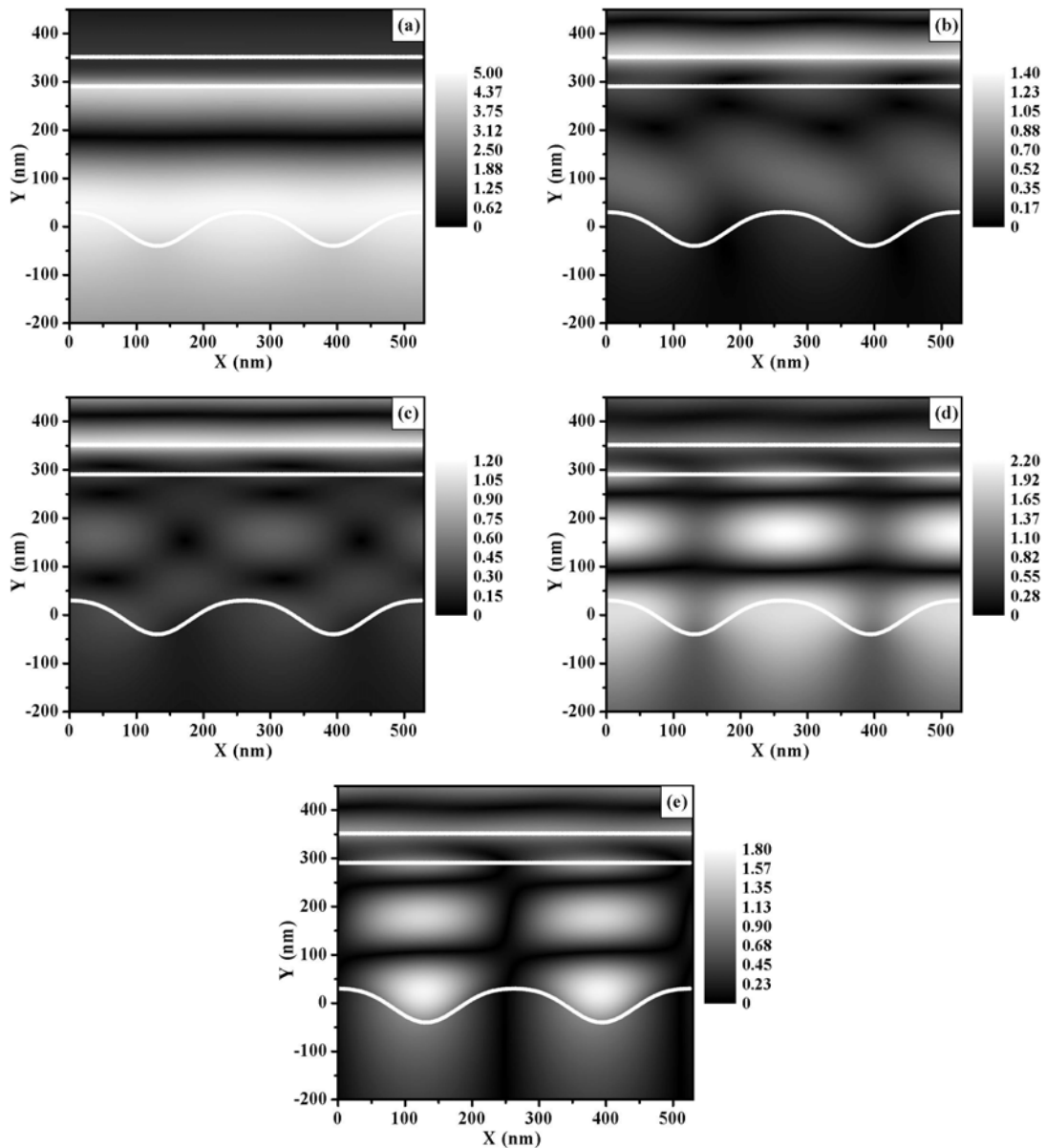


**Figure 5.3.8** The magnetic field amplitude distribution for the guided modes resonance at polar angle  $\theta = 45^\circ$  and azimuth angle  $\varphi = 40^\circ$  for (a)  $f = 0.394 \times 10^{15}$  Hz, (b)  $f = 0.585 \times 10^{15}$  Hz, (c)  $f = 0.643 \times 10^{15}$  Hz, (d)  $f = 0.682 \times 10^{15}$  Hz and (e)  $f = 0.729 \times 10^{15}$  Hz. The white line represents the wave guide structure.

The field distribution shown in Figure 5.3.8 (a) is for the unscattered  $TM_1$  mode. It is difficult to tell clearly the position of the maxima, one can only see a continuous field minimum in the resist waveguide medium. From Figure 5.3.6 (d), one sees that the second mode at  $\theta = 45^\circ$  is the same as the third mode at  $\theta = 58.5^\circ$ . Both of them belong to the Bragg-scattered  $TM_1$  mode. Comparing Figure 5.3.8 (b) with Figure 5.3.7 (c), the field distributions are almost the same except for the field intensity. The third mode at

$\theta = 45^\circ$  is around the mode crossing of the scattered  $TE_2$  mode and the unscattered  $TM_2$  mode. The field distributions in Figure 5.3.8 (c) clearly show the interference of these two modes. The field maximum occurring in the centre of the photoresist medium is now surrounded by four field minima. Figure 5.3.8 (d) shows the magnetic field distribution for the lower branch at the band gap where the scattered and unscattered  $TM_2$  modes cross, and Figure 5.3.8 (e) shows the field distribution for the upper branch of this band gap. The obvious two field minima per period in both Figures 5.3.8 (d) and (e) demonstrate that these modes are second order modes. In Figure 5.3.8 (d), the maxima are observed to align with the troughs of the resist grating in contrast with Figure 5.3.8 (e), in which the maxima are observed to align with the peaks. From Figure 5.3.6 (d), one sees that the last two modes at  $\theta = 45^\circ$  are much closer to the first BZ boundary ( $2k_{xz}/k_g = 1.305$ ) and belong to the different branch of the counterpropagating waveguide modes respectively. For counterpropagating waveguide modes that cross at the first Brillouin-zone boundary standing waves are expected which consist of two eigensolutions. The antinodes of the magnetic field of one solution are positioned under troughs of the corrugation (as shown in Figure 5.3.8 (d)), whereas for the second solution they are positioned under the peaks (as shown in Figure 5.3.8 (e)). The asymmetry of the wave guide structure causes an energy difference between the two solutions, leading to a band gap.

## 5.4 Summary

In this chapter, the band structures of a planar waveguide structure with different thickness of photoresist guide medium are modelled. It is shown how the thickness of the waveguide medium modifies the dispersion of SPP modes and guided modes.

Following this, we have explored the optical properties of a short-pitch periodically corrugated photoresist waveguide structure on a thin silver tunnel barrier at  $10^\circ$  steps over the azimuth angle range  $\varphi = 0^\circ$  to  $90^\circ$ . Reflectivity data at each  $\varphi$  for 5 different incident angles ( $\theta = 45^\circ, 48.4^\circ, 51.8^\circ, 55.2^\circ$ , and  $58.5^\circ$ ) have been measured and mapped on to the theoretical plots. Experimental data show excellent agreement with the model calculations. By comparing the predicted band structure with both TM and TE reflectivity all the modes supported by the structure are identified. Both

experimental data and theoretical fitting show that the introduction of the corrugation into the wave guide introduces band gaps in the dispersion of the guided modes. These band gaps raise their central frequencies with increasing azimuth angle  $\varphi$ . By comparing the central frequency of band gaps at different azimuth angles, the nature of the band gap that is **not** two dimensional has been demonstrated. In addition, when the azimuth angle  $\varphi \neq 0^\circ$  or  $90^\circ$  polarisation conversion leads to anti-crossings where different types of modes cross. To understand the character of each of the modes, the optical magnetic field distributions at azimuth angle  $\varphi = 40^\circ$  at each resonant frequency for polar angles of  $\theta = 58.5^\circ$  and  $45^\circ$  are explored. The field distributions help to distinguish the order of the modes and demonstrate the cause of the energy splitting at the mode-crossing.

In the context of emissive devices the presence of the energy gap can inhibit the emission if the emission frequency lies in the gap. Both the band-gaps caused by the modes self-crossing at the Brillouin zone boundary and the anti-crossings caused by different modes crossing at other than the Brillouin zone boundary can play an important role in controlling the emission in such corrugated waveguide structures.

# Chapter 6

## Grating-coupled SPPs and Waveguide Modes in a Silver-Dielectric-Silver Structure

### 6.1 Introduction

In chapter 5 we have investigated the optical properties of a waveguide structure consisting of a dielectric layer deposited on a planar silver film and noted the potential applications of this simpler waveguide structure. In fact, in many practical devices the waveguide structures are microcavities comprising a pair of highly reflecting mirrors separated by a dielectric film. The mirrors used in such structures may be either dielectric stacks or more simply metal layers. For the case of metal mirrors SPPs may be supported as well as waveguide modes (if the dielectric is thick enough). In this chapter, we shall explore the optical response of such a silver-dielectric-silver structure – a metallic microcavity.

As mentioned in chapter 3, on a flat metal surface the localised SPP mode cannot be directly excited by incident photons because the wave vector of the SPP mode for any given frequency is greater than that of a photon-polariton of the same frequency in the adjacent dielectric i.e., it is nonradiative. In order to optically excite the SPP mode, the in-plane momentum of incident photons must be suitably increased. Lupton *et al.* [2000] have shown that a microcavity with periodic texture can be used to provide an increase in light emitting efficiency by allowing some of the energy that would be lost in a planar microcavity device to be recovered as useful radiation. In addition to an efficiency increase, structures possessing wavelength-scale texture produce photonic band-gaps (Abram and Bourdon [1996], Lee *et al.* [1999], and Salt and Barnes [1999]). Such photonic band-gaps may play an important role in controlling spontaneous emission, and, combining them with waveguide structures, can lead to an increase in such control by placing the photonic band edge at the emission wavelength (Dowling *et al.* [1994], Kitson *et al.* [1998], Barnes [1999], and Salt and Barnes [2000]). The design and fabrication of metallic nanostructures combining surface wave properties with microcavity resonant behaviour opens up substantial new device potential.

In the first section of this chapter, the simplest microcavity structure consisting

of two planar silver mirrors (one of them is semi-infinite) separated by a layer of photoresist are investigated. By theoretically modelling the band structures, reflectivity, and optical field distribution at the resonant frequency, the optical properties of the planar silver microcavity are explored. A momentum splitting of TM and TE polarized waveguide modes in the dispersion curves is also explained.

In the second section, we shall study the visible electromagnetic (EM) response of a silver-photoresist-silver layered microcavity structure in which the upper interface between the photoresist and the silver is periodically corrugated. By recording the visible reflection spectra and mapping the experimental data to a plot of reflectivity as a function of frequency and in-plane wave vector, the SPP and waveguide band structure is elaborated. In particular, the presence of a flat band caused by the anti-crossings between the SPP mode and waveguide modes is confirmed experimentally. This flat band resonant frequency may be tuned by varying the amplitude of the corrugation. To fully understand the character of all the modes uncovered, the optical field distribution at the resonant frequency for each of the modes is explored.

## 6.2 Planar Silver Microcavity

In this section, we shall theoretically investigate the optical properties of a planar silver microcavity within the Kretschmann-Raether configuration. The sample used here is similar to that used in the previous section 5.2, except that it has a semi-infinite cladding silver layer. A schematic of the sample geometry together with the coordinate system is shown in Figure 6.2.1, where  $\theta$  is the incident angle,  $t$  is the thickness of the silver tunnel barrier, and  $d$  is the thickness of the photoresist layer. The position of  $y = 0$  corresponds to the bottom silver/photoresist interface.

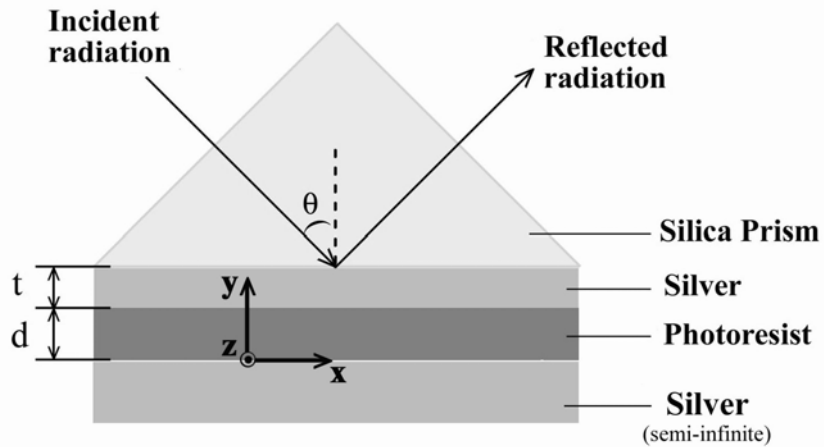


**Figure 6.2.1** Schematic diagram illustrating the sample and the coordinate system used in this work. Here  $t$  is the thickness of the silver tunnel barrier,  $\theta$  is the polar angle, and  $d$  is the thickness of the photoresist layer. The silver cladding layer is semi-infinite. The silica substrate is optically attached to the silica prism with matching fluid.

Figure 6.2.2 shows the band structure for the planar metallic microcavity with a thickness of the silver tunnel barrier  $t = 56.8$  nm and the photoresist layer  $d = 300.8$  nm. Note that in the calculations of this section and following sections, the refractive index of silica  $n_{\text{silica}} = 1.459$ , and the dielectric constants of the silver and photoresist are described by polynomials for both real and imaginary parts of the permittivity,

$$\varepsilon_{\text{silver}}(\omega) = -255.3185 + 198.63\omega - 60.794\omega^2 + 8.381\omega^3 - 0.43004\omega^4 + i(82.2575 - 132.79\omega + 90.474\omega^2 - 32.88\omega^3 + 6.659\omega^4 - 0.70893\omega^5 + 0.030913\omega^6), \text{ and}$$

$$\varepsilon_{\text{resist}}(\omega) = -2.35348 + 5.7749\omega - 2.5344\omega^2 + 0.53253\omega^3 - 0.052274\omega^4 + 0.0018284\omega^5 + i(0.01319 - 8.7131 \times 10^{-16}\omega - 1.1024 \times 10^{-3}\omega^2 - 1.6659 \times 10^{-24}\omega^3 + 9.663 \times 10^{-5}\omega^4 - 1.4567 \times 10^{-18}\omega^5)$$

where  $\omega = (2\pi c/\lambda) \times 10^{-15} \text{ s}^{-1}$ . In the band structure, both the evanescent modes and waveguide modes are observed. The two modes,  $SPP_1$  and  $SPP_2$ , indicated by the open squares in Figure 6.2.2 are the SPP modes that are supported by the silver/photoresist and silica/silver interface. The modes indicated by the open triangles, circles, and stars are the first, second, and third order TM/TE polarized waveguides respectively. The important feature to note in Figure 6.2.2 is the presence of the antisymmetric coupled SPP mode –  $SPP_1$ . This mode is well known in parallel plate waveguide transmission

lines used in microwave applications (Cheng [1989]). In this case, we note that this mode extends below the usual cavity cutoff frequency of  $0.2695 \times 10^{15}$  Hz, continuing all the way to zero frequency. At low values of in-plane wave vector, the other coupled-SPP mode is the more familiar lowest order  $\text{TM}_1$  mode of the microcavity. At high in-plane wave vectors the two modes become degenerate and follow the dispersion curve of the single interface SPP that propagates along the silver/photore sist interface.

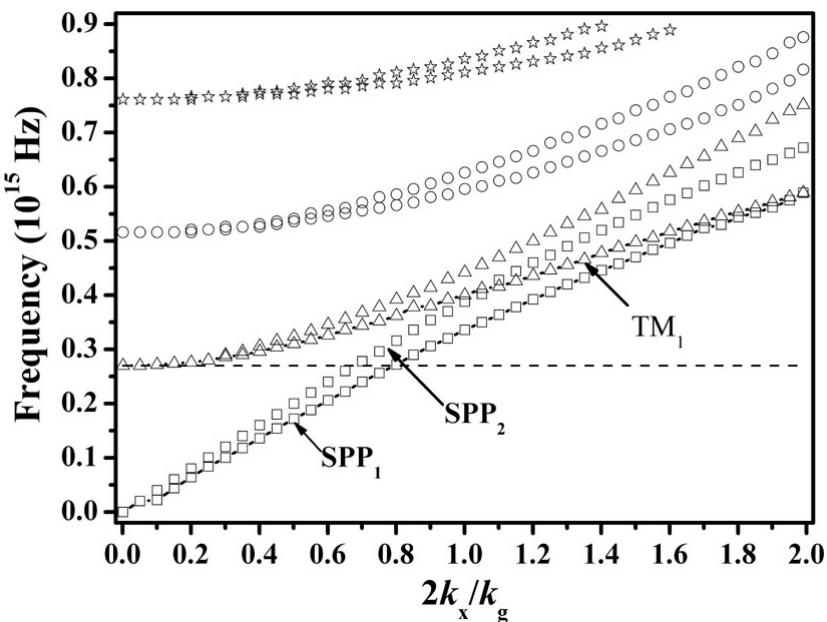


**Figure 6.2.2** Band structure for the planar silver microcavity with thickness of the silver film  $t = 56.8$  nm and the photore sist layer  $d = 300.8$  nm. The open squares represent the SPP modes that are supported by the silica/silver and silver/photore sist interface. The open triangles, circles, and stars indicate the first, second, and third order TM/TE polarized waveguide modes respectively. The horizontal line represents the usual cavity cutoff frequency  $0.2695 \times 10^{15}$  Hz.

To identify each of the waveguide modes, the theoretical TM and TE polarized reflectivities are plotted in Figure 6.2.3. We have used the labels  $\text{TM}_m$  and  $\text{TE}_m$  to identify the various TM and TE wave guide modes, where  $m$  is an integer indicating the  $m^{\text{th}}$  order of the guided mode. By comparing the band structure with the reflectivity, one can see that  $\text{TE}_m$  and  $\text{TM}_m$  waveguide modes locate at the same frequency with the value of in-plane wave vector  $2k_x/k_g = 0$ . As each waveguide mode increases in wave vector, differences in the reflectivity at the upper and lower interfaces of the waveguide for TM and TE polarization cause the mode to split into two. The TE polarized wave

guide mode ( $\text{TE}_m$ ) is then situated higher in frequency to the TM polarized wave guide mode ( $\text{TM}_m$ ), for the same value of the in-plane wave vector. Note that in the visible range only  $\text{TE}_1/\text{TM}_1$  and  $\text{TE}_2/\text{TM}_2$  waveguide modes are accessible with a thickness of the photoresist  $d = 300.8 \text{ nm}$ .

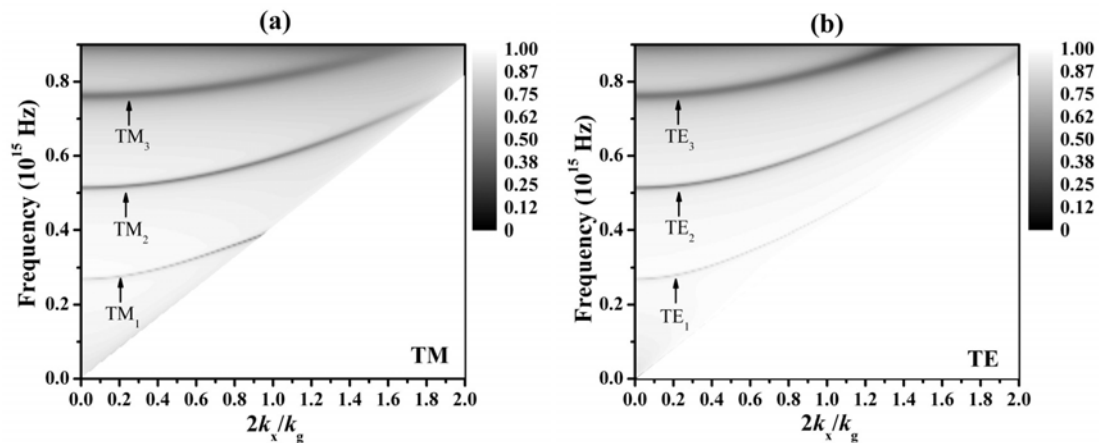


**Figure 6.2.3** The theoretical reflectivity as a function of frequency and in-plane wave vector for (a) TM polarization and (b) TE polarization. The white triangular region in the bottom right corner indicates the inaccessible region beyond the silica light line.

To understand the general form of the waveguide modes of a planar microcavity, let us consider the simpler case of the non-absorbing waveguide medium bounded by a pair of perfect silver mirrors and  $k_x = 0$  (normal incidence, propagation in the  $y$  direction). In this case, the boundary conditions for perfect mirrors are described by

$$E_{x(y=0)} = E_{x(y=d)} = 0.$$

This then gives solutions for  $E_x$  of the form

$$E_x(y) = E_0 \sin(k_y y),$$

with

$$k_y = \frac{m\pi}{d},$$

which then leads to

$$\omega_m = ck_y = \frac{cm\pi}{d},$$

where  $m$  is an integer. This equation represents a series of standing waves (waveguide modes), whose schematic  $E_x$  field profiles are represented by dashed lines in Figure 6.2.4 for the first three standing waves ( $m = 1, 2, 3$ ). Also shown in Figure 6.2.4 is the

time averaged  $|E_x|$  component of field distributions at normal incidence for 1<sup>st</sup>, 2<sup>nd</sup>, and 3<sup>rd</sup> order waveguide modes with resonant frequency  $f = 0.2695 \times 10^{15}$  Hz,  $0.514 \times 10^{15}$  Hz, and  $0.7615 \times 10^{15}$  Hz respectively. In Figure 6.2.4 (a), for the first order waveguide mode, clearly there is only one field maximum in the waveguide centre. In Figure 6.2.4 (b), for the second order waveguide mode, two field maxima separated by a field minimum in the waveguide centre are observed. Similarly, for the third order waveguide mode, three field maxima spaced by two field minima are observed readily in Figure 6.2.4 (c). Hence, the number of field maxima contained within the waveguide medium is equal to the order of the waveguide mode.

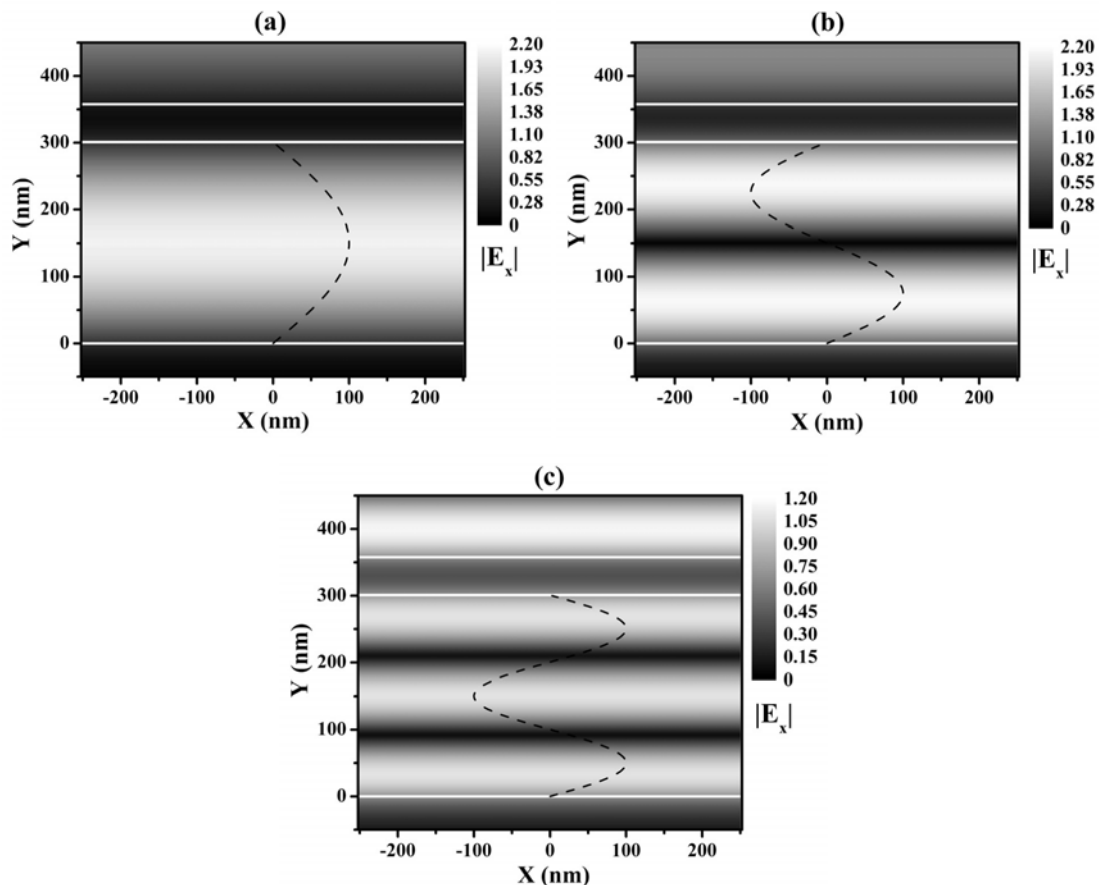


**Figure 6.2.4** Time averaged  $|E_x|$  component of field distributions at  $\theta = 0^\circ$  for (a) first order wave guide mode,  $f = 0.2695 \times 10^{15}$  Hz, (b) second order wave guide mode,  $f = 0.514 \times 10^{15}$  Hz, and (c) third order wave guide mode,  $f = 0.7615 \times 10^{15}$  Hz. The dashed lines schematically show the  $E_x$  field profiles for 1<sup>st</sup>, 2<sup>nd</sup>, and 3<sup>rd</sup> order standing wave.

### 6.3 Corrugated Silver Microcavity

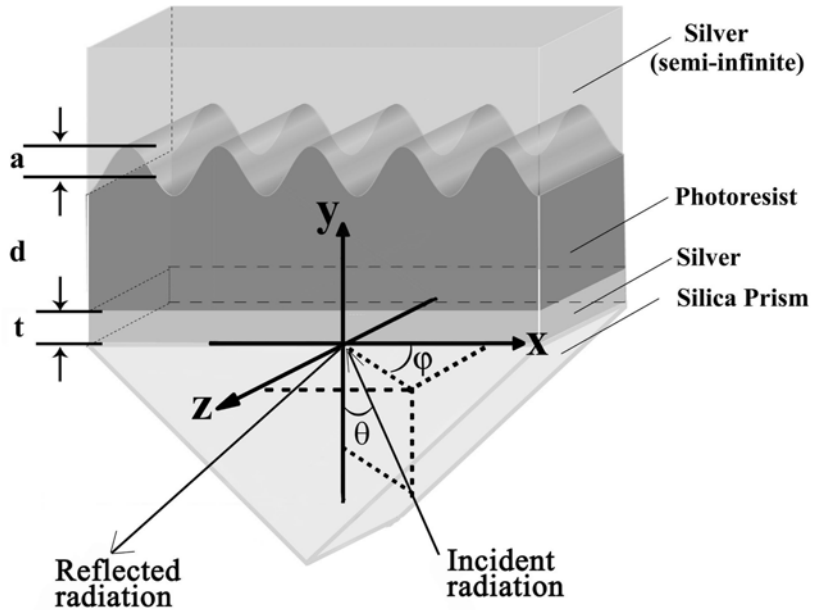


**Figure 6.3.1** Schematic diagram illustrating the sample, the coordinate system, and the experimental geometry used in this work. Here  $a$  is the grating amplitude,  $t$  is the thickness of the silver tunnel barrier,  $\theta$  is the polar angle,  $\varphi$  is the azimuth angle, and  $d$  is the average thickness of the photoresist layer. The silica substrate is optically attached to the silica prism with matching fluid. Note in our experiments to set the different azimuth angles ( $\varphi$ ) only the sample is rotated, not the prism.

We have now investigated the optical properties of the planar silver microcavity. Let's turn to the corrugated silver microcavity. In Figure 6.3.1 a schematic view of the structure and associated coordinate system under study is shown. In brief, to fabricate the sample a thin silver film (acting as the entrance optical tunnel barrier and a reasonable cavity mirror), having a thickness of  $\sim 57$  nm was deposited by vacuum evaporation onto a flat silica substrate. The silver thickness chosen is such as to provide significant reflectivity while being thin enough to ensure that there is suitable strength of tunnelling of the evanescent optical field. On to this silver substrate is spin-coated a layer of Shipley SPR700 photoresist to give a waveguide layer of approximately 350 nm thickness. For such a thickness the lowest two order wave guide modes should be accessible in the visible range. The sample is then exposed to an interference pattern, and developed in NaOH solution. The pitch,  $\lambda_g$ , of the grating is set at 252 nm. On top of this now-corrugated layer is deposited an optically thick (approximately 200 nm)

layer of silver by thermal evaporation. Finally the microcavity sample on its silica substrate is optically attached to a 45° silica prism using matching fluid to avoid unwanted reflections from the substrate/air interface. Note in our experiments to set the different azimuth angles ( $\phi$ ) only the sample is rotated, not the prism. The layered structure is described by

$$y_1(x) = d + t, \\ y_2(x) = t, \\ y_3(x) = a_0 \sin(k_g x + \phi_0) + \dots + a_N \sin((N+1)k_g x + \phi_N) + \dots,$$

where  $y_1(x)$ ,  $y_2(x)$ , and  $y_3(x)$  are the profiles of silica/thin silver interface, thin silver/photoresist interface, and photoresist/thick silver interface respectively,  $t$  is the thickness of the bottom silver layer,  $d$  is the average thickness of the photoresist layer,  $a_N$  is the amplitude of the  $N^{\text{th}}$  order harmonic component of the grating, and  $k_g = 2\pi/\lambda_g$  is the grating vector, which runs parallel to the  $x$  axis.

To determine the dispersion of the modes associated with the structure, absolute reflectivity spectra are recorded as scans in wavelength ( $410 \leq \lambda_0 \leq 850$  nm) at various fixed angles. The output from a white-light source was spectrally selected using a mono-chromator and this light was then set to be p-polarised, Transverse Magnetic (TM) or s-polarised, Transverse Electric (TE) and made incident on the bottom surface of the silver tunnel barrier through the prism. A second polariser, also set to TM or TE polarisation, is placed directly in front of the detector. When the frequency and in-plane wave vector of the incident light matches a mode, the reflectivity will show a resonant dip. In this way, by noting all the reflectivity dips, a dispersion diagram is acquired. Reflectivity data was obtained at two azimuth angles,  $\phi = 0^\circ$  (the grating grooves being perpendicular to the incident plane) and  $\phi = 90^\circ$  (the grating grooves are parallel to the incident plane) and at 20 different polar angles ( $4.9^\circ \leq \theta \leq 65.0^\circ$ ) for both TM and TE polarisation. Figure 6.3.2 illustrates typical TM and TE polarized wavelength dependent absolute reflectivity data together with the modelling results for  $\phi = 0^\circ$  and  $\phi = 90^\circ$  at different polar angles. Modelling was achieved using the scattering matrix approach to the method of Chandezon *et al*, which we have mentioned in the chapter 2. To facilitate modelling over the visible domain the permittivity of the silver and photoresist are given by polynomials that have been mentioned in the previous section, although it is

known that for the thinner silver film these bulk permittivities may not be exact, they are still suitable to yield a good fit to the data. The refractive index of the silica is for simplicity taken as fixed at  $n = 1.459$ . The best comparison between the model and the experimental data is achieved, as shown in Figure 6.3.2 (a) – (d), when the following fitting parameters are used:  $a_0 = 40.3$  nm,  $\phi_0 = 0^\circ$ ,  $a_1 = -8.4$  nm,  $\phi_1 = -90^\circ$ ,  $a_2 = -2.4$  nm,  $\phi_2 = 0^\circ$ ,  $t = 56.8$  nm, and  $d = 300.8$  nm.

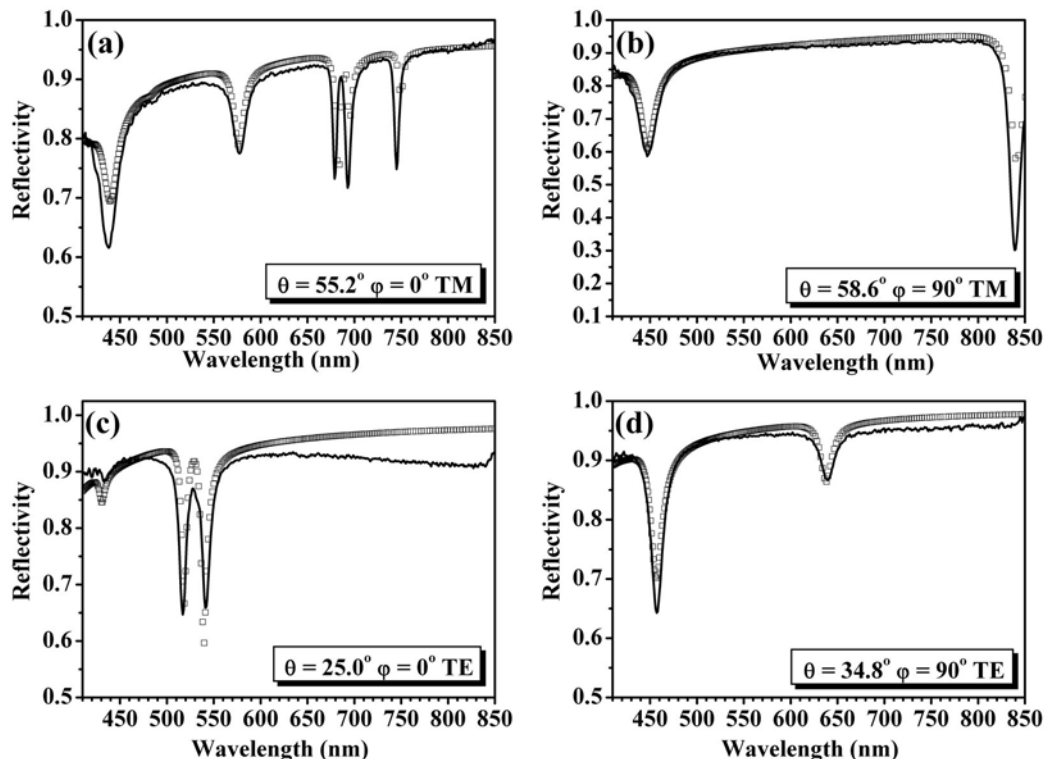
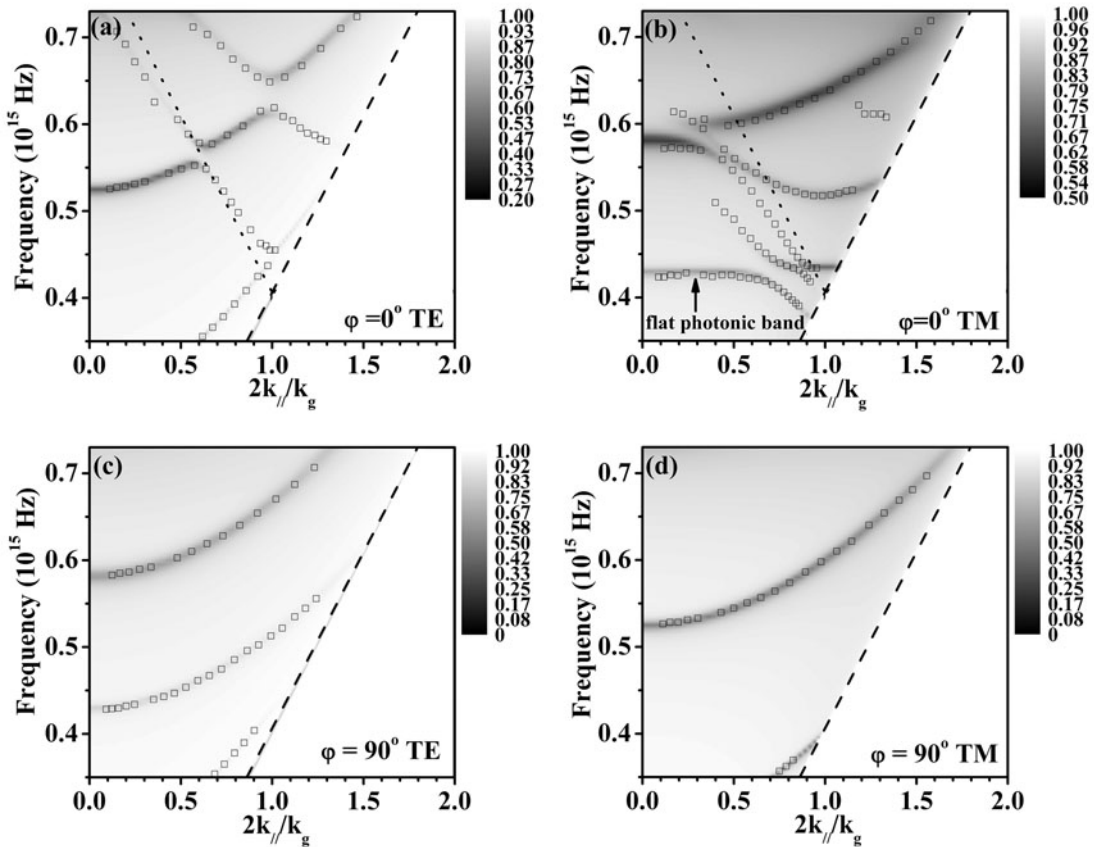


**Figure 6.3.2** The results of the wavelength-dependent reflectivity for TM polarization at angles (a)  $\theta = 55.2^\circ$ ,  $\phi = 0^\circ$ , and (b)  $\theta = 58.6^\circ$ ,  $\phi = 90^\circ$ , and for TE polarization at angles (c)  $\theta = 25.0^\circ$ ,  $\phi = 0^\circ$ , and (b)  $\theta = 34.8^\circ$ ,  $\phi = 90^\circ$ . The solid lines on each of the graphs correspond to the experimental data. The black open squares are theoretically modelled results.

### 6.3.1 Effective Mean Thickness of the Waveguide Medium

Figure 6.3.1.1 shows the model TM and TE reflectivities as a function of frequency ( $f = c/\lambda$ ) and in-plane wave vector ( $k_{\parallel}$ ) for  $\phi = 0^\circ$  and  $\phi = 90^\circ$  respectively, with the experimental data (indicated as open black squares) also being mapped onto this plot. The white triangular area in the bottom right corner of these plots indicates the

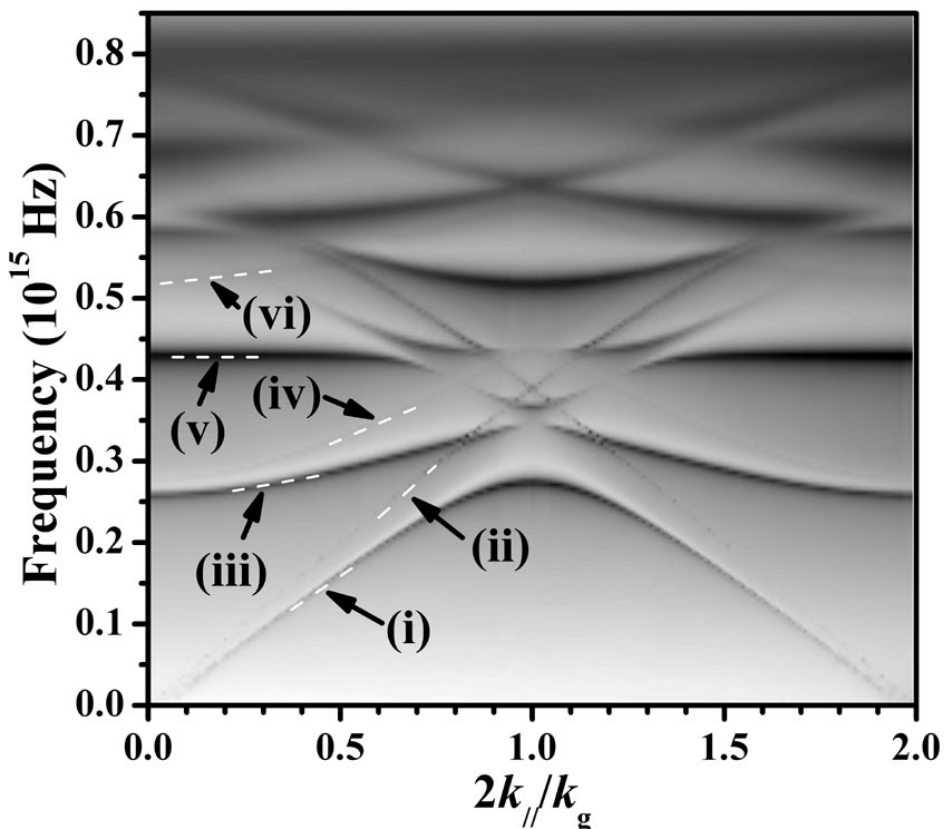
inaccessible region beyond the silica light line.



**Figure 6.3.1.1** The theoretical TE reflectivity for (a)  $\phi = 0^\circ$  and (c)  $\phi = 90^\circ$ , and TM reflectivity for (b)  $\phi = 0^\circ$  and (d)  $\phi = 90^\circ$  as a function of frequency and in-plane wave vector. The open black squares are the mapped reflection dips that are taken from the experimental reflectivity spectra. The dashed straight line indicates the silica light line. The dotted line in the upper two diagrams represents the first order diffracted silica light line. The white triangular region in the bottom right corner indicates the inaccessible region beyond the silica light line.

To identify each of the modes observed in the TM and TE dispersion curves, it is necessary to study the band structure of this metallic microcavity. Figure 6.3.1.2 shows the model band structure, obtained by inspection of the scattering matrix of the system, for all the modes (both TM and TE polarisation) supported by the waveguide structure over a certain range of frequency and in-plane wave vector at  $\phi = 0^\circ$ , including the evanescent modes. Modes labelled (i) and (ii) in Figure 6.3.1.2, which are beyond the silica light line are SPP modes supported by the silver/photoresist interface and the silica/silver interface respectively. The modes (iii) and (iv) are the  $TM_1$  and  $TE_1$  wave

guide modes, and mode (vi) is the  $\text{TE}_2$  guided mode. Mode (v) appears flattened by the interaction of the unscattered  $\text{TM}_2$  guided mode with both the Bragg-scattered silver/photoresist SPP mode and the Bragg-scattered  $\text{TM}_1$  guided mode. We will discuss this flat band in more detail later.



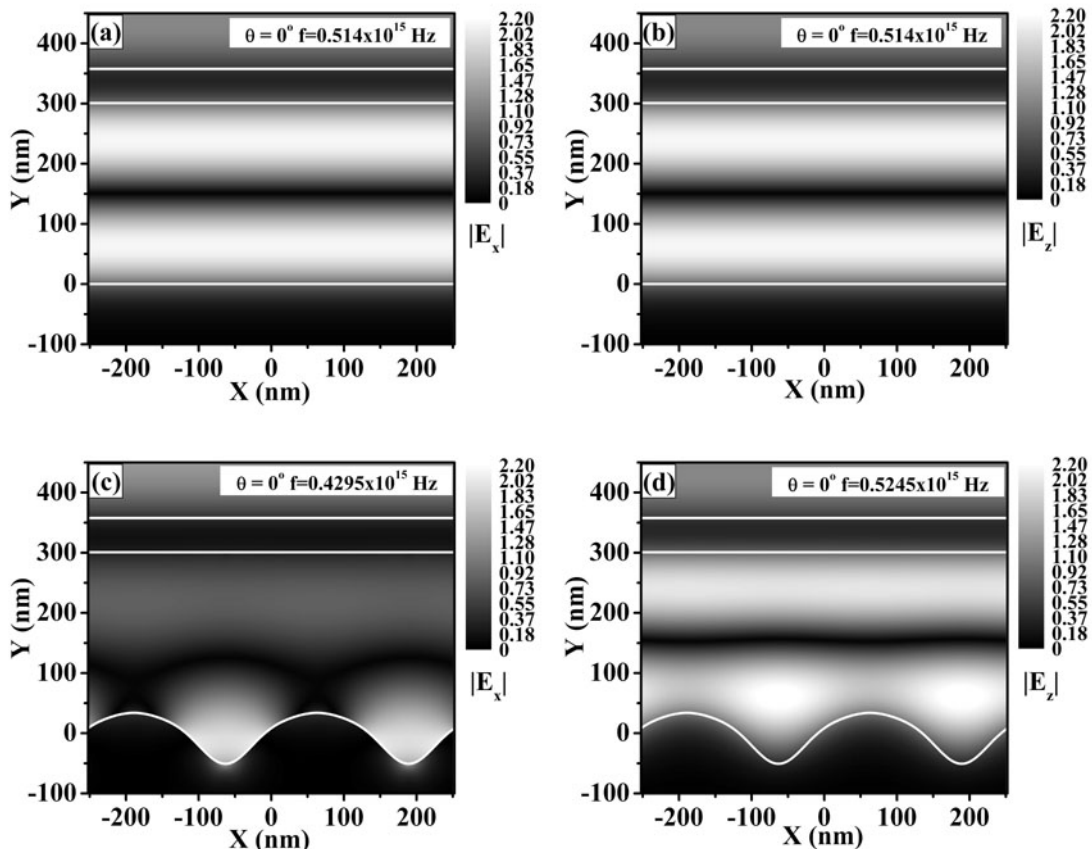
**Figure 6.3.1.2** The theoretical band structure for the waveguide structure at  $\varphi = 0^\circ$ . The unscattered modes can be identified as (i) SPP mode that is supported by silver/photoresist interface, (ii) the SPP mode that propagates at the silver/silica interface, (iii)  $\text{TM}_1$  waveguide mode, (iv)  $\text{TE}_1$  guide mode, and (vi)  $\text{TE}_2$  mode respectively. Note the flat character of mode (v).

Figure 6.3.1.1 (d) shows the TM reflectivity for an azimuth angle of  $\varphi = 90^\circ$ . By comparison with the band structure shown in Figure 6.3.1.2, the two modes that can be accessed in the visible range are identified as the  $\text{TM}_1$  and  $\text{TM}_2$  guided modes. Similarly, Figure 6.3.1.1 (c) shows the TE reflectivity for an azimuth angle of  $\varphi = 90^\circ$ , with the two lowest modes in the visible range being identified as the  $\text{TE}_1$  and  $\text{TE}_2$  guided modes respectively. A feature of note is that the  $\text{TE}_1$  and  $\text{TE}_2$  guided modes at  $\varphi = 90^\circ$  are red-shifted compared to the  $\text{TE}_1$  and  $\text{TE}_2$  guided modes at  $\varphi = 0^\circ$  shown in Figure 6.3.1.1 (a).

This frequency shift arises due to the different effective mean thickness of the waveguide medium that is sensed by incident radiation with different electric field directions relative to the grating, as noted by others (see e.g. Watts *et al.* [1997]).

To understand this frequency red-shift, the electric field profiles are investigated. Figures 6.3.1.3 (a) and (b) show the time averaged  $|E_x|$  and  $|E_z|$  profiles at normal incidence for the  $TE_2$  guided mode with a resonant frequency of  $0.514 \times 10^{15}$  Hz at  $\varphi = 90^\circ$  and  $\varphi = 0^\circ$  in a planar microcavity structure, in which the thickness of the upper silver layer and resist waveguide medium are 56.8 nm and 300.8 nm respectively. For TE polarisation at  $\varphi = 90^\circ$  and  $\varphi = 0^\circ$  there can be no difference, and thus the  $|E_x|$  profile at  $\varphi = 90^\circ$  and  $|E_z|$  profile at  $\varphi = 0^\circ$  are identical. By contrast, in a corrugated microcavity the  $|E_x|$  field distribution for the  $TE_2$  guided mode at  $\varphi = 90^\circ$  and the  $|E_z|$  field distribution at  $\varphi = 0^\circ$ , plotted in Figure 6.3.1.3 (c) and (d), show a marked difference. For TE at  $\varphi = 0^\circ$  the incident electric field is parallel to the grating grooves while at  $\varphi = 90^\circ$  it is parallel to the grating vector. It is apparent that the locations of field maxima and minima in the y-direction in Figure 6.3.1.3 (b) and (d), in which the e-field is parallel to the grating grooves, are almost identical. This is because incident radiation polarised accordingly will penetrate the grooves of the corrugation, reflecting directly from the grating surface and giving a reflection as if from a flat interface at the mean surface position. Thus the field maxima and minima will be almost unchanged from an equivalent planar system resulting in an unchanged resonant frequency. However, when the electric field is normal to the grating grooves, a circulating field may be set up in the grooves, as shown in Figure 6.3.1.3 (c), which leads to an increase in effective mean thickness of the guiding medium (evidenced by the change in y-position of the field node). Therefore, in the microcavity structure with corrugations, for a given in-plane wave vector, the  $TE_m$  guided mode excited at  $\varphi = 90^\circ$  is always situated at a lower frequency than the same order  $TE_m$  guided mode at  $\varphi = 0^\circ$ . A similar analysis can be applied to the TM guided modes except that, due to the switch of the e-field orientation with azimuthal angle when compared to TE polarised light, the  $TM_m$  guided modes at  $\varphi = 0^\circ$  will now occur red-shifted relative to the  $TM_m$  guided modes at  $\varphi = 90^\circ$ . This is clearly evident in Figure 6.3.1.1 (b) and (d). Also note that SPP modes can be accessed by TE polarisation at  $\varphi = 90^\circ$ . By comparison with the band structure in Fig. 4, the highest frequency mode in the visible range in Figure 6.3.1.1 (c) is identified as the

SPP mode that is supported at the resist/silver interface.



**Figure 6.3.1.3** Time averaged  $|E_x|$  and  $|E_z|$  profiles for TE<sub>2</sub> guided modes at  $\theta = 0^\circ$ . (a)  $|E_x|$  profile in the planar structure at  $f = 0.514 \times 10^{15}$  Hz,  $\varphi = 90^\circ$ , (b)  $|E_z|$  profile in the planar structure at  $f = 0.514 \times 10^{15}$  Hz,  $\varphi = 0^\circ$ , (c)  $|E_x|$  profile in the microcavity structure with corrugations at  $f = 0.4295 \times 10^{15}$  Hz,  $\varphi = 90^\circ$ , and (d)  $|E_z|$  profile in the microcavity structure with corrugations at  $f = 0.5245 \times 10^{15}$  Hz,  $\varphi = 0^\circ$ . The thickness of the upper silver layer and resist waveguide medium are 56.8 nm and 300.8 nm for the planar structure.

### 6.3.2 Band-gaps and anti-crossings in the dispersion curves

In this corrugated microcavity, due to the introduction of the periodicity, all of the modes may be “reflected” at the BZ boundary, which causes crossings between the different branches. This gives rise to photonic band-gaps and flat band regions due to the interactions at these crossing points. Figure 6.3.1.1 (a) shows the TE reflectivity at  $\varphi = 0^\circ$ . In this case, the incident optical electric field is parallel to the grating grooves, and hence no SPP modes are excited. By comparing with the band structure in Figure 6.3.1.2, it is clear that only TE<sub>1</sub> and TE<sub>2</sub> guided modes can be accessed in the visible

range. At the first BZ boundary  $2k_{\parallel}/k_g = 1$ , two band-gaps are observed, with central frequencies of  $f_c \approx 0.445 \times 10^{15}$  Hz and  $f_c \approx 0.632 \times 10^{15}$  Hz. (Though these are not clear in Figure 6.3.1.2, due to the complex form of the TE and TM combined band structure, they are clearly evident in Figure 6.3.1.1). The band-gap with the lower central frequency is caused by the crossing of the unscattered  $TE_1$  guided mode and the Bragg-scattered  $TE_1$  guided mode (scattering from  $+ k_g$ ). The band gap at the higher central frequency is formed by the crossing of the unscattered  $TE_2$  mode and the Bragg-scattered  $TE_2$  guided mode (scattering from  $+ k_g$ ). This band gap formation at the first BZ boundary is well known, being caused by the formation of two standing waves.

To understand the physics of the band-gaps, it is a helpful to investigate the time averaged field distributions for the coupled guided modes. Since there are no  $E_x$  and  $E_y$  ( $x$ ,  $y$ , and  $z$  axis defined in Figure 6.3.1) components of the electric field for TE polarisation incident at  $\varphi = 0^\circ$ , we plot the  $|E_z|$  profiles at the resonant frequencies of  $0.6545 \times 10^{15}$  Hz and  $0.6125 \times 10^{15}$  Hz at polar angles  $\theta = 38.2^\circ$  and  $41.6^\circ$  in Figure 6.3.2.1 (a) and (b) respectively. Clearly we see from Figure 6.3.1.1 (a) that the two modes considered here belong to the upper and lower branch of the band gap ( $f_c \approx 0.632 \times 10^{15}$  Hz) respectively. Relative to the corrugation, the field maxima in Figure 6.3.2.1 (a) are observed to align with the peaks of the grating in contrast with Figure 6.3.2.1 (b), in which the maxima are observed to align with the troughs.

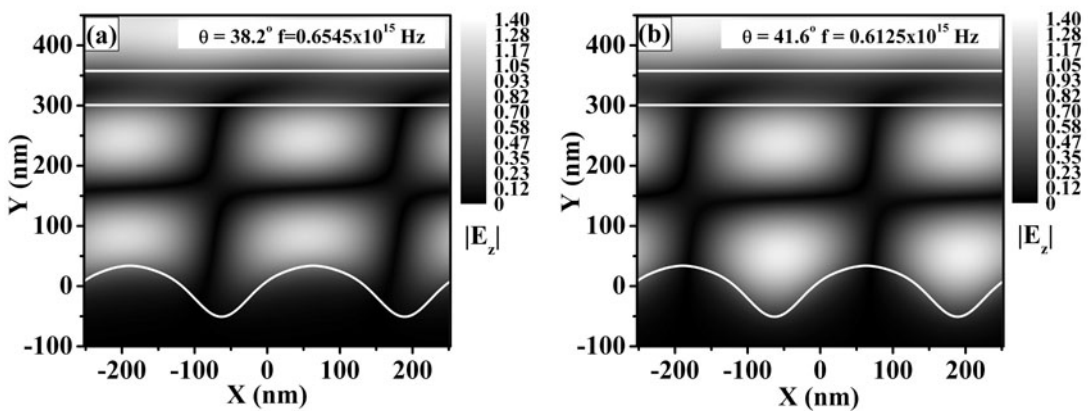


**Figure 6.3.2.1** Time averaged  $|E_z|$  profiles for TE polarization  $\varphi = 0^\circ$  at (a)  $f = 0.6545 \times 10^{15}$  Hz and  $\theta = 38.2^\circ$ , (b)  $f = 0.6125 \times 10^{15}$  Hz and  $\theta = 41.6^\circ$ . The top white solid line represents the silica/silver interface; the middle one represents the silver/resist plane interface and the bottom, corrugated, one represents the silver/resist interface.

In addition to these band-gaps at the first BZ boundary, an anti-crossing between the Bragg-scattered TE<sub>1</sub> mode (scattering from  $+ k_g$ ) and the unscattered TE<sub>2</sub> guided mode arises in the visible range within the Brillouin zone ( $2k_{\parallel}/k_g \approx 0.6$ ). The time averaged  $|E_z|$  component of field distributions are shown in Figure 6.3.2.2 for the modes around this anti-crossing at the resonant frequencies of  $0.5765 \times 10^{15}$  Hz (upper branch of the anti-crossing) and  $0.554 \times 10^{15}$  Hz (lower branch of the anti-crossing) at polar angle  $\theta = 25.0^\circ$  and azimuth angle  $\varphi = 0^\circ$ . Relative to the corrugation, in Figure 6.3.2.2 (a) the field maxima near to the silver/resist interface with corrugations are observed in the peaks and close to the silver/resist plane interface locate align the troughs in contrast with Figure 6.3.2.2 (b), in which the field maxima near to the silver/resist corrugated interface are observed in the troughs and close to the silver/resist plane interface locate align the peaks. This reveals that the anti-crossing formation within the Brillouin zone is also caused by the formation of two standing waves. Therefore, the band-gap and anti-crossing have a common explanation.

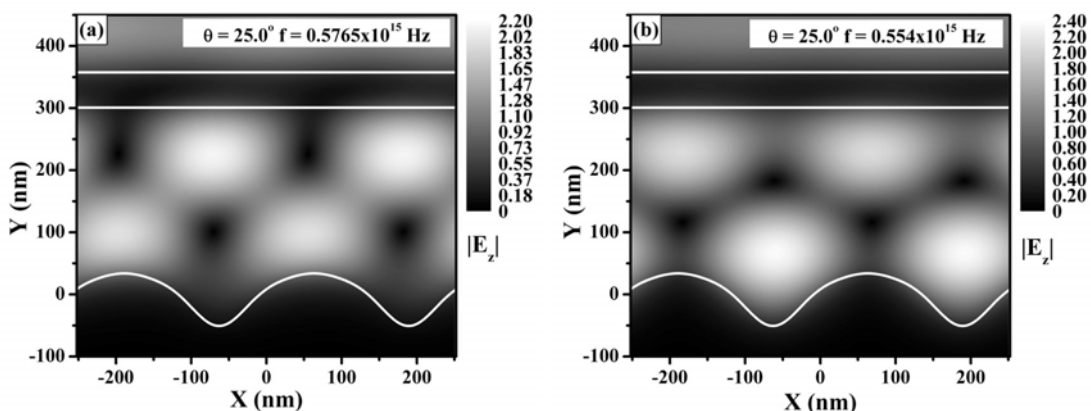


**Figure 6.3.2.2** Time averaged  $|E_z|$  profiles for TE polarization with  $\theta = 25.0^\circ$  and  $\varphi = 0^\circ$  at (a)  $f = 0.5765 \times 10^{15}$  Hz and (b)  $f = 0.554 \times 10^{15}$  Hz. The white solid lines represent the profile of the structure.

### 6.3.3 Flat photonic band with TM polarization

At an azimuthal angle of  $\varphi = 0^\circ$ , the TM polarized dispersion curve becomes more complicated, as shown in Figure 6.3.1.1 (b). The major reason is that grating coupling allows the SPP modes supported at both the resist/silver and silver/silica interfaces to be excited. Consequently, in addition to the crossings between the TM

guided modes, the scattered SPP modes may also interfere with the TM guided modes. In this section, we focus on the flat band that is readily observed in Figure 6.3.1.1 (b) and Figure 6.3.1.2.

To clearly demonstrate how the corrugation modifies the dispersion curves we have investigated the microcavity for corrugations of different amplitude. In Figure 6.3.3.1 (a) – (d), the band structure associated with the microcavity at  $\varphi = 0^\circ$ , for amplitudes of corrugation of 5 nm, 15 nm, 30 nm, and 40 nm respectively are plotted. For these calculations, the corrugation is supposed to be purely sinusoidal, the thickness of the upper silver layer is 56.8 nm, and the mean thickness of the waveguide resist medium is 300.8 nm. The TM modes in Figure 6.3.3.1(a) can be identified as being (i) the unscattered SPP at the silver/resist interface, (ii) the unscattered SPP at the silver/silica interface, (iii) the unscattered  $\text{TM}_1$  guided mode, (iv) the unscattered  $\text{TM}_2$  guided mode, (v) the Bragg-scattered SPP at the silver/resist interface, coupled via a Bragg-scatter of  $+ k_g$ , (vi) the Bragg-scattered  $\text{TM}_1$  guided mode, coupled via a Bragg-scatter of  $+ k_g$ , (vii) the Bragg-scattered SPP at the silver/silica interface, coupled via a Bragg-scatter of  $+ k_g$ , and (viii) the Bragg-scattered  $\text{TM}_2$  guided mode, coupled via a Bragg scatter of  $+ k_g$ .

Figure 6.3.3.1 (a) clearly shows that at points where the modes cross each other band-gaps and anti-crossings may be observed. We have discussed the reason for the formation of band-gaps and anti-crossings in the case of TE polarization at  $\varphi = 0^\circ$ . Here, we concentrate on the anti-crossing caused by the unscattered  $\text{TM}_2$  guided mode (mode iv) interfering with both the scattered  $\text{TM}_1$  mode (mode vi) and the scattered SPP mode (mode v). This area is indicated by the dashed line boxes in Figure 6.3.3.1. The resonant frequency at normal incidence of the flat band clearly reduces as the grating amplitude is increased. This is partly because the effective mean thickness of the guiding medium increases, as mentioned previously, such that the  $\text{TM}_2$  guided mode will be red-shifted with increasing amplitude. In addition to this the inter-mode coupling, which causes the clear anti-crossing behaviour between the  $\text{TM}_2$  guided mode and both the silver/resist SPP mode and the  $\text{TM}_1$  guided mode present at small amplitudes, becomes stronger leading to larger anti-crossing gaps. These strong anti-crossings explain the large difference between the observed dispersion of the mode on these corrugated samples with that observed for planar samples. From Figure 6.3.3.1 (d), we can clearly see that when the amplitude is increased to 40 nm, the reduction of the excitation frequency of

the TM<sub>2</sub> guided mode coupled with the anti-crossing leads to the very flat dispersion of the TM<sub>2</sub> guided mode which is situated at about  $0.4503 \times 10^{15}$  Hz.

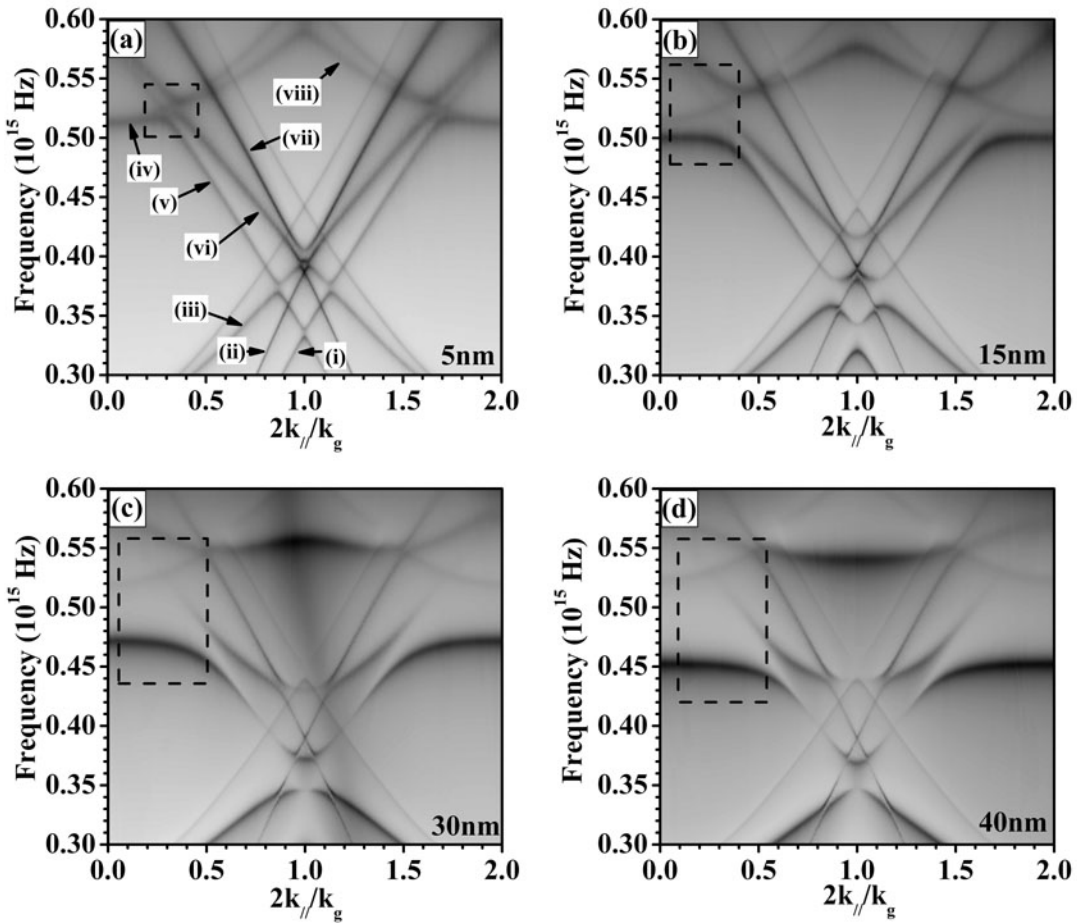


**Figure 6.3.3.1** The theoretical band predictions for the waveguide structure at  $\varphi = 0^\circ$ , with a sinusoidal grating of amplitude (a) 5 nm, (b) 15 nm, (c) 30 nm, and (d) 40 nm. The modes in (a) can be identified as (i) unscattered SPP at the silver/resist interface, (ii) unscattered SPP at the silver/silica interface, (iii) unscattered TM<sub>1</sub> guided mode, (iv) unscattered TM<sub>2</sub> guided mode, (v) scattered SPP at the silver/resist interface ( $+k_g$ ), (vi) scattered TM<sub>1</sub> guided mode ( $+k_g$ ), (vii) scattered SPP at the silver/silica interface ( $+k_g$ ), and (viii) scattered TM<sub>2</sub> guided mode ( $+k_g$ ). The dashed line box in each plot indicates the anti-crossing caused by mode iv (unscattered TM<sub>2</sub> guided mode) interfering with both mode vi (scattered TM<sub>1</sub> mode) and mode v (scattered SPP mode).

This flat photonic band is also confirmed by our experiments as shown in Figure 6.3.1.1 (b), where it is situated at  $0.43 \times 10^{15}$  Hz. By investigating the fields at near normal incidence for this resonance, shown in Figure 6.3.3.2, the mixed TM<sub>2</sub> guided mode / SPP character of the mode is clearly evident, confirming the influence of the anti-crossing on the formation of the flat band.

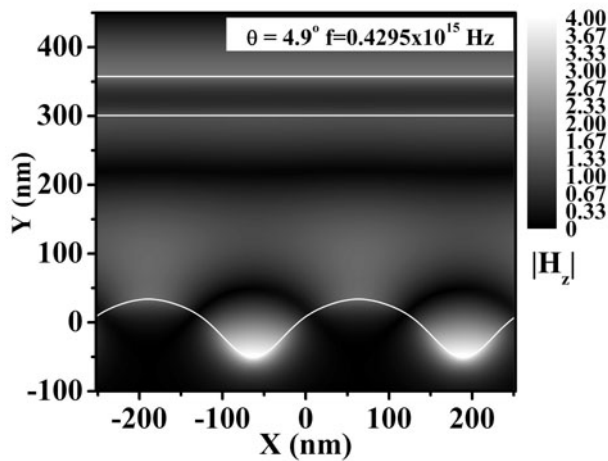


**Figure 6.3.3.2** Time averaged  $|H_z|$  profile for the mode at  $\phi = 0^\circ$  with a resonant frequency  $f = 0.4295 \times 10^{15}$  Hz and polar angle  $\theta = 4.9^\circ$ .

Also it is worth investigating further the modification of the band structure with increasing amplitude of the corrugation. In Figure 6.3.3.3, the band structures are plotted for the microcavity with amplitudes of corrugation of 60 nm, 75 nm, 100 nm, and 140 nm respectively. As shown in Figure 6.3.3.3 (a) – (c), when the amplitude is increased to 60 nm, 75 nm, and 100 nm, the  $TM_2$  guided mode has been red-shifted to  $0.425 \times 10^{15}$  Hz,  $0.405 \times 10^{15}$  Hz, and  $0.381 \times 10^{15}$  Hz (at normal incidence) respectively. Clearly the  $TM_2$  guided mode can not be considered as a flat band and has a positive gradient with increasing in-plane wave vector. However, when the amplitude is increased to 140 nm, a flat photonic band is observed again. In this case, the  $TM_2$  guided mode is situated at  $\sim 0.35 \times 10^{15}$  Hz, at which a band gap caused by interference between the scattered/unscattered  $TM_1$  guided modes is located. The  $TM_2$  guided mode may now interact with this band gap resulting in a flat photonic band.

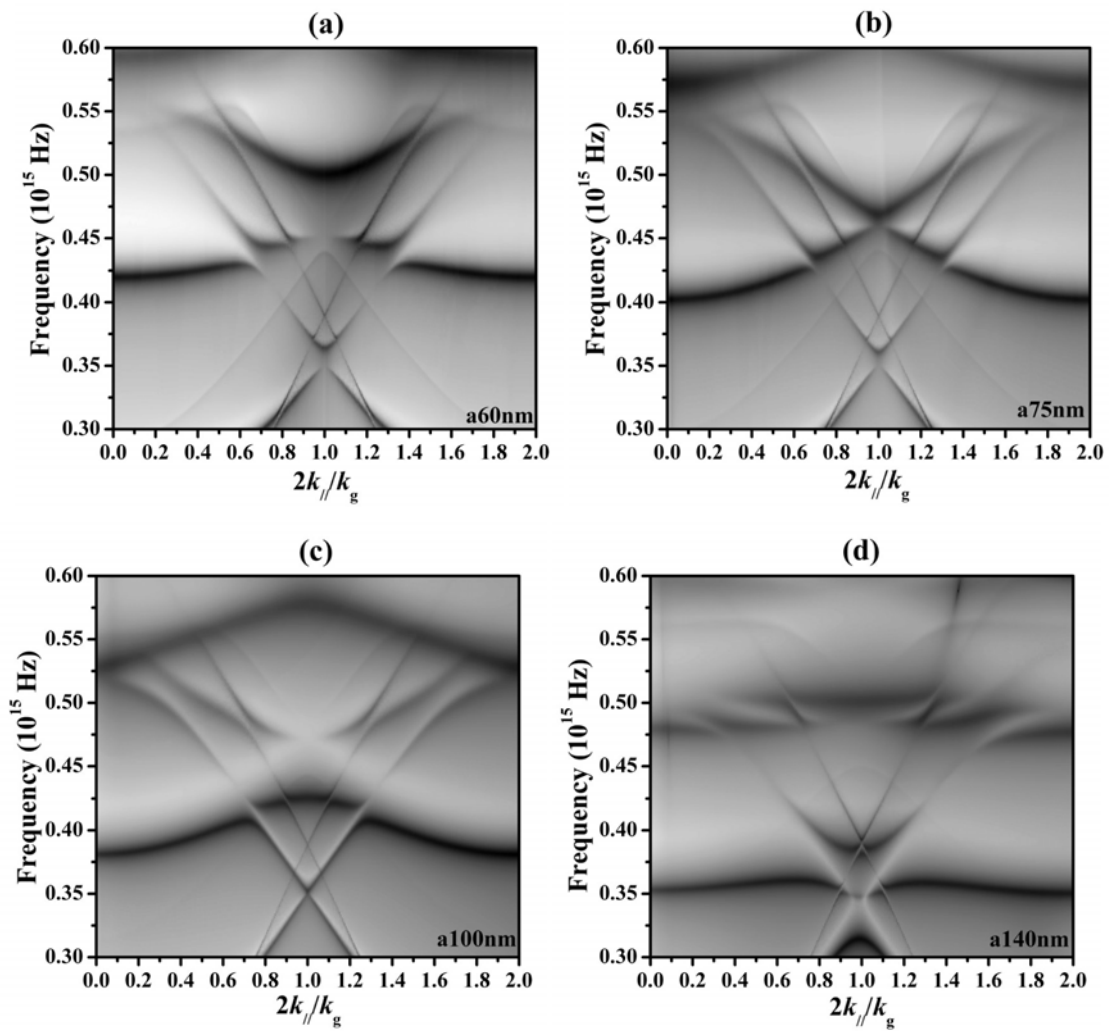


**Figure 6.3.3.3** The theoretical band predictions for the waveguide structure at  $\varphi = 0^\circ$ , with sinusoidal grating of amplitudes (a) 60 nm, (b) 75 nm, (c) 100 nm, and (d) 140 nm.

## **6.4 Summary**

The band structures and TM/TE reflectivities are theoretically investigated for a planar silver microcavity in the first section. We demonstrate that when the thickness of the photoresist waveguide medium is  $\sim 300.8$  nm only the first two waveguide modes can be accessed in the visible range. The momentum splitting of TM and TE waveguide modes are observed as each waveguide mode increases in wave vector, due to the differences in the reflectivity at the upper and lower interfaces of the waveguide for TM and TE polarization.

In the second section, the visible electromagnetic response of a silver-dielectric-silver structure in which the upper interface between the dielectric and the metal is periodically corrugated has been explored at azimuth angles of  $\varphi = 0^\circ$  and  $90^\circ$ . Reflection spectra ( $410 \leq \lambda_0 \leq 850$  nm) at both  $\varphi$  for 20 different polar angles ( $4.9^\circ \leq \theta \leq 65.0^\circ$ ) and for both TM and TE polarisation have been measured and mapped on to a plot of reflectivity as a function of frequency and in-plane wave vector. The photonic band-gaps at the Brillouin zone boundary and anti-crossings within the Brillouin zone are observed directly in the experimental dispersion curves. The presence of a flat photonic band caused by the anti-crossings between surface plasmon polaritons and waveguide modes is confirmed experimentally. It is worth noting that the resonant frequency of this flat photonic band can be designed through appropriate choice of thickness of the guide medium and the amplitude of the grating. To understand the nature of these results, the optical field distribution at the resonant frequency is explored.

In the context of emissive devices both the band-gaps at the Brillouin zone boundary and the anti-crossings within the Brillouin zone can play important roles in controlling the emission from such waveguide structures. In particular, the flat photonic bands are important for all-angle efficient enhancement in light emitting diodes and photodetectors.

# Chapter 7

## Coupled Surface Plasmon Polaritons on Thin Silver Gratings in the Classical Mount

### 7.1 Introduction

In chapter 3 and chapter 4, we investigated the surface plasmon polaritons on single interface silver gratings. In this chapter we will explore in the classical mount coupled SPP resonances on thin silver slabs with corrugations on both sides, for which SPPs may be excited on both interfaces.

As already stated on a flat metal surface, a SPP mode cannot be directly excited by incident radiation from the adjacent dielectric. In order to optically excite the SPP mode, the in-plane momentum of the incident radiation must be suitably increased. This momentum enhancement may generally be achieved by using a coupling prism as in the Otto or Kretschmann-Raether geometry, or employing a surface relief grating. In the case of grating coupling, the wave vector of the incident light is changed by the addition or subtraction of integer multiples of the grating wave vector via diffraction, making direct coupling between the SPP and radiation possible. For a sufficiently thick (optically opaque) metal film there is only one SPP mode described as the single interface SPP (SISPP) (Schoenwald *et al* [1973]).

However in the optical domain for thinner metal layers ( $< 100$  nm) bounded by dielectrics with identical dielectric functions, the SISPPs on the two interfaces are degenerate and will interfere with one another to form two coupled SPPs described as the long range SPP (LRSPP) and the short range SPP (SRSPP). Thus at the same in-plane momentum two coupled SPP modes of different frequencies will be formed which are distinguished by having different surface charge density distributions. The higher frequency LRSPP mode has an asymmetric charge distribution between the top and bottom surfaces with the electric field predominantly normal to the surface inside the

metal. Conversely, the lower frequency SRSPP has a charge distribution which is symmetric between the top and bottom surfaces with the electric field essentially parallel to the surface. Over the last thirty years, resonant coupling of incident photons to LRSPP and SRSPP modes on both planar thin metal films (Boersch *et al* [1966], Otto [1969], Sarid [1981], Stegeman *et al* [1982], and Hickernell and Sarid [1986]) and corrugated thin metal films (Inagaki *et al* [1985] and Dutta Gupta *et al* [1987]) has been the subject of several studies. Excitement in this area of optical research was rekindled by the observation of substantially enhanced optical transmission through metallic films having a periodic array of subwavelength size holes by Ebbesen and co-workers (Ebbesen *et al* [1998], Ghaemi *et al* [1998], and Kim *et al* [1999]). They found unexpectedly high transmission peaks in their spectra, which may arise due to the excitation of surface plasmons on either side of the metal film. This suggests that coupled SPP modes on this type of structure may be important. Surprisingly there are rather few detailed experimental studies of simple corrugated thin metal films. Recently, Hooper and Sambles [2004] modelled coupled SPPs on thin metal slabs corrugated on both surfaces, where the corrugations on each side had the same pitch, 400 nm, a fundamental harmonic ( $k_g$ ) amplitude of 10 nm, and a first harmonic ( $2k_g$ ) component of 5 nm (using a sin wave Fourier series representation this was 90° out of phase with the  $k_g$  component). They reported a rather interesting evolution of the SISPP as the metal film was made thinner with the band gap formed from the two standing wave SISPPs apparently moving away from the Brillouin zone centre and becoming an anti-crossing between the SRSPP and LRSPP modes. They noted that the LRSPP and SRSPP evolve directly from the high and low-energy branches of the SISPP band gap modes.

In the first section of this chapter, the coupled SPP resonances of a planar silver slab bounded with media having silica index are investigated by using a coupling prism in the Otto geometry. In the second section we shall experimentally and theoretically study the two coupled SPPs (the SRSPP and the LRSPP) on a thin symmetrically surrounded silver grating in the visible range, particularly noting that a band gap appears within the Brillouin zone, formed by the anti-crossing of the LRSPP scattered by  $+k_g$  and the SRSPP scattered by  $-k_g$ . We will show that the  $2k_g$  component in the grating profile is the key factor leading to the appearance of this band gap.

## 7.2 SRSPP and LRSPP on Planar Silver Slabs

In this section, we shall consider an optically thin silver slab bounded by dielectrics with identical dielectric functions. The optical properties of such a structure are investigated theoretically. The geometry and coordinate system under study is shown in Figure 7.2.1, where  $t$  is the thickness of the silica gap (refractive index  $n_2 = 1.5$ ),  $d$  is the thickness of the silver film, and  $\theta$  is the polar angle. A dielectric prism with a refractive index of  $n_3 = 2.5$  is optically attached to the top surface of the silica gap to create the Otto geometry.

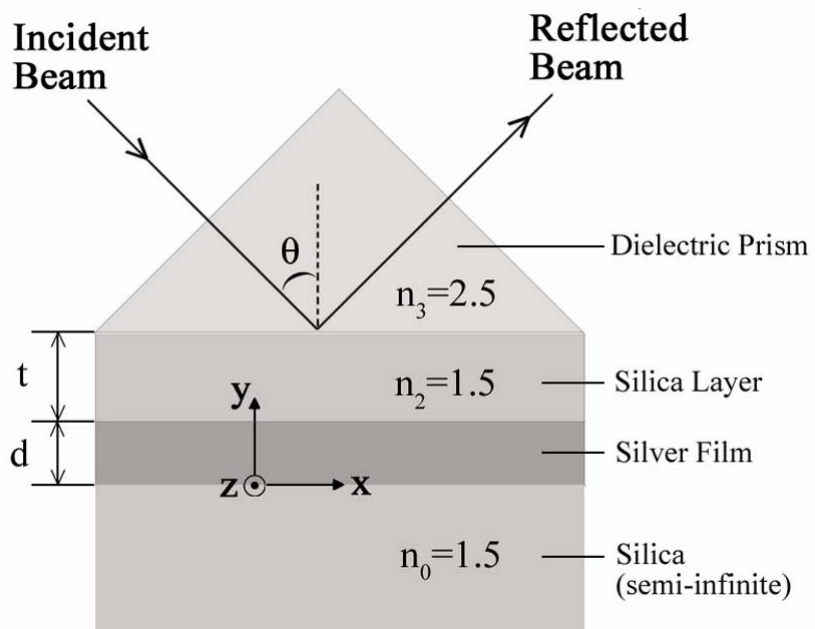


**Figure 7.2.1** Schematic diagram illustrating the geometry and coordinate system. Here  $t$  is the thickness of the silica layer,  $d$  is the thickness of the silver film, and  $\theta$  is the polar angle. A dielectric prism with refractive index of 2.5 is optically attached to the top surface of the silica layer. The position  $y = 0$  corresponds to the bottom silver/silica interface.

To more clearly demonstrate the formation of coupled SPPs of thin silver slabs, numerically modelled reflectivity as a function of incident angles ( $35^\circ \leq \theta \leq 45^\circ$ ) and thickness of silver film ( $0 \leq d \leq 150$  nm) for TM polarized incident light with a fixed frequency  $f = 0.501 \times 10^{15}$  Hz is shown in Figure 7.2.2 (a). In this calculation the

permittivities of the silver are described by  $\epsilon_r = -16.6$  and  $\epsilon_i = 0.4$ . The thickness of the silica gap is set to  $t = 440$  nm. As shown in Figure 7.2.2 (a), the dispersion relation of coupled SPPs on a planar silver slab clearly involves a splitting of the single planar interface SPP dispersion curve into two separate dispersion curves, with the LRSPP curve shifted down in incident angles (for a given frequency of incident radiation), and the SRSPP curve shifted up in incident angles (for a given frequency of incident radiation). The size of the splitting between the LRSPP and SRSPP is predominantly determined by the thickness of the silver film.

Also plotted in Figure 7.2.2 (b) is the TM polarized angle-scan reflectivity for thicknesses of the silver film of  $d = 140$  nm and  $40$  nm. At the larger silver film thickness  $d = 140$  nm, the two branches of the coupled SPPs converge to the incident angle at which the SPP would occur on a single silica/silver interface. Each of these two SPPs has an evanescent wave extending both into the dielectric medium and into the metal film. Due to the thickness of the silver film the evanescent waves inside the metal that belong to the two SPPs do not significantly overlap. As the film thickness decreases, the evanescent waves of the otherwise decoupled modes begin to overlap, and a transverse standing wave is established. The degenerate SPP mode therefore splits into one symmetrical (SRSPP) and one antisymmetrical (LRSPP) mode, as shown in Figure 7.2.2 (b) for  $d = 40$  nm.

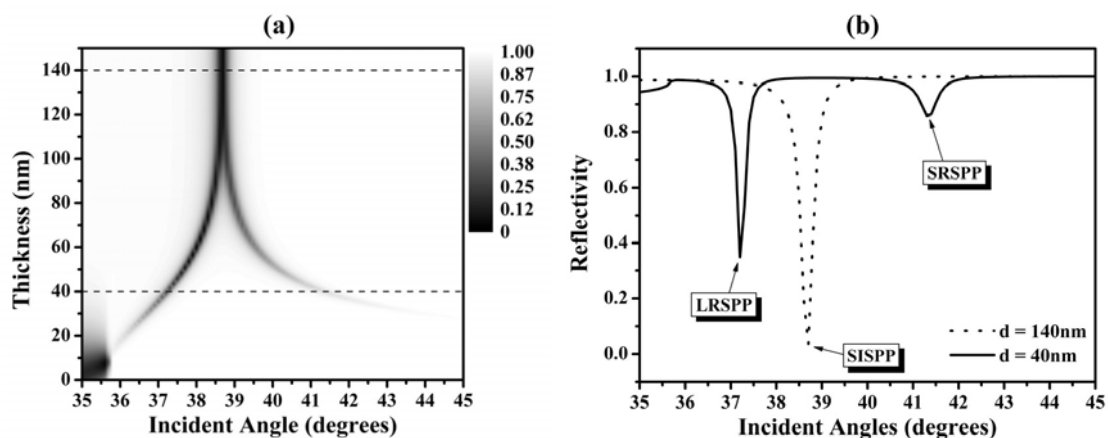


**Figure 7.2.2** (a) TM polarized reflectivity as a function of thickness of silver film and incident angles for incident light with a fixed frequency  $f = 0.501 \times 10^{15}$  Hz and the thickness of silica gap  $t = 440$  nm. (b) TM polarized angle-scan reflectivity for thicknesses of silver film  $d = 40$  nm and  $140$  nm at a fixed frequency

$$f = 0.501 \times 10^{15} \text{ Hz.}$$

These two SPPs have different charge distributions which are schematically shown in Figure 7.2.3. The long range SPP has a charge distribution which is anti-symmetric between the top and bottom surfaces (in other words if there is a positive/negative charge density on the top surface there is a corresponding negative/positive charge density on the bottom surface), as shown in Figure 7.2.3 (a). Conversely, as shown in Figure 7.2.3 (b) the short range SPP has a charge distribution which is symmetric between the top and bottom surfaces (a positive/negative charge density on the top surface has a corresponding positive/negative charge density on the bottom surface).

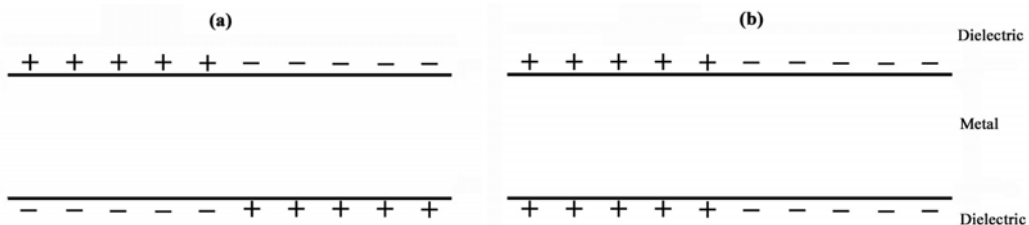


**Figure 7.2.3** Schematics showing the charge distributions for (a) the LRSPP, and (b) the SRSPP.

Due to the different surface charge density distributions, the two coupled modes have different field distributions associated with each mode, and therefore have different level of damping. The damping difference between the LRSPP and the SRSPP means that their propagation distances increase and decrease, respectively, as the film thickness decreases. The instantaneous  $E_x(y)$  (parallel to the silver film) and  $E_y(y)$  (perpendicular to the silver film) components of the electric field distributions of the two modes for the silver film with a thickness of  $d = 40$  nm are shown in Figure 7.2.4. Note that for the LRSPP as shown in Figure 7.2.4 (a), at about the center of the film the  $E_x$  component of the field has a value of zero, while in Figure 7.2.4 (b) for the SRSPP the  $E_y$  component of the field has a value of zero. It is also clear that the LRSPP has a lower proportion of its fields within the metal film than has the SRSPP, and hence the attenuation of the LRSPP is lower than that of the SRSPP. As the film thickness is decreased the proportion of the fields within the metal film is further diminished, leading to a LRSPP with an increased propagation range.

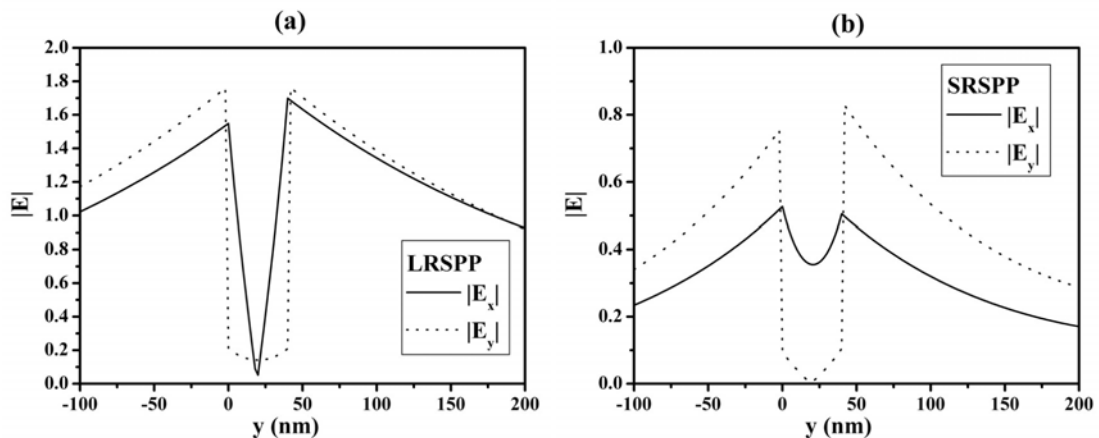


**Figure 7.2.4** Instantaneous electric field profiles for the (a) LRSPP and (b) SRSPP.  $E_x$  and  $E_y$  ( $x$  and  $y$  defined in Figure 7.2.1) are parallel and perpendicular components respectively. The silver film locates between  $y = 0$  and  $y = 40$  nm.

### 7.3 Coupled SPPs on Thin Silver Gratings in the Classical Mount

In the previous section we have investigated two coupled SPP modes, the SRSPP and the LRSPP, on a planar silver film bounded with identical silica media using prism coupling. In this section, we shall consider the LRSPP and SRSPP excited with grating coupling on a thin silver grating.

Figure 7.3.1 shows the geometry of the thin silver grating bounded with identical silica media, and the associated coordinate system used in this study. In this section we only consider the case for TM polarized incident radiation with the sample in the “classical” mount, grating grooves oriented perpendicular to the plane of incidence. The profile describing the thin silver grating is given by  $[y_1(x) = a_0\sin(k_gx) + a_1\sin(2k_gx + \phi)]$  for the lower silver-silica interface and  $[y_2(x) = a_0\sin(k_gx) + a_1\sin(2k_gx + \phi) + d]$  for the upper silver-silica interface. Here  $d$  is the mean thickness between the two surfaces,  $\phi$  is the phase shift between the  $2k_g$  component and the  $k_g$  component,  $a_0$  and  $a_1$  are the amplitudes of the  $k_g$  and  $2k_g$  components with  $k_g = 2\pi/\lambda_g$  ( $\lambda_g$  is the grating pitch) the grating vector, which runs parallel to the  $x$  axis.

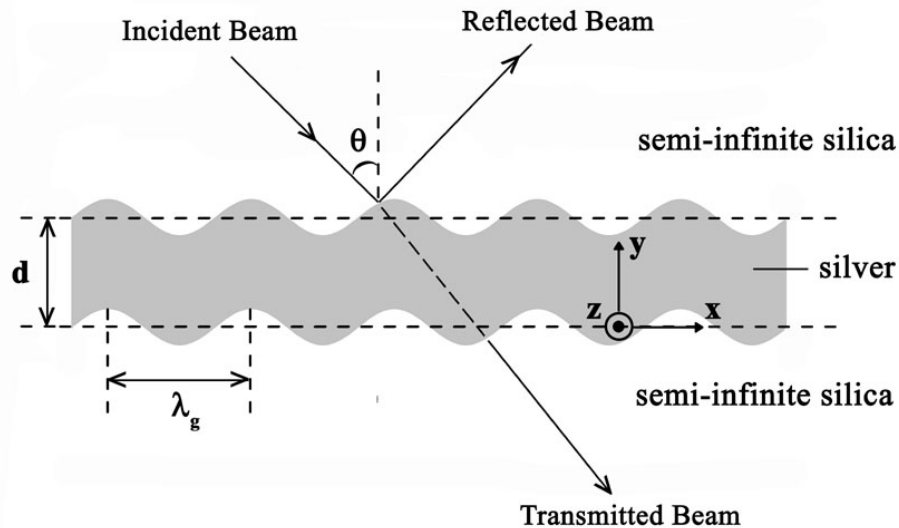


**Figure 7.3.1** Schematic diagram illustrating the sample, coordinate system, and experimental geometry used in this work. Here  $\lambda_g$  is the grating pitch,  $d$  is the thickness of the silver layer, and  $\theta$  is the polar angle. The silver layer is bounded with identical silica media.

Firstly we shall consider the simplest case of a thin silver grating with the profile having only a fundamental harmonic (pure sinusoidal profile). Figure 7.3.2 shows the modelled zeroth order reflection ( $R$ ), transmission ( $T$ ), and absorption ( $A = 1 - R - T$ ) as a function of frequency and film thickness for normal incidence ( $\theta = 0^\circ$ ) on a silver film with conformal sinusoidal corrugations (fundamental amplitude  $a_0 = 20$  nm and pitch  $\lambda_g = 335$  nm) on both sides in the classical mount. In the calculations of this section, for the silver across the visible spectrum both the real and imaginary parts of its permittivity are described by polynomials,

$$\varepsilon_r(\omega) = -255.3185 + 198.63\omega - 60.794\omega^2 + 8.381\omega^3 - 0.43004\omega^4,$$

$$\varepsilon_i(\omega) = 83.2575 - 132.79\omega + 90.474\omega^2 - 32.88\omega^3 + 6.6591\omega^4 - 0.70893\omega^5 + 0.030913\omega^6,$$

where  $\omega = 2\pi c/\lambda$  ( $10^{-15}$  s $^{-1}$ ).

It is clear from Figure 7.3.2 that the size of the splitting between the LRSPP and SRSPP is predominantly determined by the thickness of the silver film. At large film thickness the two branches of the coupled SPPs converge to the frequency at which the SPP would occur on a single interface silver grating of the same parameters. However, as the film thickness is decreased the LRSPP approaches the diffracted order light line ( $f = 0.609 \times 10^{15}$  Hz) asymptotically, and the SRSPP reduces in frequency and rapidly

approaches 0 for very thin silver films. Note in the small thickness region the second order SRSPP is readily observed.

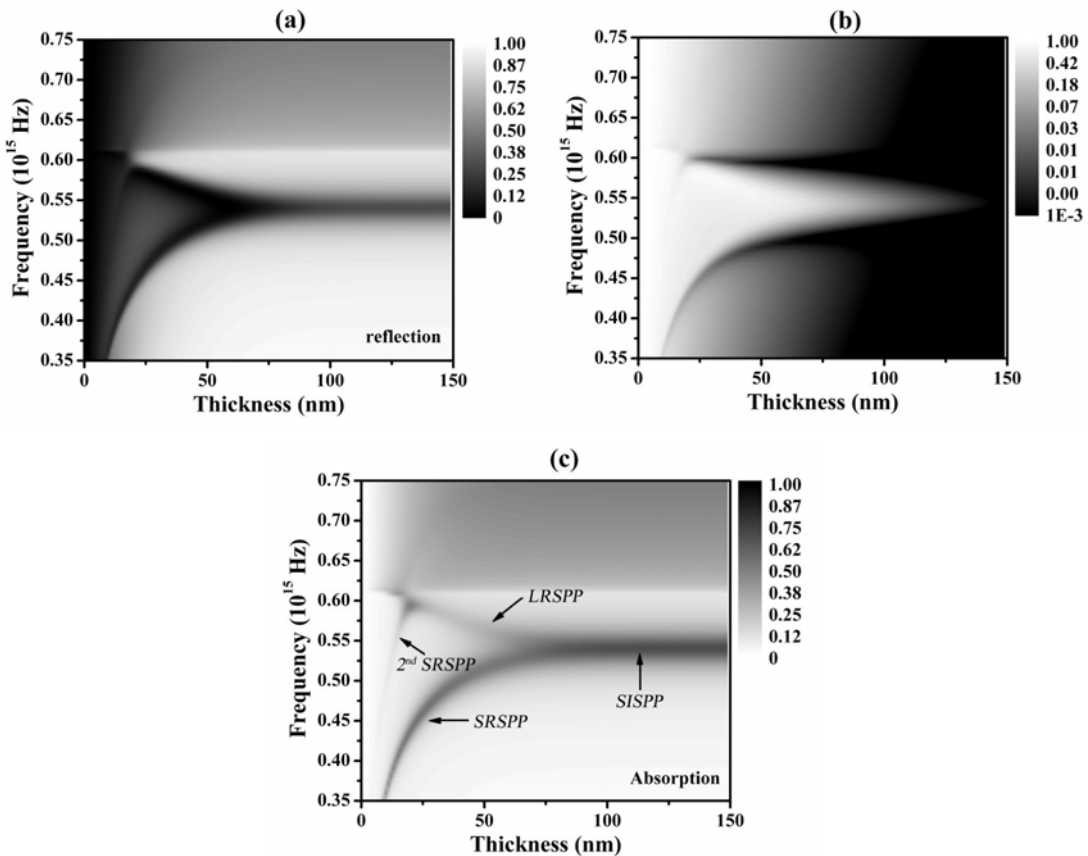


**Figure 7.3.2** The optical response, (a) reflection, (b) transmission (log scale), and (c) absorption as a function of frequency and silver film thickness at normal incidence for a silver film with conformal sinusoidal corrugations (fundamental amplitude  $a_0 = 20$  nm and pitch  $\lambda_g = 335$  nm) on both sides in the classical mount.

It is well known that in reflection the singly-diffracted SPP modes of a single metal grating produce reflectivity minima in the zero order beam, since the re-radiated light is in anti-phase with the specularly reflected light (Raether [1988]). With light incident on one surface, because of the attenuation through the film, any re-radiated SPP light scattering from the other surface is much weaker than that re-radiated from the first surface, and so both the SRSPP and LRSPP are still seen as reflectivity minima, as shown in Figure 7.3.2 (a). In transmission, the resultant zeroth order transmitted fields will be predominantly due to scattering from the bottom surface, and the charge distributions for the LRSPP and SRSPP are  $\pi$  out of phase with each other. Therefore

the two modes will show the opposite features in the zeroth order transmission, as shown in Figure 7.3.2 (b). The SRSPP shows a transmission minimum followed by a maximum, while the LRSPP shows a transmission maximum followed by a minimum. This implies that the phase of the re-radiated light is approximately  $+\pi/2$  out of phase with the directly transmitted light in the case of the LRSPP, and  $-\pi/2$  in the case of the SRSPP. Also note that in Figure 7.3.2 (c) the absorption of the two coupled SPP modes are similar to each other, except that the absorption due to the SRSPP for thinner silver film is slightly higher than that of the LRSPP.

We shall now consider experimentally and theoretically the more complicated case of adding a higher harmonic to the grating profile. The experimental sample is prepared by first depositing by thermal evaporation a 27 nm silver film onto a silica grating formed by optical lithography which has a  $2k_g$  component in addition to the fundamental  $k_g$  component with a pitch of  $\lambda_g = 335$  nm (for details of fabricating the silica grating and introducing higher harmonics refer to chapter 2). This structure is then made into an optically symmetric system by the use of index matching fluid to couple two silica prisms symmetrically to the silver grating. This forms an optically symmetric silver grating with respect to the silica medium. The geometry of the sample and associated coordinate system has already been shown in Figure 7.3.1. For clarity, we label the silica prism attached to the silica substrate the 1<sup>st</sup> prism and the other attached to the silver the 2<sup>nd</sup> prism. For an unblazed grating, as here, the phase shift  $\phi$  between the  $2k_g$  component and the  $k_g$  component must be  $\pm \pi/2$ . Then, dependent on from which side the radiation is incident, both the cases of  $\phi = +\pi/2$  and  $\phi = -\pi/2$  may be explored.

As discussed above both the SRSPP and LRSPP are seen as reflection minima in the reflectivity spectra. Hence, by measuring the reflectivity data as a function of wavelength ( $450 \leq \lambda_0 \leq 800$  nm) at various fixed polar angles and noting all the reflectivity minima, the dispersion diagram of the SPP modes associated with the structure is acquired.

Figure 7.3.3 illustrates the typical wavelength-dependent absolute reflectivity data together with the modelling results for light incident from the 1<sup>st</sup> prism and 2<sup>nd</sup> prism respectively at polar angles of  $\theta = 6.2^\circ$  and  $24.96^\circ$ . The theoretical method employed here is based upon a conical version of the differential formalism originally developed by Chandeson *et al* (1982). Both the real and imaginary parts of the

permittivity of the silver are described by polynomials given above. These polynomials inevitably pertain to somewhat different silver to that explored here in thin film form, but they are a good enough approximation to allow adequate modelling. Because of this and for simplicity in fitting data to a model the refractive index of the bounding silica is treated as non-dispersive with  $n = 1.459$ .

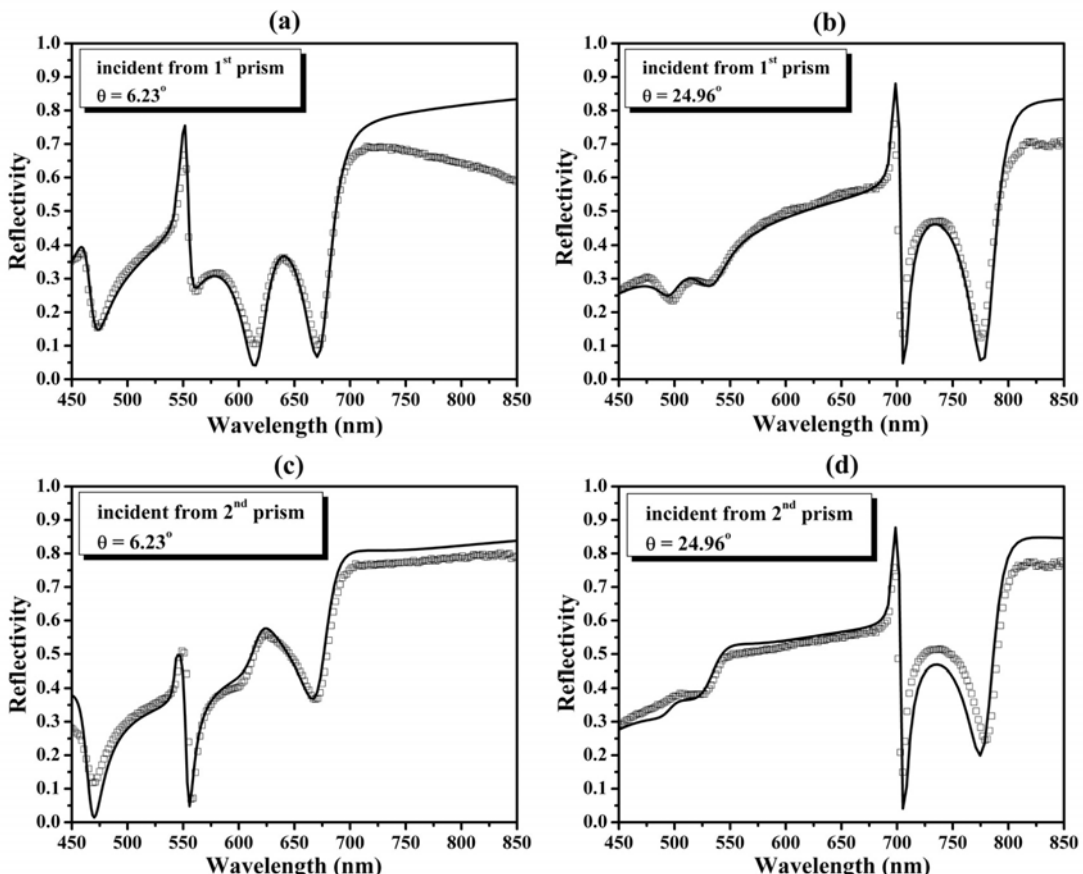


**Figure 7.3.3** Typical wavelength-dependent absolute reflectivity data (open squares) together with the model fits (solid lines) when the light is incident from the 1<sup>st</sup> prism with a  $+\pi/2$  phase shift between the first harmonic and the fundamental at polar angle (a)  $\theta = 6.2^\circ$  and (b)  $\theta = 25.0^\circ$ , and from the 2<sup>nd</sup> prism with  $-\pi/2$  phase shift at polar angle (c)  $\theta = 6.2^\circ$  and (d)  $\theta = 25.0^\circ$ . The density of experimental data points has been reduced for clarity.

In Figure 7.3.3 (a) and (b) (incident from the 1<sup>st</sup> prism), the best comparison between the model and the experimental data is achieved when the profiles of the two surfaces are set to  $[20 \sin(k_g x) + 5 \sin(2k_g x + \pi/2) + 27]$  nm for the incident interface and  $[20 \sin(k_g x) + 5 \sin(2k_g x + \pi/2)]$  nm for the transmitting interface. When the light is incident from the 2<sup>nd</sup> prism the phase shift  $\phi$  between the  $2k_g$  and  $k_g$  components

changes sign from  $+\pi/2$  to  $-\pi/2$ . Then using the profiles described as  $[20 \sin(k_g x) + 5 \sin(2k_g x - \pi/2) + 27]$  nm for the incident interface and  $[20 \sin(k_g x) + 5 \sin(2k_g x - \pi/2)]$  nm for the transmitting interface the theoretical modelling also agrees well with the experimental reflectivity data as shown in Figure 7.3.3 (c) and (d).

For grating structures, due to the introduction of the periodicity, all of the modes in momentum space are “reflected” at the Brillouin zone (BZ) boundary (Bragg scattering) resulting in crossing points between the different branches. Figure 7.3.4 shows the model band structures computed by inspection of the scattering matrices of the systems in the classical mount over a range of frequencies and in-plane wave vectors ( $k_x$ ) for silver gratings of different profiles. The profiles describing the structures in Figure 7.3.4 (a) – (d) are: (a)  $[20 \sin(k_g x)]$  nm, (b)  $[20 \sin(k_g x) + 5 \sin(2k_g x + \pi/2)]$  nm, (c)  $[20 \sin(k_g x)]$  nm for the bottom surface and  $[20 \sin(k_g x) + 27]$  nm for the top surface, and (d)  $[20 \sin(k_g x) + 5 \sin(2k_g x + \pi/2)]$  nm for the bottom surface and  $[20 \sin(k_g x) + 5 \sin(2k_g x + \pi/2) + 27]$  nm for the top surface. In this work the focus of interest is the crossing points that arise through scattering of one wave by  $-k_g$  and the other by  $+k_g$ . At these crossing points it is the  $2k_g$  component of the profile which plays the primary role in producing any band gap. Second order scattering from the  $k_g$  component can also have a similar effect, however, this second order process is very weak for the small amplitudes of the primary component used here and need not be considered in the present study.

As shown in Fig. 7.3.4 (a) and (b), the self-crossing point which arises from scattering by  $\pm k_g$  only occurs at  $k_x = 0$  (normal incidence). For a pure sinusoidal profile thick grating of the amplitude used here there is no significant splitting at this crossing point as shown by the absence of a band gap in Figure 7.3.4 (a). However if a  $2k_g$  component is added to the profile, a band gap is observed at this crossing point as shown in Figure 7.3.4 (b). The different energy SISPPs at the band edges are associated with the different positions of the surface charge density maxima (and hence optical field density distributions) with respect to the  $2k_g$  component of the grating profile. The extrema of both the normal field component and the surface charge distribution for the higher energy SISPP mode occur at the troughs of the  $2k_g$  component, whereas for the lower energy SISPP mode they are located at the peaks of the  $2k_g$  component.

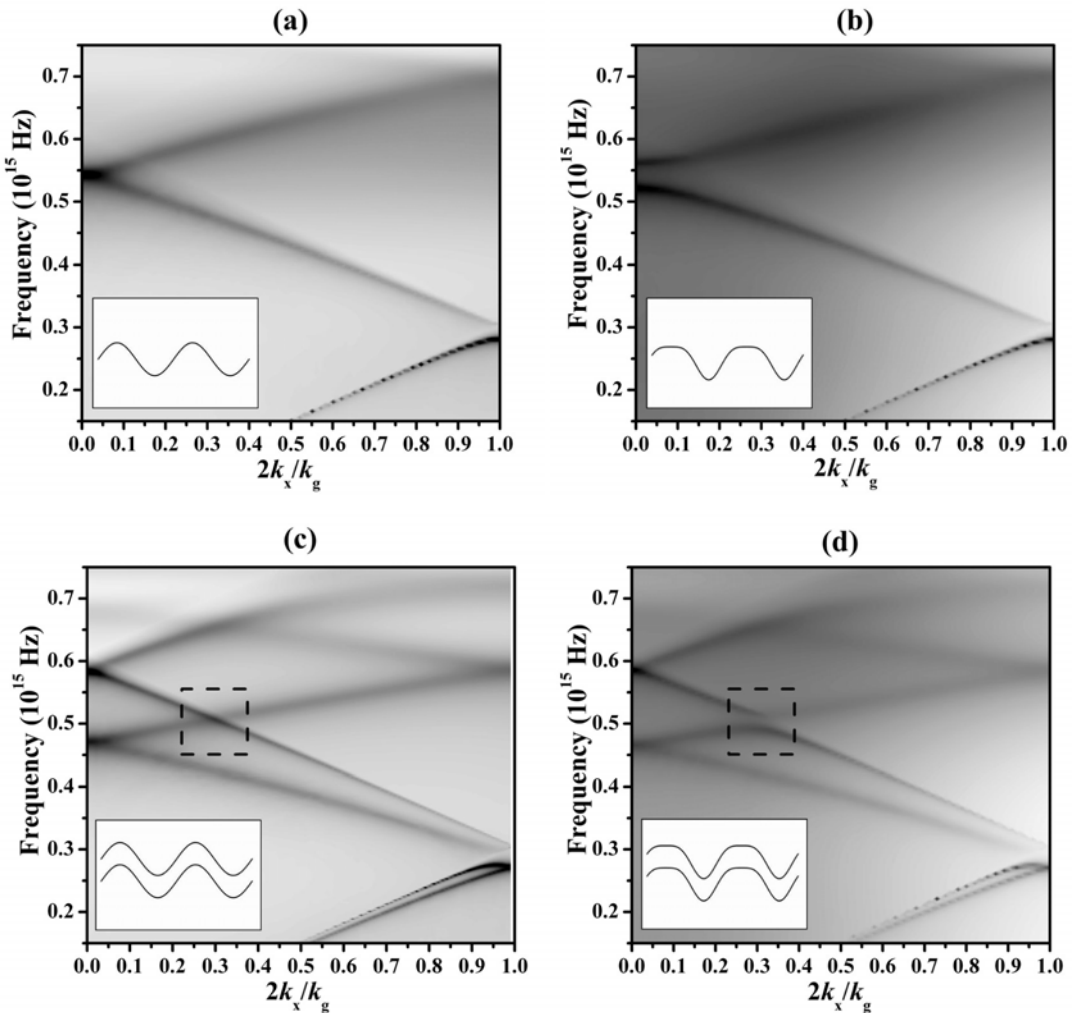


**Figure 7.3.4** The model band structures for silver gratings having different profiles in the classical mount.

The profile describing the structures is given by (a)  $[20 \sin(k_g x)]$  nm, and (b)  $[20 \sin(k_g x) + 5 \sin(2k_g x + \pi/2)]$  nm, and (c)  $[20 \sin(k_g x)]$  nm for the bottom surface and  $[20 \sin(k_g x) + 27]$  nm for the top surface, and (d)  $[20 \sin(k_g x) + 5 \sin(2k_g x + \pi/2)]$  nm for the bottom surface and  $[20 \sin(k_g x) + 5 \sin(2k_g x + \pi/2) + 27]$  nm for top surface. The inset graphs correspond to the gratings that have been used in the calculations.

The dashed line box in the last two graphs indicates the crossing point that arises from scattering of the

LRSPP by  $+k_g$  and scattering of the SRSPP by  $-k_g$ .

In the case of a thin film corrugated on both sides, the SISPP will split into two coupled LRSPP and SRSPP modes and both of these might then be expected to be scattered by the  $2k_g$  component, forming band gaps. As shown in Figure 7.3.4 (c) and (d), there are two crossing points at  $k_x = 0$ , one arises from the scattering of SRSPPs (at lower frequency) by  $\pm k_g$ , while the other (at higher frequency) arises from the scattering of LRSPPs. In addition to the self-crossing points, an additional third crossing point occurs in the BZ between  $k_x = 0$  and  $k_x = k_g/2$ , as indicated by the dashed line box in

Figure 7.3.4 (c) and (d). This arises from scattering of the LRSPP by  $+k_g$  and scattering of the SRSPP by  $-k_g$ . In Figure 7.3.4 (c), because there is no  $2k_g$  component there is no significant splitting at the crossing points. By contrast, as already indicated, when the  $2k_g$  component is finite one expects band gaps to open up. Figure 7.3.4 (d) clearly shows that at the third crossing point an anti-crossing occurs, while at the two self-crossing points at  $k_x = 0$  no similar band gap appears, in stark contrast to Figure 7.3.4 (b). This is somewhat surprising. Later in this chapter, we will discuss the splitting of the third crossing point and explain the reason for the lack of band gaps at the two self-crossing points (occurring at  $k_x = 0$ ) even when there is a  $2k_g$  component present in the structure.

In addition to the wavelength dependent absolute reflectivity data taken at polar angle  $\theta = 6.2^\circ$  and  $25.0^\circ$  as shown in Figure 7.3.3, reflectivity data was also taken at 11 other polar angles ( $\theta = 5.2^\circ, 5.5^\circ, 7.0^\circ, 7.8^\circ, 8.6^\circ, 9.5^\circ, 10.4^\circ, 11.3^\circ, 12.3^\circ, 13.3^\circ$ , and  $18.9^\circ$ ) for both  $\phi = +\pi/2$  and  $\phi = -\pi/2$ . Figure 7.3.5 shows the model reflectivity as a function of frequency and in-plane wave vector, with the experimental data (corresponding to the positions of the reflection minima) indicated as open white squares mapped onto this plot.

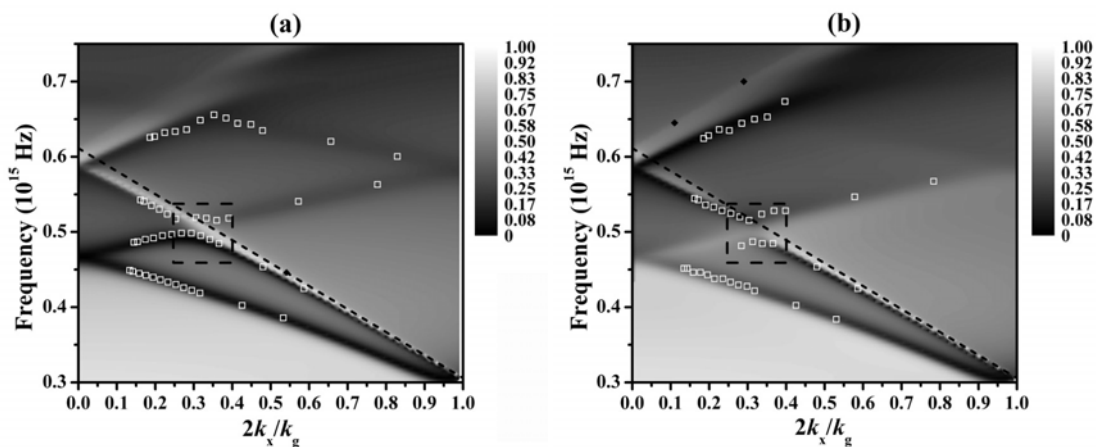


**Figure 7.3.5** The model TM reflectivity as a function of frequency and in-plane wave vector with light incident from (a) the 1<sup>st</sup> prism and (b) the 2<sup>nd</sup> prism. The open white squares are the mapped reflection dips that are taken from the experimental reflectivity spectra. The dashed straight line indicates the first order diffracted light line. The dashed line box indicates the crossing point between the LRSPP and the SRSPP.

The anti-crossing between the LRSPP and the SRSPP that occurs at  $2k_x/k_g \approx 0.29$  is confirmed directly by the experimental data, as indicated by the dashed line boxes in Figure 7.3.5 (a) and (b). As expected the LRSPP has approached the diffracted order light line, while the SRSPP has reduced in frequency with reduction in film thickness. These two effects are observed in Figure 7.3.5 with the first order LRSPP modes (scattering from  $+k_g$ ) being close to the diffracted light line (indicated as a dashed straight line) and the first order SRSPP modes being further away from the diffracted light line.

We now turn our attention to the physics of the three crossing points mentioned previously. The lack of band gaps at the crossings of the forward and backward propagating LRSPPs and SRSPPs at normal incidence is a special case and will be discussed in detail later. The anti-crossing behaviour evident when the LRSPP and SRSPP cross at finite  $k_x$  on the other hand is readily understandable. Typically, when any two modes of appropriate symmetry cross each other anti-crossing behaviour is likely since the interaction strength between the two modes, caused by their field overlap, is rarely zero. Thus it is not surprising that an interaction, and hence a band gap is evident in this case.

An explanation of the lack of band gaps at the crossings of the forward and backward propagating LRSPPs and SRSPPs at  $k_x = 0$  is however somewhat more complicated. In this case it is helpful to investigate the time averaged  $|H_z|$  component of the field distributions and the instantaneous  $E_{xy}$  vector fields for these two coupled SPP modes. In Figure 7.3.6 we plot the  $|H_z|$  profiles together with the instantaneous  $E_{xy}$  vector fields of the SRSPP ( $f = 0.467 \times 10^{15}$  Hz) and the LRSPP ( $f = 0.579 \times 10^{15}$  Hz) modes excited at normal incidence ( $\theta = 0^\circ$ ) on the structure as described for Figure 7.3.5 (a) (incident from the 1<sup>st</sup> prism with  $\phi = +\pi/2$ ). First note the different surface charge density distributions for the SRSPP and the LRSPP. As shown in Figure 7.3.6 (c), for the SRSPP, the spatial variation of the surface charge density distribution along the bottom surface is in phase with that on the top surface (symmetric distribution), while for the LRSPP in Figure 7.3.6 (d), the bottom surface has the opposite surface charge density to the top surface. Also note that, as shown in Figure 7.3.6 (a) and (b), the  $|H_z|$  component has a region of zero-value inside the thin metal film for the SRSPP while there is no such region for the LRSPP.

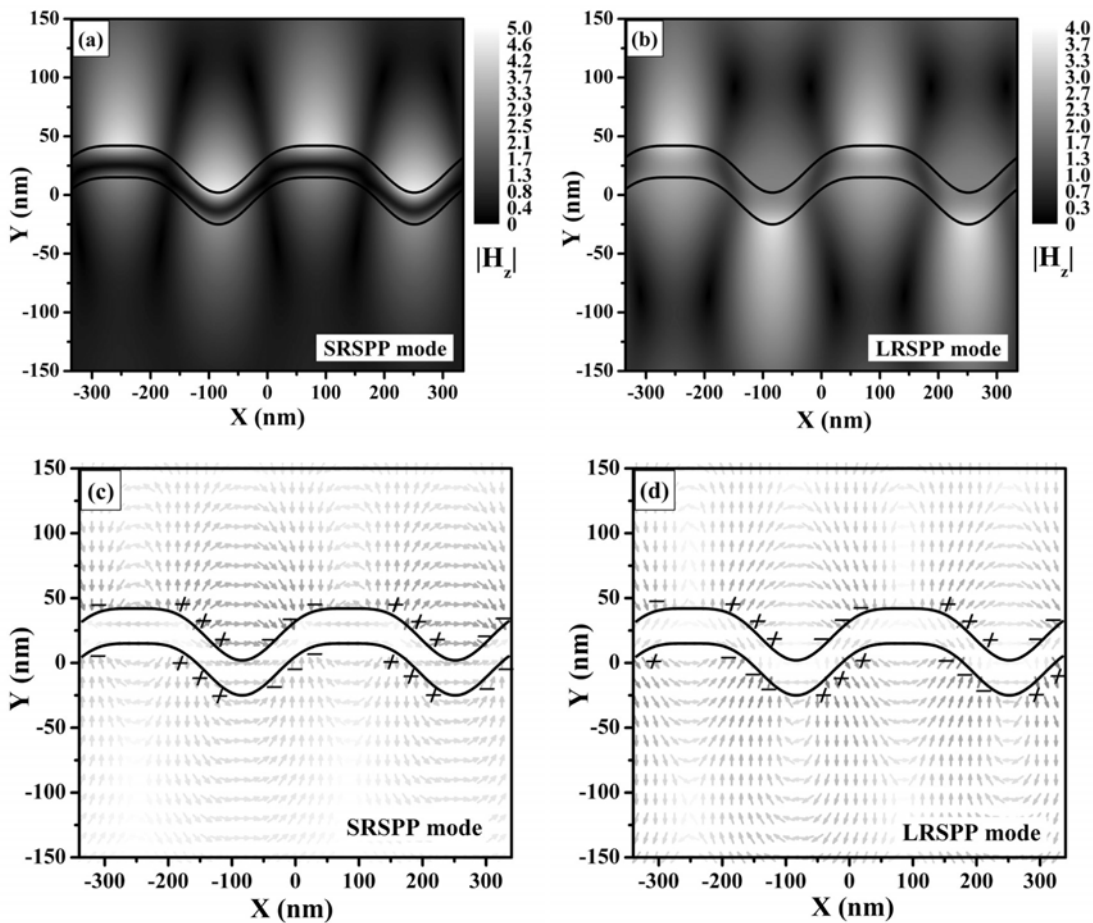


**Figure 7.3.6** Time averaged  $|H_z|$  component of the fields of (a) the SRSPP and (b) the LRSPP modes that can be excited at normal incidence, together with the instantaneous  $E_{xy}$  vector fields for (c) the SRSPP and (d) the LRSPP modes on the same structure as described in Figure 7.3.4(a) (incident from the 1<sup>st</sup> prism with the phase shift  $\phi = +\pi/2$ ). The continuous black lines represent the thin metal grating.

By comparing Figure 7.3.6 (c) and (d), we can also see that the maximum surface charge density for both the SRSPP and the LRSPP occur on the sides of the grating grooves. This is because at normal incidence there will be no component of the electric field normal to the surface where the surface has zero gradient, hence only the modes with surface charge density maxima on the sides of the grating grooves may couple to the incident light. The key issue here is then the position of these surface charge density maxima relative to the  $2k_g$  component of the grating. We know that for a single interface grating, the  $2k_g$  component opens up a band gap where the modes cross each other, with the higher energy ( $\omega^+$ ) band edge having its surface charge density maxima at the troughs of the  $2k_g$  component, and the lower energy ( $\omega^-$ ) band edge having its surface charge density maxima located at the peaks of the  $2k_g$  component.

Now we should consider the role that the  $2k_g$  component plays in the thin metal grating structure at normal incidence. As mentioned above, at  $k_x = 0$  there are two self-crossing points caused by two LRSPP modes and two SRSPP modes respectively.

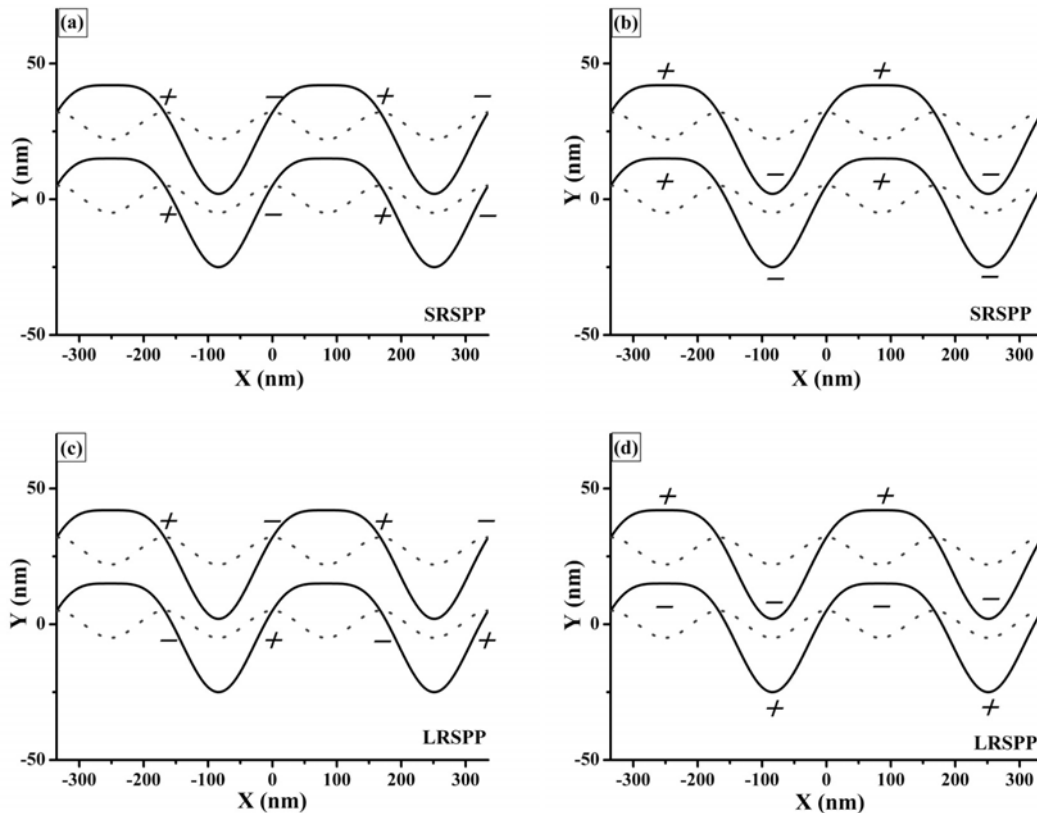
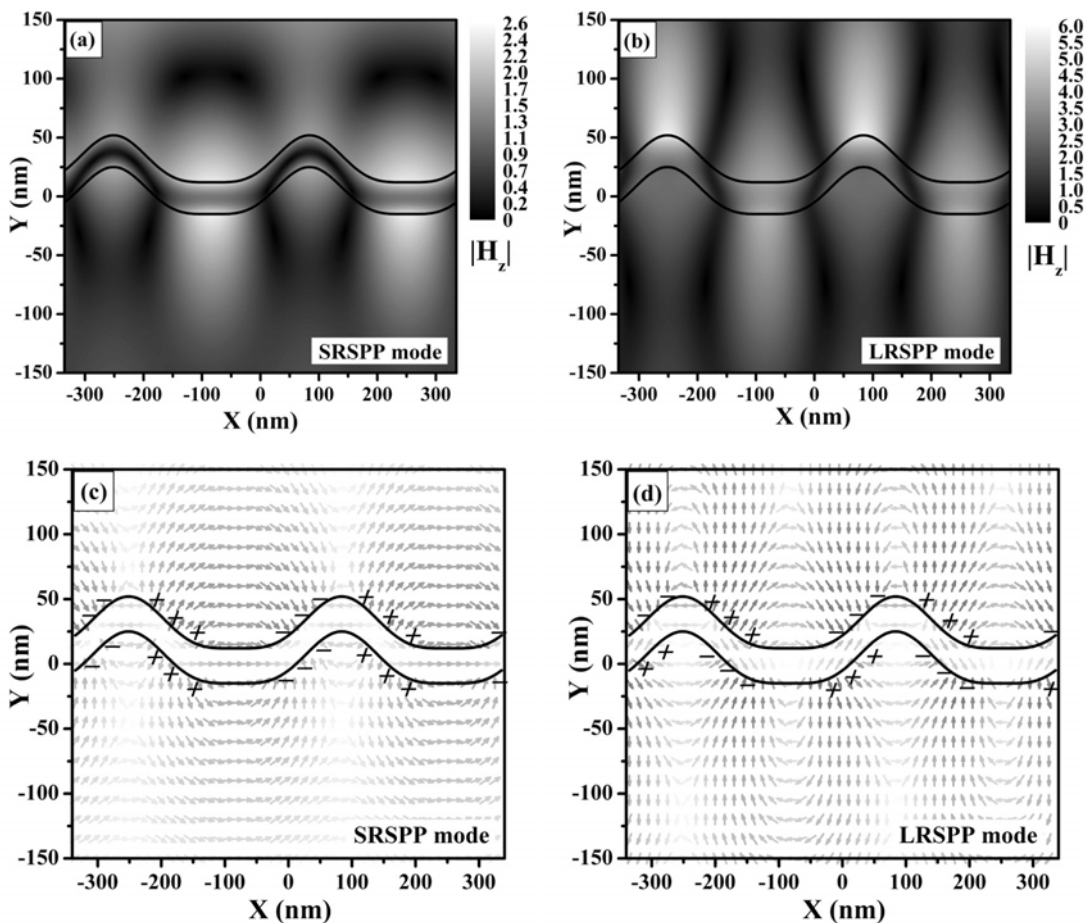


**Figure 7.3.7** Schematics showing the positions of maximum surface charge density of the possible standing wave coupled modes for normal incidence that may be excited on the structure. The black lines represent the thin metal grating. The dashed lines indicate the  $2k_g$  component of the grating.

Figure 7.3.7 schematically shows the positions of maximum surface charge density of these four possible solutions relative to the  $2k_g$  component of the grating (indicated as dashed lines). For one possible solution of the lower frequency self-crossing point (the SRSPP self-crossing point), as shown in Figure 7.3.7 (a), the positions of maximum surface charge density occur at the peaks of the  $2k_g$  component (low energy,  $\omega^-$ ) while equivalent positions on the bottom surface occur at the troughs of the  $2k_g$  component (high energy,  $\omega^+$ ). Figure 7.3.7 (b) shows another possible solution with the correct symmetry in that on the top interface the surface charge density maxima occur at the troughs of the  $2k_g$  component (high energy,  $\omega^+$ ) and the surface charge density maxima occur at the peaks of the  $2k_g$  component (low energy,

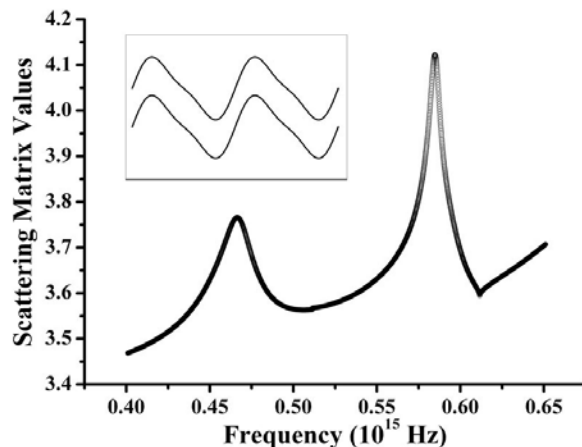
$\omega^-$ ). From this it is apparent that the two possible solutions for SRSPP modes will have the same energy. Hence, at the SRSPP self-crossing point, even with the existence of a  $2k_g$  component in the profile, we should expect that **no** band gap arises. For the same reason, as shown in Figure 7.3.7 (c) and (d), the two possible solutions for the LRSPP modes will also have the same energy at the LRSPP self-crossing point.

Figure 7.3.8 shows the  $|H_z|$  profiles together with the instantaneous  $E_{xy}$  vector fields for the SRSPP ( $f = 0.475 \times 10^{15}$  Hz) and the LRSPP ( $f = 0.581 \times 10^{15}$  Hz) excited at normal incidence on the structure as described for Figure 7.3.5 (b) (incident from 2<sup>nd</sup> prism with  $\phi = -\pi/2$ ). The same discussions and arguments as given for Figure 7.3.6 can be applied to the case of Figure 7.3.8.



**Figure 7.3.8** Time averaged  $|H_z|$  component of the fields of (a) the SRSPP and (b) the LRSPP modes that can be excited at normal incidence, together with the instantaneous  $E_{xy}$  vector fields for (c) the SRSPP and (d) the LRSPP modes on the same structure as described in Figure 7.3.5 (b) (incident from the 2<sup>nd</sup> prism with phase shift  $\phi = -\pi/2$ ). The continuous black lines represent the thin metal grating.

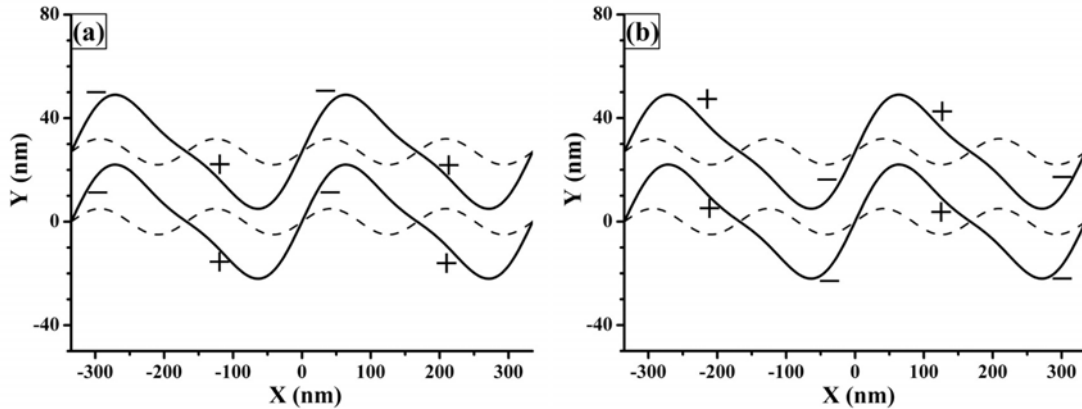
Of course if there is an appropriate phase shift between the  $2k_g$  component and the fundamental, for example  $\phi = 0^\circ$ , then the grating is ‘blazed’. Here the focus of interest is the crossing points that arise at  $k_x = 0$  through scattering of one wave by  $-k_g$  and the other by  $+k_g$ . Figure 7.3.9 shows the modes obtained by direct inspection of the scattering matrices of the systems in the classical mount over a range of frequencies for in-plane wave vector  $k_x = 0$ . The profile describing the thin silver grating in Figure 7.3.9 is given by  $[20 \sin(k_g x) + 5 \sin(2k_g x)]$  nm for the bottom surface and  $[20 \sin(k_g x) + 5 \sin(2k_g x) + 27]$  nm for the top surface. The two peaks shown in Figure 7.3.9 positioned at  $f = 0.468 \times 10^{15}$  Hz and  $0.584 \times 10^{15}$  Hz are the SRSPP and LRSPP modes respectively. Note that the corrugations on both sides are still conformal. It is clear that at normal incidence for both SRSPP and LRSPP there are still **no** band gaps.



**Figure 7.3.9** The values taken from the scattering matrix calculated for a thin silver grating in the classical mount over a range of frequencies at normal incidence. The inset graph corresponds to the grating that has been used in the calculations. The profile describing the structure is given by  $[20 \sin(k_g x) + 5 \sin(2k_g x)]$  nm for the bottom surface and  $[20 \sin(k_g x) + 5 \sin(2k_g x) + 27]$  nm for the top surface. Note that the phase shift  $\phi$  between  $2k_g$  and  $k_g$  is 0.

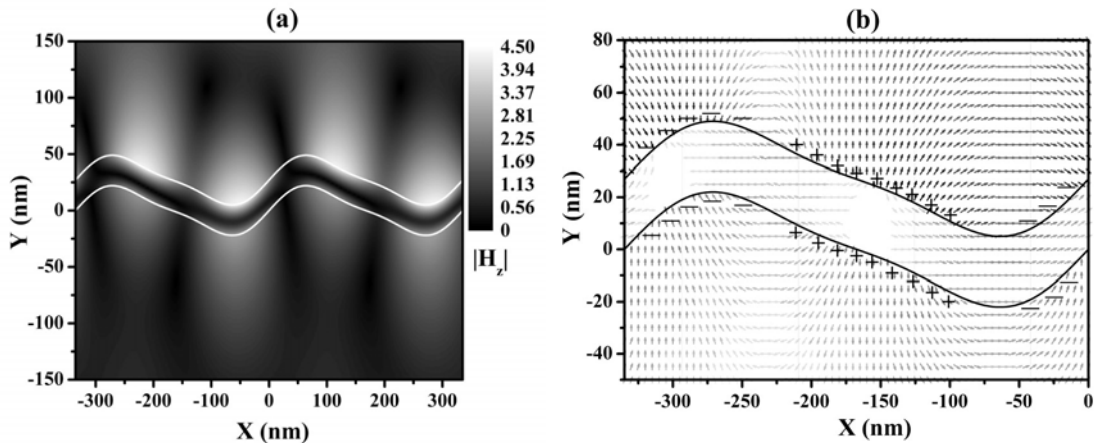
The same explanation as given for the case of conformal non-blazed thin silver gratings can be applied to explain the lack of band gaps at the SRSPP and LRSPP self-crossing points for conformal blazed thin silver gratings. Figure 7.3.10 schematically shows the positions of maximum surface charge density of two possible SRSPP solutions relative to the  $2k_g$  component of the grating (indicated as dashed lines). One clearly sees that when on the top interface the surface charge density maxima occur at

the troughs (peaks) of the  $2k_g$  component, correspondingly on the bottom surface the maxima occur at the peaks (troughs) of the  $2k_g$  component. Obviously the two possible solutions for SRSPP modes will have the same energy ( $\omega^- + \omega^+$ ), and **no** band gap arises at the self-crossing points for normal incidence.



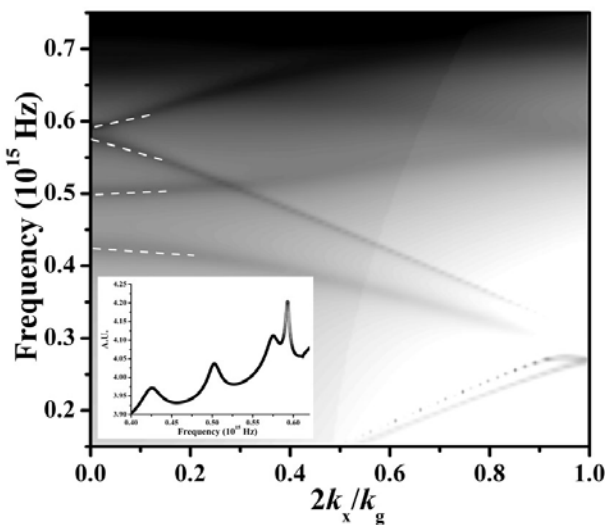
**Figure 7.3.10** Schematics showing the positions of maximum surface charge density of the possible short range SPP modes for normal incidence that may be excited on the structure. The black lines represent the thin metal grating. The dashed lines indicate the  $2k_g$  component of the grating.

Figure 7.3.11 shows the  $|H_z|$  profiles together with the instantaneous  $E_{xy}$  vector fields of the SRSPP ( $f = 0.468 \times 10^{15}$  Hz) mode excited at normal incidence ( $\theta = 0^\circ$ ) on the structure as described for Figure 7.3.9 (with phase shift  $\phi = 0^\circ$ ). First note that the  $|H_z|$  component has a region of zero-value inside the thin metal film, as shown in Figure 7.3.11 (a), which is caused by the symmetric charge density distributions for SRSPP. As we have already mentioned above, at normal incidence only the modes with surface charge density maxima on the sides of the grating grooves may couple to the incident light. Hence for a non-blazed grating, only one possible SRSPP solution having the surface charge density as shown in Figure 7.3.7 (a) can be excited, while another possible solution associated with Figure 7.3.7 (b) can not be excited. However for a blazed grating with phase shift  $\phi = 0^\circ$ , since the peaks and troughs of the  $2k_g$  component occur at equivalent points with respect to the  $k_g$  component, both of the two possible SRSPP solutions associated with Figure 7.3.10 (a) and (b) should be excited at normal incidence. This mixed charge density distribution is clearly confirmed in Figure 7.3.11 (b).



**Figure 7.3.11** Time averaged  $|H_z|$  component of the fields (a) together with the instantaneous  $E_{xy}$  vector fields (b) of the SRSPP mode ( $f = 0.468 \times 10^{15}$  Hz) that can be excited at normal incidence on the same structure as described in Figure 7.3.9 (with phase shift  $\phi = 0^\circ$ ). The continuous lines represent the thin metal grating.

Now we have seen that even with the existence of a  $2k_g$  component in the profile of a conformal thin silver grating there are **no** band gaps at normal incidence for both the SRSPP and the LRSPP modes. It is worth investigating how to open up the band gaps at normal incidence for thin silver gratings. Figure 7.3.12 shows the model band structure of a thin silver grating with non-identical corrugations on each of interfaces; the modes are indicated by white dashed lines. The profile describing the structure is given by  $[20 \sin(k_g x) + 5 \sin(2k_g x - \pi/2)]$  nm for the bottom surface and  $[20 \sin(k_g x) + 5 \sin(2k_g x + \pi/2) + 27]$  nm for the top surface. Note that the phase shifts  $\phi$  on the top and bottom surfaces are  $-\pi/2$  and  $+\pi/2$  respectively. Obviously in Figure 7.3.12 two band gaps open up at normal incidence for the SRSPP and the LRSPP modes respectively. Four peaks are readily observed in the inset graph of Figure 7.3.12, which corresponds to the model dispersion of the optical modes for  $k_x = 0$ . Also note that at the crossing point (arising from the LRSPP scattered by  $+k_g$  and the SRSPP scattered by  $-k_g$ ) the anti-crossing behaviour which was observed within the Brillouin zone for a conformal thin silver grating as shown in Figure 7.3.4 (d) disappears for the non-conformal structure considered here. This must be because the wave-function overlap between the two modes at the crossing point is zero.



**Figure 7.3.12** The model band structure for silver gratings in the classical mount. The profile describing the structure is given by  $[20 \sin(k_g x) + 5 \sin(2k_g x - \pi/2)]$  nm for the bottom surface and  $[20 \sin(k_g x) + 5 \sin(2k_g x + \pi/2) + 27]$  nm for top surface. The inset graph corresponds to the model dispersion of the optical modes over a range of frequencies for  $k_x = 0$ .

Again by investigating the positions of maximum surface charge density of the possible solutions relative to the  $2k_g$  component of the grating we can explain why the band gaps open up for the SRSPP and the LRSPP modes at normal incidence for non-conformal thin silver gratings. Figure 7.3.13 schematically shows the surface charge density maxima positions of two possible SRSPP solutions. For one possible solution, as shown in Figure 7.3.13 (a), the positions of maximum surface charge density occur at the peaks of the  $2k_g$  component (low energy,  $\omega^-$ ) and equivalent positions on the bottom surface also occur at the peaks of the  $2k_g$  component (low energy,  $\omega^-$ ). Similarly, for another possible solution, as shown in Figure 7.3.13 (b), the surface charge density maxima occur at the troughs of the  $2k_g$  component (high energy,  $\omega^+$ ) on both the top and bottom interfaces. Thus the two possible solutions for SRSPP modes will have different energies,  $\omega^-$  for low energy branch and  $\omega^+$  for the high energy branch, and a band gap arises at the SRSPP self-crossing point. For similar reasons, at the LRSPP self-crossing point a band gap will also open up.

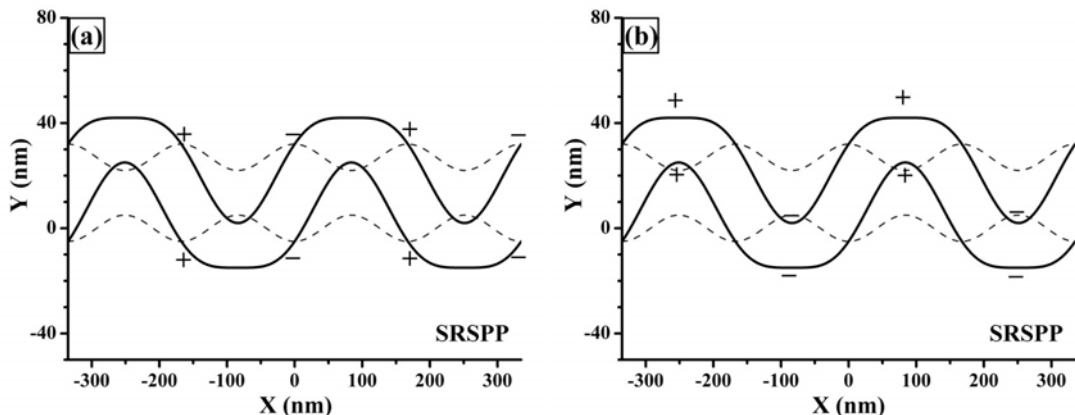


**Figure 7.3.13** Schematics showing the positions of maximum surface charge density of the possible short range SPP modes for normal incidence that may be excited on the structure. The black lines represent the thin metal grating. The dashed lines indicate the  $2k_g$  component of the grating.

If we examine the thin silver grating shown in Figure 7.3.13 carefully, one can see that the width of the vertical cross section of the grating is modulated in the  $x$ -direction. This leads to the question is this thickness modulation the only required condition to open up the band gaps at normal incidence for the SRSPP and LRSPP modes. Figure 7.3.14 shows the model band structure of a non-conformal thin silver grating, in which the SRSPP and LRSPP modes scattering from  $\pm k_g$  are indicated by white dashed lines. The profile describing this structure, as shown in the bottom-left inset graph of Figure 7.3.14, is given by  $[10 \sin(k_g x)]$  nm for the bottom surface and  $[-10 \sin(k_g x) + 27]$  nm for the top surface. Obviously in such a thin grating which has no  $2k_g$  component the thickness of the silver film is also modulated in the  $x$ -direction. However, as shown in Figure 7.3.14, **no** band gaps are opened up at normal incidence for SRSPP and LRSPP modes, only two peaks are observed in the upper right inset graph of Figure 7.3.14. This implies that two conditions, non-identical corrugations on each side of the thin grating and the existence of a  $2k_g$  component, must be fulfilled to open up band gaps at normal incidence for the SRSPP and LRSPP modes.

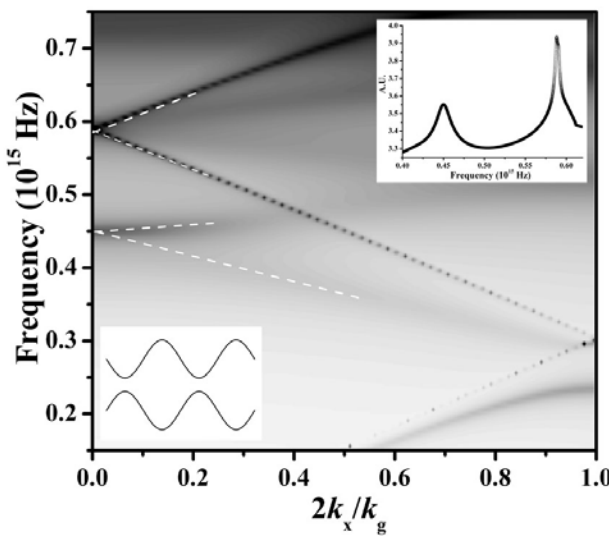


**Figure 7.3.14** The model band structure for silver gratings in the classical mount. The profile describing the structure is given by  $[10 \sin(k_g x)]$  nm for the bottom surface and  $[-10 \sin(k_g x) + 27]$  nm for the top surface. The inset graph (bottom-left) corresponds to the grating that has been used in the calculations. The inset graph (upper-right) corresponds to the model dispersion of the optical modes over a range of frequencies for  $k_x = 0$ .

## 7.4 Summary

In this chapter the two coupled surface plasmon polaritons (the SRSPP and the LRSPP) on a thin planar silver film bounded by identical dielectric media have been investigated theoretically with prism coupling. The numerically modelled reflectivity as a function of incident angle and thickness of silver film for TM polarized incident light with a fixed frequency clearly shows that the SISPP mode splits into the SRSPP and LRSPP modes with decreasing thickness of silver film. We described the two coupled modes and the effect of the metal film thickness and incident angle upon the features in the zeroth order optical response (reflection, transmission, and absorption) for the system with identical sinusoidal corrugations on both sides. More interesting results have been investigated experimentally and modelled theoretically in the visible range when a small  $2k_g$  component is added to the grating profile. Wavelength dependent absolute reflectivity data for TM polarized incident radiation at different polar angles in the “classical” mount leads to a mapping of the dispersion curve of the various SPP modes as a function of frequency and in-plane wave vector. It is shown that the  $2k_g$

component in the grating profile is the key factor leading to the appearance of band gaps in these relatively shallow gratings. Interestingly the band gap which would appear on a single metal surface (supporting just the SPP mode) for normal incidence radiation does not appear in the two self-crossing points of the LRSPP modes and the SRSPP modes at normal incidence for thin gratings with identical corrugations on both sides. This is because of the symmetry of the standing wave states of the expected two modes relative to the  $2k_g$  component of the grating. However a band gap does appear within the Brillouin zone, formed by the anti-crossing of the LRSPP scattered by  $+k_g$  and the SRSPP scattered by  $-k_g$ .

Finally we considered the case where the two corrugations on each surface are not conformal, and we focused on the self-crossing points at  $k_x = 0$  (normal incidence). We found that only when two conditions that the structure is non-conformal and has a  $2k_g$  component are fulfilled does the band gaps open at  $k_x = 0$  for both the LRSPP and the SRSPP modes.

## Chapter 8

# Coupled Surface Plasmon Polaritons on Thin Silver Gratings in the Conical Mount

### 8.1 Introduction

In chapter 7 we investigated the case of coupled SPPs (SRSPP and LRSPP) on thin silver gratings in the classical mount for TM polarization. In this chapter we shall explore the excitation of coupled SPPs on conformal thin shallow silver gratings in the conical mount ( $\phi = 90^\circ$ ) for both TE and TM polarizations. There will be two main sections of this chapter. The first section will consider single silver/silica interface gratings. This mainly follows the work of Watts *et al.* [1997] where they observed not only the excitation of an SPP by TE radiation, but also a new and strikingly sharp SPP resonance in the TM polarized reflectivity, for large amplitude gratings oriented with the grating vector perpendicular to the plane of incidence. We will follow this work and via modelling show that when the amplitude of the grating is relatively small (compared to the grating pitch) it is still possible to excite the SPP at  $\phi = 90^\circ$  with TM polarized incident light, though this SPP resonance is very weak.

In the second section we shall investigate the coupled SPPs (the LRSPP and the SRSPP) on thin silver gratings at azimuth angle  $\phi = 90^\circ$ . In the conical mount both TM and TE polarized radiation can be coupled to the LRSPP and SRSPP. In particular, on coupling TM polarized radiation to the SPP at  $\phi = 90^\circ$  a new and strikingly strong SPP resonance is observed on thin silver gratings even with very shallow corrugations. It is found that the coupling strength of this SPP mode is enhanced greatly compared to that of the SPP mode on a single interface grating having the same pitch and corrugation depth. This strong resonance for a shallow thin silver grating is explored using modelling programs and its presence is confirmed experimentally in the visible part of the spectrum. In addition the optical field distributions at the resonant frequency are explored showing that this SPP mode is the SRSPP mode.

## 8.2 SPPs on Single Interface Metal Gratings in the Conical Mount

In chapter 3 we mentioned that TE polarized radiation may be used to excite the SPP on a single interface zero-order grating at  $\varphi = 90^\circ$ . Conversely TM polarized light which has a component of its electric field normal to the surface for non-zero polar angles, is expected not to strongly excite an SPP  $\varphi = 90^\circ$ . However Watts *et al.* [1997] discovered a strikingly sharp SPP resonance when TM polarized light was incident upon a large amplitude single interface silver grating at azimuth angle  $\varphi = 90^\circ$  (the conical mount). In this section we shall follow their work but concentrate on shallow corrugations. Figure 8.2.1 shows the geometry considered, the polar angle  $\theta$  and the azimuth angle  $\varphi$  define the orientation of the incident beam with respect to the grating vector. Note that in this chapter the azimuth angle  $\varphi$  is always set to  $90^\circ$ .

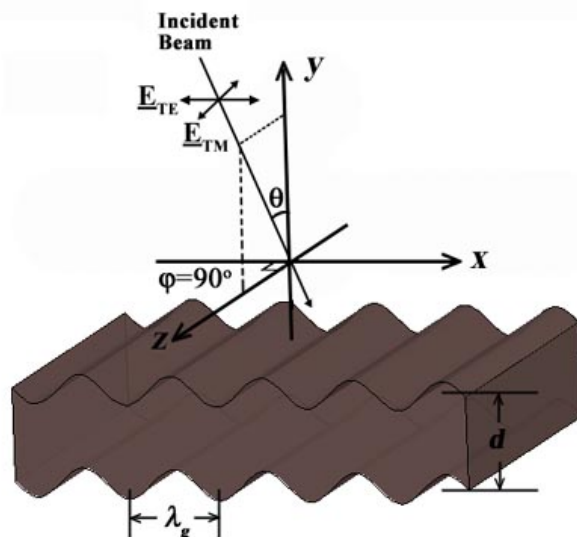


**Figure 8.2.1** Schematic diagram illustrating the sample and coordinate system used in this work. Here  $\lambda_g$  is the grating pitch,  $d$  is the thickness of the silver layer,  $\theta$  is the polar angle, and  $\varphi$  is the azimuth angle which is set to  $90^\circ$  in this chapter. The silver layer is bounded with silica media.

The orientation of the electric field for both TM and TE polarizations is also shown in Figure 8.2.1. The incident electric field  $\mathbf{E}$  may be written as:

$$\mathbf{E} = E \mathbf{p} \exp(i \mathbf{k} \cdot \mathbf{r}) \quad 8.2.1$$

where  $E$  is the field amplitude and  $\mathbf{p}$  is the polarization unit vector. In the coordinate system as shown in Figure 8.2.1, the vectors  $\mathbf{p}$  and  $\mathbf{k}$  can be projected onto  $x$ -,  $y$ -, and  $z$ -axis, giving

$$\mathbf{k} = n_0 k_0 (\sin \theta \cos \varphi \hat{x} - \cos \theta \hat{y} - \sin \theta \sin \varphi \hat{z}) \quad 8.2.2$$

$$\mathbf{p}_{TM} = \cos \theta \cos \varphi \hat{x} + \sin \theta \hat{y} + \cos \theta \sin \varphi \hat{z} \quad 8.2.3$$

$$\mathbf{p}_{TE} = -\sin \varphi \hat{x} + 0 \hat{y} + \cos \varphi \hat{z} \quad 8.2.4$$

where  $n_0$  is the refractive index of the silica. Two tangents of the grating surface are  $\hat{x} + f' \hat{y}$  and  $\hat{z}$ , where  $f' = k_g a \cos k_g x$  is the gradient of the surface function  $y = f(x) = a \sin k_g x$ ,  $a$  being the grating amplitude. The cross product of these two tangents gives the unit normal vector

$$\hat{\mathbf{n}} = \frac{f' \hat{x} - \hat{y}}{\sqrt{1 + f'^2}} \quad 8.2.5$$

which leads to the local normal components of  $\mathbf{p}$  given by

$$\mathbf{p}_{TM} \cdot \hat{\mathbf{n}} = \frac{f' \cos \theta \cos \varphi - \sin \theta}{\sqrt{1 + f'^2}} \quad 8.2.6$$

$$\mathbf{p}_{TE} \cdot \hat{\mathbf{n}} = -\frac{f' \sin \varphi}{\sqrt{1 + f'^2}} \quad 8.2.7$$

From equations 8.2.6 and 8.2.7 it is clear that normal components of  $\mathbf{p}$  remain finite at  $\varphi = 90^\circ$  for both TM and TE polarizations, provided that in the TM case  $\theta$  is nonzero. Thus both polarizations can couple to SPPs. The local normal components of the electric field at the surface are explicitly, for  $\varphi = 90^\circ$ :

$$\mathbf{E}_{TM} \cdot \hat{\mathbf{n}} = -\frac{A_{TM} \sin \theta}{\sqrt{1 + f'^2}} \exp[-in_0 k_0 (a \cos \theta \sin k_g x + z \sin \theta)] \quad 8.2.8$$

$$\mathbf{E}_{TE} \cdot \hat{\mathbf{n}} = -\frac{A_{TE} f'}{\sqrt{1 + f'^2}} \exp[-in_0 k_0 (a \cos \theta \sin k_g x + z \sin \theta)] \quad 8.2.9$$

In the limit of small amplitude  $a$ , equations 8.2.8 and 8.2.9 can be expanded as

$$\mathbf{E}_{TM} \cdot \hat{\mathbf{n}} = -A_{TM} \left( \sin \theta - \frac{ik_0 a \sin 2\theta}{2} \sin k_g x \right) \exp(-in_0 k_0 z \sin \theta) \quad 8.2.10$$

$$\mathbf{E}_{TE} \cdot \hat{\mathbf{n}} = -A_{TE} k_g a (\cos k_g x) \exp(-in_0 k_0 z \sin \theta) \quad 8.2.11$$

The induced local surface charge is proportional to  $\mathbf{E} \cdot \hat{\mathbf{n}}$ , and the maxima occur at the extrema of the grating ( $k_g x = N\pi + 0.5\pi$ ) for TM polarization and at the points of maximum gradient ( $k_g x = N\pi$ ) for TE polarization, where  $N$  is an integer.

Figure 8.2.2 shows the theoretical TE and TM polarized reflectivity as a function of frequency and amplitude at  $\theta = 25.0^\circ$  and  $\varphi = 90^\circ$  for a 252 nm pitch sinusoidal silver grating bounded with silica media. In the calculations, the thickness of the silver film is set to  $d = 500$  nm, and a Drude model with  $\omega_p = 1.32 \times 10^{16}$  rad/s and  $\tau = 1.45 \times 10^{-14}$  s is used to describe the silver, with the refractive index of the silica being fixed of  $n_{\text{silica}} = 1.459$ . Obviously when the thickness of the silver film is set to 650 nm the structure can be considered as a single interface silver grating. The main region of interest is to the left of the dashed line in Figure 8.2.2 at  $f = 0.896 \times 10^{15}$  Hz, which represents the Rayleigh anomaly. In this interesting region, Figure 8.2.2 (a) clearly shows two well coupled SPP resonances for TE polarization. The mode that can be accessed at higher frequency and higher amplitude is the second order SPP mode, which is not considered here. We only concentrate on the lowest frequency mode which emerges at a frequency of  $f = 0.731 \times 10^{15}$  Hz in the lower amplitude region. As described in chapter 3, this coupled SPP is a standing wave in the  $x$  direction having its field extrema at the points of the steepest surface gradient. This is readily coupled to by TE radiation since there is significant surface charge induced at the steepest gradient parts of the surface. As shown in the inset graph of Figure 8.2.2 (a), the optimum 100% coupling for this TE mode occurs at an amplitude of  $a \approx 4$  nm.

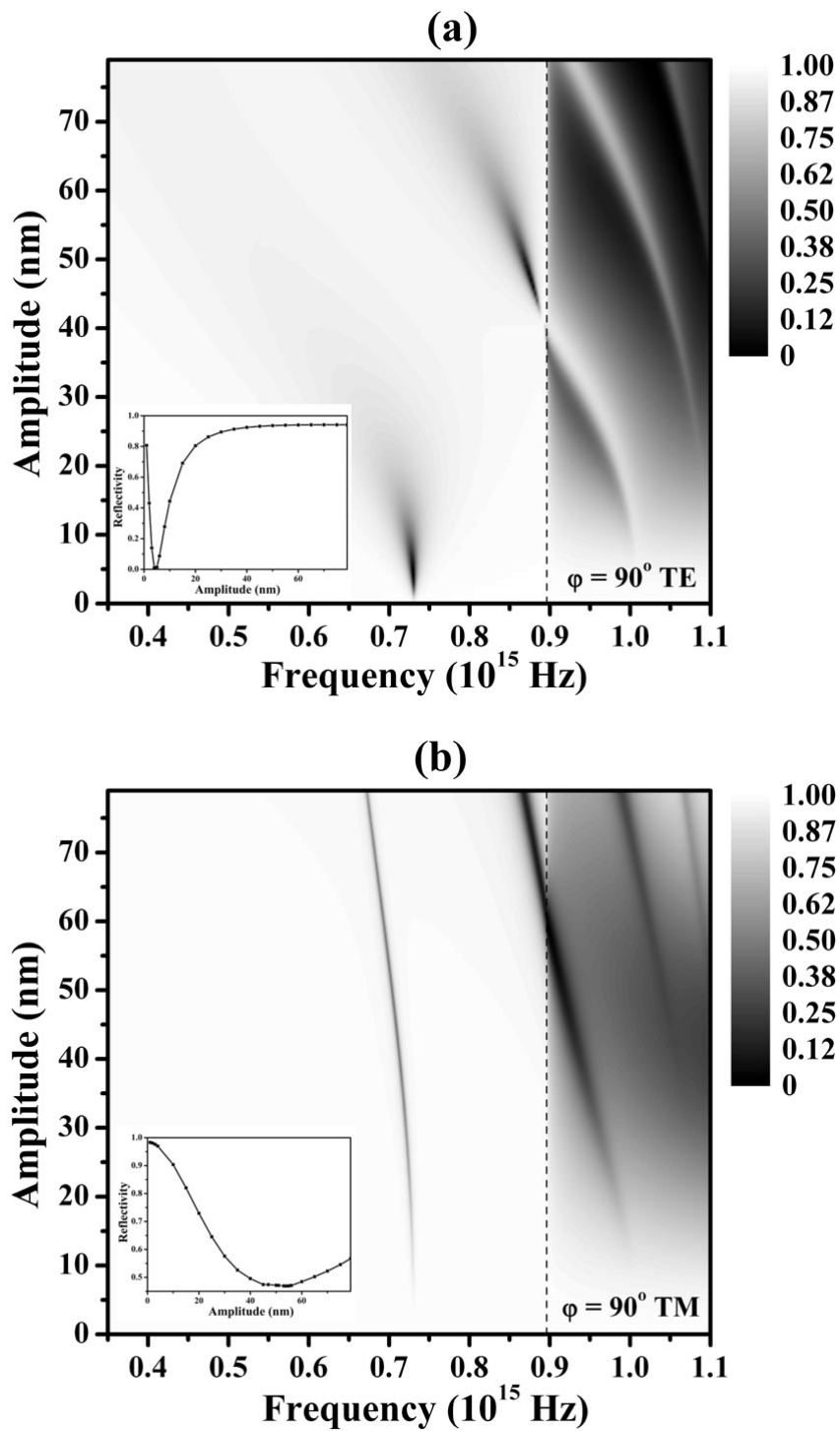


**Figure 8.2.2** Model reflectivity, for (a) TE and (b) TM polarized radiation incident upon a 252 nm pitch sinusoidal silver grating at  $\theta = 25.0^\circ$  and  $\phi = 90^\circ$ , plotted as a function of the frequency and the amplitude. The dashed line represents the pseudo-critical edge. The inset graph plots the reflectivity minimum as a function of amplitude for the lowest frequency mode.

The most original physics is found in Figure 8.2.2 (b), where SPP resonances represented by reflection minima are excited by TM polarized light at  $\varphi = 90^\circ$ . Again we concentrate on the lowest frequency mode, which is also a standing wave in the  $x$  direction and propagates along the  $z$  direction with field maxima at the extrema of the grating surface. This coupling of TM radiation to the SPP at  $\varphi = 90^\circ$  arises because of the phase shift ( $4\pi a n_{\text{silica}}/\lambda_0 \cos\theta$ ) of the incident radiation between the top and bottom of the grating grooves, which leads directly to a change in the amplitude of the local surface charge in an  $xy$  plane thereby allowing coupling to the SPP on the silver/silica interface. Since the phase shift of the incident radiation is proportional to the amplitude, for shallow corrugations coupling to the TM SPP mode at  $\varphi = 90^\circ$  should be very weak. As shown in the inset graph of Figure 8.2.2 (b), at  $a = 10$  nm the coupling strength of this TM mode for  $\theta = 25.0^\circ$  is only 10%, and the maximum coupling strength  $\sim 50\%$  occurs for an amplitude  $a \approx 55$  nm (compare with 4 nm for the TE case).

To more clearly demonstrate the nature of the coupling of TM and TE radiation to the SPP at  $\varphi = 90^\circ$  it is instructive to investigate their optical field profiles. Figure 8.2.3 shows the instantaneous  $E_{xy}$  vector fields at  $\theta = 25.0^\circ$  and  $\varphi = 90^\circ$  for the TM excited SPP mode ( $f = 0.729 \times 10^{15}$  Hz) and the TE excited SPP mode ( $f = 0.725 \times 10^{15}$  Hz) on the silver grating with an amplitude of 10 nm. First note the different surface charge density distributions along the silica/silver interface for the TE and TM excited modes. As shown in Figure 8.2.3 (a), for the TE mode, the maximum surface charge density occurs on the sides of the grating grooves, since there is always a component of electric field normal to the grating surface at the point of steepest gradient. As mentioned above, in the TM polarized case a surface charge density oscillation at the grating surface is induced because of the difference in path length experienced by a photon striking the top of the groove compared with one impinging near the trough. Hence we find that the surface charge centers are located at the grating peaks and troughs for the TM mode, as shown in Figure 8.2.3 (b). Also note that at  $\varphi = 90^\circ$ , and on excitation of the SPP, there will be two surface waves propagating along the metal surface with propagation angles of  $\pm\Psi$ . These two eigenmodes may be coupled together via two successive  $k_g$  scattering events, setting up a standing wave in the  $x$  direction. The nature of this standing wave in the  $x$  direction is readily shown in Figure 8.2.3, where the period of the standing wave is the same as the grating pitch.

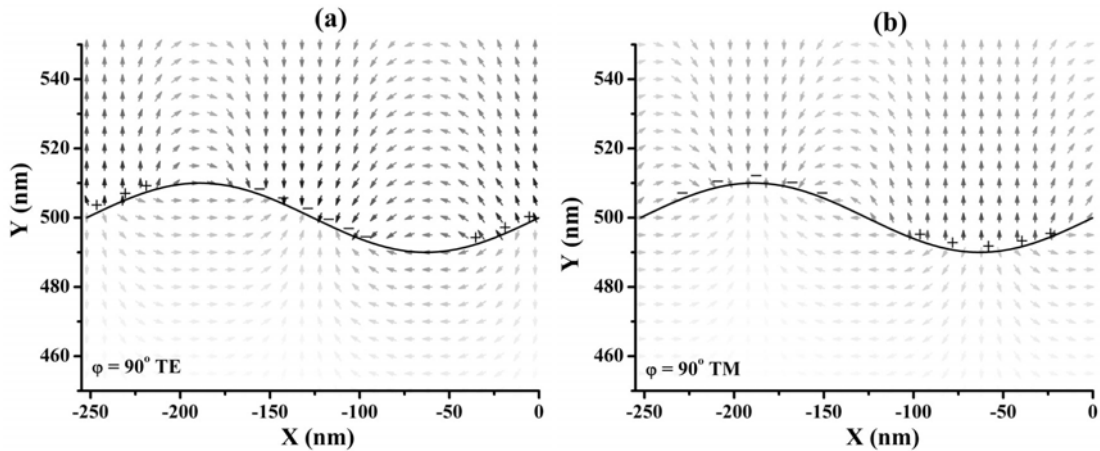


**Figure 8.2.3** Instantaneous electric field vector  $E_{xy}$  distributions at  $\theta = 25.0^\circ$  and  $\varphi = 90^\circ$  for (a) TE mode (resonant frequency  $f = 0.725 \times 10^{15} \text{ Hz}$ ) and (b) TM mode (resonant frequency  $f = 0.729 \times 10^{15} \text{ Hz}$ ) on the silver grating with a pitch of 252 nm and an amplitude of 10 nm. The black line represents the silica/silver corrugated interface.

In addition, on excitation of the SPP at  $\varphi = 90^\circ$ , two coupled surface waves will propagate along the  $z$  direction. Figure 8.2.4 shows the instantaneous electric field vector  $E_{xz}$  distributions on the corrugated silica/silver interface at  $\theta = 25.0^\circ$  and  $\varphi = 90^\circ$  for the TM excited mode ( $f = 0.729 \times 10^{15} \text{ Hz}$ ) and the TE excited mode ( $f = 0.725 \times 10^{15} \text{ Hz}$ ) on the same structure as described in Figure 8.2.3. The fields in Figure 8.2.4 are plotted in the  $x$ - $z$  plane where the solid and dashed lines represent the grating peak and trough respectively. Again we can see that the maximum surface charge density locates on the sides of the grating for TE polarization and at the grating peaks and troughs for TM polarization. Note in the  $z$  direction the surface charge centers change sign periodically. This obviously implies that the SPP is propagating along the  $z$  direction. Also note the different relative positions of surface charge centers for the TM and TE modes. As shown in Figure 8.2.4 (b), for the TM excited mode, the surface charge centers at the grating trough have a shift in the  $z$  direction relative to the nearest charge centers at the grating peak, while for the TE excited mode in Figure 8.2.4 (a) the two charge centers located on the nearest sides of the grating are at the same  $z$  coordinate.

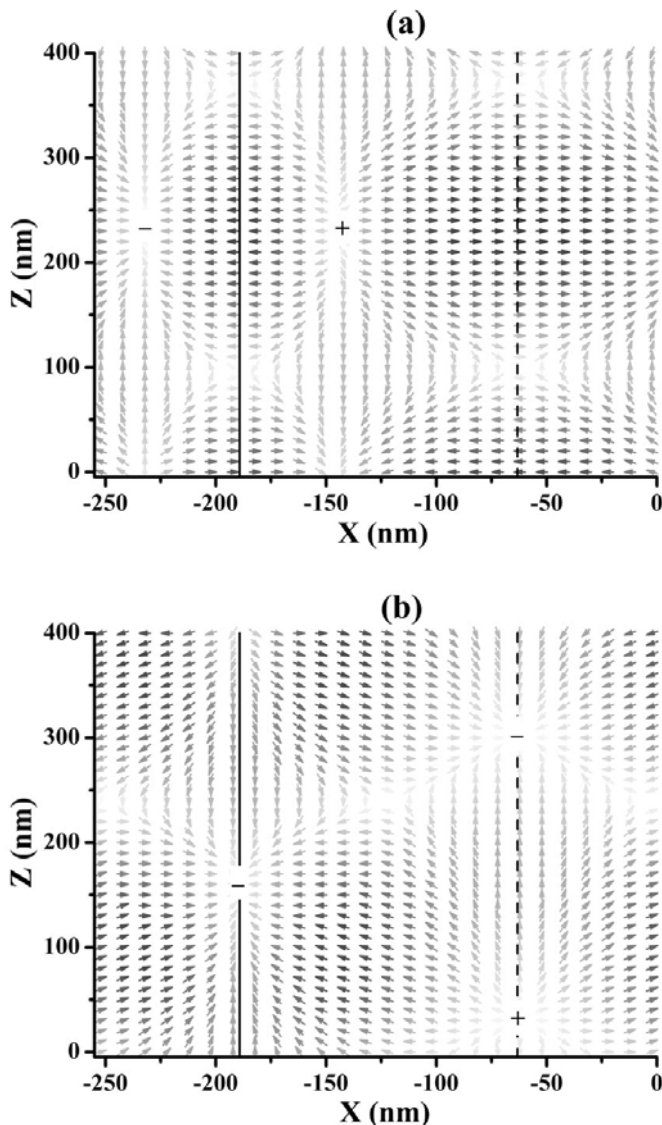


**Figure 8.2.4** Instantaneous electric field vector  $E_{xz}$  distributions on the grating surface of (a) TE mode ( $f = 0.725 \times 10^{15}$  Hz) and (b) TM mode ( $f = 0.729 \times 10^{15}$  Hz) at  $\theta = 25.0^\circ$  and  $\varphi = 90^\circ$  for the silver grating with a pitch of 252 nm and an amplitude of 10 nm. The fields are plotted in the  $x$ - $z$  plane and one repeat period of the structure is shown ( $\lambda_g$ ). Solid black line ( $x = -189.2$  nm) represents the grating peak. Dashed black line ( $x = -63.2$  nm) represents the grating trough.

A metallic single interface grating may redirect an incident photon into different channels: zero-order reflection, diffracted order reflections, and absorption. In this chapter, since we only concentrate on the non-diffractive (zero-order) region, the grating can be considered as a zero-order grating, and therefore there are no high diffractive order reflections. The energy conservation requires:  $A + R = 1$ . In the optimum 100% coupling case,  $R = 0$ ,  $A$  becomes 1, i.e., the whole energy is absorbed in

the metal. Figure 8.2.5 shows theoretical TE and TM polarized absorption ( $A = 1 - R$ ) as a function of incident angle and grating amplitude for 381 nm ( $f = 0.785 \times 10^{15}$  Hz) radiation incident upon a 252 nm pitch sinusoidal silver grating in the conical mount. First note the absorption for TE polarization, as shown in Figure 8.2.5 (a), increases with increasing amplitude and reaches its maximum at an amplitude of 5 nm. As mentioned in chapter 3, the coupling condition is mainly determined by the relation between the radiative damping ( $\Gamma_{\text{rad}}$ ) and the non-radiative damping ( $\Gamma_i$ ):  $\Gamma_{\text{rad}} < \Gamma_i$  – under coupling;  $\Gamma_{\text{rad}} = \Gamma_i$  – optimum coupling;  $\Gamma_{\text{rad}} > \Gamma_i$  – over coupling. In this case, when the amplitude increases from 0 to 5 nm the coupling condition changes from under coupling to optimum coupling. As the amplitude is increased further over-coupling occurs, and the absorption shallows and broadens. While for the TM polarization case, in the whole amplitude region from 0 to 22 nm as shown in Figure 8.2.5 (b), the coupling condition is under coupling and hence the absorption increases with increasing amplitude.

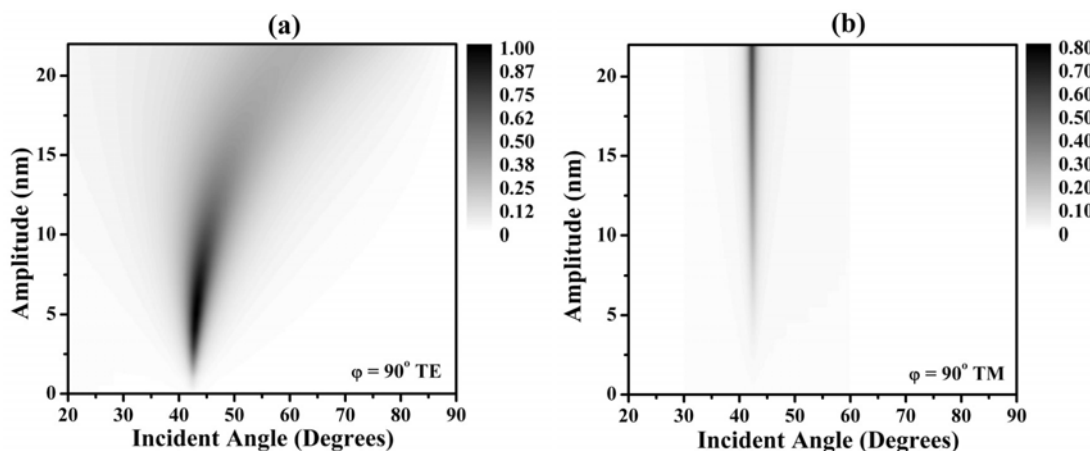


**Figure 8.2.5** Theoretical Absorption ( $A = 1 - R$ ), for (a) TE and (b) TM polarized 381 nm ( $f = 0.785 \times 10^{15}$  Hz) radiation incident upon a 252 nm pitch sinusoidal silver grating at  $\varphi = 90^\circ$ , plotted as a function of incident angle and amplitude.

Also note the difference of the mode width and central position for TE and TM polarizations. In the TE polarized case, as shown in Figure 8.2.5 (a), the mode width increases significantly and the mode central position shifts to higher incident angle with increasing amplitude, while for the TM polarization case, as shown in Figure 8.2.5 (b), both the mode width and the central position do not have any significant changes. The resonant mode width ( $\Delta\theta$ ) is determined by and proportional to the total damping term

$(\Gamma_{\text{rad}} + \Gamma_i)$ , and the propagation length is proportional to the  $1/\Delta\theta$ . To obtain the absorption mode width, the shape of the absorption mode has been fitted by a Lorentz function,

$$f(x) = f_0 + \frac{2A}{\pi} \frac{w}{4(x - x_c)^2 + w^2} \quad 8.2.12$$

Then the full width at half maximum (FWHM) for this function is found by finding the half-maximum points  $x$ ,

$$f(x) = \frac{1}{2}[f(x_{\max}) + f_0] \quad 8.2.13$$

It is obvious from equation 8.2.12 that  $f(x_{\max})$  occurs at  $x_{\max} = x_c$ . Hence,

$$f(x) = \frac{1}{2}[f(x_c) + f_0] = f_0 + \frac{2A}{\pi} \frac{w}{w^2} \quad 8.2.14$$

By solving equation 8.2.14 we obtain:

$$x_{\pm} = x_c \pm \frac{w}{2} \quad 8.2.15$$

and the FWHM is given by:

$$\text{FWHM} = x_+ - x_- = w \quad 8.2.16$$

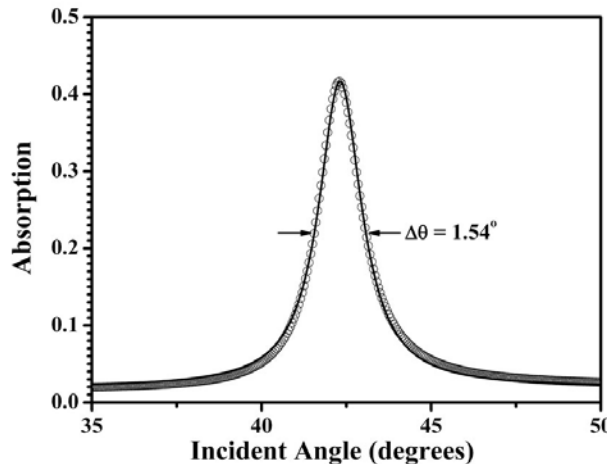


**Figure 8.2.6** Typical angle-scan TM polarized absorption peak for 381 nm ( $f = 0.785 \times 10^{15}$  Hz) radiation incident upon a 252 nm pitch sinusoidal silver grating at  $\varphi = 90^\circ$ . Open circles represent the theoretical calculation results. The solid line represents the fitted Lorentz function with parameters:  $f_0 = 0.01935$ ,  $x_c = 42.31553$ ,  $w = 1.53536$ , and  $A = 0.95851$ .

Figure 8.2.6 shows a typical angle-scan absorption peak (open circles) taken from Figure 8.2.5 (b) for TM polarized 381 nm ( $f = 0.785 \times 10^{15}$  Hz) radiation incident upon a sinusoidal silver grating with pitch of 252 nm and amplitude of 16 nm in the conical mount, together with the fitted Lorentz function peak (solid line). The parameters used in the Lorentz fitting are  $f_0 = 0.01935$ ,  $x_c = 42.31553$ ,  $w = 1.53536$ , and  $A = 0.95851$ . Then the parameter  $w$  gives the FWHM  $\Delta\theta = 1.54^\circ$ .

By fitting a Lorentzian to the absorption peak at each amplitude for both TE and TM polarizations, the absorption mode width is obtained. This is plotted against  $a^2$  in Figure 8.2.7. As already discussed in chapter 3 the total damping term is expected to increase linearly with  $a^2$  to first order for the TM polarized single-interface SPP (SISPP) at  $\varphi = 0^\circ$ . For the TE excited SISPP at  $\varphi = 90^\circ$  such a linear relation between the mode width ( $\Delta\theta$ ) and  $a^2$  is readily observed in Figure 8.2.7 for the small amplitude region, indicated by a dotted line for TE polarization. Note the FWHM of the TE excited SISPP mode is always greater than that of the TM excited SISPP mode, i.e., coupling of TM and TE polarized radiation of the same frequency to the SISPP on the same single-interface grating in the conical mount leads to a SISPP that propagates further when excited by TM polarized radiation than when excited by TE polarized radiation.

Also note the mode width of the TE excited SISPP increases rapidly with increasing amplitude, i.e., the mode becomes much broader. At an amplitude of 20 nm, the mode width  $\Delta\theta$  reaches approximately  $30^\circ$ . The most interesting aspect of Figure 8.2.7 is that the mode width ( $\Delta\theta$ ) is almost invariant with grating amplitude for TM excitation. This means that the total damping term ( $\Gamma_{\text{rad}} + \Gamma_i$ ), and also the propagation length, of the TM excited SISPP in the conical mount is a constant in the small amplitude region [0 – 22 nm], effectively the grating produces no significant radiation damping, which is dominated by Joule heating loss in the media.

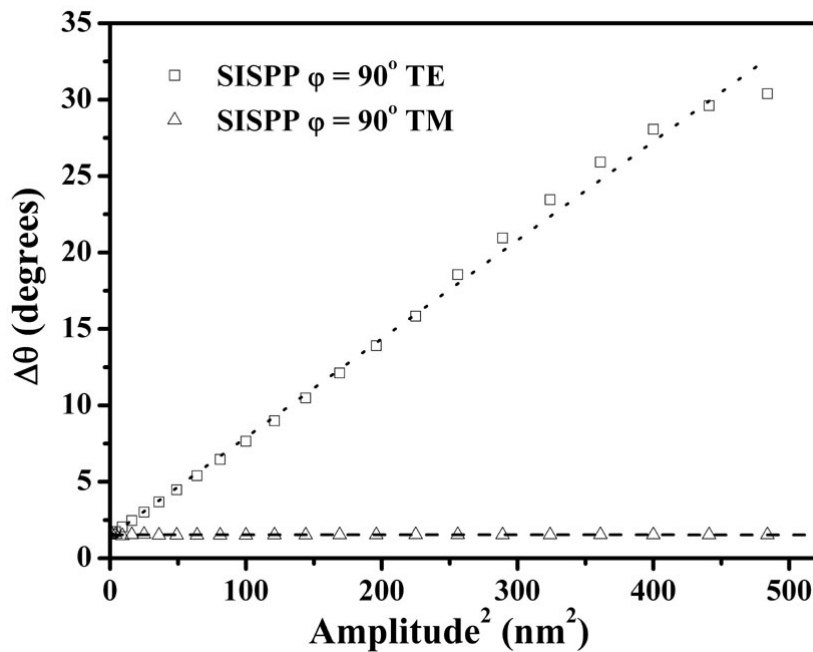


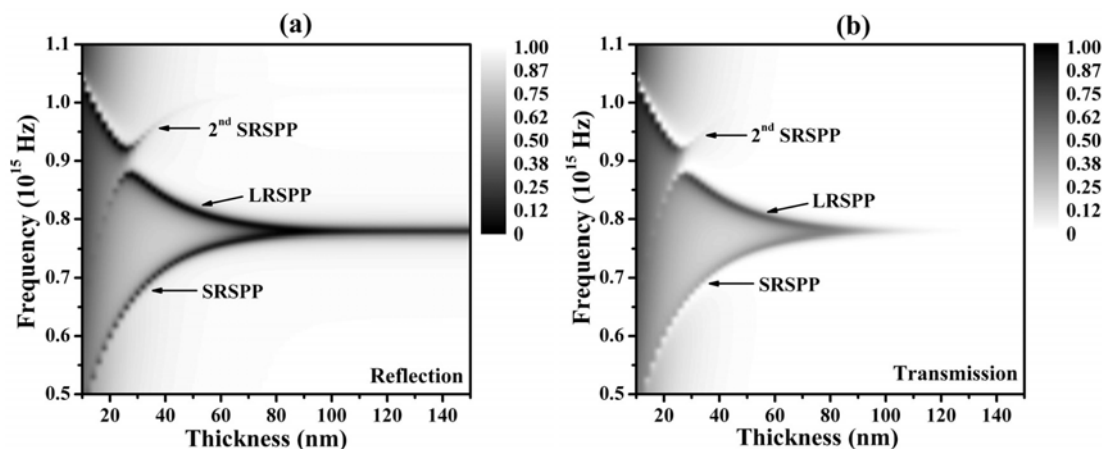
**Figure 8.2.7** The mode width ( $\Delta\theta$ ) of TE and TM polarized absorption peak for 381 nm ( $f = 0.785 \times 10^{15}$  Hz) radiation incident upon a 252 nm pitch sinusoidal silver grating at  $\varphi = 90^\circ$ , plotted against the amplitude square ( $a^2$ ). Open triangles represent the TM polarized single-interface SPP (SISPP) case. Open squares represent the TE polarized SISPP case. Dashed and dotted lines represent the linear fitting for TM and TE polarizations respectively.

### 8.3 SPPs on Thin Metal Gratings in the Conical Mount

As described in chapter 7 it is possible to couple the TM polarized radiation to the SPP on both surfaces of an optically thin metal grating in the classical mount ( $\varphi = 0^\circ$ ). These two SPPs will then couple together, and in doing so they form two different types of coupled SPP modes, known as the long range SPP (LRSPP), and the short range SPP (SRSPP). Also in the previous section we have modelled coupling of both TM and TE polarized radiation to the SPP on single interface silver gratings in the conical mount ( $\varphi = 90^\circ$ ). In this section we shall explore the LRSPP and the SRSPP on thin silver gratings bounded with silica media in the conical mount. The structure and coordinate system under consideration in this section is the same as that shown in Figure 8.2.1, but the thickness of the silver film ( $d$ ) is less than 100 nm.

### 8.3.1 Coupling TE polarized radiation to coupled SPPs

In the conical mount ( $\varphi = 90^\circ$ ) for TE polarized radiation there are always non-zero components of electric field normal to the sides of grating grooves, and hence TE polarized light is readily coupled to the SPP. At normal incidence ( $\theta = 0^\circ$ ) the configuration of the electric fields relative to the grating are exactly the same for TM radiation incident in the classical mount and TE radiation incident in the conical mount. Therefore, at normal incidence the coupling of TE polarized radiation to the SPP in the conical mount is equivalent to the coupling of TM polarized radiation to the SPP in the classical mount. The later case has already been investigated in chapter 7, and the excitation of the SRSPP and the LRSPP on a metallic thin film grating has also been demonstrated. In this section, coupling of TE polarized radiation to the SRSPP and the LRSPP on a metallic thin film grating in the conical mount ( $\varphi = 90^\circ$ ) for non-zero incident angles will be explored.



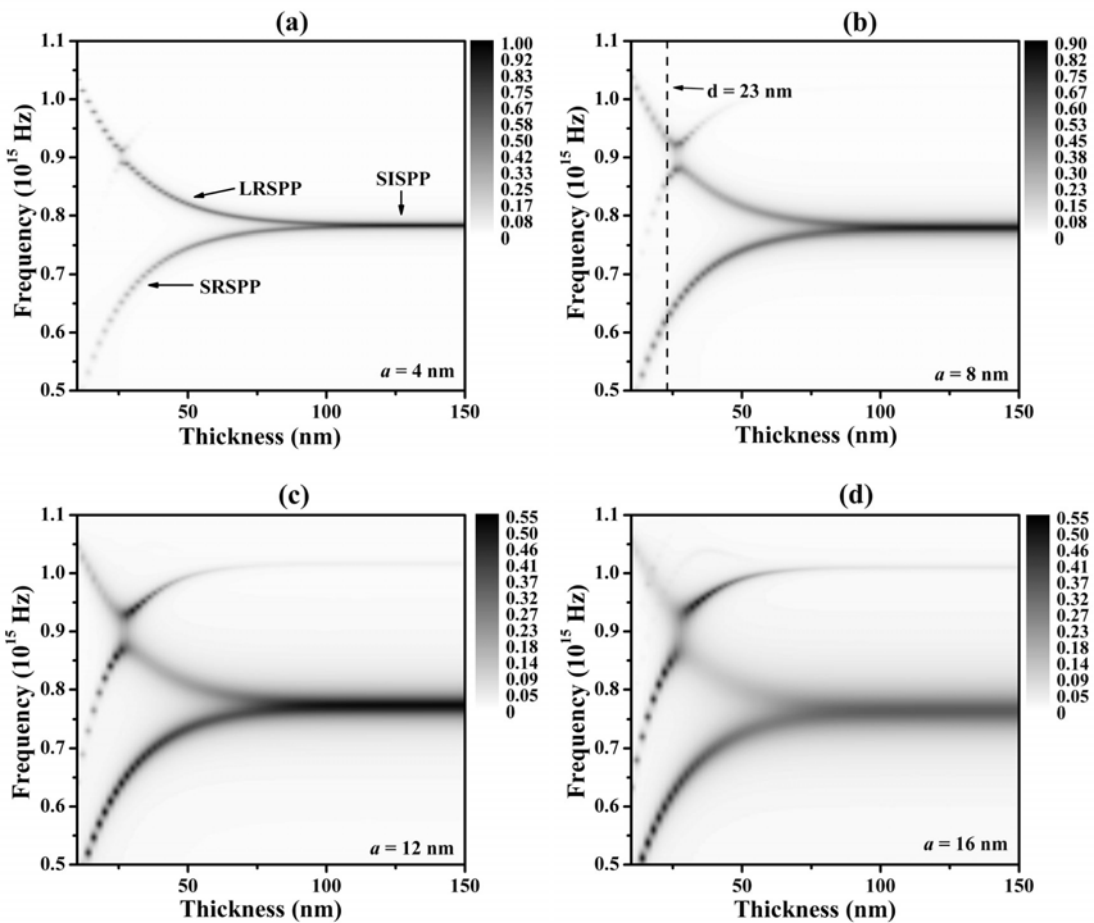
**Figure 8.3.1.1** Theoretical TE polarized (a) reflection and (b) transmission as a function of frequency and thickness at  $\theta = 42.3^\circ$  in the conical mount ( $\varphi = 90^\circ$ ) for a thin silver grating with conformal sinusoidal corrugations (fundamental amplitude  $a_0 = 8$  nm and pitch  $\lambda_g = 252$  nm) on both sides.

Figure 8.3.1.1 shows the theoretical TE polarized transmission and reflection as a function of frequency and thickness at  $\theta = 42.3^\circ$  in the conical mount ( $\varphi = 90^\circ$ ) for a thin silver grating with conformal sinusoidal corrugations (fundamental amplitude  $a_0 = 8$  nm and pitch  $\lambda_g = 252$  nm) on both sides. In the calculations, the Drude model with  $\omega_p = 1.32 \times 10^{16}$  rad/s and  $\tau = 1.45 \times 10^{-14}$  s is used to describe the dielectric constant of

silver. We assume that the bounding silica media (non-absorptive material) has a frequency-independent optical permittivity  $\epsilon_{\text{silica}} = 2.1286 + 0.0i$ .

As can be seen from Figure 8.3.1.1 (a), when the thickness of the silver film  $d > 100$  nm only one single interface SPP (SISPP) mode giving a reflection minimum is excited. As the thickness decreases the SISPP splits into two coupled SPP modes, the SRSPP and the LRSPP. The frequency separation of these two modes increases with decreasing thickness of silver film. Note the first order pseudo critical edge associated with the structure considered here for  $\theta = 42.3^\circ$  is located at a frequency  $f_c = 1.097 \times 10^{15}$  Hz. Therefore, in the conical mount case the zero-order region for  $\theta = 42.3^\circ$  ranges in frequency from 0 to  $1.097 \times 10^{15}$  Hz. Also note in the small thickness region the second order SRSPP is readily observed, and interferes with the LRSPP to form a significant anti-crossing around  $d \approx 26$  nm and  $f \approx 0.9 \times 10^{15}$  Hz. As expected the transmission, Figure 8.3.1.1 (b), shows similar mode behaviour, except that the resonant modes in the optical transmission are represented by transmission peaks.

As mentioned in the previous section, a zero-order single-interface metallic grating may redirect incident photon energy into two different channels, reflection and absorption. Similarly, a zero-order metallic thin film grating may redirect the incident energy into three different channels: transmission (T), reflection (R), and absorption (A). Again energy conservation requires:  $A + T + R = 1$ . Note in the thin film case, due to the existence of transmission the coupling strength is specified by the height of the absorption peak. Figure 8.3.1.2 shows the theoretical TE polarized resonant absorption ( $A = 1 - R - T$ ) in the conical mount as a function of frequency and thickness at  $\theta = 42.3^\circ$  for thin silver gratings with the same pitch  $\lambda_g = 252$  nm but different fundamental amplitude. It is obvious from Figure 8.3.1.2 that the coupling strength of the LRSPP is always smaller than that of the SISPP for all amplitudes. For the SRSPP the coupling strength is observed to be less than that of the SISPP at smaller amplitude ( $a = 4$  and  $8$  nm). On increasing the amplitude to  $12$  nm, as shown in Figure 8.3.1.2 (c), the coupling strength of the SRSPP becomes almost the same level as that of the SISPP. Further increasing the amplitude to  $16$  nm, as shown in Figure 8.3.1.2 (d), the coupling strength of the SRSPP is now greater than that of the SISPP.



**Figure 8.3.1.2** Theoretical TE polarized absorption as a function of frequency and silver film thickness at  $\theta = 42.3^\circ$  for thin silver film gratings with same pitch  $\lambda_g = 252$  nm but different fundamental amplitude (a)  $a_0 = 4$  nm, (b)  $a_0 = 8$  nm, (c)  $a_0 = 12$  nm, and (d)  $a_0 = 16$  nm in the conical mount ( $\varphi = 90^\circ$ ). The dashed line represents the thickness  $d = 23$  nm.

To more clearly understand the nature of the TE excited coupled SPP at  $\varphi = 90^\circ$  it is worth investigating the optical field profiles. As shown in Figure 8.3.1.2 (b), in the zero-order region for the thickness of silver film  $d = 23$  nm (indicated by a dashed line) and amplitude  $a = 8$  nm there are three accessible SPP modes: the SRSPP ( $f = 0.625 \times 10^{15}$  Hz), the second order SRSPP ( $f = 0.859 \times 10^{15}$  Hz), and the LRSPP ( $f = 0.933 \times 10^{15}$  Hz). Figure 8.3.1.3 shows the instantaneous  $E_{xy}$  vector fields for these three SPP modes. First note the surface charge density maxima for both the SRSPP and the LRSPP locate at the sides of the grating grooves. Figure 8.3.1.3 also clearly shows the symmetric and anti-symmetric surface charge density distributions for the SRSPP and the LRSPP.

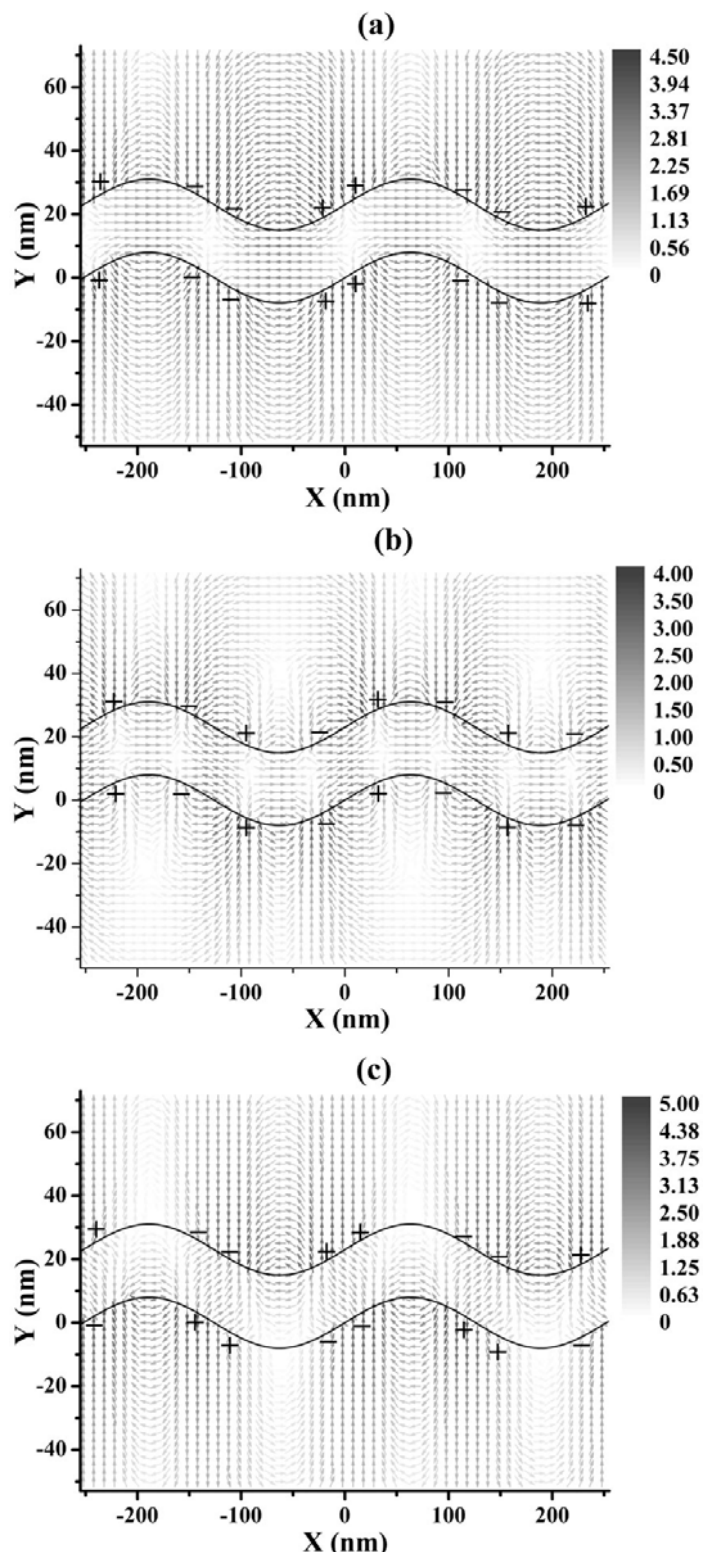


**Figure 8.3.1.3** Instantaneous  $E_{xy}$  vector fields of (a) the SRSPP ( $f = 0.625 \times 10^{15}$  Hz), (b) the second order SRSPP ( $f = 0.859 \times 10^{15}$  Hz), and (c) the LRSPP ( $f = 0.933 \times 10^{15}$  Hz) that can be excited on a thin silver film grating with thickness of 23 nm, pitch of 252 nm and amplitude of 8 nm at  $\theta = 42.3^\circ$  and  $\phi = 90^\circ$ .

The continuous lines represent the thin metal grating.

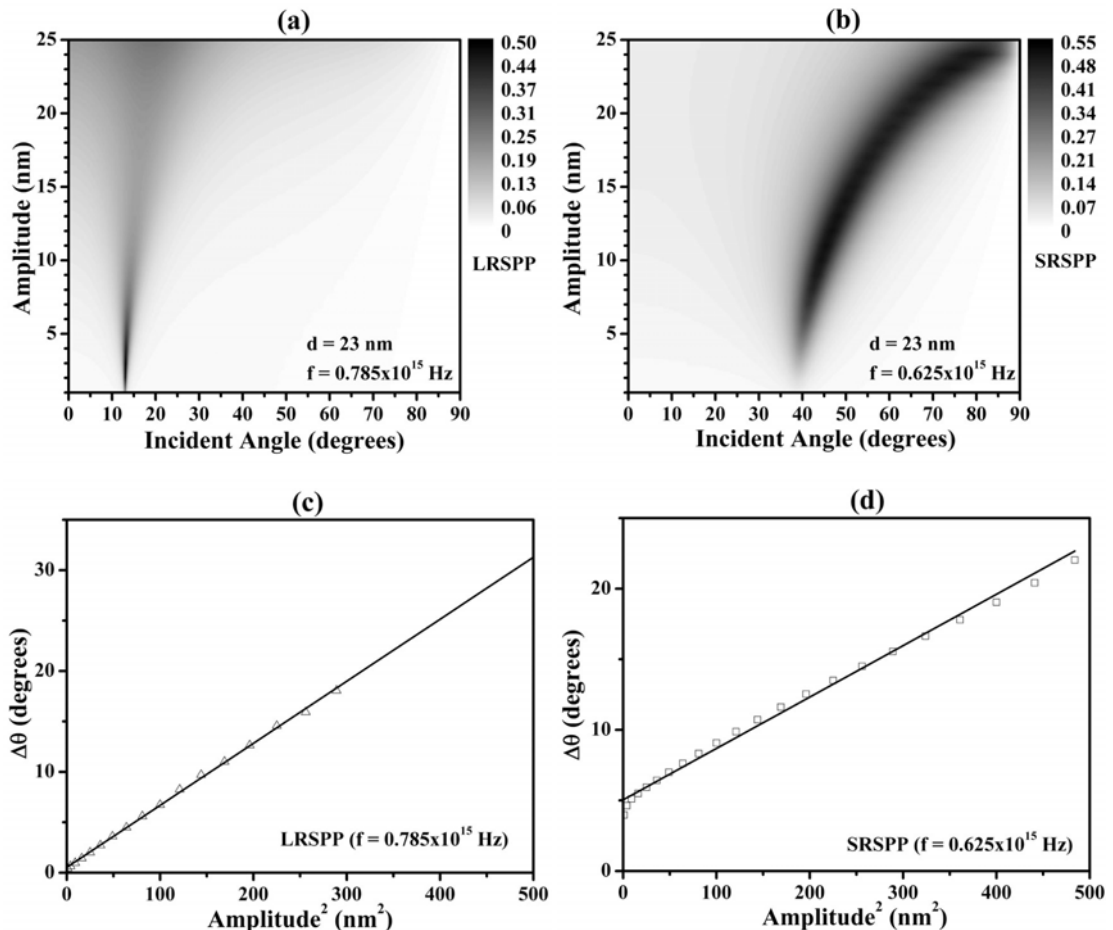


**Figure 8.3.1.4** Theoretical TE polarized Absorption ( $A = 1 - R - T$ ) as a function of incident angle and amplitude for (a) the LRSPP excited by a fixed frequency  $f = 0.785 \times 10^{15}$  Hz and (b) the SRSPP excited by a fixed frequency  $f = 0.625 \times 10^{15}$  Hz on a 252 nm pitch thin silver grating with thickness of 23 nm in the conical mount, together with the mode width ( $\Delta\theta$ ) of (c) the LRSPP and (d) the SRSPP absorption peak plotted against the amplitude square ( $a^2$ ).

Now we should demonstrate the total damping term for TE polarization in the thin film case at  $\phi = 90^\circ$ . Since the frequency separation between the LRSPP and the SRSPP is large, at one fixed incident frequency the LRSPP and the SRSPP can not be accessed at the same time. Hence in the angle-scan calculations the fixed frequencies  $f = 0.785 \times 10^{15}$  Hz and  $0.625 \times 10^{15}$  Hz are chosen to excite the LRSPP and the SRSPP respectively. Figure 8.3.1.4 (a) and (b) show theoretical TE polarized absorption ( $A = 1 - R - T$ ) as a function of incident angle and grating amplitude for the LRSPP and the SRSPP respectively on a 252 nm pitch thin silver grating with thickness of 23 nm in the conical mount. As mentioned above, by using the Lorentz function to fit the absorption peak at each amplitude, the mode width ( $\Delta\theta$ ) is acquired and this is plotted against  $a^2$  in

Figures 8.3.1.4 (c) and (d). A linear relation between  $\Delta\theta$  and  $a^2$  is readily observed in Figure 8.3.1.4 (c). It is not so apparent in Figure 8.3.1.4 (d). Compared Figure 8.3.1.4 (c) with Figure 8.2.7, it is found that the mode width of the LRSPP is always smaller than that of the SISPP, i.e., the propagation length of the LRSPP is longer than that of the SISPP for TE excitation on a 23 nm thin silver grating in the conical mount.

### 8.3.2 Coupling TM polarized radiation to coupled SPPs

In the first section of this chapter following the studies of Watts *et al.* [1997] we investigated the possible coupling of TM polarized radiation to the SPP on a single-interface metallic grating in the conical mount. It is found that such coupling on shallow gratings is very weak, and generally is not considered in practice. However, in our experiments a strong coupling is observed for TM polarized radiation incident on a shallow thin silver grating. To our knowledge, this is the first observation of such a strong coupling.

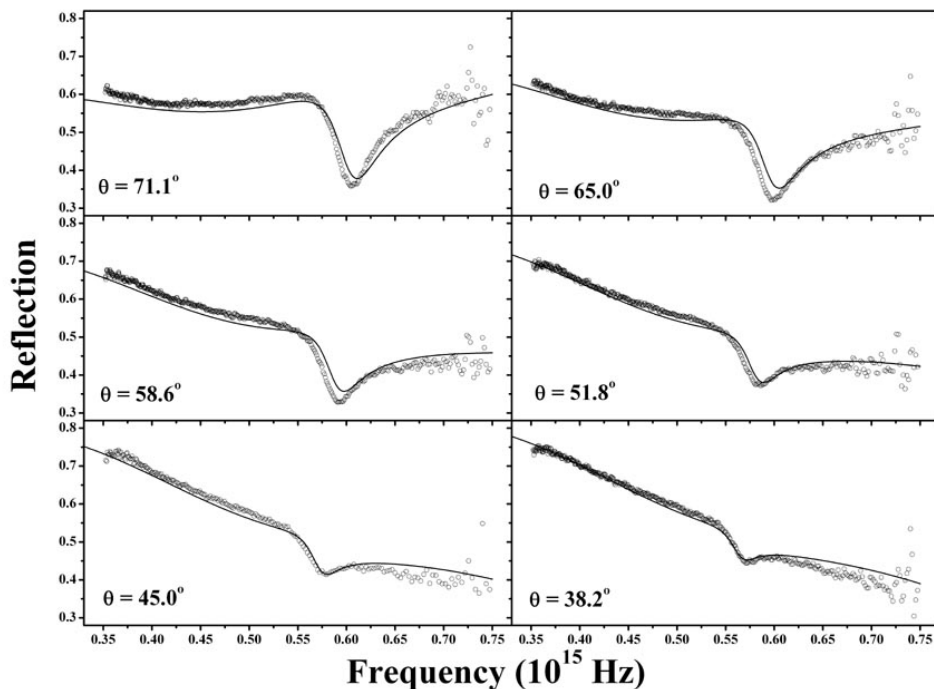


**Figure 8.3.2.1** Experimental wavelength-dependent reflectivity data (open circles) together with the model fits (solid lines) when TM polarized light is incident on a thin silver sinusoidal grating with thickness of 23 nm, pitch of 252 nm, and amplitude of 8 nm at different polar angles  $\theta = 71.1^\circ, 65.0^\circ, 58.6^\circ, 51.8^\circ, 45.0^\circ$ , and  $38.2^\circ$  in the conical mount ( $\phi = 90^\circ$ ).

Figure 8.3.2.1 illustrates the TM polarized wavelength-dependent absolute reflectivity data together with the model results for light incident on a thin silver grating pitch of  $\lambda_g = 252$  nm at different polar angles of  $\theta = 71.1^\circ, 65.0^\circ, 58.6^\circ, 51.8^\circ, 45.0^\circ$ , and  $38.2^\circ$  in the conical mount. The theoretical method employed here is based upon a conical version of the differential formalism originally developed by Chandezon *et al* [1982]. In the calculations here, for silver across the visible spectrum both the real and imaginary parts of its permittivity are described by polynomials,

$$\varepsilon_r(\omega) = -255.3185 + 198.63\omega - 60.794\omega^2 + 8.381\omega^3 - 0.43004\omega^4,$$

$$\varepsilon_i(\omega) = 83.2575 - 132.79\omega + 90.474\omega^2 - 32.88\omega^3 + 6.6591\omega^4 - 0.70893\omega^5 + 0.030913\omega^6,$$

where  $\omega = 2\pi c/\lambda (10^{-15} \text{ s}^{-1})$ , and for simplicity in fitting data to a model the refractive index of the bounding silica is treated as non-dispersive with  $n = 1.459$ . These polynomials inevitably pertain to somewhat different silver to that explored here in thin film form, but they are a good enough approximation to allow adequate modelling. In Figure 8.3.2.1, the best comparison between the model and the experimental data is achieved when the profiles of the two surfaces are set to  $[8 \sin(k_g x) + 23]$  nm for the incident interface and  $[8 \sin(k_g x)]$  nm for the transmitting interface. One sees that strong coupling occurs at  $f \approx 0.6 \times 10^{15}$  Hz at higher incident angles ( $\theta = 71.1^\circ, 65.0^\circ, 58.6^\circ$ ), while at smaller incident angles the coupling is still relatively weak.

As mentioned in the previous section, in the thin film case the height of the absorption peak is used to indicate the coupling strength. To obtain the experimental absorption spectra, the wavelength-dependent transmission data at polar angle  $\theta = 65.0^\circ$  are also measured. Then the experimental absorption data may be acquired according to the energy conservation  $A = 1 - R - T$ . Figure 8.3.2.2 shows the experimental TM polarized reflection, transmission, and absorption data at a polar angle of  $\theta = 65.0^\circ$ . Also plotted in Figure 8.3.2.2 are theoretical reflection, transmission, and absorption on a plane silver film with thickness of 23 nm at  $\theta = 65.0^\circ$ . Note at a resonant frequency  $f = 0.595 \times 10^{15}$  Hz a significant absorption peak (indicated by open stars) is readily observed in Figure 8.3.2.2.

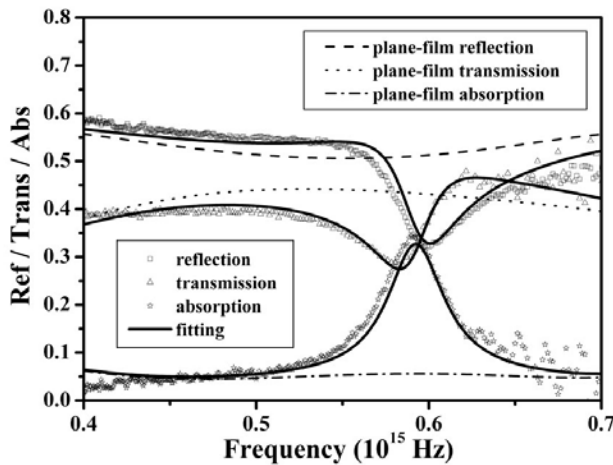


**Figure 8.3.2.2** Experimental reflection (open squares), transmission (open triangles), and absorption (open stars) together with the model fits (solid lines) when the TM polarized light is incident on a thin silver sinusoidal grating with thickness of 23 nm, pitch of 252 nm, and amplitude of 8 nm at polar angle  $\theta = 65.0^\circ$  in the conical mount ( $\varphi = 90^\circ$ ). Also theoretical reflection (dashed line), transmission (dotted line), and absorption (dash-dotted line) for a plane thin silver film with thickness of 23 nm are plotted.

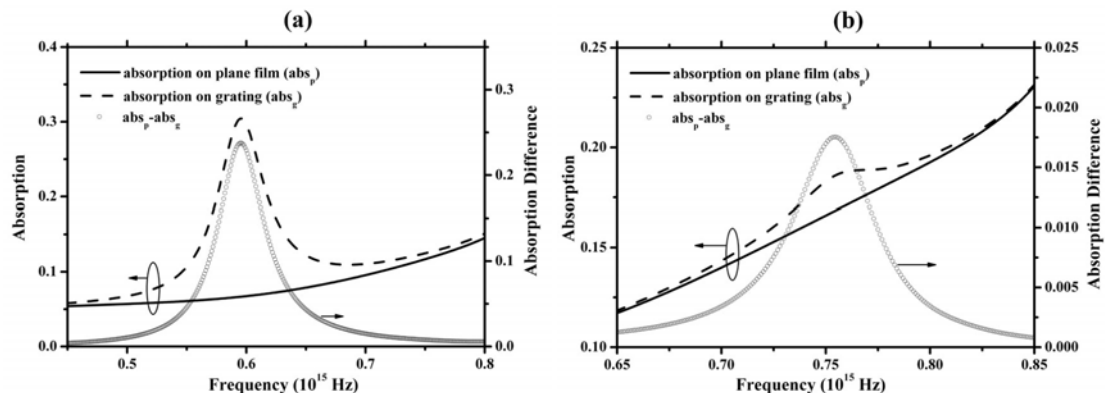


**Figure 8.3.2.3** Theoretical TM Absorption ( $A = 1 - R - T$ ) at polar angle  $\theta = 65.0^\circ$  in the conical mount for (a) a thin silver film with corrugation (dashed line) and without corrugation (solid line) together with the absorption difference (open circles) and (b) a single-interface with corrugation (dashed line) and without corrugation (solid line) together with the absorption difference (open circles). The thickness of the thin silver film is 23 nm. The corrugation in both cases has a pitch of 252 nm and amplitude of 8 nm.

To more clearly demonstrate that the coupling strength for the thin film grating case has been greatly increased, the theoretical TM polarized absorption at polar angle  $\theta = 65.0^\circ$  in the conical mount for both the thin silver film (with and without corrugation) case and single-interface (with and without corrugation) case are plotted in Figure 8.3.2.3, where the thickness of the thin silver film is 23 nm and the corrugation in both cases has a pitch of 252 nm and amplitude of 8 nm. Also plotted in Figure 8.3.2.3 is the

absorption difference between corrugated case and non-corrugated case. As shown in Figure 8.3.2.3 (b), for the single-interface case the coupling strength (the height of the absorption peak) of the mode (known as the SISPP) at resonant frequency  $f = 0.754 \times 10^{15}$  Hz is as small as 0.018, while in the thin film case the coupling strength at resonant frequency  $f = 0.595 \times 10^{15}$  Hz is 0.238, as shown in Figure 8.3.2.3 (a). Hence, it is obvious that the coupling strength at the resonant frequency for the thin film grating case has been enhanced  $0.238/0.018 \approx 13$  times.

Now we shall identify the mode observed at the resonant frequency  $f = 0.595 \times 10^{15}$  Hz. It is instructive to investigate the optical fields. Figure 8.3.1.3 shows the instantaneous  $E_{xy}$  vector fields for such a strongly coupled SPP mode. Comparing the surface charge density on the top surface to the density on the bottom surface, it clearly reveals a symmetric charge density distribution. Therefore the mode at resonant frequency  $f = 0.595 \times 10^{15}$  Hz is the SRSPP mode on a thin silver grating. Also note the surface charge density maxima on both top and bottom surfaces locate on the grating peaks and troughs; at these positions there are maximum normal components of electric field for TM polarization in the conical mount.

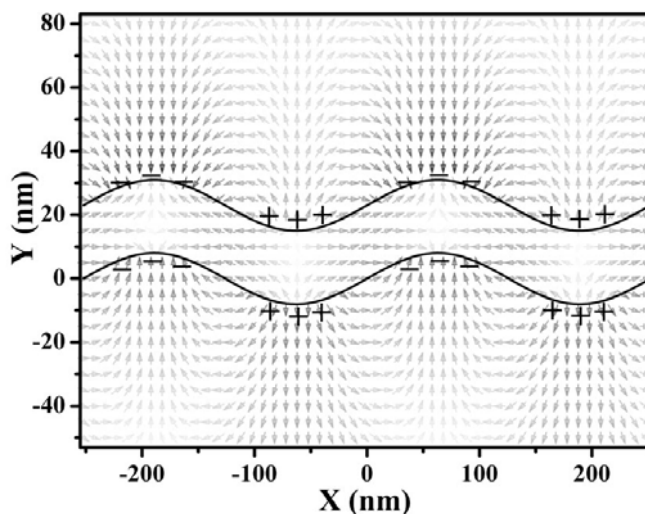


**Figure 8.3.2.4** Instantaneous  $E_{xy}$  vector fields at resonant frequency  $f = 0.595 \times 10^{15}$  Hz for a thin silver film grating ( $d = 23$  nm,  $\lambda_g = 252$  nm, and  $a = 8$  nm) at  $\theta = 65.0^\circ$  and  $\varphi = 90^\circ$ . The continuous lines represent the thin metal grating.

It is known that with film thickness decreasing the SISPP mode splits into two coupled SPP modes: the SRSPP and the LRSPP. In the conical mount for TM

polarization we have investigated the SRSPP on thin film gratings above. Now we shall concentrate on coupling of TM polarized radiation to the LRSPP on thin film gratings in the conical mount. Note since the LRSPP has moved out of the visible region for thin silver grating with a pitch of 252 nm, in the calculations the dielectric constant of silver which was described as polynomials above is now replaced by a Drude model with  $\omega_p = 1.32 \times 10^{16}$  rad/s and  $\tau = 1.45 \times 10^{-14}$  s.

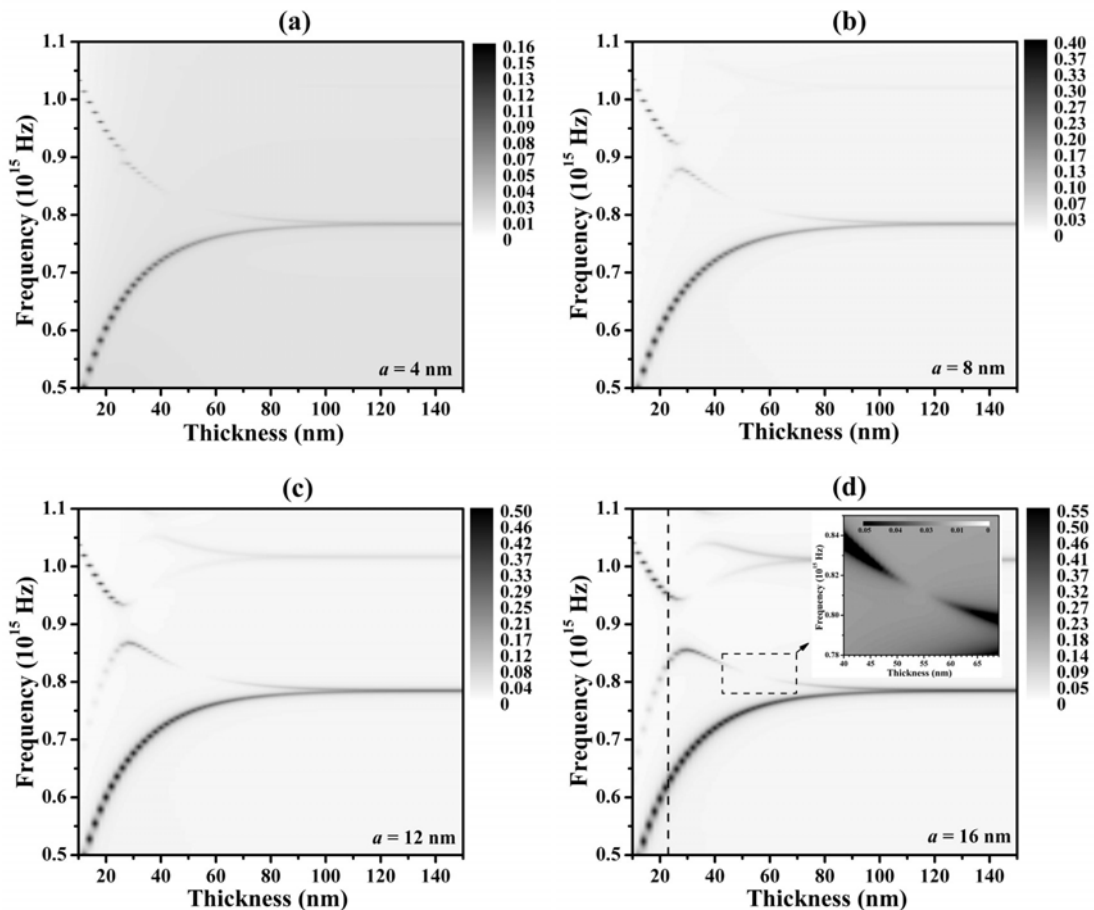


**Figure 8.3.2.5** Theoretical TM polarized Absorption ( $A = 1 - R - T$ ) as a function of frequency and silver film thickness at  $\theta = 42.3^\circ$  for thin silver film gratings with the same pitch  $\lambda_g = 252$  nm but different fundamental amplitude (a)  $a = 4$  nm, (b)  $a = 8$  nm, (c)  $a = 12$  nm, and (d)  $a = 16$  nm in the conical mount ( $\varphi = 90^\circ$ ). The dashed line represented the thickness  $d = 23$  nm.

Figure 8.3.2.5 shows the theoretical TM polarized resonant absorption ( $A = 1 - R - T$ ) as a function of frequency and thickness of silver film at  $\theta = 42.3^\circ$  for thin silver gratings with the same pitch  $\lambda_g = 252$  nm but different fundamental amplitude in the conical mount. It is obvious that the absorption for the SRSPP and the SISPP is

increased with increasing grating amplitude from 4 nm to 16 nm. Also in the smaller thickness region the absorption for the LRSPP is significantly increased with increasing amplitude. In the final part of this section we will demonstrate how the absorption for the SRSPP, the LRSPP and the SISPP change in detail with increasing amplitude. Also note the second order SRSPP shifts down its resonant frequency rapidly with decreasing film thickness, and in the small thickness region it interferes with the LRSPP to form an anti-crossing centred around  $d \approx 26$  nm and  $f \approx 0.9 \times 10^{15}$  Hz. With increasing amplitude the interaction between the second order SRSPP and the LRSPP becomes stronger, and hence the gap between the higher frequency branch and the lower frequency branch becomes larger.

As indicated by a dashed line in Figure 8.3.2.5 (d) for the thickness of silver film  $d = 23$  nm and amplitude  $a = 16$  nm, in the zero-order region there are three accessible SPP modes: the SRSPP ( $f = 0.629 \times 10^{15}$  Hz), the second order SRSPP ( $f = 0.83 \times 10^{15}$  Hz), and the LRSPP ( $f = 0.95 \times 10^{15}$  Hz). The instantaneous  $E_{xy}$  vector field distribution for the SRSPP ( $f = 0.595 \times 10^{15}$  Hz) has already been investigated in Figure 8.3.2.4 on a thin silver grating with thickness of 23 nm and amplitude of 8 nm at  $\theta = 65.0^\circ$  and  $\varphi = 90^\circ$ . Here only the instantaneous  $E_{xy}$  vector fields for the second order SRSPP and the LRSPP excited on a thin silver film grating with thickness of 23 nm and amplitude of 16 nm at  $\theta = 42.3^\circ$  and  $\varphi = 90^\circ$  are shown in Figure 8.3.2.6. First note the different surface charge density distributions for the LRSPP and the second order SRSPP. As shown in Figure 8.3.2.6 (b), for the second order SRSPP, the spatial variation of the surface charge density distribution along the bottom surface is in phase with that on the top surface (symmetric distribution), while for the LRSPP in Figure 8.3.2.6 (a), the bottom surface has the opposite surface charge density to the top surface (anti-symmetric distribution). By comparing Figure 8.3.2.6 and Figure 8.3.2.4, one sees clearly that the surface charge density maxima for both the SRSPP and the LRSPP occur at the grating peaks and troughs. Also note that, as shown in Figure 8.3.2.6 (b) the surface charge density maxima for the second order SRSPP locate on the sides of the grating grooves in addition to at the grating peaks and troughs.

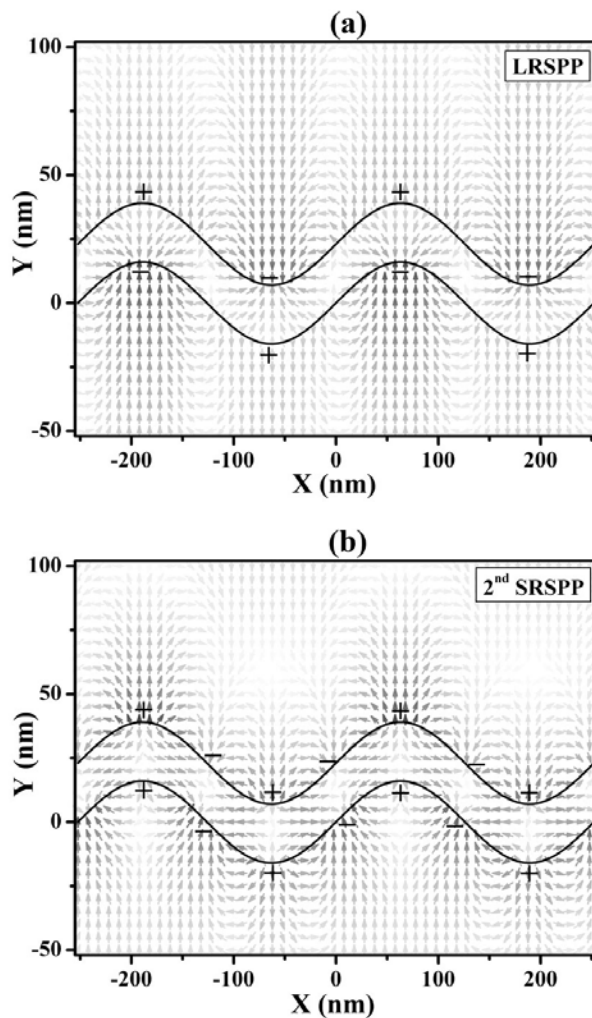


**Figure 8.3.2.6** Instantaneous  $E_{xy}$  vector fields of (a) the LRSPP ( $f = 0.95 \times 10^{15}$  Hz) and (b) the second order SRSPP ( $f = 0.83 \times 10^{15}$  Hz) that can be excited on a thin silver film grating with thickness of 23 nm, pitch of 252 nm and amplitude of 16 nm at  $\theta = 42.3^\circ$  and  $\varphi = 90^\circ$ . The continuous lines represent the thin metal grating.

Figure 8.3.2.5 also shows a very interesting coupling strength change for the LRSPP and the second order SRSPP. With the decrease of thickness the coupling strength for both the LRSPP and the second order SPP first decreases to almost zero, and then the coupling strength increases again. For the TE polarization case, as shown in Figure 8.3.1.2, no similar phenomenon is observed for the second order SRSPP and the LRSPP. Leaving the detailed analysis of this phenomenon for further studies, we would like to only show a series of optical fields for the LRSPP on a thin silver grating with the same amplitude of 16 nm but different thicknesses around the position where the minimum coupling strength occurs.

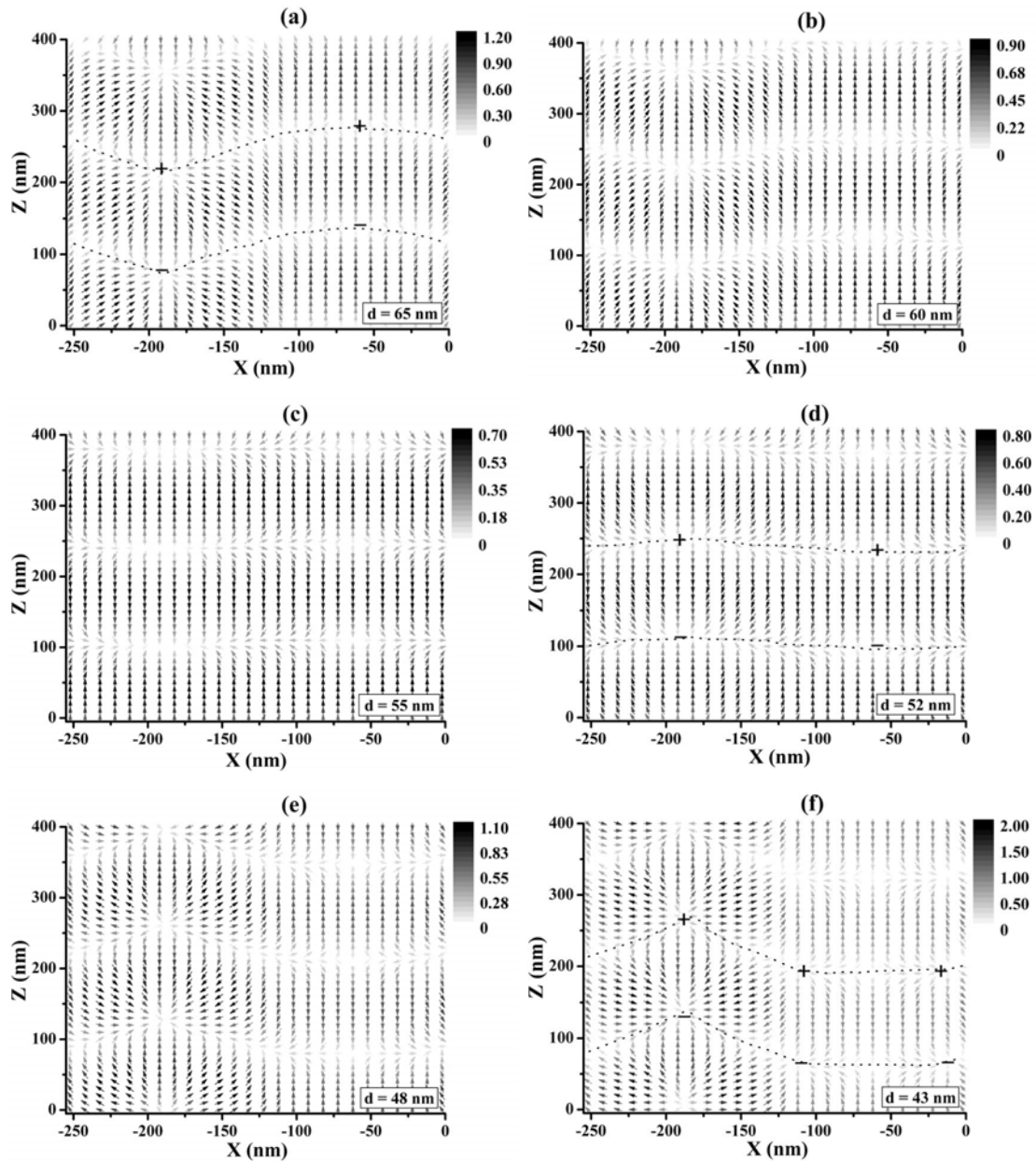


**Figure 8.3.2.7** Instantaneous electric field vector  $E_{xz}$  distributions at  $\theta = 42.3^\circ$  and  $\varphi = 90^\circ$  for the LRSPP on the top surface of a thin silver grating with a same pitch of 252 nm and a same amplitude of 16 nm but different thicknesses (a)  $d = 65$  nm,  $f = 0.801 \times 10^{15}$  Hz, (b)  $d = 60$  nm,  $f = 0.8055 \times 10^{15}$  Hz, (c)  $d = 55$  nm,  $f = 0.811 \times 10^{15}$  Hz, (d)  $d = 52$  nm,  $f = 0.8151 \times 10^{15}$  Hz, (e)  $d = 48$  nm,  $f = 0.8216 \times 10^{15}$  Hz, and (f)  $d = 43$  nm,  $f = 0.831 \times 10^{15}$  Hz. The fields are plotted in the  $x$ - $z$  plane and one repeat period of the structure is shown ( $\lambda_g$ ). The grating peak and trough locate at  $x = -189.2$  nm and  $-63.2$  nm respectively.

As clearly shown in the inset graph of Figure 8.3.2.5 (d), at a thickness  $d \approx 52$  nm the coupling strength for the LRSPP has a minimum which is almost zero. Figure 8.3.2.7 shows the instantaneous  $E_{xz}$  vector fields distributions on the top surface for the

LRSPP on a thin silver grating (pitch  $\lambda_g = 252$  nm, amplitude  $a = 16$  nm) with different thicknesses  $d = 43, 48, 52, 55, 60$ , and  $65$  nm. Note the instantaneous  $E_{xz}$  vector field on the top surface shown here is a result of interference between the incident fields and the fields reflected from both the top surface and the bottom surface. As discussed in Figure 8.2.4 (b) for the instantaneous  $E_{xz}$  vector field distributions of the TM excited SISPP on the surface, the surface charge centers at the grating trough have a shift in the  $z$  direction relative to the nearest charge centers at the grating peak. Similarly such a shift between the surface charge centers at the grating trough and grating peak is also observed in Figure 8.3.2.7 (a) for a thickness of  $65$  nm, where a dotted line connects all of the nearest surface charge with the same sign. With decrease of thickness, as shown in Figure 8.3.2.7 (b) and (c) the shift between the surface charge centers at the grating peak and trough becomes smaller. At a thickness of  $\sim 52$  nm, as shown in Figure 8.3.2.7 (d), such a shift becomes almost zero, i.e., the line (indicated as a dotted line) connecting all of the nearest surface charge with the same sign is almost horizontal. Under these circumstances the interference between all of the fields above the top surface makes the instantaneous  $E_{xz}$  vector field distribution on the top surface look like the field distribution for a plane film giving thus no coupling. On further decrease of the film thickness, as shown in Figure 8.3.2.7 (e) and (f), the shift between the surface charge centers at the grating peak and trough increases again. By comparing Figure 8.3.2.7 (f) with (a), it is found that in Figure 8.3.2.7 (a) the surface charge centers at the grating trough shifts along  $+z$  direction relative to the surface charge centers at the grating peak, however in Figure 8.3.2.7 (f) the centers at the grating trough shifts in the opposite direction ( $-z$ ) relative to the centers at the grating peak. Also note in Figure 8.3.2.7 (f), two surface charge centers on the sides of the grating grooves are readily observed, which is clear evidence of the interference between the LRSPP and the second order SRSPP.

Now we shall demonstrate the total damping term for TM polarization in the thin film case at  $\varphi = 90^\circ$ . Figure 8.3.2.8 (a) and (b) show theoretical TM polarized absorption ( $A = 1 - R - T$ ) as a function of incident angle and grating amplitude for the LRSPP excited by a fixed frequency  $f = 0.785 \times 10^{15}$  Hz and the SRSPP excited by a fixed frequency  $f = 0.625 \times 10^{15}$  Hz respectively on a 252 nm pitch thin silver grating with thickness of 23 nm in the conical mount.

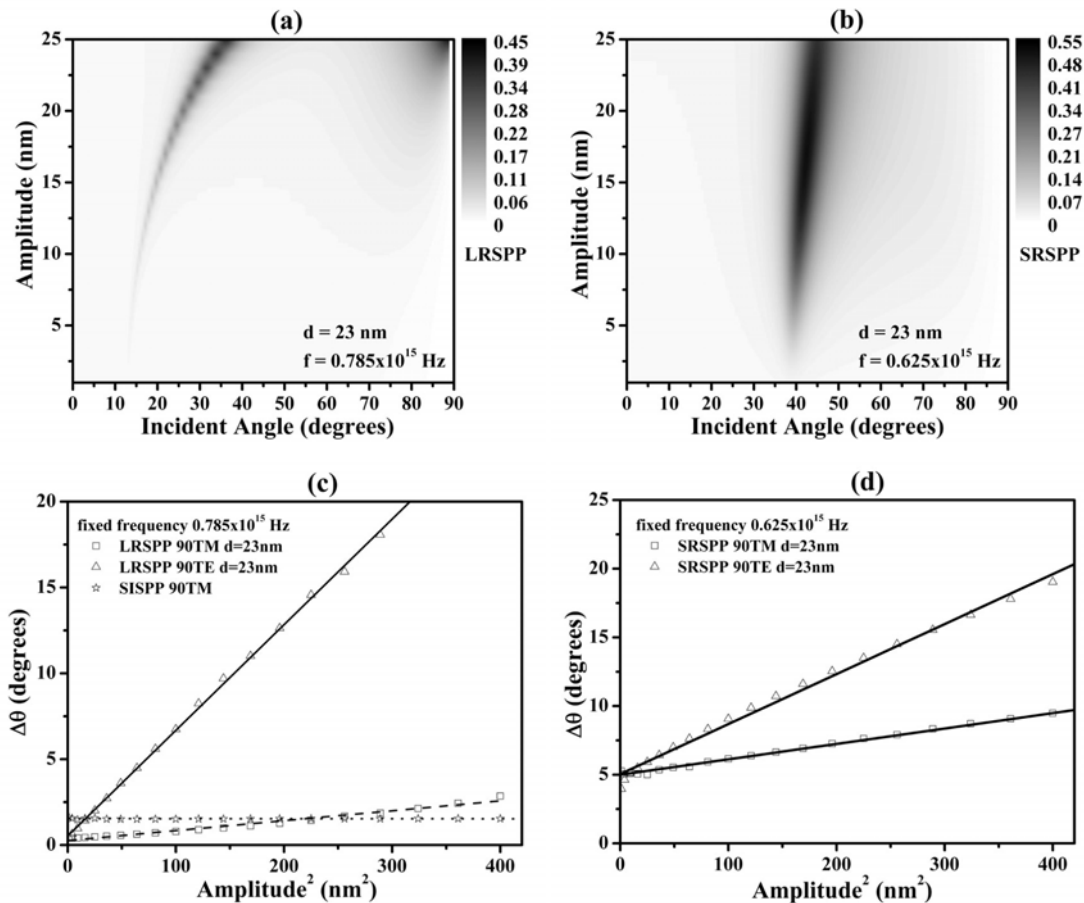


**Figure 8.3.2.8** Theoretical TM polarized Absorption ( $A = 1 - R - T$ ) as a function of the incident angle and the amplitude for (a) the LRSPP excited by a fixed frequency  $f = 0.785 \times 10^{15}$  Hz and (b) the SRSPP excited by a fixed frequency  $f = 0.625 \times 10^{15}$  Hz on a 252 nm pitch thin silver grating with thickness of 23 nm in the conical mount, together with the mode width  $\Delta\theta$  of (c) the LRSPP and (d) the SRSPP absorption peak plotted against the amplitude square ( $a^2$ ).

At each amplitude the absorption peak is fitted using a Lorentz function described above, and then the mode width  $\Delta\theta$  is given by the parameter  $w$ . Figures 8.3.2.8 (c) and (d) show the linear relation (indicated as open squares) between the mode width and  $a^2$  for the LRSPP and the SRSPP respectively. Also plotted in Figure 8.3.2.8 (c) is the mode width for the TE excited LRSPP and the TM excited SISPP that has been shown in Figure 8.2.7 and Figure 8.3.1.4 (c). One sees obviously that with increasing amplitude the mode width of the TE polarized LRSPP (indicated as open triangles) is always larger than that of the TM polarized LRSPP, i.e., the TM polarized LRSPP propagation length is larger than the TE polarized LRSPP propagation length. It

is also found that the TM polarized LRSPP mode width line crosses the TM excited SISPP mode width line (indicated as open stars) at an amplitude of  $a_c \approx 15$  nm. Hence at  $a_c$  the LRSPP and the SISPP for TM excitation in the conical mount propagate the same distance. When the amplitude is smaller than  $a_c$  the TM excited LRSPP propagation length is longer, and the TM excited SISPP propagation length is longer if the amplitude is larger than  $a_c$ . To compare the propagation length between the TE excited SRSPP and the TM excited SRSPP, the TE excited SRSPP mode width (indicated as open triangles) at a fixed frequency  $f = 0.625 \times 10^{15}$  Hz is also plotted in Figure 8.3.2.8 (d). At the same amplitude it is clear that the TM excited SRSPP propagation length is longer than the TE excited SRSPP propagation length.

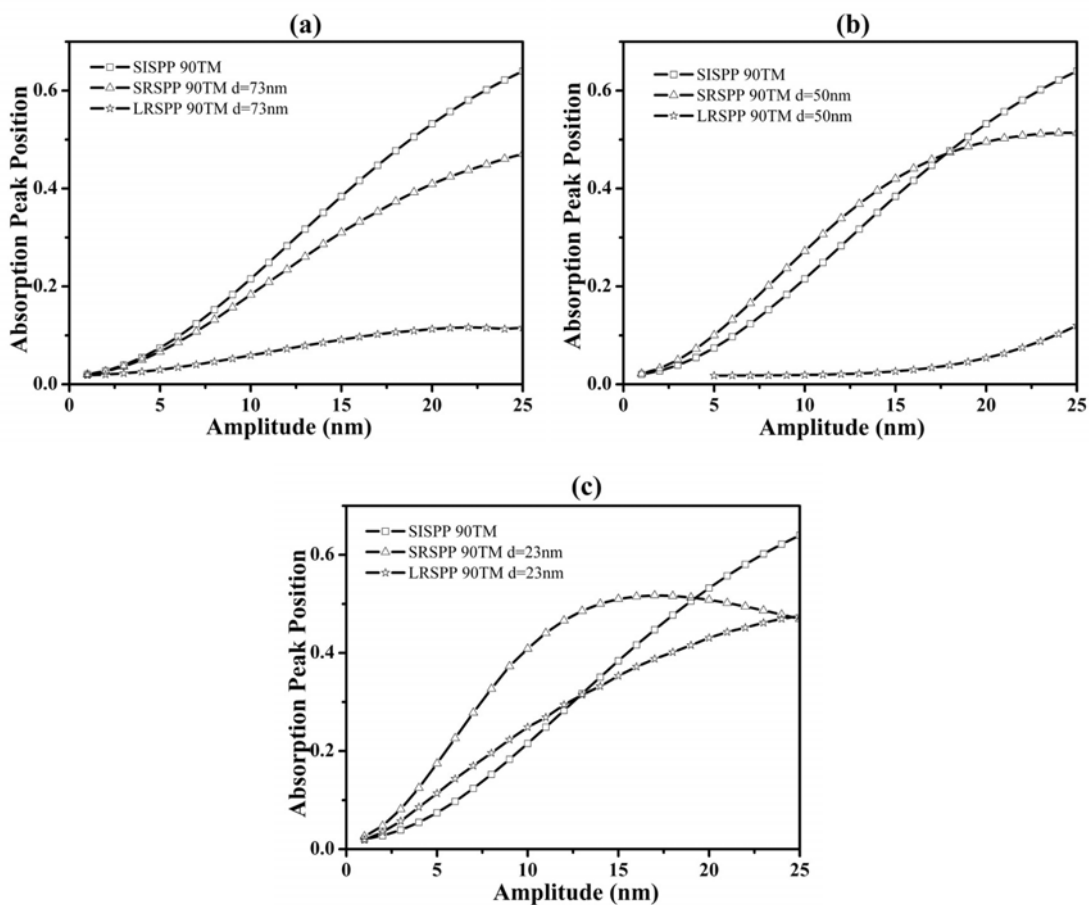


**Figure 8.3.2.9** Theoretical TM excited SRSPP (indicated as open triangles) and LRSPP (indicated as open stars) absorption peak height as a function of amplitude at  $\theta = 42.3^\circ$  and  $\varphi = 90^\circ$  for different film thicknesses (a)  $d = 73$  nm, (b)  $d = 50$  nm, and (c)  $d = 23$  nm. The absorption peak height for the TM excited SISPP (indicated as open squares) is also plotted in each of graphs.

To more clearly demonstrate the TM excited SRSPP resonant absorption enhancement on a thin silver grating at  $\varphi = 90^\circ$  discussed at the beginning of this section, it is instructive to investigate the coupling strength for the SRSPP and the LRSPP at different film thicknesses and amplitudes. Figure 8.3.2.9 shows the TM excited SRSPP and the TM excited LRSPP absorption peak height (coupling strength) as a function of the amplitude for different film thicknesses  $d = 73, 50,$  and  $23\text{ nm}$  at  $\theta = 42.3^\circ$  and  $\varphi = 90^\circ$ . For comparison, the TM excited SISPP absorption peak height (indicated as open squares) is also plotted against the amplitude in each of the graphs of Figure 8.3.2.9. As shown in Figure 8.3.2.9 (a), for a thin silver grating with a thickness of  $73\text{ nm}$ , the absorption for the SRSPP (indicated as open triangles), the LRSPP (indicated as open stars), and the SISPP increases with increasing amplitude. At each amplitude, the absorption for both the SRSPP and the LRSPP is less than that for the SISPP. At  $d = 73\text{ nm}$ , no absorption enhancement occurs for the SRSPP compared to the SISPP. When the thickness is  $50\text{ nm}$ , as shown in Figure 8.3.2.9 (b), in the amplitude region  $0\text{ nm} < a < 18\text{ nm}$  the absorption for the SRSPP is slightly higher than that for the SISPP, i.e., a small absorption enhancement occurs. On further decrease of the film thickness to  $23\text{ nm}$ , a significant absorption enhancement for the SRSPP is readily observed in Figure 8.3.2.9 (c) in the amplitude region  $0\text{ nm} < a < 19\text{ nm}$ . For the smaller amplitude region  $0\text{ nm} < a < 13\text{ nm}$  the absorption for the LRSPP is enhanced compared to the absorption for the SISPP. By comparing these plots in Figure 8.3.2.9, it is found that the phenomenon of the SRSPP absorption enhancement observed in our experiments is a special case, which only occurs for a thin film grating with relatively shallow corrugations.

Finally in this section, we explore the fundamental absorption in the zero-order metallic grating caused by Joule heating of the metal. The mean quantity of heat evolved per unit time and volume  $Q$  (Landau and Lifshitz [1960]) is given by:

$$Q = \frac{\omega}{8\pi} (\varepsilon'' |E|^2 + \mu'' |H|^2) \quad 8.3.2.1$$

where  $\varepsilon''$  is the imaginary part of the metal permittivity and  $\mu''$  is set to 0 here. Figure 8.3.2.10 shows the time averaged  $|E_{\text{total}}|^2$  distributions for the TM excited SRSPP ( $f = 0.6296 \times 10^{15}\text{ Hz}$ ) on a thin silver grating ( $d = 23\text{ nm}$ ,  $\lambda_g = 252\text{ nm}$ , and  $a = 8\text{ nm}$ ) and the TM excited SISPP ( $f = 1.0207 \times 10^{15}\text{ Hz}$ ) at  $\theta = 42.3^\circ$  in the conical mount. The

absorption for these two SPP modes are  $A_{srsp} = 0.3269$  and  $A_{sispp} = 0.0272$  respectively, and the ratio of  $A_{srsp}/A_{sispp} \approx 12$ . By integrating the  $|E_{\text{total}}|^2$  for the SRSPP and the SISPP inside the metal and combining the equation 8.3.2.1, we obtain a ratio of  $Q_{srsp}/Q_{sispp} \approx 12$ . The two ratios having the same value is clear evidence that the absorption in a zero-order metallic grating is only caused by the Joule heating of the metal.

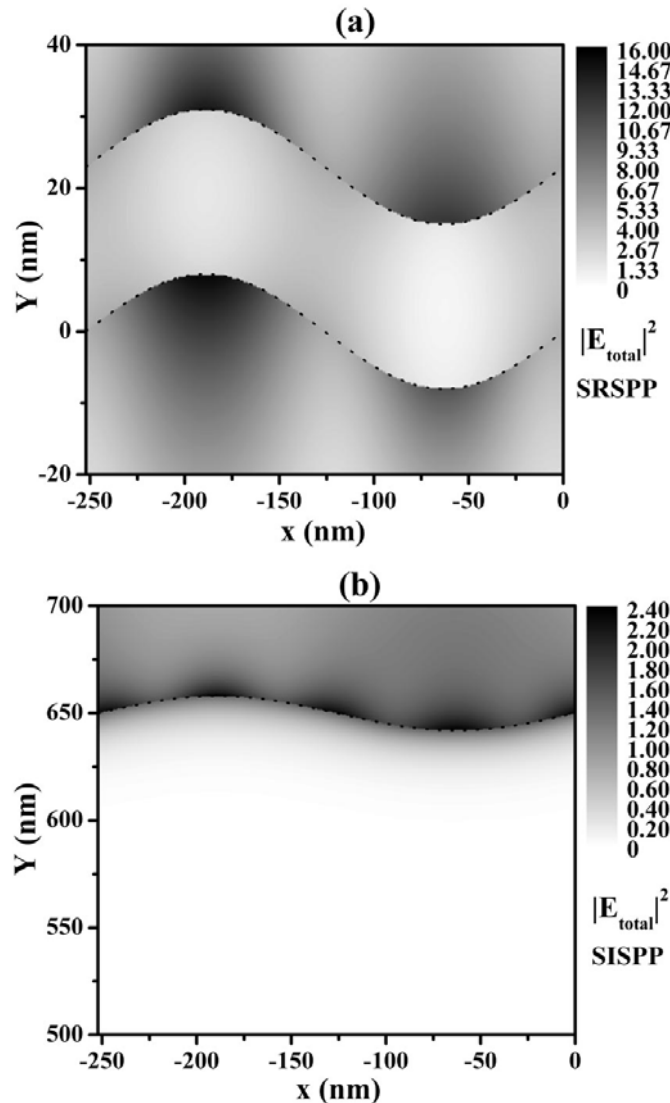


**Figure 8.3.2.10** Time averaged  $|E_{\text{total}}|^2$  distributions for the TM excited SRSPP ( $f = 0.6296 \times 10^{15}$  Hz) on a thin silver grating ( $d = 23$  nm,  $\lambda_g = 252$  nm, and  $a = 8$  nm) and the TM excited SISPP ( $f = 1.0207 \times 10^{15}$  Hz) at  $\theta = 42.3^\circ$  in the conical mount. The dotted line represents the silica/silver interface.

## 8.4 Summary

In this chapter the excitation of the SISPP on a single-interface metal grating bounded by silica media in the conical mount ( $\phi = 90^\circ$ ) is investigated for both TE and TM polarizations. It is shown that in the conical mount TE polarized radiation can be well coupled to the SPP. In addition for TM polarization, it is theoretically shown that when the amplitude of the grating is relatively small (compared to the grating pitch) it is still possible to excite the SISPP in the conical mount, though the coupling strength is very weak. The relation between the SISPP mode width for both TE and TM polarizations and grating amplitude is also investigated, where a linear dependence on  $a^2$  is observed for the TE case. The propagation length of the TE excited SISPP decreases rapidly with increasing the amplitude. However the propagation length of the TM excited SISPP in the conical mount is almost a constant in the small amplitude region.

The coupled SPPs (the LRSPP and the SRSPP) on thin silver gratings in the conical mount are investigated for both the TE and TM polarizations as well. The absorption as a function of thickness and frequency is investigated extensively for different amplitudes. Two interesting phenomena are found in the TM polarization case. First the coupling strength of the TM excited LRSPP and the TM excited second order SRSPP both have an almost zero minimum with decreasing film thickness. The instantaneous  $E_{xz}$  vector field distributions are investigated for the LRSPP around this minimum coupling strength. Due to the interference between the incident fields and the reflected fields (from both the top surface and the bottom surface), at some thicknesses the resulting fields on the grating top surface look like the fields in the plane thin film case. Second the first observation of strong coupling to a TM excited SPP is observed experimentally on a thin silver grating with shallow corrugations in the conical mount. It is found that the coupling strength of this new SPP mode is enhanced greatly compared to that of the TM polarized SISPP mode on a single interface grating with the same pitch and corrugation. By exploring the optical field distributions at the resonant frequency this new SPP mode is identified as the SRSPP mode. Finally the propagation length of the SRSPP and the LRSPP for both TM and TE excitations are investigated in the small amplitude region.

# **Chapter 9**

## **Conclusions and Future Work**

### **9.1 Summary of Thesis**

In this thesis original experimental investigations of the optical response of various surface relief metallic structures are presented, with associated theoretical discussions. The focus is on the SPPs and waveguide modes supported by metallic gratings with either single or two interfaces and metallic microcavities.

In the work on very deep single interface silver gratings a thorough study of reflectivity in the visible regime has been undertaken. Initially the case of sinusoidal deep silver gratings with different depths is explored. From comparison of the dispersion curves for gratings with different amplitudes, the prediction that the SPP modes shift to lower frequency, and become flat banded effectively localized modes with increasing grating amplitude is verified experimentally and theoretically. However due to over-coupling the self-coupled SPP modes in deep sinusoidal gratings are extremely broad and shallow. To more clearly demonstrate the nature of the self-coupled SPPs the case of narrow Gaussian-grooved deep silver gratings is also studied. The modelling studies have shown far more pronounced reflectivity minima and a family of self-coupled SPPs, which are extremely flat banded with fields highly localized within the grooves, and which occur even in the zero order region of the spectrum. Experimental efforts were made to confirm the theoretical predictions for narrow Gaussian-grooved gratings. However due to the rough grating groove side surface, it was not possible to fit the reflectivity data obtained to theory. However the experimental dispersion of these modes was found to be very similar to the modelled dispersion, and therefore we believe that it is these self-coupled SPP modes which have been excited. The main new result which is of interest in the experiments is that sharp reflection peaks occur for high incident angles.

The next section of the thesis concerned SPPs and waveguide modes supported by metallic microcavities consisting of an optically thin silver film coated with a layer

of waveguide medium having a periodically modulated upper surface, with or without a cladding silver layer. Firstly the optical properties of a short-pitch periodically corrugated photoresist waveguide structure on a thin silver tunnel barrier are explored for TM polarization over the azimuth angle range  $\varphi = 0^\circ$  to  $90^\circ$ . By comparing the predicted band structure with both TM and TE reflectivity all the modes supported by the structure are identified. Both experimental data and theoretical fitting show that the introduction of the corrugation into the waveguide produces band gaps in the dispersion curves. Typically only the photonic band gaps caused by the modes self-crossing at the Brillouin zone boundary have been previously studied. In this section a new kind of band gap, an anti-crossing, which may also have potential applications, caused by different types of modes crossing at other than the Brillouin zone boundary are extensively explored at azimuth angles other than  $\varphi = 0^\circ$  or  $90^\circ$ . As an extension to the work on metallic microcavities without cladding metal layers a thorough reflectivity study of metallic microcavities with a semi-infinite cladding metal layer is explored at azimuth angles  $\varphi = 0^\circ$  and  $90^\circ$  for both TM and TE polarizations. The photonic band-gaps at the Brillouin zone boundary and anti-crossings within the Brillouin zone are observed directly in the experimental dispersion curves. In particular a flat photonic band caused by the anti-crossings between SPPs and waveguide modes in the TM polarized dispersion curves at the azimuth angle  $\varphi = 0^\circ$  is presented. Further, the resonant frequency of this flat photonic band can be designed through appropriate choice of thickness of the guide medium and the amplitude of the grating.

In the third section of this thesis, attention focuses on a topic that is generating great interest amongst the research community at the present time. Initially the case of a two-interface thin silver film sinusoidal grating bounded with silica media is explored in the classical mount (azimuth angle  $\varphi = 0^\circ$ ) for TM polarization, showing that the single-interface SPP (SISPP) mode splits into two coupled SPP modes, the long-range SPP (LRSPP) and the short-range SPP (SRSPP), with decreasing thickness of silver film. More interesting results have been investigated experimentally and theoretically in the visible range when a small  $2k_g$  component is added to the grating profile. It is found that the  $2k_g$  component in the grating profile is the key factor leading to the appearance of a band gap within the Brillouin zone, formed by the anti-crossing of the LRSPP scattered by  $+k_g$  and the SRSPP scattered by  $-k_g$ . Interestingly the band gap which would appear

on a single-interface silver grating for normal incidence radiation does not appear in the two self-crossing points of the LRSPP modes and the SRSPP modes at normal incidence for thin gratings with identical corrugations on both sides. The reason for this interesting result is because of the symmetry of the standing wave states of the expected two modes relative to the  $2k_g$  component of the grating. Following this the case where the two corrugations on each surface are not conformal is explored theoretically. It is found that to open up band gaps at normal incidence for the SRSPP and the LRSPP modes two conditions, non-identical corrugations on each side of the thin grating and the existence of a  $2k_g$  component, must be fulfilled.

The most exciting result arises in the coupling of TM polarized radiation to the SPP on thin silver film shallow gratings in the conical mount ( $\varphi = 90^\circ$ , the grating vector perpendicular to the incidence plane). Since in general TM polarized light is not considered to excite the SPP on a single-interface metallic grating in the conical mount (due to the very weak coupling), in the past one hundred years there are almost no experimental and theoretical efforts undertaken to explore the SPP excited by TM polarized radiation in the conical mount, except that of the special case on a very deep single-interface metallic grating reported by Watts *et al.* [1997]. It is very surprising that in our experiments strong TM polarized coupling to a SPP mode is observed on a thin silver film grating with small amplitude. The instantaneous electric fields distributions at resonant frequency show that this strongly coupled mode is the SRSPP mode. A thorough theoretical study of such a thin silver film shallow grating in the visible regime has been presented in the conical mount for both TM and TE polarizations. In addition to the resonant absorption enhancement for the SRSPP, a second original phenomenon is observed – that at some thicknesses zero coupling strength occurs for the TM excited LRSPP due to the interference between the incident field and the reflected fields.

## 9.2 Possible Applications

SPPs have, so far, been somewhat successfully applied in chemical and biological sensors, where their sensitivity to the refractive index of the dielectric adjacent to the metal surface is used to determine changes in the local environment at the interface.

Here we would like to demonstrate several other possible applications for which they may be of use.

The SPPs on high-aspect ratio metal gratings (chapter 4) could produce selective absorption of light over a wide range of frequencies, which is relatively independent of the angle of incidence. Two dimensional gratings would be even better. These flat bands may have potential applications in selective absorbers or in resonant enhanced Raman scattering. In particular, the sharp reflection peaks that we have observed in the experiments for high incident angles may be of interest for filtering applications.

In metallic microcavities (chapter 5 and 6) the introduction of the corrugation into the waveguide introduces band gaps in the dispersion curves. In the context of emissive devices the presence of energy gaps can inhibit the emission if the emission frequency lies in the gap. Both the band-gaps caused by the modes self-crossing at the Brillouin zone boundary and the anti-crossings caused by different modes crossing at other than the Brillouin zone boundary can play an important role in controlling the emission in waveguide structures. In particular, the flat photonic bands (chapter 6) caused by the anti-crossings between SPPs and waveguide modes in the TM polarized dispersion curves are important for all-angle efficient enhancement in light emitting diodes (LEDs) and photodetectors. Here again 2-D gratings would be even better with either square or hexagonal in-plane symmetry.

### **9.3 Future Work**

Though in this thesis we have successfully designed some experiments to confirm aspects of some predicted results, there are indeed a large number of potentially interesting future studies. Here only a small selection of ideas is listed.

For example, in chapter 4 we have attempted to fabricate very deep short-pitch narrow Gaussian-grooved single-interface silver gratings to experimentally observe a family of self-coupled SPPs. However experimental samples fabricated by using the template method described in chapter 2 always have rough surfaces, which results in a lot of unexpected energy loss. It would be of great interest if the deep metallic grating fabrication problems could be overcome to give samples with smooth surfaces.

It is worth noting that very few studies of the coupling of TM polarized radiation to SPPs on thin metallic film gratings in the conical mount have been reported. In chapter 8, we have investigated the resonant absorption enhancement for the SRSPP in details. In our calculations a second original phenomenon, that at some thicknesses zero coupling strength for the TM excited LRSPP, is found to occur. However until now no complete explanation has been found for this new result. To achieve a thorough understanding of this phenomenon, why the zero coupling strength is only observed for the TM polarized LRSPP while no such a similar phenomenon is observed for the TE polarized LRSPP has to be answered. Hence further theoretical and modelling work on thin metallic film gratings in the conical mount should be undertaken. Once a thorough understanding is obtained, a full experimental study could be undertaken in the visible regime through appropriate choice of grating pitch.

In addition the corrugations of the structures studied in this thesis are one dimensional. The most obvious future work is to extend the corrugations from one dimension to two dimensions. As described in chapter 2, a multiple exposure technique has been applied to successfully fabricate two dimensional photoresist gratings. Similar to the fabrication of one dimensional corrugated structures, two dimensional (2-D) experimental corrugated structures, such as 2-D deep single-interface metallic gratings, 2-D corrugated metallic microcavities and 2-D thin metallic film gratings, could certainly be manufactured. These 2-D structures should also have very interesting optical properties. In particular a multi-layer multi-shape modelling method for bi-gratings would be required to be developed to understand the new experimental results.

## **Publications**

1. Z. Chen, I. R. Hooper, and J. R. Sambles, “Low dispersion surface plasmon-polaritons on deep silver gratings”, *Journal of Modern Optics* **53**, 1569 (2006).
2. Z. Chen, I. R. Hooper, and J. R. Sambles, “Photonic bandgaps for grating-coupled waveguide modes with a silver tunnel barrier”, *New Journal of Physics* **9**, 251 (2007).
3. Z. Chen, I. R. Hooper, and J. R. Sambles, “Grating-coupled surface plasmon polaritons and waveguide modes in a silver-dielectric-silver structure”, accepted by *Journal of the Optical Society of America A* in September 2007.
4. Z. Chen, I. R. Hooper, and J. R. Sambles, “Coupled surface plasmons on thin silver gratings”, submitted to *Journal of Optics A* in September 2007.
5. Z. Chen, I. R. Hooper, and J. R. Sambles, “Photonic bandgaps for grating-coupled surface plasmon polaritons and waveguide modes in metallic microcavities”, OSA Nanophotonics, July 18<sup>th</sup>-21<sup>st</sup>, 2007, China (*oral presentation*).

Other publications intended for submission in the near future include:

1. A paper on the coupled SPP modes found on thin silver film gratings bounded by silica in the conical mount described in chapter 8.

## References

- Abram I. & Bourdon G. 1996 *Phys. Rev. A* **54** 3476
- Barnes W. L. 1999 *J. Lightwave Tech.* **17** 2170
- Barnes W. L., Preist T. W., Kitson S. C. & Sambles J. R. 1996 *Phys. Rev. B* **54** 6227
- Boersch H., Geiger J., Imbusch A. & Niedrig N. 1966 *Phys. Lett.* **22** 146
- Bryan-Brown G. P., Sambles J. R. & Hutley M. C. 1990 *J. Mod. Opt.* **37** 1227
- Chandezon J., Dupuis M. T., Comet G. & Maystre D. 1982 *J. Opt. Soc. Am.* **72** 839
- Chandezon J., Maystre D. & Raoult D. 1980 *J. Optics (Paris)* **11** 235
- Cheng D. K. 1989 *Field and Wave Electromagnetics* (Addison-Wesley, Reading, MA)
- Depine R. A. & Lester M. 2001 *J. Mod. Opt.* **48** 1405
- Dowling J. P., Scalora M., Bloemer M. J. & Bowden C. M. 1994 *J. Appl. Phys.* **75** 1896
- Dupta Gupta S., Varada G. V. & Agarwal G. S. 1987 *Phys. Rev. B* **36** 6331
- Ebbesen T. W., Lezec H. J., Ghaemi H. F., Thio T. & Wolff P. A. 1998 *Nature (London)* **391** 667
- Elston S. J., Bryan-Brown G. P. & Sambles J. R. 1991 *Phys. Rev. B* **44** 6393
- Fano U. 1941 *J. Opt. Soc. Am.* **31** 213
- Ferrell R. 1958 *Phys. Rev.* **111** 1214

## References

---

- Garcia-Vidal F. J., Sanchez-Dehesa J., 1999 *J. Lightwave Tech.* **17** 2191  
Dechelette A., Bustarret E., Lopez-Rios T.,  
Fournier T. & Pannetier B.
- Ghaemi H. F., Thio T., Grupp D. E., 1998 *Phys. Rev. B* **58** 6779  
Ebbesen T. W. & Lezec H. J.
- Hibbins A. P. & Sambles J. R. 2000 *Phys. Rev. E* **61** 5900
- Hibbins A. P. & Sambles J. R. 2000 *J. Appl. Phys.* **87** 2677
- Hooper I. R. & Sambles J. R. 2004 *Phys. Rev. B* **70** 045421
- Hooper I. R. & Sambles J. R. 2002 *Phys. Rev. B* **65** 165432
- Hornauer D. & Raether H. 1973 *Opt. Commun.* **7** 297
- Hickernell R. K. & Sarid D. 1986 *J. Opt. Soc. Am. B* **3** 1059
- Hutley M. C. 1982 *Diffraction Gratings*  
(Academic Press)
- Inagaki T., Goudonnet J. P. & Arakawa E. T. 1986 *J. Opt. Soc. Am.* **7** 992
- Inagaki T., Motosuga M., Arakawa E. T. & Goudonnet JP 1985 *Phys. Rev. B* **32** 6238
- Kim T. J., Thio T., Ebbesen T. W., Grupp D. E. & Lezec H. J. 1999 *Opt. Lett.* **24** 256
- Kitson S. C., Barnes W. L. & Sambles J. R. 1998 *J. Appl. Phys.* **84** 2399
- Kretchmann E. & Raether H. 1968 *Z. Naturf. A* **23** 2135
- Landau L. D. & Lifshitz E. M. 1960 *Electrodynamics of continuous media* (Course of theoretical physics, Oxford: Pergamon Press)
- Lee R. K., Painter O. J., D'Urso B., Scherer A. & Yariv A. 1999 *Appl. Phys. Lett.* **74** 1522

## References

---

- Li L. 1995 *Opt. Comm.* **114** 406
- Lopez-Rios T., Mendoza F., Garcia-Vidal F. J., Sanchez-Dehesa J. & Pannetier B. 1998 *Phys. Rev. Lett.* **81** 665
- Lupton J. M., Matterson B. J., Samuel I. D. W., Jory M. J. & Barnes W. L. 2000 *Appl. Phys. Lett.* **77** 3340
- Maradudin A. A. 1983 *J. Opt. Soc. Am* **73** 759
- Müller K. G., Veith M., Mittler-Neher S. & Knoll W. 1997 *J. Appl. Phys.* **82** 4172
- Nash D. J. & Sambles J. R. 1996 *J. Mod. Opt.* **43** 81
- Nash D. J., Cotter N. P. K., Wood E. L., Bradberry G. W. & Sambles J. R. 1995 *J. Mod. Opt.* **42** 423
- Otto A. 1969 *Z. Phys.* **219** 227
- Otto A. 1968 *Z. Phys.* **216** 398
- Park S., Lee G., Song S. H., Oh C. H. & Kim P. S. 2003 *Opt. Lett.* **28** 1870
- Porto J. A., Garcia-Vidal F. J. & Pendry J. B. 1999 *Phys. Rev. Lett.* **83** 2845
- Preist T. W., Cotter N. P. K. & Sambles J. R. 1995 *J. Opt. Soc. Am. A* **12** 1740
- Raether H. 1988 *Surface Plasmons on Smooth and Rough Gratings* (Springer-Verlag, Berlin)
- Rayleigh Lord 1907 *Phil. Mag.* **14** 213
- Ritchie R. H. & Eldridge H. B. 1961 *Phys. Rev.* **126** 1935
- Salakhutdinov I. F., Sychugov V. A. & Parriaux O. 1998 *Quantum Electron.* **28** 983
- Salt M. G., Andrew P. & Barnes W. L. 2001 *J. Opt. Soc. Am. B* **18** 240

## References

---

- Salt M. G. & Barnes W. L. 2000 *Phys. Rev. B* **61** 11125
- Salt M. G. & Barnes W. L. 1999 *Opt. Commun.* **166** 151
- Sarid D. 1981 *Phys. Rev. Lett.* **47** 1927
- Schoenwald J., Burstein E. & Elson J. M. 1973 *Solid State Commun.* **12** 185
- Sobnack M. B., Tan W. C., Wanstall N. P., Preist T. W. & Sambles J. R. 1998 *Phys. Rev. Lett.* **80** 5667
- Stegeman G. I., Burke J. J. & Hall D. G. 1982 *Appl. Phys. Lett.* **41** 906
- Steinmann W. 1960 *Phys. Rev. Lett.* **15** 470
- Strong J. 1935 *Phys. Rev.* **48** 480
- Tan W. C., Preist T. W., Sambles J. R. & Wanstall N. P. 1999 *Phys. Rev. B* **59** 12661
- Teng Y.-Y. & Stern E. A. 1967 *Phys. Rev. Lett.* **19** 511
- Watts R. A., Preist T. W. & Sambles J. R. 1997 *Phys. Rev. Lett.* **79** 3978
- Watts R. A. & Sambles J. R. 1997 *Opt. Comm.* **140** 179
- Watts R. A., Sambles J. R. & Harris J. B. 1997 *Optics Com.* **135** 189
- Weber M. G. & Mills D. L. 1985 *Phys. Rev. B* **31** 2510
- Went H. E. & Sambles J. R. 2001 *Appl. Phys. Lett.* **79** 575
- Wood E. I., Sambles J. R., Cotter N. P. K. & Kitson S. C. 1995 *J. Mod. Opt.* **42** 1343
- Wood R. W. 1902 *Phil. Mag.* **4** 396